An Optimised Oscillation Analysis of MINOS Beam Data

Andrew John Culling
of
Emmanuel College, University of Cambridge

A dissertation submitted to the University of Cambridge
for the degree of Doctor of Philosophy

Abstract

This thesis presents results of the MINOS long baseline neutrino oscillation experiment. Charged Current interactions of ν_μ from the NuMI beamline have been recorded in both the Near and Far Detectors between May 2005 and February 2006, corresponding to 1.27×10^{20} protons being delivered to the NuMI target. Several techniques for improving the sensitivity of an oscillation measurement are discussed and their impact assessed. 378 events are observed in the Far Detector during this period, compared to a prediction of 459 ± 31 events when the observed Near Detector spectrum is extrapolated to the Far Detector over the 735 km baseline with no oscillations. In addition to this deficit of observed events, there is also evidence for spectral distortion in the Far Detector. A maximum likelihood analysis is used to determine the best fit point and allowed regions in Δm^2_{23} and $\sin^2 2\theta_{23}$ parameter space. The best fit values for Δm^2_{23} and $\sin^2 2\theta_{23}$ are found to be $2.55^{+0.39}_{-0.24} \times 10^{-3}\,\mathrm{eV}^2$ and > 0.87 (68% C.L.) respectively.

Declaration

This dissertation is the result of my own work, except where explicit reference is made to the work of others, and has not been submitted for another qualification to this or any other university. This dissertation does not exceed the word limit for the respective Degree Committee.

Andrew Culling

Acknowledgements

This thesis would not have been possible without the help and support of many people, for which I am extremely grateful. In particular I would like to thank Mark Thomson, my supervisor, for being incredibly clever and not laughing at me when I ask really stupid questions. It has also been a great pleasure to work with the Cambridge HEP group and I would like to thank Andy Blake, Andy Buckley, Cauis Howcroft, Chris Jones, Alan Phillips, Martin and Chris White for making my time in the group a lot more fun than it had to be. Special mention must go to my office mates, John Chapman and John Marshall without whose tolerance for my inability to code, mood swings, strange noises and alternative sense of humour, would have made the last 3 years a lot more dysfunctional. The support of the MINOS collaboration has been invaluable in carrying out this work and I'd particularly like to thank David Petyt and Niki Saoulidou for their advice on my analysis.

Of the many friends I have made at Cambridge, I'd like to thank the past and present members of CUFC and CUMPC for allowing me to live like an undergrad for the last three years and making sure that I never looked forward to Thursday mornings, Daniel Haworth for producing some amazing quotes, Jonathan Davies for taking so long over his thesis to provide me with company and Harriet Brown for teaching me all about monkeys and the Sexual Offences Act 2003.

I'd also like to thank my parents for (gastronomically at least) keeping me in the manner to which I have become accustomed. Finally, I must mention 'Ted' Culling, possibly the bravest cat in the world, whose struggle against FIV was an inspiration to me during some of the low points of the last three years. He will be missed.

EDWARD POGADEMUS CULLING, 1996 - 2006

Contents

"... Your cleverest poets will not give you leave to be just and good, even if you want to. For here was Minos, a man who exceeded all men in cruelty, and who enslaved with his navies the inhabitants of continent and islands alike, and yet they honour him by placing in his hand a sceptre of justice and give him a throne in Hades to be umpire of spirits ..."

— Flavius Philostratus, Life of Apollonius of Tyana 3.25

Chapter 1

Introduction

"The most important fundamental laws and facts of physical science have all been discovered, and these are now so firmly established that the possibility of their ever being supplemented in consequence of new discoveries is exceedingly remote."

— Albert Abraham Michelson

Over the last 76 years the neutrino has come from very humble beginnings to become considered as a particle that has played a critical role in the evolution of our universe. The concept of a light, neutral, spin-1/2 particle that was emitted along with an electron during β decay was introduced by Pauli in 1930 [1] as a 'desperate remedy' to the continuous energy spectrum of what should have been two body β decay. This particle was officially named the 'neutrino' by Fermi and the development of his golden rule of β decay in 1934 [2] put the neutrino on a solid theoretical grounding.

The first direct observation of the electron anti-neutrino came from a reactor experiment by Reines and Cowan in 1956 [3] and this was followed by the discovery of the muon [4] and tau [5] neutrinos in 1962 and 2001 respectively, completing the list of particles expected from the Standard Model. The helicity of the electron neutrino was measured to be -1 in 1958 [6], and the failure to observe any right-handed neutrinos taking part in the weak interaction led to the belief that they were fully polarised, so massless. This was unsurprising as attempts to directly measure neutrino masses by looking closely at the kinematics of decays producing neutrinos have only resulted in upper limits [7–9] and recent results from cosmology put these limits even lower [10]. During this time, it also was found that neutrinos must play a vital role in solar physics both being an essential

part of the CNO cycle [11] and being the driving force behind supernovae explosions [1].

As time went by, a mass of evidence began to point towards discrepancies in the observed spectra of electron neutrinos from the sun [12] compared to the Standard Solar Model. Also the observed ratio of muon and electron neutrinos produced by interactions of cosmic rays with the upper atmosphere [1] significantly deviated from expectation, given the reactions producing them. A possible solution to these problems had already been postulated by Pontecorvo in 1958 [13], with the idea of that it was possible for neutrinos to switch flavour or 'oscillate' as they travelled, meaning that there was no actual deficit in the solar or atmospheric neutrino flux, it was just that the flavour content of the flux was changing. However, this idea had the slightly controversial requirement that it was only possible for the neutrinos to oscillate if they had mass. The results of the Super Kamiokande [14], SNO [15] and Kamland [16] experiments show very good agreement with the neutrino oscillation hypothesis and it is now well established as the solution to the solar and atmospheric neutrino anomalies.

The NuMI-MINOS experiment is one of several next generation neutrino oscillation experiments that, instead of relying on neutrinos from the sun or upper atmosphere, use a man-made beam of neutrinos created using an accelerator. MINOS aims to further confirm the existence of oscillations and to accurately measure the parameters which control the phenomenon. The MINOS detectors use a tracking calorimeter with a magnetic field, meaning not only is it possible to fully reconstruct the energy of neutrino events but it is also able to determine the charge of any lepton produced, thereby identifying events caused by neutrinos and anti-neutrinos. This thesis details the first attempt to extract the oscillation parameters from NuMI beam events in the MINOS detectors.

In Chapter 2 the current experimental results and background theory of neutrino oscillations will be covered. Chapter 3 details the instrumentation and operation of the NuMI beamline and three MINOS detectors as well as the Monte Carlo simulation used for the experiment. The process of reconstructing neutrino events and estimating their energy is detailed in chapter 4. Chapters 5 and 6 concern event selection and comparisons between data and Monte Carlo for the Near and Far Detectors respectively. A Bayesian approach is used to develop a method to assign an energy resolution for each event and its use in extraction of the oscillation parameters is presented in Chapter 7. The conclusions of this thesis are set out in Chapter 8, results are summarised and consideration is given to the sensitivity of future measurements.

Chapter 2

Neutrino Physics

"Knowledge must come through action; you can have no test which is not fanciful, save by trial."

— Sophocles, Trachiniae

2.1 Neutrino Masses

In its current form the Standard Model makes no predictions for neutrino masses and the failure to observe right handed neutrinos taking part in the weak interaction, led many to believe they were fully polarised, so massless. However, since their discovery, several attempts have been made to directly measure the masses of neutrinos but they have only been able to obtain limits. Most of these experiments worked by studying the energy spectra of decays involving neutrinos and looking closely at the end-points to see if there is any deviation from what would be expected from a massless particle. The current limits are summarised as:

$$m_{\nu_e} \leq 2.3\,\mathrm{eV}/c^2 \text{ (95\% C.L., from } {}^3H \rightarrow {}^3He + e^- + \overline{\nu}_e) \text{ [7]},$$

$$m_{\nu_\mu} \leq 170\,\mathrm{keV}/c^2 \text{ (90\% C.L., from } \pi^+ \rightarrow \mu^+ + \nu_\mu) \text{ [8]},$$

$$m_{\nu_\tau} \leq 15.5\,\mathrm{MeV}/c^2 \text{ (95\% C.L., from } \tau \rightarrow 5\pi + \nu_\tau) \text{ [9]}.$$

Another limit on neutrino masses has come from the slightly unexpected field of cosmology. By studying galactic power spectra, which are sensitive to the galaxy's total matter density and using the Cosmic Microwave Background to constrain degeneracies of the effect of neutrino masses on these spectra, it is possible to put a limit on the total mass of all three neutrino flavours:

$$\Sigma m_\nu < 0.75\,\mathrm{eV}\ (2\sigma)\,[10].$$

A final method for measuring neutrino masses is to observe neutrinoless double beta ($0\nu\beta\beta$) decay [17]. This can only occur in isotopes where two neutrino double beta ($2\nu\beta\beta$) decay is possible and requires the neutrino to be a Majorana particle (i.e. the neutrino is its own antiparticle). The signal for $0\nu\beta\beta$-decay is two final state electrons whose energies add to the Q value of the nuclear transition and the $0\nu\beta\beta$ rate varies with Q^5 (as opposed to Q^{11} for $2\nu\beta\beta$-decay). The half-life for $0\nu\beta\beta$-decay can be used to extract the effective neutrino Majorana mass. Officially no experiment has observed $0\nu\beta\beta$-decay, with the most sensitive giving a limit of $m_\nu < 0.35\,\mathrm{eV}$ (90% C.L.).

2.2 Neutrino Oscillations

The flavour of a neutrino is defined by the flavour of the lepton that it produces when it undergoes a charged current interaction (the flavour of the lepton being defined by its mass). If the neutrino flavour eigenstates (that take part in the weak interaction) are not aligned with the neutrino mass eigenstates, then it is possible to express the flavour eigenstates (ν_e,ν_μ,ν_τ) as linear superpositions of the mass eigenstates (ν_1,ν_2,ν_3).

$$\begin{pmatrix} \nu_e \\ \nu_\mu \\ \nu_\tau \end{pmatrix} = \begin{pmatrix} U_{e1} & U_{e2} & U_{e3} \\ U_{\mu 1} & U_{\mu 2} & U_{\mu 3} \\ U_{\tau 1} & U_{\tau 2} & U_{\tau 3} \end{pmatrix} \begin{pmatrix} \nu_1 \\ \nu_2 \\ \nu_3 \end{pmatrix}$$

where U is the Pontecorvo-Maki-Nakagawa-Sakata (PMNS) lepton mixing matrix. The mass eigenstates will propagate as:

$$|\nu_1(\mathbf{x})\rangle = |\nu_1(0)\rangle e^{-i\mathbf{p_1}.\mathbf{x}}$$

where $\mathbf{p_1}$ is the energy-momentum 4-vector associated with mass eigenstate ν_1 and $\mathbf{x}$ is the time-space 4-vector from its point of production. If we consider an initially pure beam of ν_μ it will propagate as:

$$|\nu_\mu(\mathbf{x})\rangle = U_{\mu 1}|\nu_1(0)\rangle e^{-i\mathbf{p_1}.\mathbf{x}} + U_{\mu 2}|\nu_2(0)\rangle e^{-i\mathbf{p_2}.\mathbf{x}} + U_{\mu 3}|\nu_3(0)\rangle e^{-i\mathbf{p_3}.\mathbf{x}}$$

If the PNMS matrix is inverted so that the mass eigenstates can be represented as linear superpositions of the weak eigenstates, then under substitution the above equation becomes:

$$\begin{aligned}|\nu_\mu(\mathbf{x})\rangle = &(U_{\mu 1}U^*_{e1}e^{-i\mathbf{p_1}.\mathbf{x}} + U_{\mu 2}U^*_{e2}e^{-i\mathbf{p_2}.\mathbf{x}} + U_{\mu 3}U^*_{e3}e^{-i\mathbf{p_3}.\mathbf{x}})|\nu_e\rangle \\ &+(U_{\mu 1}U^*_{\mu 1}e^{-i\mathbf{p_1}.\mathbf{x}} + U_{\mu 2}U^*_{\mu 2}e^{-i\mathbf{p_2}.\mathbf{x}} + U_{\mu 3}U^*_{\mu 3}e^{-i\mathbf{p_3}.\mathbf{x}})|\nu_\mu\rangle \\ &+(U_{\mu 1}U^*_{\tau 1}e^{-i\mathbf{p_1}.\mathbf{x}} + U_{\mu 2}U^*_{\tau 2}e^{-i\mathbf{p_2}.\mathbf{x}} + U_{\mu 3}U^*_{\tau 3}e^{-i\mathbf{p_3}.\mathbf{x}})|\nu_\tau\rangle\end{aligned}$$

This means that if the matrix is non-diagonal then the beam will have components of ν_e and ν_τ. The probability of observing ν_μ at a distance $\overline{\mathbf{x}}$ is:

$$P(\nu_\mu \to \nu_\mu) = |\langle\nu_\mu|\nu_\mu(\mathbf{x})\rangle|^2$$

If the expression for $|\nu_\mu(\mathbf{x})\rangle$ is substituted into the above equation and unitarity conditions applied then the expression becomes:

$$\begin{aligned}P(\nu_\mu \to \nu_\mu) = 1 &- 4|U_{\mu 1}|^2|U_{\mu 2}|^2\sin^2(\tfrac{(\mathbf{p_1}-\mathbf{p_2}).\mathbf{x}}{2}) \\ &-4|U_{\mu 1}|^2|U_{\mu 3}|^2\sin^2(\tfrac{(\mathbf{p_1}-\mathbf{p_3}).\mathbf{x}}{2}) \\ &-4|U_{\mu 2}|^2|U_{\mu 3}|^2\sin^2(\tfrac{(\mathbf{p_2}-\mathbf{p_3}).\mathbf{x}}{2})\end{aligned}$$

If it is assumed that the neutrinos are travelling at the speed of light along a particular axis then $\mathbf{\Delta p}.\mathbf{x} = \Delta E t - \Delta\overline{\mathbf{p}}.\overline{\mathbf{x}} = (\Delta E - \Delta p_x)x$. If it is also assumed that the mass of the neutrino is small compared to its energy, then a binomial expansion of $p = (E^2 - m^2)^{\frac{1}{2}}$ gives $p \sim E - \frac{m^2}{2E}$. Application of this to $\mathbf{\Delta p}.\mathbf{x} = (\Delta E - \Delta p)x$, combined with the assumption that $E_1 = E_2 = E$ gives $\mathbf{\Delta p}.\mathbf{x} = \frac{\Delta m^2 x}{2E}$ which can be inserted back into the original equation for $|\nu_\mu(\mathbf{x})\rangle$:

$$\begin{aligned}P(\nu_\mu \to \nu_\mu) = 1 &- 4|U_{\mu 1}|^2|U_{\mu 2}|^2\sin^2(\tfrac{\Delta m^2_{12}L}{4E}) \\ &-4|U_{\mu 1}|^2|U_{\mu 3}|^2\sin^2(\tfrac{\Delta m^2_{13}L}{4E}) \\ &-4|U_{\mu 2}|^2|U_{\mu 3}|^2\sin^2(\tfrac{\Delta m^2_{23}L}{4E})\end{aligned}$$

where L is the distance travelled from the point of production and $\Delta m^2_{ij} = m^2_i - m^2_j$.

A general equation, applicable to any combination of neutrino flavours, can be written in the form:

$$P(\nu_\alpha \to \nu_\beta) = \delta_{\alpha\beta} - 2\Re \sum_{j>i} U_{\alpha i} U^*_{\alpha j} U^*_{\beta i} U_{\beta j} (1 - e^{(i\Delta m^2_{ji} L/4E)})$$

where i and j are the mass eigenstates. It is possible to parameterise the PMNS mixing matrix in a similar way to the CKM matrix for quark mixing [18] based on the angles of rotation between the flavour and mass eigenstates and a complex phase, δ (which if non-zero would lead to CP violation in the lepton sector):

$$U_{PMNS} = \begin{pmatrix} c_{12}c_{13} & s_{12}c_{13} & s_{13}e^{-i\delta} \\ -s_{12} - c_{12}s_{23}s_{13}e^{i\delta} & c_{12}c_{23} - s_{12}s_{23}s_{13}e^{i\delta} & s_{23}c_{13} \\ s_{12}s_{23} - c_{12}c_{23}s_{13}e^{i\delta} & -c_{12}s_{23} - s_{12}c_{23}s_{13}e^{i\delta} & c_{23}c_{13} \end{pmatrix}$$

where $c_{ij} = \cos\theta_{ij}$ and $s_{ij} = \sin\theta_{ij}$ (for i,j = 1,2,3). It is convenient to parameterise the matrix into the following form for the interpretation of neutrino experiments:

$$U_{PMNS} = \begin{pmatrix} 1 & 0 & 0 \\ 0 & c_{23} & s_{23} \\ 0 & -s_{23} & c_{23} \end{pmatrix} \begin{pmatrix} c_{13} & 0 & s_{13}e^{-i\delta} \\ 0 & 1 & 0 \\ -s_{13}e^{i\delta} & 0 & c_{13} \end{pmatrix} \begin{pmatrix} c_{12} & s_{12} & 0 \\ -s_{12} & c_{12} & 0 \\ 0 & 0 & 1 \end{pmatrix}$$

Experimentally it has been observed that θ_{13} is small and that Δm^2 for Solar neutrino oscillations is nearly two orders of magnitude smaller than the value for Atmospheric neutrino oscillations. This means that for many purposes the two matrices containing solely terms of either θ_{12} and θ_{23} can be considered independently, making it possible to justify studying neutrino oscillations between just two flavours considering a single mass difference and mixing angle. In this case the expression for the mixing matrix becomes:

$$\begin{pmatrix} \nu_\alpha \\ \nu_\beta \end{pmatrix} = \begin{pmatrix} \cos\theta_{ab} & \sin\theta_{ab} \\ -\sin\theta_{ab} & \cos\theta_{ab} \end{pmatrix} \begin{pmatrix} \nu_a \\ \nu_b \end{pmatrix}$$

This then gives a simplified expression for the oscillation probability (where L is in units of km, E is in units of GeV and Δm^2 is in units of eV^2):

$$P(\nu_\alpha \to \nu_\beta) = |\delta_{\alpha\beta} - \sin^2 2\theta_{ab} \sin^2(1.27\Delta m^2_{ab} L/E)|$$

The amplitude of the oscillation is determined by the mixing angle, the value of L/E at which they occur, and Δm^2. When this is applied to the MINOS experiment, studying $\nu_\mu \to \nu_\tau$ oscillations with a baseline (L) of 735 km and assuming $\Delta m^2_{atm} \sim \Delta m_{23} = 2.1 \times 10^{-3}\mathrm{eV}^2$ and $\sin^2 2\theta_{23} = 1$ from Super Kamiokande [19], then the maximum probability of oscillation will occur at an Energy of ~ 1.25 GeV.

2.2.1 Matter Effects

The above analysis of neutrino oscillations has been made with the assumption that the neutrinos have been propagating through a vacuum. However, for many neutrino oscillation experiments this is not the case as they involve neutrinos that have propagated large distance through the Earth or Sun. Propagation through matter will affect neutrinos via coherent forward scattering from atomic electrons. This can take place via neutral current interactions, but with electron neutrinos charged current interactions are also possible. The effect of this scattering is to add an effective potential of the form $V = \sqrt{2} G_F n_e$ where G_F is the Fermi coupling constant and n_e is the electron number density in the material. This results in effective mixing angles and mass differences. It is particularly relevant for solar neutrinos due to the high density of solar matter. This is known as the MSW effect (after Mikheev, Smirnov and Wolfenstein [20],[21]).

2.3 Current Evidence for Neutrino Oscillations

Acceptance of the theory of neutrino oscillation has grown massively over the last few years, particularly as it provides a convincing solution to the solar and atmospheric neutrino anomalies. Aside from this major result there are also many supporting results from other experiments using neutrinos from nuclear reactors and accelerators.

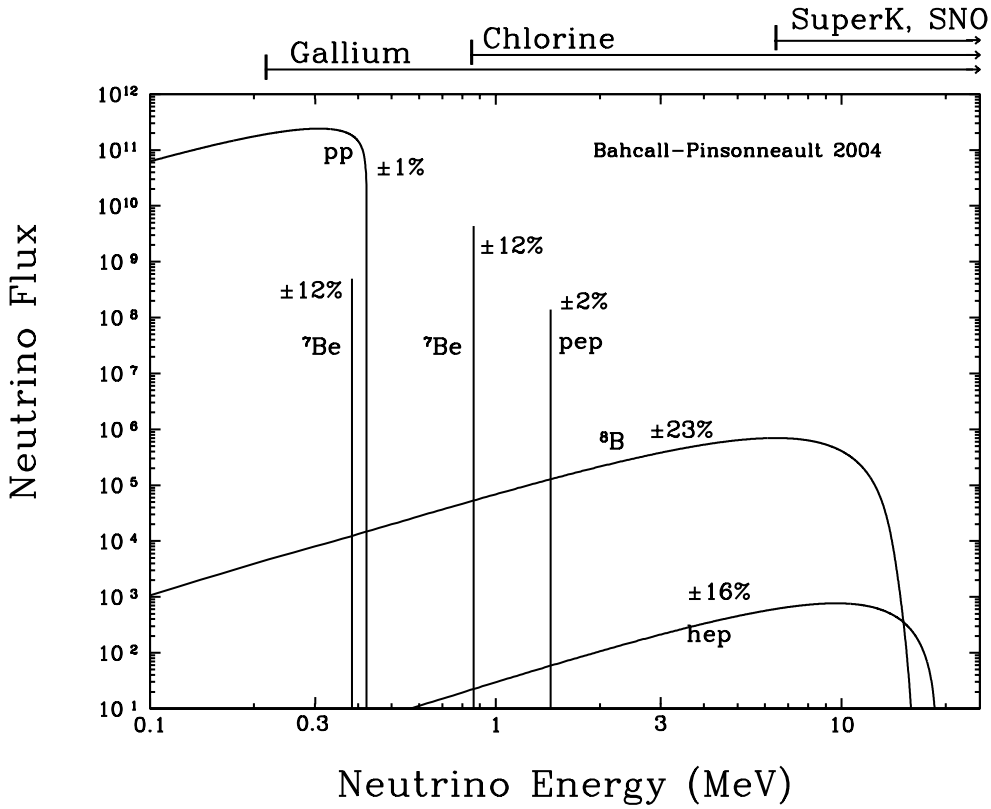

Figure 2.1: Energy spectra of ν_e produced by various nuclear processes in the sun, their relative uncertainties and which experiments are sensitive to the different energy ranges. Figure taken from [23].

2.3.1 Solar Neutrinos

The weak interaction is integral to the process of nuclear fusion that occurs within the sun as it allows the formation of deuterons from protons, permitting fusion reactions to occur that produce heavier elements through the p-p chain:

$$4p \rightarrow {}^4\mathrm{He} + 2\nu_e + 26.73 \text{ MeV}$$

This results in a large flux of electron neutrinos, the energy spectrum of which, along with ν_e from other reactions including Beryllium and Boron is calculated using the Standard Solar Model (SSM) [22]. The SSM prediction for the solar ν_e spectrum is shown in Figure 2.1.

This flux depends heavily on the temperature and luminosity of the sun, so constraints can be placed upon these fluxes through observations of these quantities. The SSM predicts the solar ν_e fluxes with uncertainties at the level of a few percent, but every experiment that has attempted to measure this flux has recorded a deficit with respect to the SSM predictions over the whole energy spectrum.

Initially this led to questioning of the accuracy of the SSM predictions, but heliosiesmological measurements [24] provided a new avenue of support for the SSM, leading to it being widely accepted by the solar physics community. The methodology of each of the solar neutrino experiment is dependent upon the energy range of the neutrinos they are attempting to observe. The experiments and results are discussed below.

2.3.2 Radiochemical Experiments

The initial evidence of a solar neutrino deficit came from the Homestake experiment [25]. This makes use of the inverse β decay reaction:

$$\nu_e + {}^{37}\mathrm{Cl} \rightarrow {}^{37}\mathrm{Ar} + e^-$$

with the ^{37}Cl being contained in 615 tons of tetrachloroethylene. The rate at which ^{37}Ar is produced determines the ν_e flux for neutrinos above the threshold energy of 0.814 MeV. The rate of ^{37}Ar production was measured monthly by flushing the tetrachloroethlyene tank with helium and passing it through a charcoal trap which absorbs the ^{37}Ar. After purification, gas-filled proportional counters are used to count the rate of Auger electrons from ^{37}Ar decays by K orbital electron capture. The tank is located 1478 m underground (4200 m water equivalent) to shield the detector from cosmic muons.

Using this method the solar ν_e flux was measured to be $2.56 \pm 0.16(stat.) \pm 0.16(syst.)$ Solar Neutrino Units (SNU), where 1 SNU $\equiv 10^{-36}$ neutrino interactions per target atom s^{-1}. This is significantly different from the SSM prediction of 8.5 ± 1.8 SNU [12].

The Homestake experiment released its first results in 1968 and in the 1980s other radiochemical experiments began taking data, namely SAGE [26], GALLEX [27] and GNO [28]. These experiments used Gallium instead of Chlorine, utilising the reaction:

$$\nu_e + {}^{71}\mathrm{Ga} \rightarrow {}^{71}\mathrm{Ge} + e^-$$

The advantage of using this reaction is its greatly reduced threshold energy of 0.233 MeV, making them sensitive to the highly abundant flux of ν_e from the p-p chain, meaning that the detectors could be relatively small. SAGE uses 60 tons of liquid Gallium and both GALLEX and GNO used 100 tons of Gallium Chloride. The production rates of ^{71}Ge were measured in a similar way to the ^{37}Ar rates in the Homestake experiment. The results of all three experiments agree well with each other, a combined GALLEX-GNO result gives a flux of 69.3 ± 5.5 SNU and a flux of $70.8^{+5.3}_{-5.2}(stat.)^{+3.7}_{-3.2}(syst.)$ SNU is measured by SAGE. As with the Homestake experiment these results show a large deficit when compared to the predicted SSM flux of 131^{+12}_{-10} SNU.

2.3.3 Water Čerenkov Experiments

Super-Kamiokande

The Super-Kamiokande (SK) experiment [14] consists of a large cylinder filled with 50 kt of ultra-pure water. It is divided into an outer detector of 18 kt lined with photomultiplier tubes (PMTs) which act as a veto against through-going cosmic muons and radioactive decays in the surrounding rock, and an inner detector of 32 kt (22.5 kt fiducial volume) lined with 11146 PMTs. The principal method of neutrino detection is from elastic scattering off electrons via the process:

$$\nu_x + e^- \rightarrow \nu_x + e^-$$

where $x = e, \mu, \tau$. The energies of the solar neutrinos are greater than the rest mass of the electron, so there is an additional charged current interaction for electron neutrinos, meaning their overall cross-section is approximately six times greater than for the other flavours. The recoiling electron produces a ring of Čerenkov light on the PMTs on the wall of the vessel allowing their detection (above a threshold of 5MeV) and reconstruction of their direction and energy. There is a strong correlation between the direction of the recoiling electron and incoming neutrino, which allows solar neutrinos to be identified as events which point back to the sun, leading to a significant reduction in background. Figure 2.2 shows the angular distribution of solar neutrino candidates and a prediction of backgrounds added to the best fit solar neutrino flux.

SK measured the solar ν_e flux to be $2.35 \pm 0.002(stat.) \pm 0.08(syst.) \times 10^6 \mathrm{cm}^2\mathrm{s}^{-1}$ [14], representing a large discrepancy with the predicted SSM flux of $5.79(1 \pm 0.23) \times 10^6 \mathrm{cm}^2\mathrm{s}^{-1}$

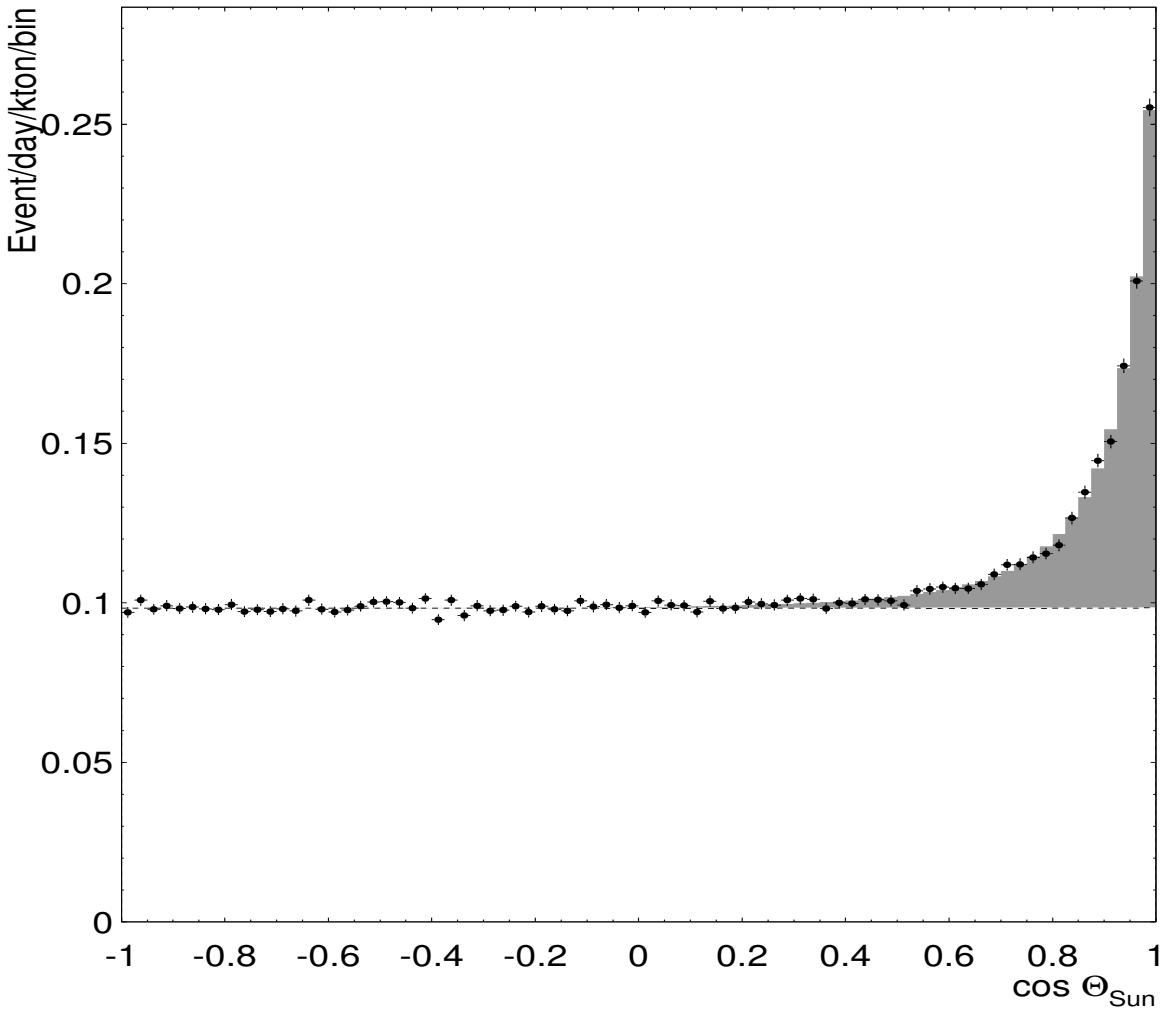

Figure 2.2: Angular distribution of SK solar neutrino candidates (black points) and prediction of backgrounds added to the best fit solar neutrino flux (shaded area). Figure taken from [14].

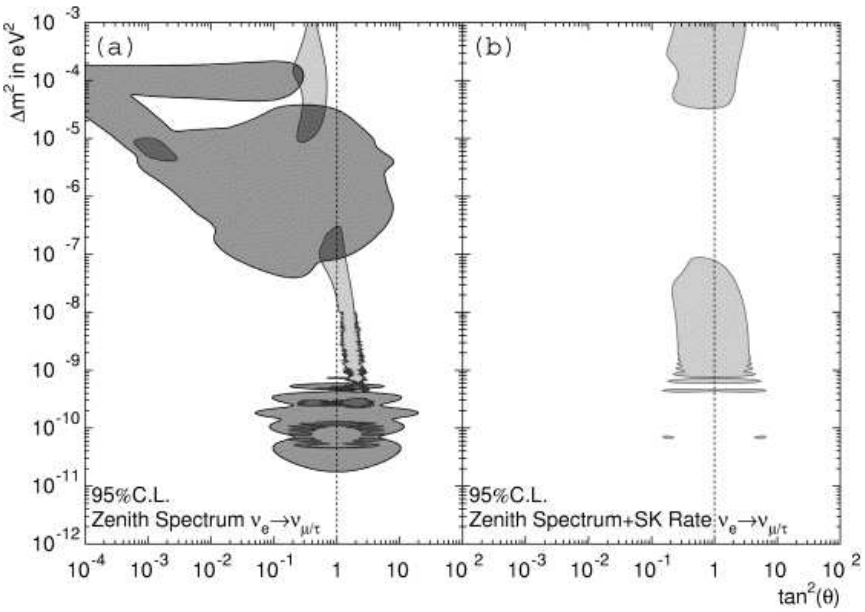

Figure 2.3: (a) SSM flux independent excluded areas (grey) using the SK zenith spectrum shape alone overlaid with the allowed regions of figure (b) in light gray. The overlap of both is shaded dark grey. (b) Allowed areas using only SK data and the SSM ^{8}B neutrino flux prediction. Both allowed regions indicate large neutrino mixing. Figure taken from [29].

[12]. No distortions were observed in the zenith angle distributions (also known as day-night distributions), looking for any variation in the flux with the neutrino path length. This allowed large regions of neutrino oscillation parameter space to be excluded, as shown in Figure 2.3.

SNO

The Sudbury Neutrino Observatory (SNO) [15] consists of 1 kt of heavy water surrounded by 9456 PMTs shielded by a further 7 kt of light water to act as a veto. It is located 2 km underground in the Creighton mine, Sudbury. The experiment detects neutrinos by three different processes:

1) Elastic Scattering via:

$$\nu_x + e^- \rightarrow \nu_x + e^-$$

where $x = e, \mu, \tau$. As before the ν_e cross-section is enhanced due to the CC contribution. The recoil electron is detected via its Čerenkov light.

2) Charged Current interactions where the neutrino interacts with the nucleus of a deuteron, only possible for ν_e:

$$\nu_e + d \rightarrow p + p + e^-$$

3) Neutral current interactions on the deuterium nucleus, possible for all flavours of neutrino:

$$\nu_x + d \rightarrow n + p + \nu_x$$

where $x = e, \mu, \tau$. In this case the neutron is detected via the γ ray emitted when it is captured by another nucleus. In the second phase of the experiment NaCl was dissolved into the water as the Cl neutron capture rate is four times higher than deuterium. In the third phase, neutrons were detected directly using an array of proportional counters hung in the fiducial volume of the detector. The gamma rays interact via Compton scattering producing energetic electrons. The Čerenkov light from neutron capture is more isotropic than for CC or ES events allowing them to be separated statistically.

SNO measured the following fluxes for the different neutrino interactions (in units of $10^6 \mathrm{cm}^2\mathrm{s}^{-1}$) [15]:

$$\text{ES: } 2.35 \pm 0.22(stat.) \pm 0.15(syst.)$$

$$\text{CC: } 1.68 \pm 0.06(stat.)^{+0.08}_{-0.09}(syst.)$$

$$\text{NC: } 4.94 \pm 0.21(stat.)^{+0.38}_{-0.34}(syst.)$$

The ability to measure the NC as well as CC flux allows the ν_e and ν_μ+ν_τ fluxes to be separated. Figure 2.4 shows how the separate measurements are consistent with one another.

The SNO results confirm the ν_e flux deficit observed in other experiments while at the same time confirming that the SSM prediction for the total neutrino flux.

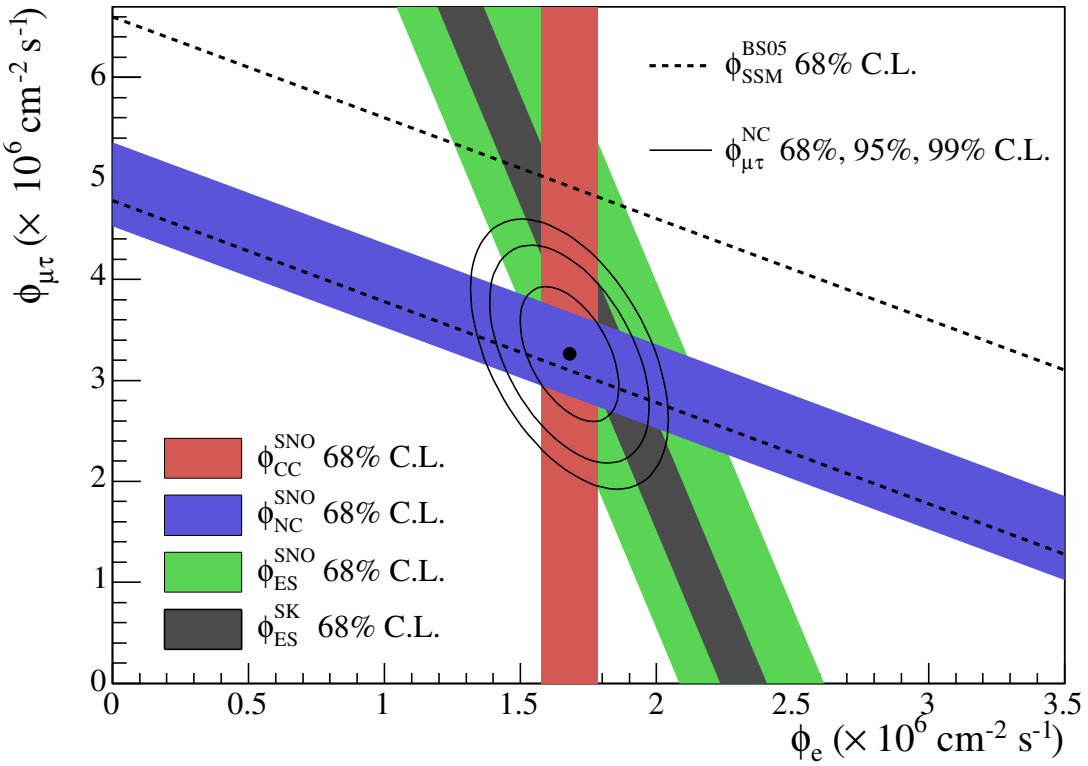

Figure 2.4: Flux of ν_μ+ν_τ versus flux of ν_e. The CC, NC and ES flux measurements are indicated by the filled bands. The total ^{8}B solar neutrino flux predicted by the SSM is shown as dashed lines, and that measured with the NC channel is shown as the solid band parallel to the model prediction. The narrow band parallel to the SNO ES result corresponds to the Super-Kamiokande result. The intercepts of these bands with the axes represent the $\pm 1\sigma$ uncertainties. The non-zero value of $\phi_{\mu\tau}$ provides strong evidence for neutrino flavour transformation. The point represents ϕ_e from the CC flux and $\phi_{\mu\tau}$ from the NC-CC difference with 68%, 95% and 99% C.L. contours included. The figure is taken from [15].

2.3.4 Reactor Experiments

The Kamioka liquid scintillator anti-neutrino detector (KamLAND) [16] consists of 1 kt of ultra pure liquid scintillator in a transparent nylon based balloon surrounded by non-scintillating oil covered by 1879 PMTs. It is based in the former home of the Kamiokande experiment and probes the same region of parameter space as the solar neutrino experiments by measuring the $\overline{\nu}_e$ spectra from Japan's nuclear reactors located an average distance of 180 km away.

The $\overline{\nu}_e$ are detected by inverse β-decay reaction:

$$\overline{\nu}_e + p \rightarrow n + e^+$$

The interactions are detected by looking for the prompt scintillation light from e^+, giving an estimate of $E_{\overline{\nu}_e}$. The delayed 2.2 MeV γ from neutron capture on Hydrogen allows for significant background reduction, with a threshold of 1.8 MeV. After a 766 ton-year exposure, the measured $\overline{\nu}_e$ flux for events with reconstructed $E_{\overline{\nu}_e} > 2.6$ MeV was $0.658 \pm 0.044(stat.) \pm 0.047(syst.)$ of the flux expected in the absence of neutrino oscillations. In addition to this flux deficiency, spectral distortion was observed as shown in Figure 2.5.

The ratio of observed to expected events as a function of $L/E_{\overline{\nu}_e}$ was also found to be consistent with the flavour oscillation hypothesis as opposed to other models as shown in Figure 2.6. The other models usually considered as a alternative to neutrino oscillations are neutrino quantum decoherence [30] and neutrino decay [31]. Neutrino quantum decoherence is a process whereby flavour change can occur due to loss of coherence of the neutrinos quantum mechanical phases. In the Standard Model this is possible if the neutrinos have travelled a very large distance (e.g. arriving at Earth from supernovae) as the mass eigenstates will propagate at different velocities. However, physics beyond the Standard Model, usually quantum gravity, is required for decoherence to be observed on the length scales of solar and atmospheric neutrino experiments. Neutrino decay considers the possibility that the neutrino mass states are unstable, meaning that neutrinos can decay either into a neutrino of another flavour, a sterile neutrino or unknown particles.

The KamLAND results taken in combination with the solar neutrino flux measurements put substantial constraints on the oscillation parameters as shown in Figure 2.7 and give best fit values of $\Delta m^2_{solar} = 7.9^{+0.6}_{-0.5} \times 10^{-5}\,\mathrm{eV}^2$ and $\tan^2\theta_{solar} = 0.40^{+0.10}_{-0.07}$.

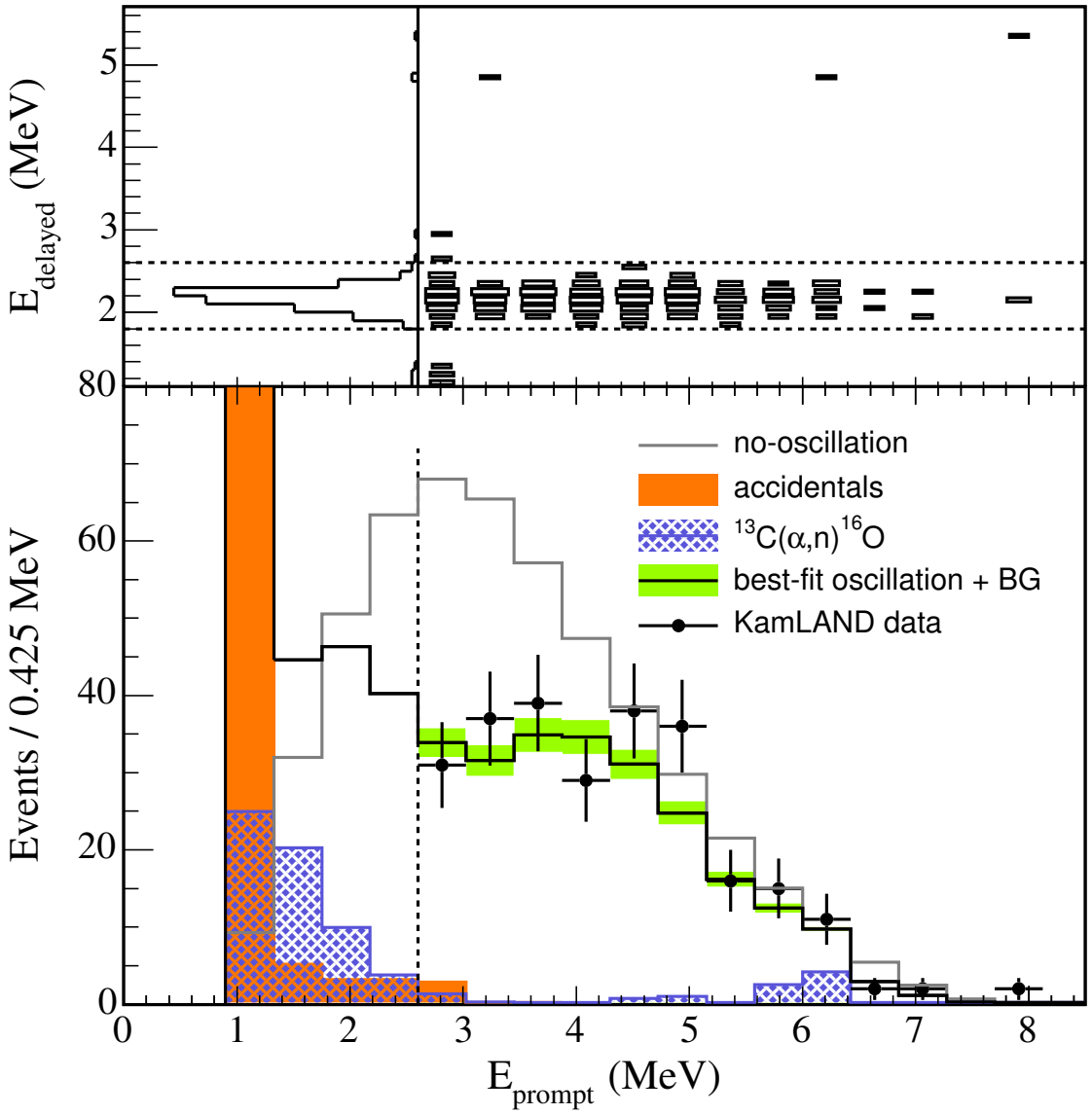

Figure 2.5: (a) The correlation between the prompt and delayed event energies after cuts. The three events with $E_{delayed} \approx 5$ MeV are consistent with neutrino capture on carbon. (b) Prompt event energy spectrum of $\overline{\nu}_e$ candidate events with associated background spectra. The shaded region indicates the systematic error in the best-fit reactor spectrum above 2.6 MeV. Figure taken from [16].

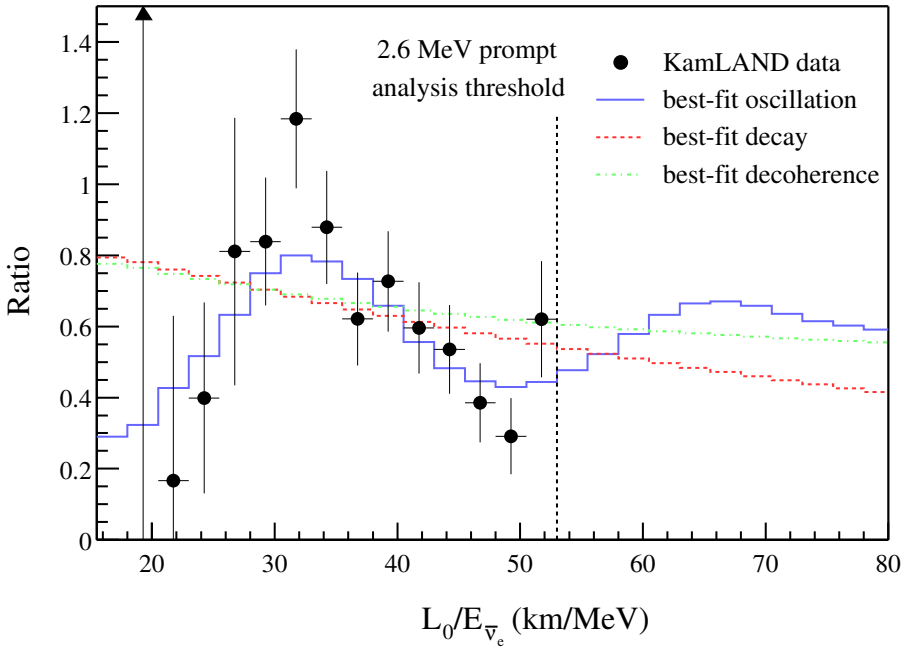

Figure 2.6: Ratio of the observed $\overline{\nu}_e$ spectrum to the expectation for no-oscillation versus $L_0/E_{\overline{\nu}_e}$. The curves show the expectation for the best-fit oscillation, best-fit decay and best-fit decoherence models taking into account the individual time-dependent flux variations of all reactors and detector effects. The data points and models are plotted with $L_0 = 180$ km, as if all anti-neutrinos detected in KamLAND were due to a single reactor at this distance. Figure taken from [16].

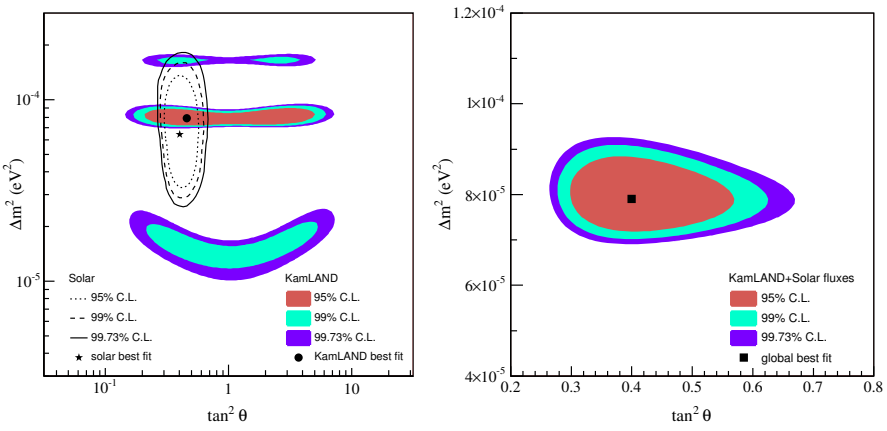

Figure 2.7: (a) Neutrino oscillation parameter allowed from KamLAND anti-neutrino data (shaded regions) and solar neutrino experiments (lines). (b) Result of a combined two-neutrino oscillation analysis from KamLAND and the observed solar neutrino fluxes under the assumption of CPT invariance. The fit gives $\Delta m^2 = 7.9^{+0.6}_{-0.5} \times 10^{-5}\,\mathrm{eV}^2$ and $\tan^2\theta = 0.40^{+0.10}_{-0.07}$ including the allowed 1-sigma parameter range. Figure taken from [16].

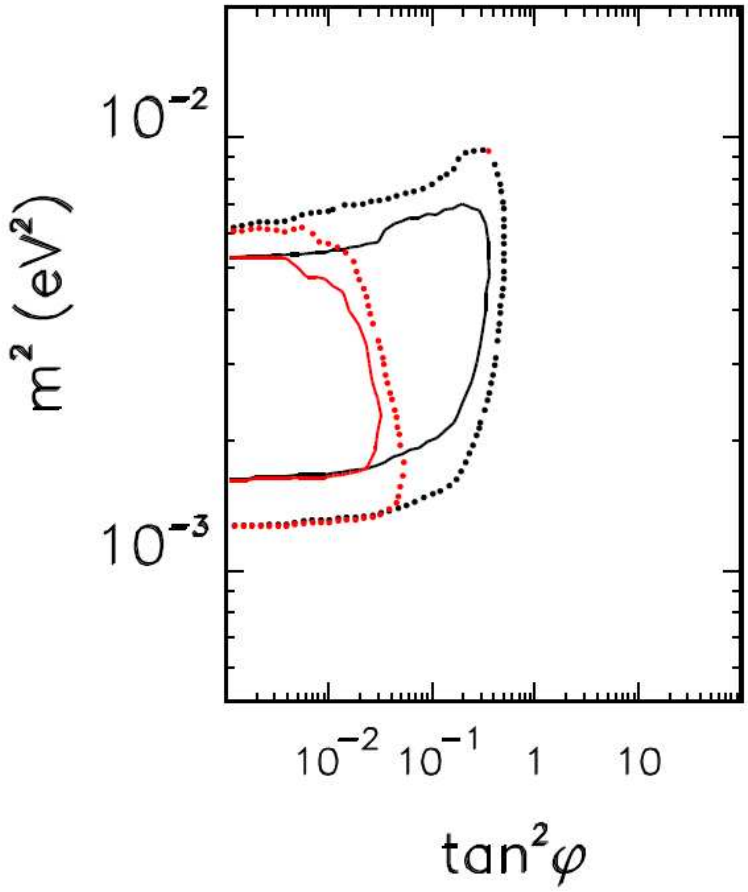

Figure 2.8: 90% (solid line) and 99% (dotted line) C.L. limits in the $\Delta m^2_{23}, \tan^2\theta_{13}$ parameter space obtained from Super-Kamiokande alone (black line) and CHOOZ + Super-Kamiokande (red line), taken from [32].

2.3.5 CHOOZ and θ_{13}

The CHOOZ experiment [32] used a 1km baseline and Gadolinium loaded liquid scintillator detector to search for evidence of neutrino oscillations in the flux of $\overline{\nu}_e$ from the twin reactors of the CHOOZ nuclear power station in Northern France. The flux was measured via the inverse β decay reaction, as with other reactor experiments. No evidence was found for neutrino oscillations in the $\overline{\nu}_e$ disappearance mode. However, when the results are combined with knowledge of the oscillation parameters connected with solar and atmospheric neutrino oscillations and the full 3-flavour oscillation framework considered, it is possible for the experiment to put a limit on the mixing angle of the sub-dominant oscillation mode, θ_{13} as shown in Figure 2.8.

This subdominant mode is important as it gives a mechanism for CP violation in the lepton sector if θ_{13} is non-zero. A new generation of proposed experiments will attempt to measure θ_{13} either using reactors (e.g. Double CHOOZ [33], Daya Bay [34]) or looking for ν_e appearance in a ν_μ beam (e.g. NOvA [35], T2K [36]).

2.3.6 Atmospheric Neutrinos

The upper atmosphere of the Earth is constantly being bombarded by cosmic rays, the vast majority of which are protons with a smaller component of heavier nuclei. The interaction of the cosmic rays with the nuclei leads to a flux of atmospheric neutrinos from the following processes:

$$p + N \rightarrow n\pi^{\pm} + X$$

$$\pi^{\pm} \rightarrow \mu^{\pm} + \nu_\mu(\overline{\nu}_\mu)$$

$$\mu^{\pm} \rightarrow e^{\pm} + \nu_e(\overline{\nu}_e) + \overline{\nu}_\mu(\nu_\mu)$$

Which leads to the ratio:

$$R = \frac{N(\nu_\mu + \overline{\nu}_\mu)}{N(\nu_e + \overline{\nu}_e)} \sim 2$$

This ratio rises for higher neutrino energies as the muons that produce the ν_e and $\overline{\nu}_e$ have more energy and therefore longer lifetimes due to relativistic effects, meaning they are less likely to decay before reaching the surface of the Earth. Experiments designed to study the flux of atmospheric neutrinos typically work by detecting charged current neutrino interactions and using the produced lepton to determine the flavour, direction and energy of the incident neutrino with a tracking calorimeter or water Čerenkov detector. The first atmospheric neutrino results were from the IMB [37] and Kamiokande [38] experiments in 1986 and 1988 respectively. Both of these experiments observed a deficit in R′, the ratio of the measured and Monte Carlo prediction of R. The Kamiokande experiment measured R′ to be $0.57^{+0.08}_{-0.07}(syst.) \pm 0.07(stat.)$. At the same time two iron calorimeter experiments, Frejus [39] and NUSEX [40] measured a ratio consistent with Monte Carlo prediction, although with less statistical precision. This discrepancy in R′ was known as the atmospheric neutrino anomaly. Measured R′ values for several atmospheric neutrino experiments are shown in Figure 2.9. The systematic error on the

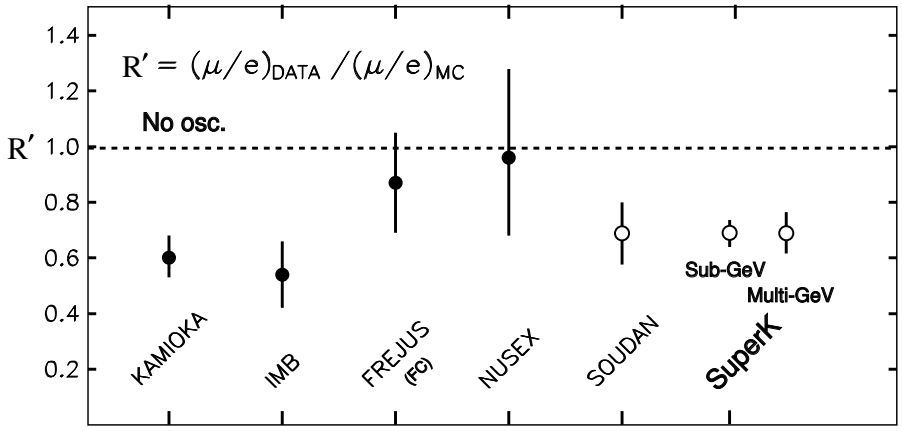

Figure 2.9: R′ measurements from several atmospheric neutrino experiments, taken from [42]

flux of atmospheric neutrinos was 20%, mainly due to the uncertainties in hadronic production models and the energy spectra of the cosmic rays. However, as a ratio of fluxes was being calculated, many of the systematics cancelled out, leading to a systematic error on R′ of $\sim 5\%$ [41]. The solution to the atmospheric neutrino anomaly and the acceptance of neutrino oscillation by the physics community, came from the 1998 results of the Super-Kamiokande experiment.

SK measured the zenith angle (a description of zenith angle and baseline is shown in Figure 2.10) dependency for the electron and muon neutrino fluxes and observed a large deficit in the flux of muon neutrinos at large zenith angles (i.e. that have come up through the Earth) whereas the electron neutrino sample agreed well with the MC prediction over all zenith angles as shown in Figure 2.11. The results are consistent with $\nu_\mu \rightarrow \nu_\tau$ oscillations with $\sin^2 2\theta_{23} > 0.92$ and $1.5 \times 10^{-3} < \Delta m^2_{23} < 3.4 \times 10^{-3}\,\mathrm{eV}^2$ at 90% C.L. as shown in Figure 2.12.

As well as the zenith angle study, SK was also able to reconstruct the energy of the incident neutrinos. This allowed it to probe the distortion in the L/E spectrum as shown in Figure 2.13. This shows that the flavour oscillation hypothesis provides the best description of the data. The SK results are confirmed by the results from Soudan 2 [44] (a 1 kt tracking iron calorimeter located in the Soudan mine, Minnesota) and MACRO [45] (an underground experiment using liquid scintillator and streamer tubes based at Gran Sasso, Italy). The oscillation fits of these experiments are shown in Figure 2.14.

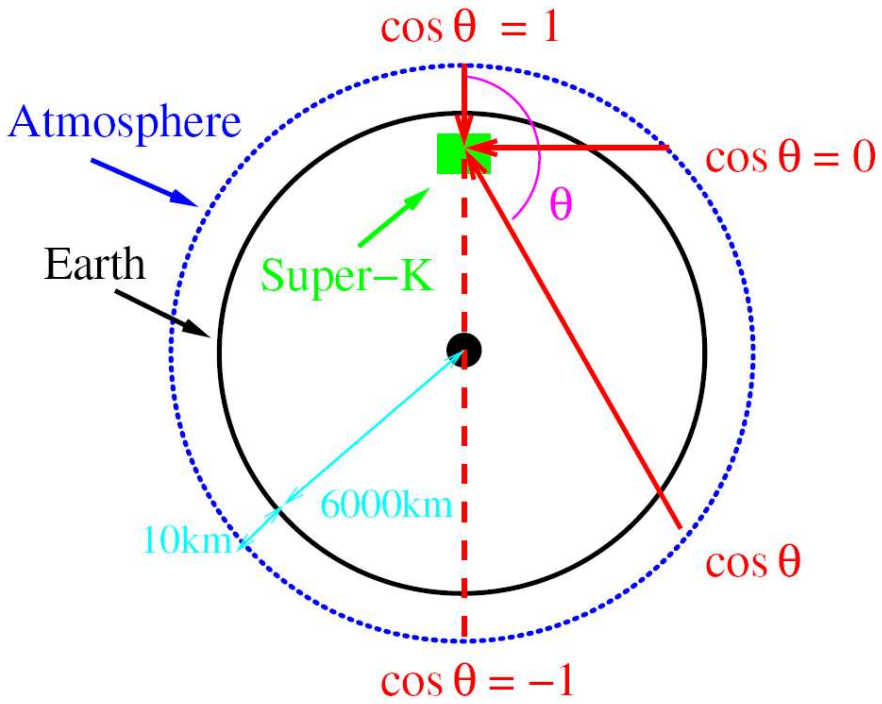

Figure 2.10: Diagram showing relation between zenith angle and baseline for atmospheric neutrinos, taken from [43].

The MINOS experiment, designed to search for neutrino oscillations in a ν_μ beam (see Section 3), has also been able to study atmospheric neutrinos [47]. Using data from a 418 day exposure of the 5.4 kt MINOS Far Detector, 107 atmospheric ν_μ are observed compared to an MC expectation of 127 ± 13. Timing information is used to determine direction, and the observed to expected ratio of up/down neutrino direction ratios, $R^{data}_{up/down}/R^{MC}_{up/down}$, is calculated to be $0.62^{+0.19}_{-0.14}(stat.) \pm 0.02(syst.)$. The hypothesis of no oscillations is excluded at 98% using an extended maximum likelihood analysis. The detector's magnetic field allows ν_μ and $\overline{\nu}_\mu$ to be identified. The observed to expected charge ratio, $R^{data}_{\overline{\nu}_\mu/\nu_\mu}/R^{MC}_{\overline{\nu}_\mu/\nu_\mu}$ is found to be $0.96^{+0.38}_{-0.27}(stat.) \pm 0.15(syst.)$.

2.3.7 Accelerator Experiments

Accelerator experiments are designed to make high precision measurements of the parameters of the neutrino oscillation modes already discovered through studying atmospheric and solar neutrinos. The neutrinos are created by focusing the pions and kaons produced when a high energy proton beam is incident upon a target. The pions and kaons then decay to produce a beam of ν_μ. The energy spectrum of the beam is measured with a

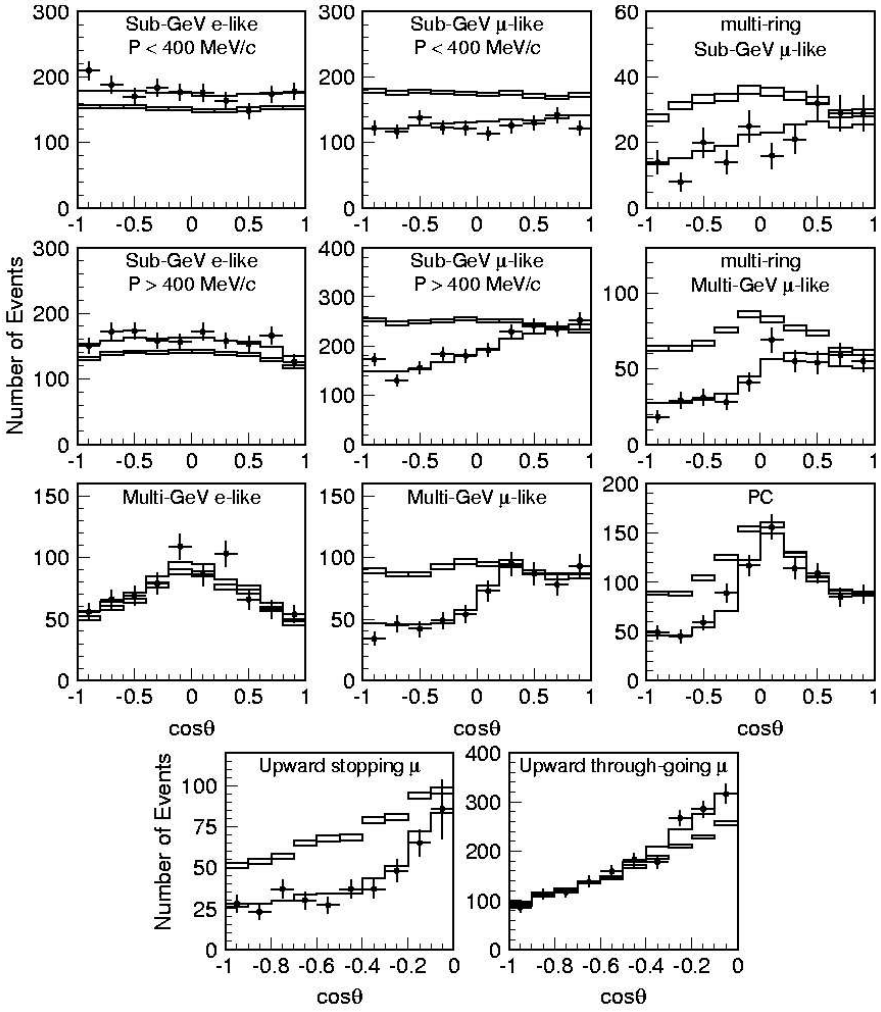

Figure 2.11: The zenith angle distribution for fully contained 1-ring events, multi-ring events, partially contained (PC) events and upward muons. The sample is also divided into ranges of neutrino energy, with events with a visible energy less than 1.33 GeV being referred to as 'Sub-GeV' and those with more as 'Multi-GeV'. The points show the data, box histograms show the non-oscillated Monte Carlo events and the lines show the best fit expectations for $\nu_\mu \to \nu_\tau$ oscillations with $\sin^2 2\theta = 1.00$ and $\Delta m^2 = 2.1 \times 10^{-3}\,\mathrm{eV}^2$, taken from [19].

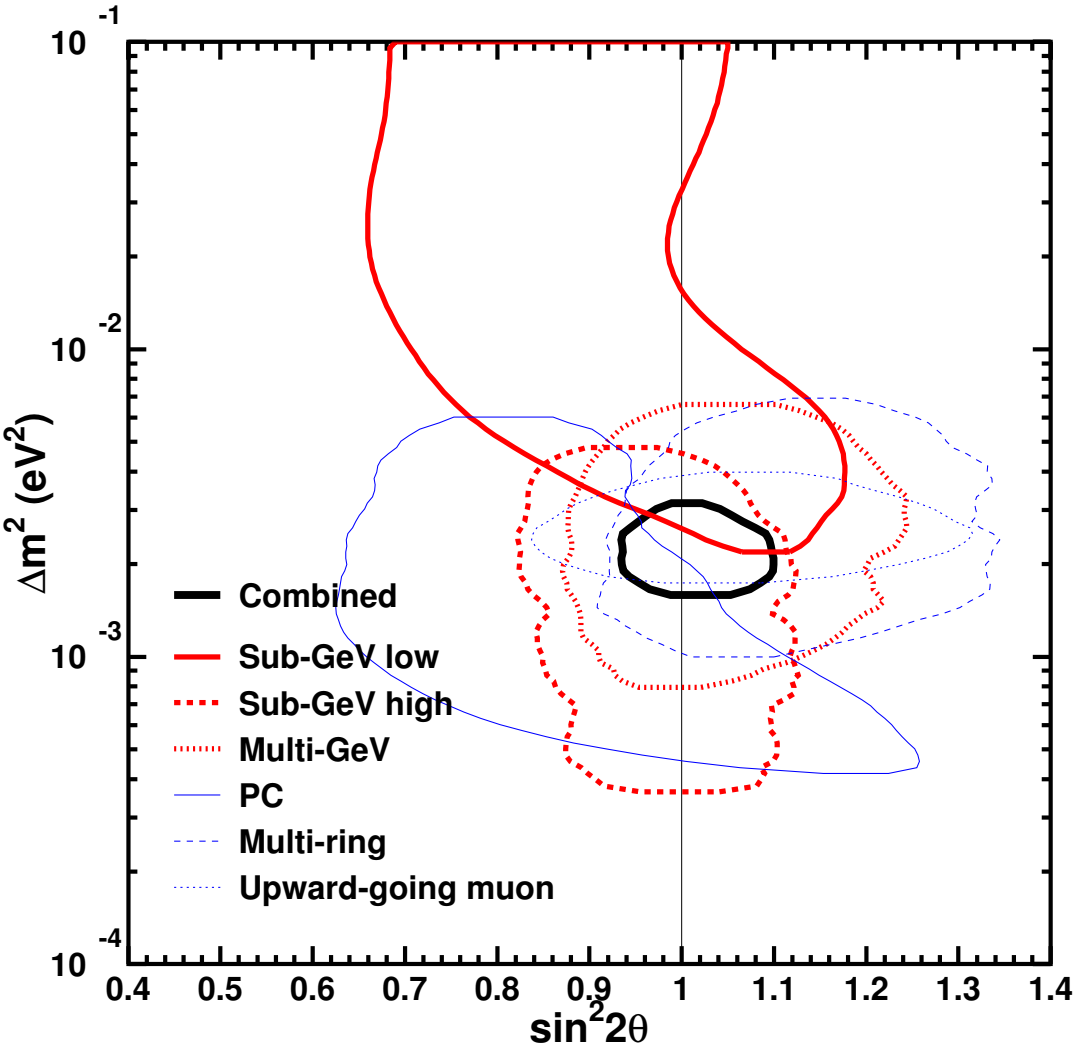

Figure 2.12: 90% confidence level allowed oscillation parameter regions for $\nu_\mu \to \nu_\tau$ oscillations from six subsamples, taken from [19].

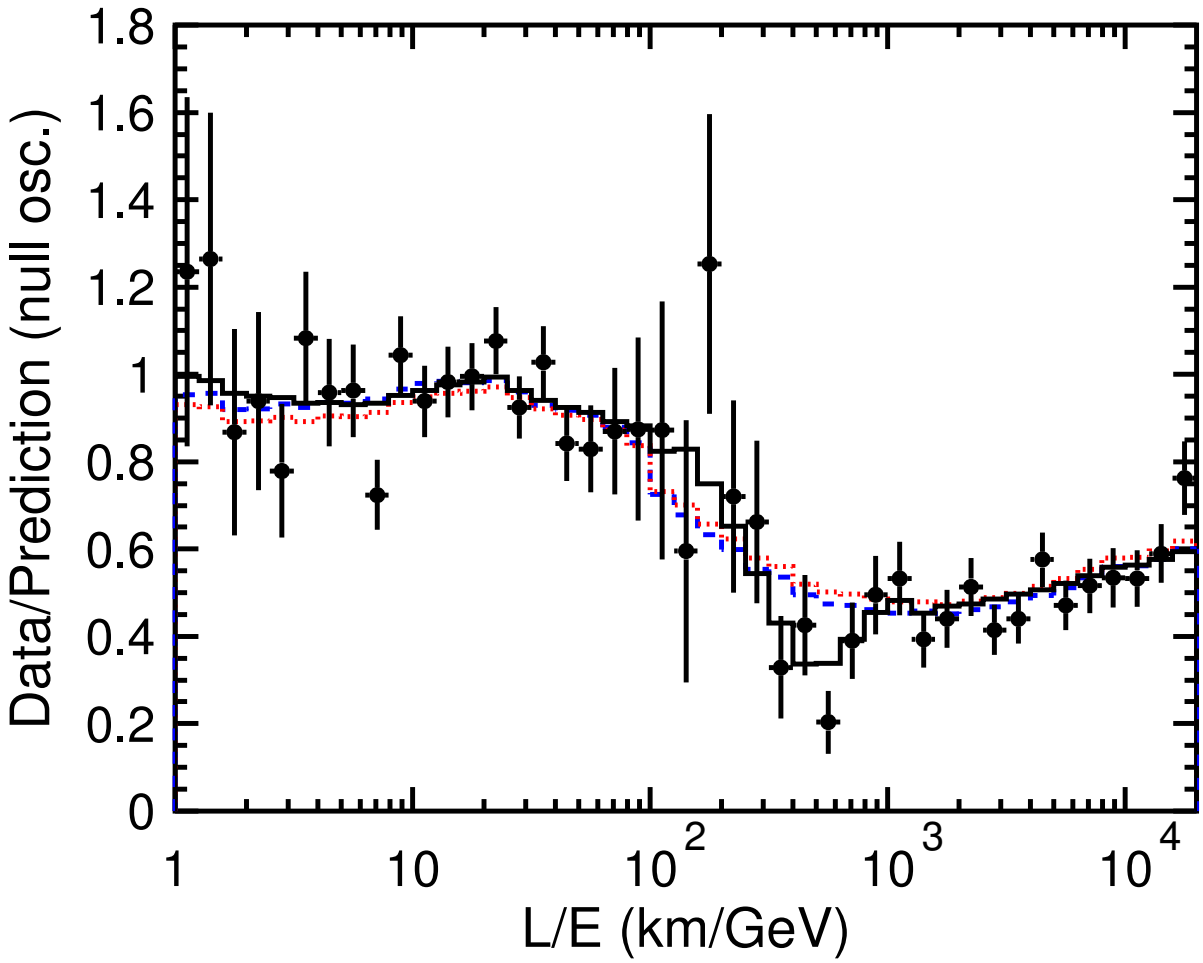

Figure 2.13: Ratio of the data to the MC expectation without neutrino oscillation (points) as a function of the reconstructed L/E together with the best-fit expectation for 2-flavour $\nu_\mu \to \nu_\tau$ oscillations (solid line). Also shown are the best-fit expectations for neutrino decay (dashed line) and neutrino decoherence (dotted line), taken from [46].

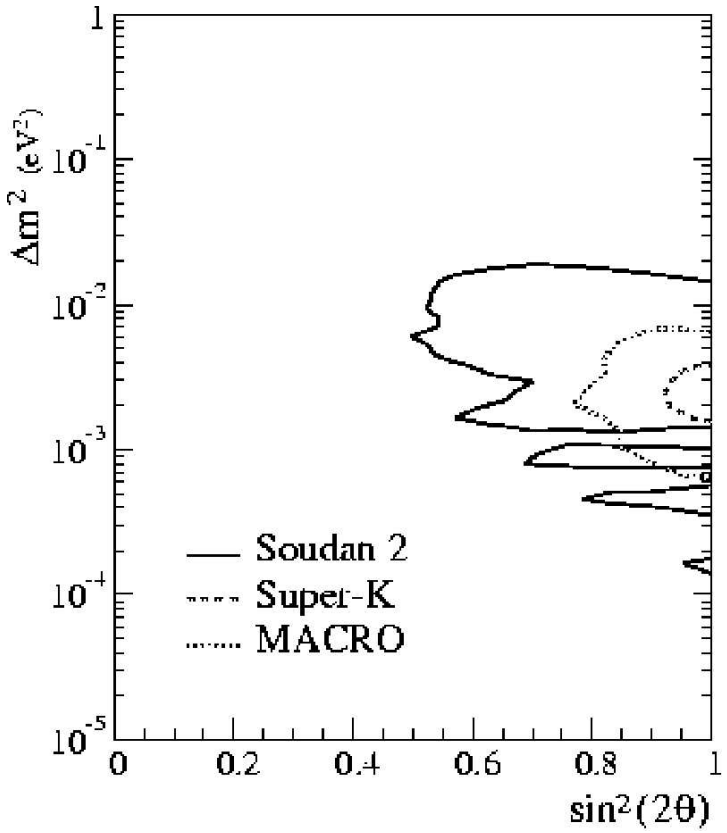

Figure 2.14: The Soudan 2 90% confidence allowed region in $\sin^2 2\theta, \Delta m^2$ (solid line) compared with the most recent allowed regions of Super-Kamiokande (dashed line) and MACRO (dotted line), taken from [44].

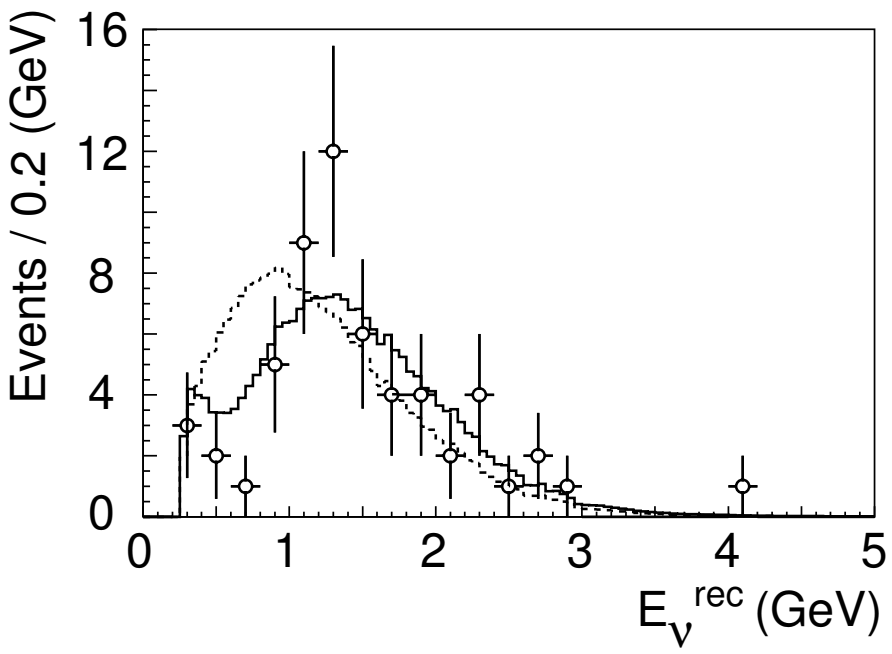

Figure 2.15: Reconstructed E_ν spectra for K2K data (points with error bars), best fit MC expectation with oscillations (solid line) and no oscillations (dashed line), figure taken from [48].

detector close to the production point, where the probability of oscillation is negligible. The neutrino beam is then allowed to propagate for several hundred kilometres before being incident on another detector. This second detector is typically of the same design as the first to minimise systematic error. The oscillated spectrum is measured at the second detector and the oscillation parameters extracted.

The KEK-to-Kamioka (K2K) experiment [48] uses a 98% pure ν_μ beam with a mean energy of 1.3 GeV produced at the KEK accelerator laboratory. The beam spectrum is measured with a 1 kt water Čerenkov detector and a fine grained detector system. The spectrum is remeasured at the SK detector 250km away. After studying data corresponding to 8.9×10^{19} PoT (protons on target) 107 events are detected compared to the 151^{+12}_{-10} events predicted in the absence of oscillations. 57 of these events are determined to be CC Quasi-Elastic (QE) interactions allowing good energy resolution using QE kinematics. These events are used to investigate spectral distortion, as shown in Figure 2.15. This gives a best fit for the oscillation parameters of $\sin^2 2\theta_{23} = 1.0$ and $\Delta m^2_{23} = 2.8 \times 10^{-3}\,\mathrm{eV}^2$.

The Liquid Scintillator Neutrino Detector Experiment (LSND) experiment [49] based

at Los Alamos used a short baseline (30m) $\overline{\nu}_\mu$ beam and a liquid scintillator detector to search for $\overline{\nu}_\mu \rightarrow \overline{\nu}_e$ oscillations. An excess of 4 standard deviations above the expected background of $\overline{\nu}_e + p \rightarrow e^+ n$ events was measured, corresponding to a best fit of $\sin^2 2\theta_{23} = 0.003$ and $\Delta \mathrm{m}^2_{23} = 1.2\,\mathrm{eV}^2$. This result is viewed with some scepticism as it is nearly 3 orders of magnitude larger than the closest measurement from atmospheric neutrinos. Results from LEP show that there are only 3 generations of neutrino that interact via the weak force, so this result would indicate the existence of a 4th 'sterile' neutrino to accommodate the extra Δm^2 value. The results of the MiniBooNE [50] experiment, based at Fermilab will attempt to confirm or exclude the LSND allowed regions, already greatly reduced by the KARMEN [51] and Bugey [52] experiments. It should also be noted that the LSND result is inconsistent with the limit on neutrino mass from cosmology as outlined earlier in this chapter.

2.3.8 Summary

The combination of Solar neutrino flux measurements and the KamLAND experiment have validated the SSM predictions and shown that $\nu_e \rightarrow \nu_\mu / \nu_\tau$ flavour oscillations are the preferred mechanism for the observed solar neutrino flux discrepancy. SK results show $\nu_\mu \rightarrow \nu_\tau$ flavour oscillations to be the favoured mechanism for the anomalous flavour ratios of atmospheric neutrinos. The limit on θ_{13} as determined by the CHOOZ and other experiments shows that coupling between the solar and atmospheric modes is very weak. Along with the large observed difference in Δm^2 values between atmospheric and solar neutrino oscillations, it is possible to conclude that $\Delta m^2_{solar} = \Delta m^2_{12} \sim 8 \times 10^{-5}\,\mathrm{eV}^2$ and $\Delta m^2_{atm} = \Delta m^2_{23} \sim \Delta m^2_{13} \sim 2.1 \times 10^{-3}\,\mathrm{eV}^2$. The SK results strongly favour near maximal mixing, $\theta_{23} \simeq \pi/4$ and KamLAND/Solar results indicate $\theta_{12} \simeq \pi/5.57$. A summary of the results of many neutrino experiments is shown in Figure 2.16.

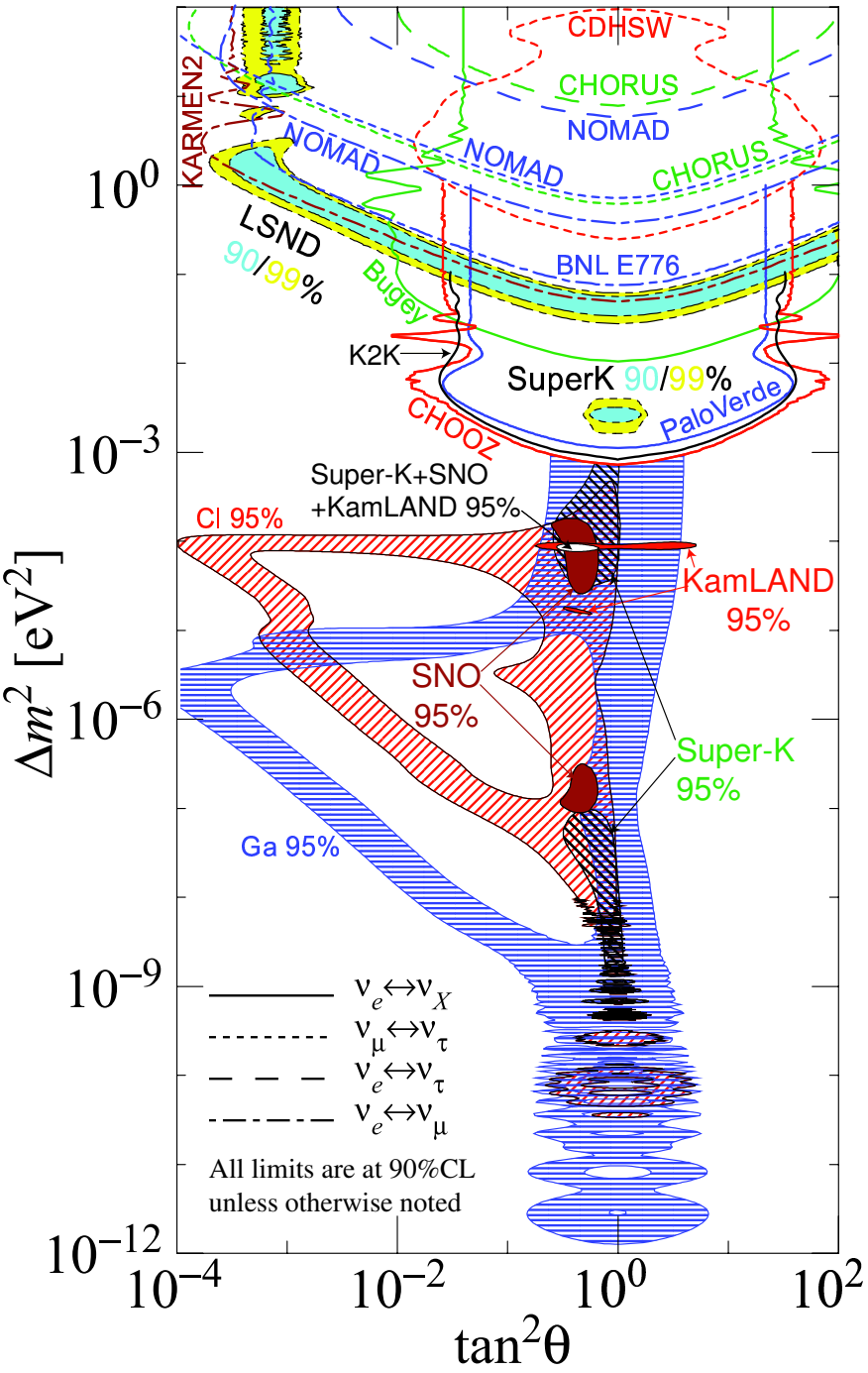

Figure 2.16: Regions of squared mass difference and mixing angle favoured or excluded by various experiments, taken from [53].

Chapter 3

MINOS

"Just because something doesn't do what you planned it to do doesn't mean it's useless."
— Thomas A. Edison

The MINOS experiment will attempt to find evidence for neutrino oscillations in the region of parameter space indicated by the atmospheric neutrino experiments. As with other long baseline experiments, it will use an accelerator to produce a beam of neutrinos. A near and far detector are used to measure the ν_μ spectra close to the point of production and after the beam has propagated a large distance to allow the oscillations to develop. Primarily MINOS is a ν_μ disappearance experiment, so any observed discrepancies in event rate or spectral distortion can then be used to extract a measurement of the oscillation parameters. The arrangement of the beam and both detectors is shown in Figure 3.1. The MINOS experiment consists of several components, which are described below.

3.1 The NuMI beam

The first process in creating the NuMI beam [54] is extracting 120 GeV primary protons from the Main Injector ring at Fermilab using a horizontal kick that can be repeated as often as every 1.9 seconds with a spill time of 8.56 μs. The beam of protons is then focused and transported down towards the NuMI target. It is then aimed towards the far detector at Soudan before interacting with the target, where it forms a spot size of

Figure 3.1: The trajectory of the MINOS neutrino beam between Fermilab and Soudan. Figure taken from [54]

1-2 mm.

The NuMI target consists of 48 water-cooled graphite fins, 20.0 mm long and 6.4 mm wide. The long and narrow shape allows as many protons as possible to interact in the target and reduces the chance of produced hadrons being re-absorbed before they can escape the target volume. The graphite is surrounded by a cylindrical aluminium casing connected to an He-filled canister to assist with heat transfer. The beam of protons interacts with the target to produce pions and kaons with wide distributions of longitudinal and transverse momenta.

Two focusing horns are then used to select the sign of the hadrons produced and to focus them along the original proton beam direction. The horns are parabolic in shape and a half sine-wave current pulse of up to 205 kA produces a toroidal magnetic field between the inner and outer conductors, making them act as lens with a focal length approximately proportional to the incoming particle's momentum. Two horns are used so that if hadrons are under/over-focused by the first horn, then the second horn will provide an additional correction, while correctly focused hadrons will be undeflected by the second horn. Both the target and horns are moveable along the beam axis. This changes the hadronic spectrum focused, enabling a large range of ν_μ spectra to be achieved, as shown in Figure 3.2. This means that MINOS is sensitive to a very wide neutrino oscillation parameter space.

After the hadrons have been focused they then enter an evacuated 675 m decay pipe, where they decay to produce ν_μ (along with a small fraction of $\overline{\nu}_\mu$ and ν_e from μ^+ and K^+_{e3} decay). At the end of the decay pipe, there is a hadron absorber, consisting of a steel covered, water-cooled aluminium core. The neutrinos then propagate through 240 m of dolomite, ensuring all decay pipe muons have interacted, before reaching the MINOS near detector. A diagram of the complete NuMI beam line is shown in Figure 3.3.

While the beam is progressing through the NuMI beamline, it is monitored at all stages. As the proton beam is transported to the NuMI target, various instruments (capacitive beam position monitors, secondary emission monitors, beam current toroids) are used to monitor its position, profile and current. The hadron flux is measured just upstream of the absorber and the muon flux is measured at 3 places as it travels through the dolomite after the absorber. When the beam enters the Near detector, it is composed of 92% ν_μ, 1% ν_e and 7% $\overline{\nu}_\mu$.

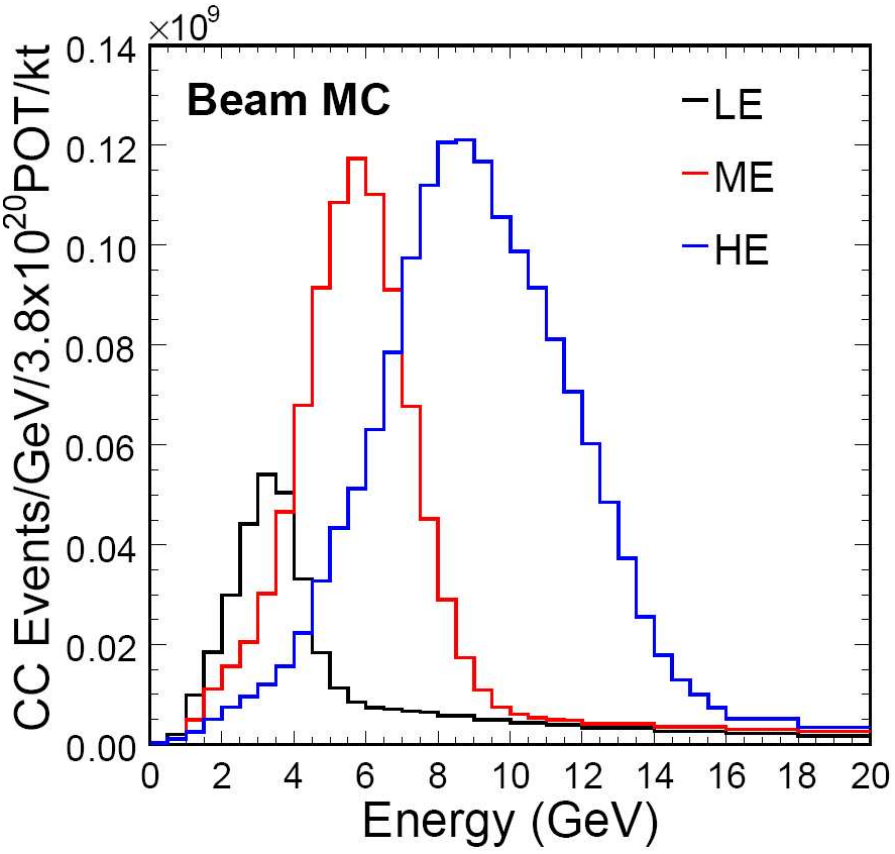

Figure 3.2: CC ν_μ spectra possible from the NuMI beam by adjusting the horn/target positions. The three configurations shown are Low Energy (LE), Medium Energy (ME) and High Energy (HE). Figure taken from [55].

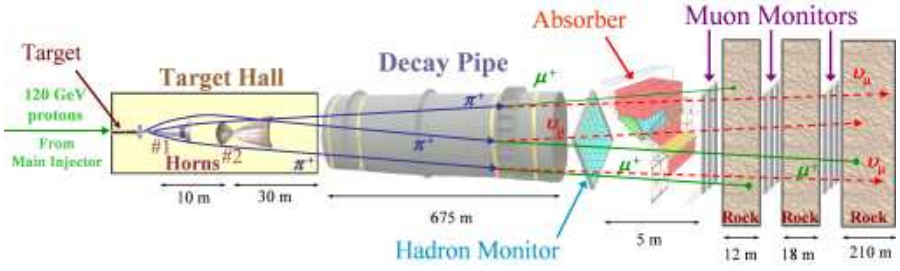

Figure 3.3: Layout of the NuMI beamline. Protons extracted from the Main Injector are incident on a graphite target to produce pions and kaons that are focused by two parabolic magnetic horns and allowed to decay into muons and ν_μ. The remaining hadrons and muons are then absorbed allowing the neutrino beam to propagate towards the Near Detector (schematic by B. Zwaska).

3.2 Detectors

MINOS uses magnetised tracking calorimeters to detect the beam neutrinos, allowing determination of both the total neutrino energy and charge sign of the associated lepton. As the experiment depends on the comparison of results from two different detectors, they have been designed to be as similar as possible to reduce systematic error. The common elements of the detectors are described here.

The detectors are steel-scintillator calorimeters, consisting of many vertically aligned planes which are made up of a 2.54 cm plane of steel, an air gap and 1 cm plane of scintillator with an overall centre-to-centre spacing of 5.94 cm. The steel has a low carbon content (between 0.04 - 0.06%) to ensure high magnetic permeability while maintaining adequate tensile strength. The scintillator is made of extruded polystyrene infused with the fluors PPO (1%) and POPOP (0.03%) that produce photons of blue light with a mean wavelength of 460 nm. Each plane of scintillator is divided up into 4.1 cm wide strips, up to 8 m long, whose orientations alternate from $+45°$ to $-45°$ from plane to plane, allowing 3-dimensional reconstruction of events in the detector.

Each scintillator strip is covered in a 0.25 mm thick reflective jacket consisting of TiO_2 infused in polystyrene. There is also a 1.3 mm groove in each strip, containing a wavelength shifting (WLS) fibre. This is required to transport the scintillation light from the point of production to the ends of the strip without it being reabsorbed by the scintillator. The strips are assembled in modules consisting of between 20 to 28 strips which are covered with a light tight aluminium skin. The end of these modules consist of a light tight plastic manifold that allows the WLS fibres to run together, where they connect to clear fibre ribbon cables which transport the light to PMTs, as shown in Figure 3.4. The detectors then use sensitive digital electronics to read out these PMT signals.

The toroidal magnetic field is produced by running a high current ($\sim 10^4$ A-turns) through a water-cooled coil in the centre of each detector. The return leg of the coil is situated outside of the main body of the detector. The currents at both detectors are chosen to give a toroidal magnetic field of 1.5 T in the steel planes. As well as allowing the identification of the charge of the lepton produced in an interaction, it also focuses negative particles (i.e. μ^-) increasing the proportion that are fully contained. The field allows the momentum of muons to be deduced from the curvature of tracks that are only partially contained within the detector. Figure 3.5 shows the shape and co-ordinate systems used for the planes in the MINOS detectors.

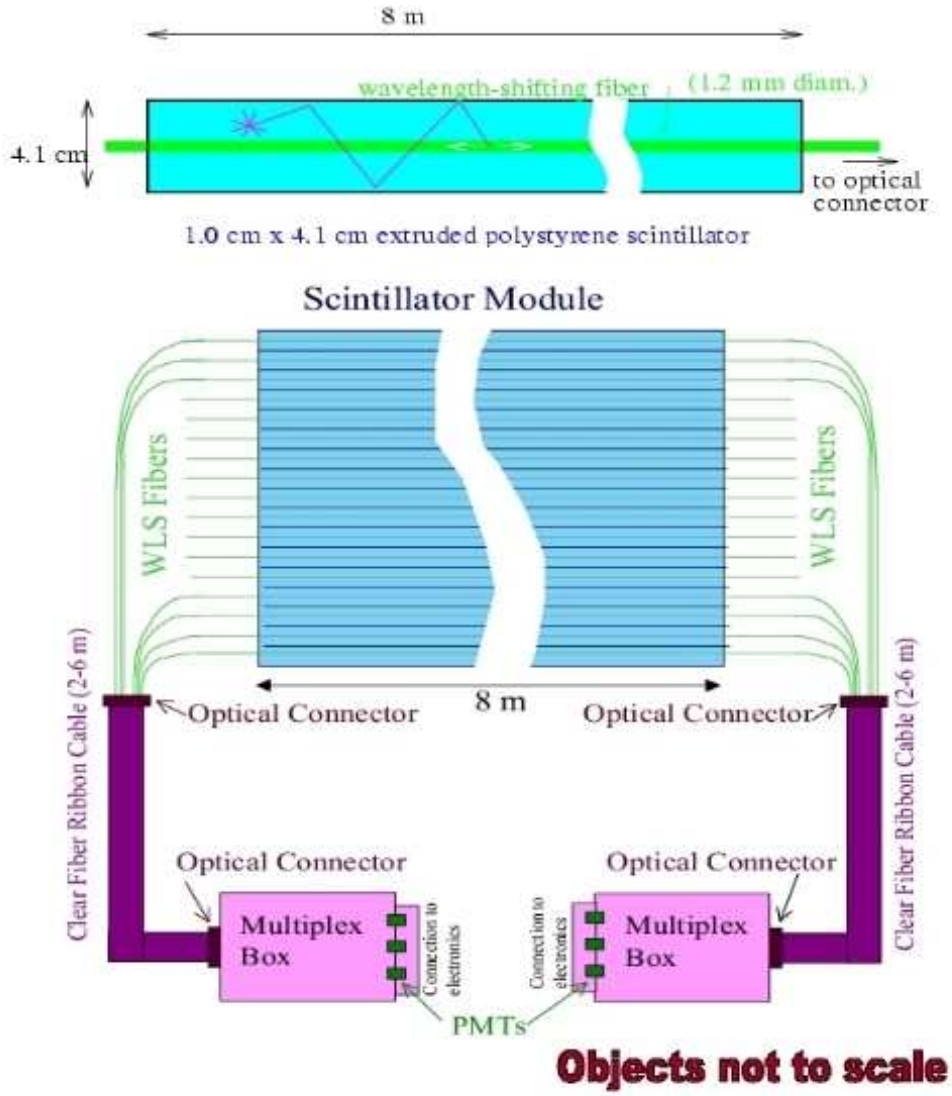

Figure 3.4: Layout of the scintillator strips, WLS fibres, clear fibres and PMTs in the MINOS Far Detector.

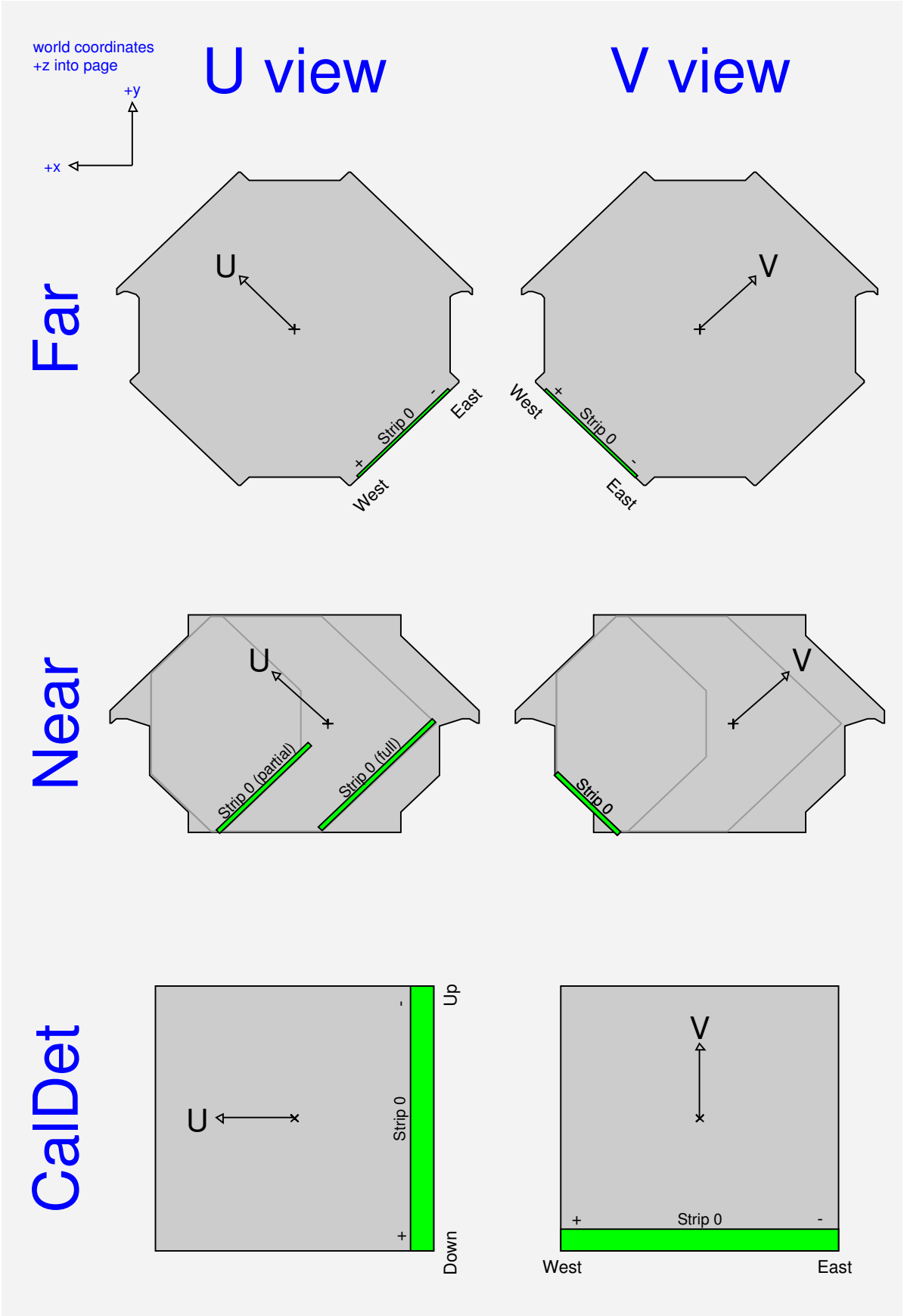

Figure 3.5: Shapes and co-ordinate systems used in the various MINOS detector planes.

3.2.1 Far Detector

The MINOS Far Detector is located 714 m below the Earth's surface (2070 m water equivalent) in the Soudan Underground Laboratory, at a baseline of 735 km from the point of beam production. It has a mass of 5.4 kt consisting of 486 8 m octagonal planes, arranged in 2 supermodules of 249 and 237 planes, of which 248 and 236 are instrumented with scintillator respectively. An air gap of 1.5 m separates the two supermodules, giving the detector a total length of approximately 30 m. Each supermodule is independently magnetised by current carrying coils that run through the centre of the supermodule and return beneath it, with each coil requiring 15 kA-turns of current to produce a 1.5T toroidal field in the steel of the detector. Each of the planes is divided up into 192 scintillator strips which are read out at both ends by Hamamatsu M16 PMTs. To reduce the large instrumentation load, 8 strips from each plane are read out by the same PMT pixel in a process called multiplexing. Each strip reads out to a unique pair of pixels (one on each side of the detector) allowing demultiplexing to take place in software and remove the 8-fold ambiguity over which strip was hit. The multiplexing takes place within a MUX box, containing three PMTs that read out one side of two planes.

The Far Detector readout electronics utilises modified VA chips, produced by IDEAS Corp. of Norway. Each VA chip is responsible for signal shaping, sampling and holding the signal from one of the three PMTs in a MUX box. Three VA chips are housed on a VA Front-end Board (VFB). The VFB signals are digitised on a VARC Mezzanine Module (VMM), six of which form part of a VA Readout Controller (VARC) where time-stamping and VA control take place. The Far Detector electronics are triggered when one of the PMTs produces a signal greater than approximately 1/3 of a photoelectron (PE), resulting in all 16 pixels in the PMT being read out and digitised in the VARC. Data are then transferred from the VARC over VME to a Readout Processor (ROP), where it is divided into second long intervals called timeframes. These are passed via a Branch Readout Processor (BRP) to one of several Trigger Processors (TPs) which are responsible for looking for physics events by time-ordering the hits in the timeframes and applying spatial or time based conditions. For the beam analysis events are selected on the basis of their temporal proximity to the beam spill. Events passing these conditions are termed 'snarls' and are collected by a Data Collection Process (DCP). A full description of the Far Detector electronics can be found in [56].

To aid the atmospheric neutrino analysis in the Far detector, a cosmic ray veto shield has been erected around the top and sides of the detector. This will allow cosmic rays

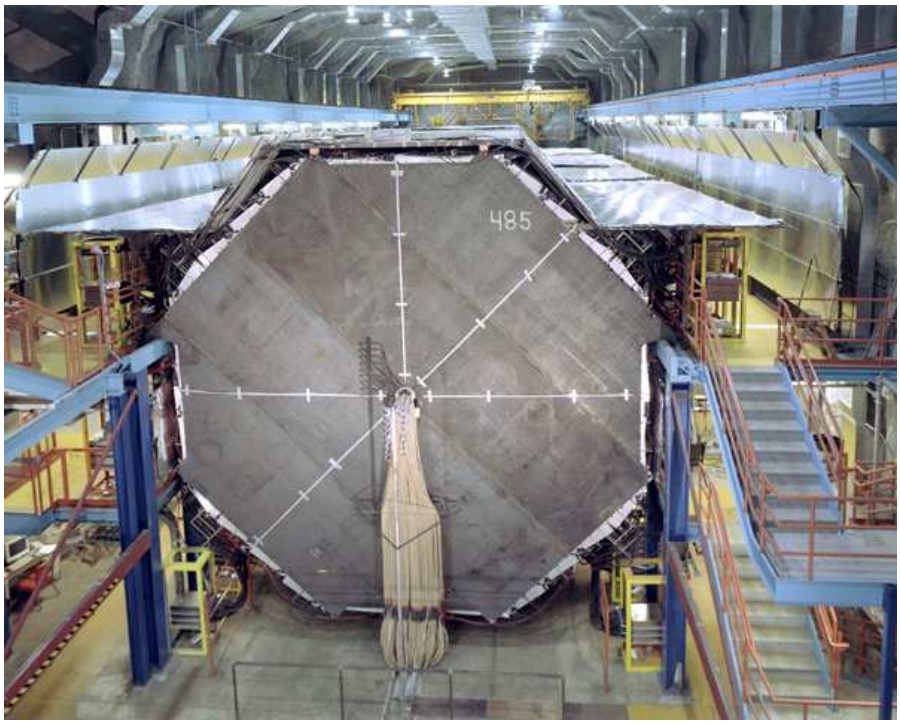

Figure 3.6: The completed MINOS Far Detector courtesy of Fermilab Visual Media Services. The magnetic coil can be seen entering through the centre of the front face of the detector. The cosmic ray veto shield can be seen on the top of the detector and the MUX boxes are housed on the sides of the detector.

to be tagged and reduces the cosmic ray background by a factor of approximately 100. The shield is made of the same scintillator strips as the main detector and the data is read out in the same fashion. Due to the steepness of cosmic tracks and knowledge of the spill time, it is not expected that cosmic ray muons will be a significant source of background for the beam analysis, so shield information will not be used. A view of the completed detector is shown in Figure 3.6.

3.2.2 Near Detector

The function of the MINOS Near Detector is to measure the unoscillated neutrino spectrum of the NuMI beam at Fermilab. The proximity of the detector to the target means that the neutrino flux is much higher than at the far detector and this along with financial considerations has led to some design differences. The Near detector has a mass of 0.98 kt and is comprised of 282 of the aforementioned steel/scintillator planes. It has an elongated octagonal cross-section, 3.8 m high and 4.8 m wide. The centre of the

detector is offset horizontally from the centre of the beam spot by 1 m. The hole for the current carrying coils is located 0.56 m horizontally from the centre of each plane. The return leg of the coils are located on the underside of the detector offset at a 45° on the opposite side to the beam spot. To produce a 1.5 T toroidal field in the beam region requires a current of 40 kA-turns in the coil.

The detector is divided in several longitudinal sections with differing instrumentation to reflect their different functions as shown in Figure 3.7:

Veto Region: The first 50 cm of steel (planes 0-20) consist of a veto region, to remove any background from neutrons produced by neutrinos interacting in the rock upstream from the detector. It also ensures that there are no end effects in the target region.

Target and Calorimeter Region: The next 1.0 m and 1.5 m of steel (planes 21-60 and 61-120) make up the target and calorimeter sections respectively. These regions allow neutrinos to interact and the events to develop, making sure that their hadronic showers are completely contained.

The planes of these three first sections of the detector are mostly partially instrumented, where the scintillator part of the plane only covers a square region, 2.8 m by 2.8 m that encompasses the beam spot. Every fifth plane is fully instrumented, allowing the tracking of muons that have left the central region of the detector.

Muon Spectrometer Region: The final 4 m of steel (planes 161-281) of the detector makes up the muon spectrometer region where only every fifth plane is fully instrumented with no scintillator on any of the planes in between. The purpose of this region is to track high energy muons from interactions in the target region of the detector. The strips in this region are fourfold multiplexed in the electronics and information from further upstream in the detector is used to remove the ambiguity.

As the length of the scintillator strips is small in the Near Detector the signal from charge being deposited in a strip is less attenuated, so light is only collected on one end of the strips. The other end is covered in reflective aluminised mylar tape to increase the amount of collected light. The light is collected with Hamamatsu M64 PMTs with 64 pixels and each of the PMT anodes is read out through a Charge-to-Current encoder (QIE) chip. The QIE chips are capable of continuous analogue processing at 53 MHz with no dead-time, which is highly desirable given the high event rate in the Near Detector. The QIE is mounted on a daughter board called a MENU module which it shares with an ADC and FIFO for data buffering. The data is digitised and stored on

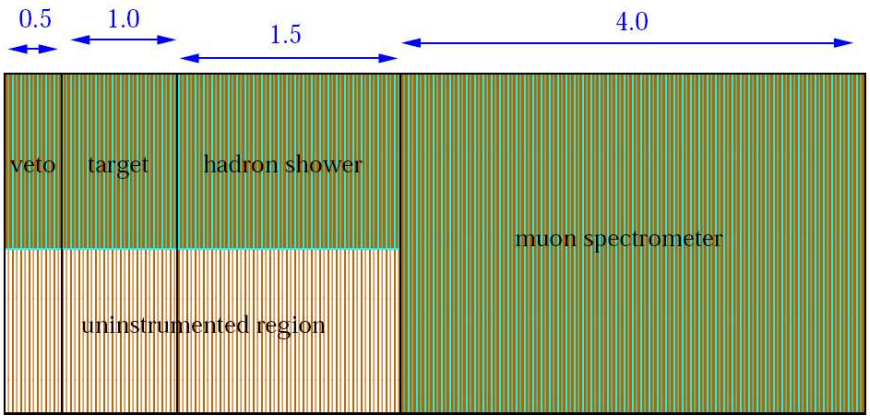

Figure 3.7: Schematic representation of the four functional parts of the MINOS near detector. The thicknesses shown (in metres) are only for the steel planes and and do not include the space occupied by scintillator planes or air gaps. The beam enters from the left and is centred on the shaded (instrumented) part of the detector.

these modules and then read out at the end of each $9\mu s$ spill. 16 MENU modules are mounted on a motherboard, called the MINDER module which is responsible for time stamping the data into 19 ns windows (buckets). It also multiplexes the data from the MENU modules to the VME readout board and provides power, control and interface functions with the QIEs. A full description of the Near Detector electronics can be found in [57]. A view of the completed detector is shown in Figure 3.8.

3.2.3 CalDet

The MINOS calibration detector (CalDet) was operated at CERN between 2001 and 2003. Its purpose was to provide absolute energy calibration and topology information for hadronic and electromagnetic interactions in the MINOS detector. It had a mass of 12 tons and was composed of 60 1 m by 1 m steel scintillator planes. Each scintillator plane contained 24 strips with orientations going from horizontal to vertical on alternating planes. Scintillator signals were transported to PMTs using the same WLS and clear fibres as in the Near and Far Detector. To allow estimation of systematic differences between the two main detectors, CalDet ran with both Far Detector electronics, Near Detector electronics and a hybrid mode where one side of the strips were read out using Far Detector electronics and the other side using Near Detector electronics. A photo of the detector can be seen in Figure 3.9.

Figure 3.8: The completed MINOS Near Detector courtesy of Fermilab Visual Media Services. The magnetic coil can be seen entering through the front face of the detector and the PMTs are housed on the left side of the detector.

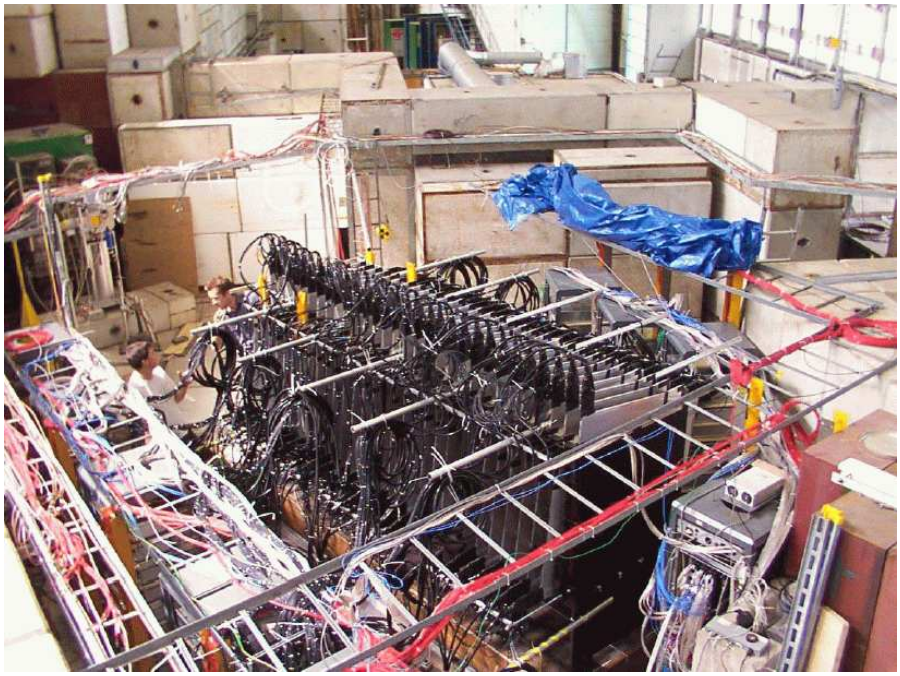

Figure 3.9: The MINOS Calibration Detector (courtesy of M. Kordosky) in the CERN PS accelerator East test beam hall. The fibres carrying the signals to the PMTs can be seen emerging from the top and sides of the scintillator planes.

Data for CalDet was taken using the T7 and T11 test beams providing a source of $p^{\pm}$, $\pi^{\pm}$, $e^{\pm}$, $\mu^{\pm}$ with momenta between 0.4 and 10 GeV/c. Analysis of the data has led to the following single particle energy resolutions [58, 59]:

$$\text{Pions: } \frac{(56.1\pm0.3)\%}{\sqrt{E}(\text{GeV})} \oplus (2.1 \pm 1.5)\%$$

$$\text{Protons: } \frac{(56.6\pm0.6)\%}{\sqrt{E}(\text{GeV})} \oplus (4.2 \pm 1.4)\%$$

$$\text{Electrons: } \frac{(21.42\pm0.06)\%}{\sqrt{E}(\text{GeV})} \oplus \frac{(4.1\pm0.2)\%}{E(\text{GeV})}$$

3.3 Detector Calibration

As the success of the MINOS experiment rests on making an accurate measurement of an energy spectrum in two detectors over a long period of time, calibration of the detectors is a very serious issue. For this purpose the Light Injection (LI) and Charge Injection (CI) systems have been developed [60]. The LI system simulates the effect of energy deposition in the scintillator strips by injecting controlled pulses of light into the WLS fibres. It comprises of 20 ultra-violet LEDs, where each LED is responsible for injecting light into 71 optical fibres each of which transport the light to the end of ten WLS fibres. Positive-Intrinsic-Negative (PIN) photodiodes monitor the intensity of the light from each LED, and their signals are shaped to resemble those of the PMTs before being read out by the rest of the detector electronics. A schematic diagram of the LI system is shown in Figure 3.10.

LI pulses are interspersed with the data taking, allowing both the non-linearity of a particular channel to be measured as well as any drift it may exhibit with time. Non-linearities in the electronics are measured using the CI system, where a specified amount of charge is deposited in the electronics over a large range to determine the response during special runs. This information is used to linearise the response of the PINs in the LI system.

Once the response, linearity and drift of each readout channel has been determined, a full strip-to-strip calibration is performed to normalise variations in the response of each scintillator strip. This is done using through-going cosmic muons as they deposit a very similar amount of charge per unit strip length. As the muon tracks are reconstructed in 3D it is possible to determine the longitudinal position along each strip where the hit

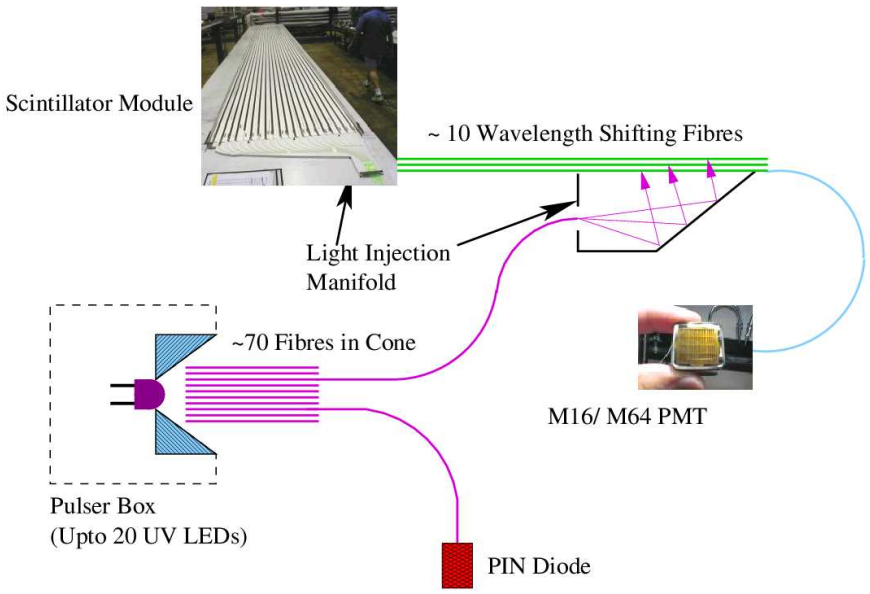

Figure 3.10: The MINOS light injection system. UV light is generated by LEDs in the Pulserbox which is routed to WLS fibres at the end of the scintillator modules. The light then propagates back to the PMTs. The amount of light injected is monitored using PIN diodes. Diagram taken from [60].

occurred using information from the neighbouring planes. This enables an attenuation correction to be calculated, taking into account the reduction in signal in transporting the scintillation light from the point of production to the end of the strips. A universal energy unit, the Muon Energy Unit (MEU, also referred to as a Minimum Ionising Particle, MIP) is defined as the detector response to a muon of energy 1 GeV travelling through a scintillator plane perpendicular to the detector plane. This quantity is determined by studying muons which come to rest in the detector, as these will have the same energy and so be on the same point of the $\mathrm{d}E/\mathrm{d}x$ curve for both detectors. For a complete description of this method see [60].

3.4 Monte Carlo Simulation

Accurate Monte Carlo simulations are essential for the successful measurement of neutrino oscillations as there must be a null oscillation Far Detector spectra to compare with data for evidence of spectral distortion or discrepancies in flux. However, to get accurate simulation in the Far Detector, it is necessary to simulate the entire NuMI

beam line, from to neutrino production to detector response. The main stages of this process are:

GNuMI: This is a GEANT-3 based simulation of the NuMI beamline. Protons are propagated to the target, modelled as a graphite box with a scaled down density to reflects the air gaps. FLUKA [61], a general purpose tool for calculations of particle transport and interactions with matter, is used to determine hadron production in the target and uses a much more detailed geometric model of the target. All the hadrons that leave the target vessel are then propagated through the secondary beamline (magnetic horns, decay pipe, etc.).

NEUGEN: A general purpose event generator [62] which simulates neutrino interactions in the energy range 100 MeV - 100 GeV and was originally used to simulate background to proton decay in the Soudan 2 experiment. Libraries of neutrino cross-sections are used to determine interaction types. It uses a modified Fermi gas model for the nucleus and takes into account of Pauli blocking and intra-nuclear scattering of pions.

GMINOS: This is a GEANT-3 based simulation of the MINOS detectors. The GCALOR package is used to simulate the hadronic interactions in the detector. The events are tracked throughout the detector and the truth hits are recorded. It also allows for configurable detector geometries, neutrino fluxes and event generators.

PhotonTransport: A program written in Object Orientated (OO) C++ and based in the ROOT Framework which is responsible for simulating the scintillator and optical fibre of the MINOS detectors. The true energy depositions from GMINOS (DigiScintHits) are used as the input for PhotonTransport that determines the scintillator response and tracks the scintillation light through the WLS and clear fibre until it reaches a PMT cathode where they generate photoelectrons (DigiPEs).

DetSim: Another OO C++ program, this takes the DigiPEs outputted from Photon-Transport and simulates the PMTs, front end electronics and DAQ for the MINOS detectors, outputting a RawDigitDataBlock as would be produced by normal data which can then propagate through the rest of the reconstruction software. DetSim simulates many features including PMT cross-talk (some signal can be detected on adjacent pixels to the one being illuminated), noise, non-linearity (PMT, VA and QIE) and triggers.

As some background studies require knowledge of the behaviour of cosmic muons in the Far Detector, these are also simulated. This is done by propagating the cosmic muon flux measured at the surface of the Earth through a digitised rock map above the

Far Detector, then simulating the detector response using GMINOS as with the beam simulation. The parameterisation of the surface cosmic muon flux can be found in [63].

Chapter 4

Event Reconstruction

"Good ideas are not adopted automatically. They must be driven into practice with courageous patience."

— Hyman Rickover

The MINOS software reconstruction chain outlined below is responsible for taking in the RawDigitDataBlocks and converting them into CandEvents with topologically identified tracks and showers. It also estimates the energy of the incoming neutrino (assuming a CC interaction) and provides the means to identify background and poor quality events for both Data and MC. Due to differences between the two detectors (expected event rate, level of multiplexing etc.) there are differences in some sections of reconstruction which will be discussed where necessary.

4.1 SGATE and SpillServer

To reduce the background from noise and cosmic muons, the detectors are only read out when the beam is passing through them. It is possible to do this by exploiting the signal that is produced by the Main Injector to tell the kicker magnet to extract protons into the NuMI beamline. This signal occurs 20 Main Injector revolutions before the firing of the magnet actually takes place, so it can be fed to the Near Detector Master Clock Controller (MCC). After waiting for the protons to be extracted and the neutrino beam produced, the MCC opens a time interval known as an SGATE during which data is

collected in the front-end buffers. The SGATE has a width of $10 - 20\,\mu$s, tuned to start $1.5\,\mu$s before the arrival of the neutrinos at the Near Detector and is wide enough to capture all signals from the neutrino interactions.

When the Near Detector timing PC receives the Main Injector signal, it promptly informs the Far Detector, where a process called SpillServer passes this information to the DAQ trigger processors. A software window is then opened with a width of $100\,\mu$s centred around the predicted arrival time of the neutrinos at the Far Detector. This prediction is based on a trivial time of flight calculation assuming the neutrinos are travelling close to the speed of light. A pre-trigger window of $30\,\mu$s before the spill trigger window is also read out every time there is a spill. The purpose of the pre-trigger window is to see what activity there was in the detector (e.g. light injection) that might cause dead-time in the spill trigger window. The hits that occur in the detectors in their respective time windows are termed snarls and their RawDigitDataBlocks are the basis for reconstructing events. A full description of these systems can be found in [64].

4.2 Blinding

To ensure no biases were introduced into the oscillation analysis through event selection in the Far Detector, the Far Detector data set is partially blinded [65] so as to destroy any signature of oscillations. The event's energy, defined as the total Analogue-to-Digital Counts (ADCs) for the event, and length, defined as the length of the largest group of planes separated by gaps smaller than three planes, are calculated. These values are inputted into a sinusoidal function with other randomly generated constants to give a value between 0 and 1. This value is compared to another randomly generated number between 0 and 1 and if the first number is greater than the second then the event is processed and included in an open data set. Events failing this condition are still processed but are held in a closed data set to be opened for the final analysis.

4.3 DeMultiplexing

The next stage of the reconstruction involves removing the eight fold ambiguity for CandDigits in the Far Detector caused by the optical summing of eight strip ends into each PMT pixel [66]. Initially CandDigits with no possible combinations with a CandDigit

on the opposite side of the detector are ignored as these are likely to be optical cross-talk (where light from one PMT pixel has leaked to an adjacent pixel). Unambiguous CandDigit combinations (known as Golden Hits), where only one pairing combination places 2 CandDigits on the same strip on a particular plane are then identified. It is also possible to reduce the multiplicity of strip CandDigit combinations with timing. If two CandDigits were from the same strip then the difference in CandDigit times would be related to the position of the CandDigit along the strip. This means that position information from a Golden Hit can be used to de-multiplex CandDigits on surrounding planes. Golden Hits are also used to define suitable positions in planes with unresolved CandDigits (e.g. interpolating between Golden Hits, projecting forwards and backwards) which can be used to reduce the multiplicity further. This process is iterated until all CandDigits are demultiplexed. Finally, a mapping of the strips to the PMT pixels is used to tag the unpaired CandDigits that are most likely to be optical cross-talk.

4.4 CandStrip

The demultiplexed (in the case of the Far Detector) CandDigits are now formed into CandStrips. In the Far Detector this involves further removal of optical cross-talk. For each CandDigit, the charges of all CandDigits associated with adjacent PMT pixels that occur within ± 40 ns are summed. If the considered CandDigit's charge is greater than 10% of this total then it is added to a CandStrip. If both CandDigits in a pair pass this condition then they are added to the same CandStrip.

In the Near Detector where the strips are only read out at one end, the CandDigits associated with a particular strip are ordered in time (as the hits are timestamped into 19 ns timing buckets there can be a large range of event times over the 9 μs spill). CandStrips are formed from CandDigits that have gaps of no greater than 60 ns between them and a total time length of less than 120 ns. Once a CandStrip has been formed on a particular strip another CandStrip can not be formed (and the CandDigits are discarded) until at least 2 μs has passed since the end of the last CandDigit of the previous CandStrip. This is to stop 'after-pulsing' of the outer pixels of the M64 PMTs from creating low pulse height false events in the same physical location as previous events in the snarl.

4.5 CandSlice

Due to the high event rates in the Near Detector, it is necessary to divide up the snarl into CandSlices, that are likely to contain individual neutrino interactions. Initially CandStrips with a charge greater than 2 Photoelectrons (PEs), not located in the muon spectrometer region are considered. Starting with the earliest CandStrip these are then added to a CandSlice. A new CandSlice is started whenever the time difference between a new CandStrip and the previous one in the list is greater than 20 ns and there are a minimum of 2 CandStrips in the current CandSlice or if adding a new CandStrip makes the CandSlice greater than 300 ns long. If there are at least two unused CandStrips then these are formed into an additional CandSlice. As different neutrino interactions may only be separated spatially rather than temporally, any CandSlice containing a gap of greater than 1 m in the z direction is split into two separate CandSlices, provided that the gap has not been caused by the coil hole. CandStrips in the muon spectrometer or with a charge less than 2 PEs are then added to the most appropriate existing CandSlice based on timing and any CandSlice with a total charge of less than 2000 ADCs is deleted.

In the Far Detector all the CandStrips in a snarl are made into a CandSlice without any alteration as the chances of overlapping events are extremely low.

4.6 Track Finding and Fitting

One of the key characteristics of Charged Current ν_μ interactions is the presence of a muon that will form a track in the MINOS detectors. Identification of the muon tracks and correct estimation of their momenta is therefore vitally important to the experiment. The first stage of this process is the track finding algorithm.

In each orientation of the detector only CandStrips in the CandSlice with charges greater than 1 PE are considered and a Hough transform [67] is carried out. A Hough transform is used to identify features in two-dimensional images, in this case straight lines. It involves transforming from (x,y) space into (m,c) or Hough space where $y_i = mx_i + c$ and is formally represented as:

$$H(m,c) = \sum_i \Delta(y_i - mx_i - c)$$

where Δ is an indicator such that $\Delta(t) = 1$ if $t = 0$ and $\Delta(t) = 0$ if $t \neq 0$. The

signature of a track is a peak in Hough space. This initial track finding is used to give estimates for the number of tracks in the event (as separate tracks will have different peaks in Hough space) and their associated intercepts and gradients. A linear fit of strip time against z position is done for the CandStrips in each view, removing any entries with residuals greater than 20 ns and refitting until no more refitting is required or there are less than 5 hits left. CandStrips from both views surviving this step are used in a combined time against z position fit to determine whether the track was propagating forwards or backwards through the detector.

The CandStrips on each plane are then formed into clusters provided they are within three strips of one another. If a cluster contains more than 5 strips then it is not used as it is considered too shower like. An iterative process of forming 2D tracks begins with the identification of track seed hits. For a considered cluster, all earlier clusters in the same view, within 8 planes and within -40/+50 ns are considered. If there is reasonable agreement between the Hough fit parameters and the extrapolation between the clusters then the earlier of the two clusters is considered to be a track seed hit. If not then the later cluster is made a track seed hit. Other track clusters are then added to the track seed hits to form 2D tracks if they are within 3 planes and they provide reasonable agreement to a charge-weighted linear fit against z for the clusters already in the 2D track. If a 2D track has less than 3 clusters or less than 10% of its planes contain clusters, then it is removed. Overlapping 2D tracks are dealt with by removing the smaller of the two tracks. As the CandStrips in the muon spectrometer have a four fold multiplicity, existing 2D tracks are extrapolated into the spectrometer region and picks up the CandStrips in the best matching demultiplexing solution.

3D tracks are then constructed by looping over combinations of U and V view 2D tracks. Those that have start times within 100 ns and have start and end points within 4 planes are formed into CandTracks. Quantities such as the direction and path length (allowing the estimate of momentum from range) can then be determined.

A second track package, the TrackFitter uses a Kalman Filter to perform additional trackfinding, improve the choice of track strips through large vertex showers and estimate the value of q/p (ratio of charge to momentum) for the track. The algorithm starts by taking the list of CandStrips in the CandTrack identified by the TrackFinder and a 5 member state vector for each plane is defined as the U and V positions, $\mathrm{d}U/\mathrm{d}z$,$\mathrm{d}V/\mathrm{d}z$ and q/p estimate. Initially the q/p value is set to zero at the vertex plane. A 5×5 propagator matrix (taking into account the effect of the magnetic field) and a 5×5 noise matrix (taking into account the effects of multiple scattering and energy loss due

to ionisation) are then evaluated for each point on the track. These are used to provide increasingly accurate estimates for q/p as the algorithm iterates forwards and backwards over the track strips using the Kalman update equations until it has converged at each plane. At the end of each iteration, the current estimate for the state vector is matched to the nearest CandStrips in the CandSlice (even if these were not the original CandStrips from the TrackFinder), and these strips provide the track strips for the next iteration. It also provides an estimate for the error on q/p. Once the fit has converged, quantities such as the direction and estimate of momentum from range are recalculated with the final list of CandStrips in the CandFitTrack. True muon tracks that traverse more than 12 planes are reconstructed with an efficiency of approximately 99%.

4.7 CandSubShower and CandShower

The identification of hadronic showers in the detector is a complex task and is done in several stages. The first stage of this process consists of grouping together strips from the CandSlice into 2D SubShowers. The CandStrips are clustered logitudinally in U and V with a gap of two planes marking the boundary between clusters. Within the longitudinal clusters transverse clustering is achieved by defining a 'Strip Window', a region within a single plane with edges defined by CandStrips with zero charge, the edge of the detector or a local minima in the charge profile. A Hough transform is then used to identify Strip Windows that lie on similar straight lines within the longitudinal clusters and these are formed into CandSubShowers. If a CandSubShower has an average number of strips per plane of less than 1.3 then it is considered to be track-like and is discarded.

The next step in shower reconstruction is the formation of 2D showers. Each view is considered separately and the longitudinally clustered CandSubShowers are taken and the charge-weighted transverse positions of their CandStrips are histogrammed to find the peak of the distribution. This is repeated for the other longitudinal sections in the same view and a 2D shower is constructed from CandSubShowers with similar peak positions. The vertex of the 2D shower is determined longitudinally by the earliest plane of the CandSubShower in the appropriate view, and transversely by the extrapolation of a Hough transform gradient to the vertex plane in each view.

3D showers are formed by matching 2D showers from U and V views. If there is a mismatch in the number of showers in each view then the lowest charge showers in

the view with the excess are discarded. Timing information and U/V pulse height asymmetry is then used to find the most appropriate combinations of U and V 2D showers to form a CandShower. Estimation of the energy of the shower is based on its total pulse-height and is discussed in 4.9.

4.8 CandEvent

The final stage of the reconstruction concerns matching up associated reconstructed objects into one of several CandEvents for each CandSlice. The first stage of this is to identify tracks (or fitted tracks if they have passed the fitter) that are buried in showers. This is done by looping over tracks and showers in the same CandSlice and if there are less than four CandStrips in the CandTrack that are not longitudinally or transversely contained by the shower then the CandTrack is removed from the list. Reconstructed objects are looped over, with the first forming a CandEvent, and paired with other objects. The level of association for the new object to be added to the CandEvent varies with the type of pairing (Shower-Shower, Track-Track and Track-Shower) but all require the difference in object time to be less than 200 ns and the difference in z position of the vertex to be less than 1 m. The difference in transverse vertex positions have to be less than 0.71 m for Shower-Shower combinations, 0.5 m for Track-Shower combinations and 0.27 m for Track-Track combinations. In the case of a pairing involving a CandTrack, transverse positions are calculated having extrapolated it to the vertex of the other paired object. If two CandEvents are associated with the same object then they are merged.

The next phase is to consider CandStrips not associated to any reconstructed object. A particular CandStrip is considered and all reconstructed events in the snarl are looped over. If the CandStrip can be associated with the most suitable CandShower (closest in space and time within 100 ns) then it is added to the shower and its properties recalculated. If there is no CandShower and the CandStrip is associated with the vertex of a CandTrack (by the same conditions) then a new CandShower is formed.

The 'Primary' CandTrack (or CandFitTrack if present) and CandShower for each CandEvent are then determined. These are the objects that will be used to determine the energies of the muon and hadronic shower. The Primary CandTrack is that which is most likely to be the muon produced in a CC interaction, as opposed to a proton or pion that has been tracked. The Primary CandShower is that produced by the hadronic

interaction at the event vertex, as opposed to a Bremsstrahlung from an energetic muon. The Primary CandTrack is selected on the basis of whichever has the most CandStrips. The Primary CandShower is the shower with the highest reconstructed energy. If the CandShower's vertex is greater than 0.5 m in the z direction from the Primary track vertex, then it is required to have a reconstructed energy greater than 2 GeV otherwise it is considered to be associated with activity along the muon track instead of the event vertex. If there is a track present in the event, then its most upstream strip is made the event vertex.

4.9 Shower Energy Reconstruction

Reconstruction of the total visible shower energy (E_{shw}) in the MINOS detectors is one of the most important areas of the experiment as it represents the largest uncertainty on the reconstructed neutrino energy. CalDet data has been used to validate the MINOS MC and now the MC will be used to obtain a conversion from shower pulse height to visible energy. The calibration is carried out using Far Detector MC and then scaled for the Near Detector to take into account the effect of slicing. Charged Current and Neutral Current showers will be calibrated separately .The MC calibrations are applied to Near Detector beam data to assess the quality of the simulation of showers. Events must pass the following quality cuts to be included in the calibration set:

- Event vertex must be more than 0.5 m from the outer edges and ends of the detector and have a radius of greater than 0.4 m. This ensures that the showers are well contained in the detector and no charge is lost either outside the detector or in the coilhole.
- There must be only 1 reconstructed event in the snarl. In the Far Detector the chances of getting two true neutrino interactions in a single snarl is negligible. This cut removes events that may have been broken up in reconstruction or showers containing neutrons that may have propagated some distance form the vertex before interacting, leading to incomplete showers.

The first stage of the calibration process depends on which shower hypothesis is being used: Charged Current, Neutral Current or Electromagnetic (showers from CC $\nu_e$interactions) each with slightly different cuts, methodologies and calibration constants.

4.9.1 Charged Current (CC) Shower Calibration

It is necessary for the CC calibration set to pass the following cuts:

- Events are true CC ν_μ interactions
- There is at least one reconstructed track that passes the track fitter. This track must also have a negative reconstructed charge. This ensures that the track is well reconstructed, maximising the chances that it will be tracked accurately through any overlap with the shower.
- There must be a Primary shower associated with the event. This ensures that showers caused by bremsstrahlung on the muon track are not used.

Figure 4.1 shows a MINOS event display for a CC ν_μ MC interaction. The muon track can clearly be seen as well as the clustering of strips around the track vertex that make up the hadronic shower. It can be seen that several strips closely matching the true path of the muon have been included in the reconstructed shower as well as the track. This means that some of the charge deposited by the muon will be added to the shower, so it is therefore necessary to remove this before shower calibration can take place. Deposition of charge by the muon will not be a uniform process due to plane-to-plane fluctuations, the possibility of the muon passing through more than one strip per plane and the creation of delta rays that may also propagate to other strips. The amount of charge removed will depend on the degree of spatial overlap between the CandTrack and CandShower, represented by the number of shared strips (i.e. CandStrips that are in both the CandTrack and CandShower). To average out the strip-to-strip fluctuations a suitable amount of charge is removed from the total CandShower pulse height. The direction cosine of the muon relative to the z axis of the detector ($\cos\theta_z$) must also be considered, as this will directly affect the pathlength of scintillator through which the muon will travel.

Initially it was assumed that it would only be necessary to remove 1 MIP/$\cos\theta_z$ per shared strip to account for the effect of the muon. However, poor tracking of the muon through the shower region typically leads to an underestimate of the number of shared strips. To correct for this, the difference between the CC and NC shower pulse heights is divided by the number of shared strips/$\cos\theta_z$ for a given true E_{shw}. A zeroth order polynomial fit to this ratio is then performed to the high E_{shw} region. This is due

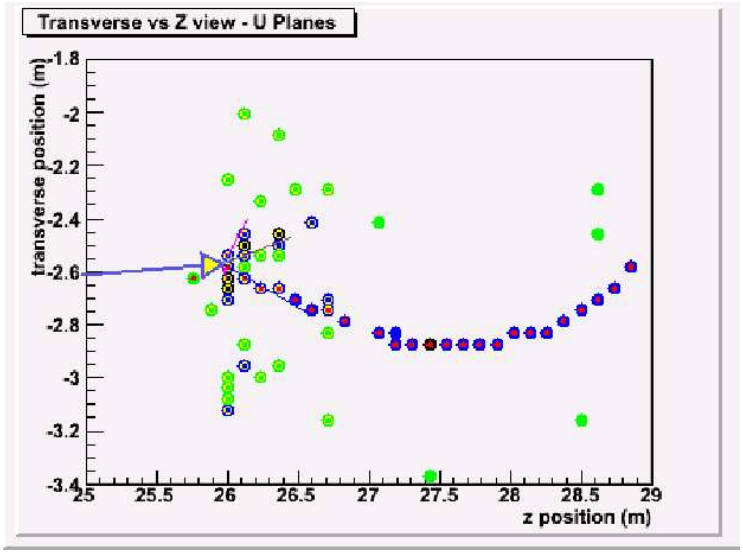

(a)

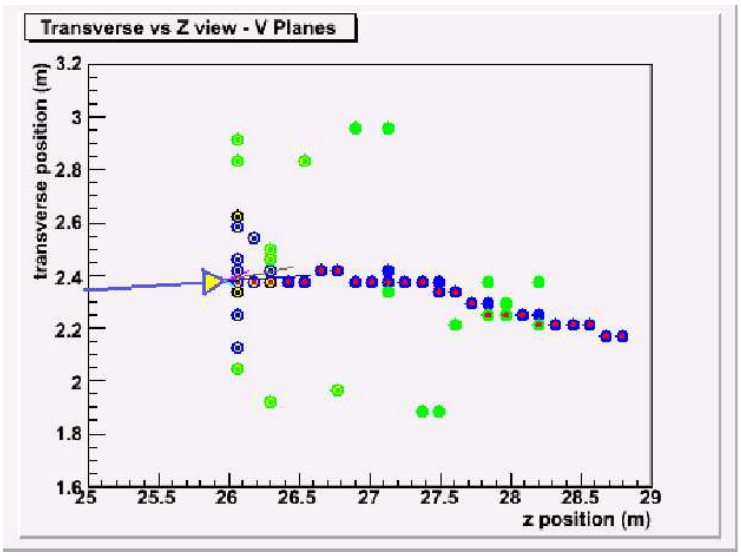

(b)

Figure 4.1: MINOS FD event display showing a CC ν_μ MC interaction and the subsequent overlap of muon track and hadronic shower in the (a) U and (b) V plane views. The coloured lines show the truth information for the event: blue arrow (inbound neutrino), dark blue line (muon), brown line (neutron), light blue line (neutral pion) and pink line (charged pion). The coloured circles represent the reconstructed strips with the colour representing the charge in PEs: green (< 2) blue (2 - 20) black (> 20). The red dots within the circles represent strips that have been included in the reconstructed track. The yellow rings within the circles represent strips that have been included in a reconstructed shower.

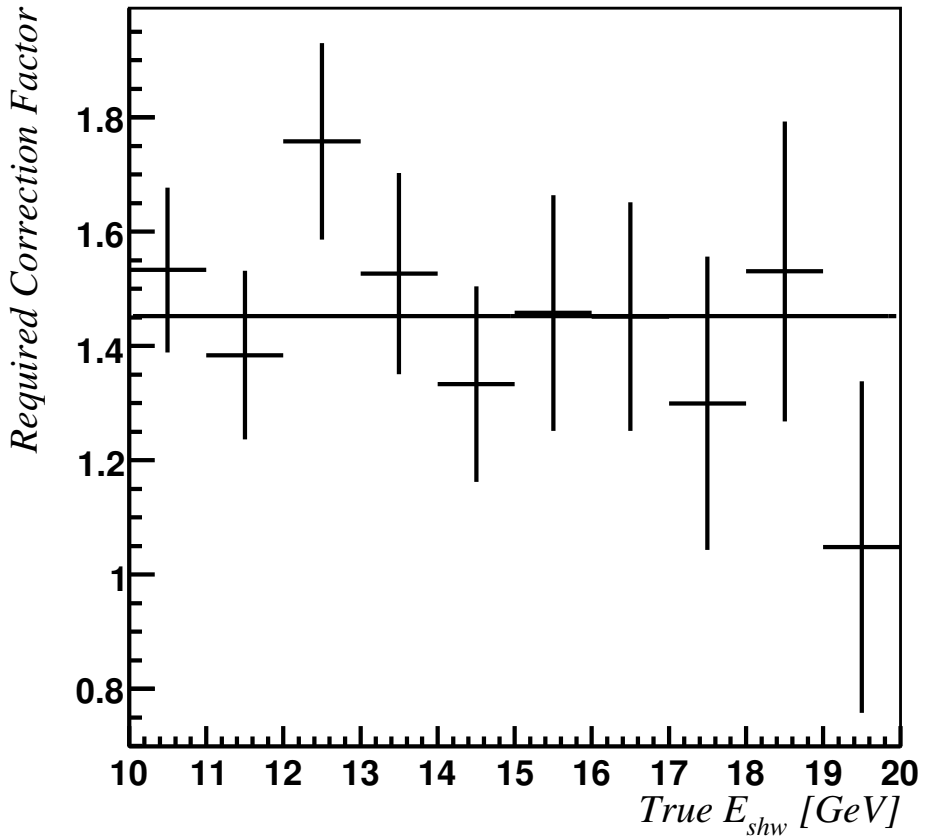

Figure 4.2: The difference between CC and NC showers pulse heights divided by 1 MIP/$\cos\theta_z$ per shared strip plotted against true E_{shw} for FD MC.

to acceptance effects and differences in electromagnetic fraction and W^2 (the squared mass of the produced hadronic system) creating differences in CC and NC shower pulse heights at low energies. The results of this fit are shown in Figure 4.2 and it can be seen that a factor of approximately 1.45 MIP/$\cos\theta_z$ per shared strip is required to make the high energy CC and NC showers agree. This method of removing the muon charge was used in version 1.18.2 of the MINOS software, which is used for the oscillation analysis described in this thesis. However, in the recent 1.24 software version an improved method for removing the muon charge was developed which is outlined below.

The momentum of the muon will have a non-negligible effect on the amount of charge it deposits in the detector. An estimate of the muon momentum is known (derived from range in the case of fully contained tracks and from curvature if only the track vertex is contained and it passed the fitter) and is used to determine $\mathrm{d}E/\mathrm{d}x$ in the scintillator.

This is done using the Bethe-Bloch equation:

$$-\frac{\mathrm{d}E}{\mathrm{d}x} = 4\pi N_A r_e^2 m_e c^2 z^2 \frac{Z}{A}\frac{1}{\beta^2}[\frac{1}{2}ln(\frac{2m_e c^2\beta^2\gamma^2 T_{max}}{I^2}) - \beta^2 - \frac{\delta}{2}]$$

where $\gamma, \beta c$ and z are the relativistic gamma factor, velocity and charge (in units of e) of the incident particle and T_{max} corresponds to the maximum energy that can be transferred to an electron in a single interaction. N_A is Avogadro's number and r_e is the classical electron radius. Z, A, I and δ correspond to the atomic number, mass number, mean excitation energy and density correction factor of the material through which the particle is passing.

The value of $\mathrm{d}E/\mathrm{d}x$ at the track vertex is calculated, assuming this is also the location of the shower vertex, and normalised to units of Minimum Ionising Particles (MIPs) defined in 3.3. The value of $\mathrm{d}E/\mathrm{d}x$ at the end of the shower is then calculated using the estimation for p/q for the last shared strip, if the event passed the TrackFitter. Otherwise it is approximated that a muon loses 1 GeV of energy over 30 detector planes, taking $\cos\theta_z$ into account. If the track does not end very far from the end of the shower then the calculated $\mathrm{d}E/\mathrm{d}x$ may be very high due to the sharp rise in the Bethe-Bloch equation at low momenta. This correction was introduced to take into account of increased $\mathrm{d}E/\mathrm{d}x$ for high energy muons, so if $\mathrm{d}E/\mathrm{d}x$ is higher at the end of the shower than at the vertex, then the factor at the vertex is used. Otherwise the average of the two values is used. The corrected CC shower charge, PH_{shw}^{CC}, is therefore:

$$PH_{shw}^{CC} = PH_{shw}^{Tot} - N_{\text{shared strips}} \times \mathrm{d}E/\mathrm{d}x \times \frac{1}{\cos\theta_z}$$

where PH_{shw}^{Tot} is the reconstructed shower pulse height (measured in MIPs) before the correction. As before the difference in CC/NC shower responses is divided by the average amount of charge removed from CC showers for a given true E_{shw} to determine any necessary correction factor. A zeroth order polynomial fit to this ratio for high true E_{shw}, as shown in Figure 4.3, returns a value of approximately 1, showing that the correct amount of charge is being removed. It also shows the distributions of shower MIPs plotted against true E_{shw} for true CC showers, NC showers and CC showers with muon charge removal. The difference in the CC and NC shower distributions can be seen to decrease at low energies as there are fewer shower strips in which the muon can deposit charge. There is good agreement between the corrected CC and NC shower distributions over a large range of true E_{shw}. It should be noted that between R1.18.2

and R1.24 software versions there were also considerable improvements to the tracking of muons in the shower region which contribute to this improvement.

To estimate the effect that this improved muon charge removal has on E_{shw} resolution, the distributions of corrected CC shower charge are studied. Using results from R1.18.2, corrected CC shower charges are calculated using the two methods for a given bin of true E_{shw}. For each bin of true E_{shw} the shower response is fitted with a Gaussian and the ratio of the width and the mean ($\sigma_{\text{pulse height}}$/mean pulse height) is calculated for each method. Figure 4.4 shows the results of this study and it can be seen that the fractional uncertainty is reduced by including the effect of muon momentum in the muon charge removal.

The corrected CC shower response is calibrated by binning the events in bins of true E_{shw}. In each energy bin the shower response is plotted, a 2 σ cut is applied to remove outliers and a Gaussian fit is performed to determine the mean and its associated error. The corrected CC pulse height can be negative at very low E_{shw} due to fluctuations in deposited muon charge. This is acceptable as it makes the distribution symmetric which is important for an accurate Gaussian fit. There are also non-Gaussian tails affecting the high side of the response distribution, particularly at low true E_{shw}. These are caused by events with low energy protons, either from QE interactions that dominate the cross-section at low energies or from a secondary interaction. Protons, due to their greater mass, have a much steeper $\mathrm{d}E/\mathrm{d}x$ curve at low momenta relative to lighter particles in the showers. This means that they will deposit most of their energy over a small distance at the end of their track. The low granularity of the MINOS detectors means that there will be large variations in pulse height depending on whether the protons come to rest in the iron or the scintillator. These tails in the shower response can severely skew the low energy fits, so each energy bin is inspected by eye to make sure that the mean of the Gaussian accurately represents the peak of the distribution.

The mean shower responses and their associated errors are then plotted against true E_{shw} and fitted with a second order polynomial for low energies and a first order polynomial for high energies. Any events that had negative reconstructed pulse height due to charge removal are now assigned reconstructed energies of zero. Figure 4.5 shows the results of the fit. It also shows the fractional energy resolution and offset as a function of true E_{shw}. The fractional energy resolution (σ_E/E) is defined as the width of the Gaussian fitted to the distribution of (reconstructed E_{shw} - true E_{shw})/true E_{shw}. The fractional energy offset ($\Delta E_{shw}/E_{shw}$) is defined as the mean of the Gaussian fitted to the distribution of (reconstructed E_{shw} - true E_{shw})/true E_{shw}. The non-linearity seen at low energies

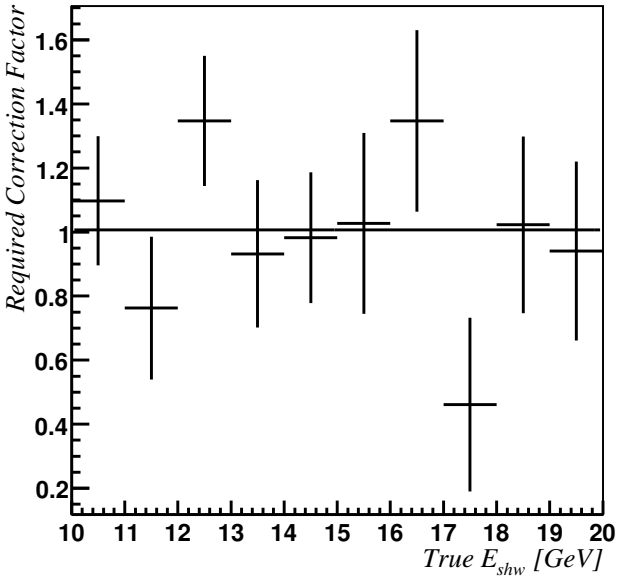

(a)

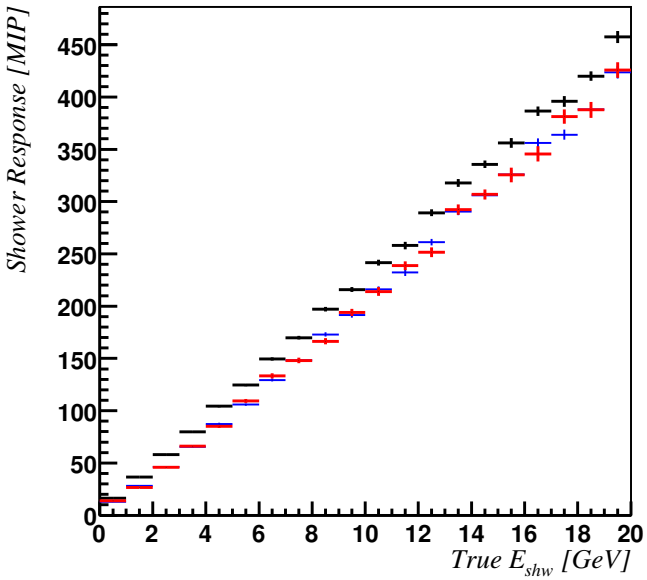

(b)

Figure 4.3: (a) The difference between CC and NC showers pulse heights divided by the muon charge correction factor plotted against true E_{shw} for FD MC. (b) Reconstructed MIPs plotted against true E_{shw} for CC (black points), NC (red points) and CC showers with muon charge removal (blue points) for FD MC.

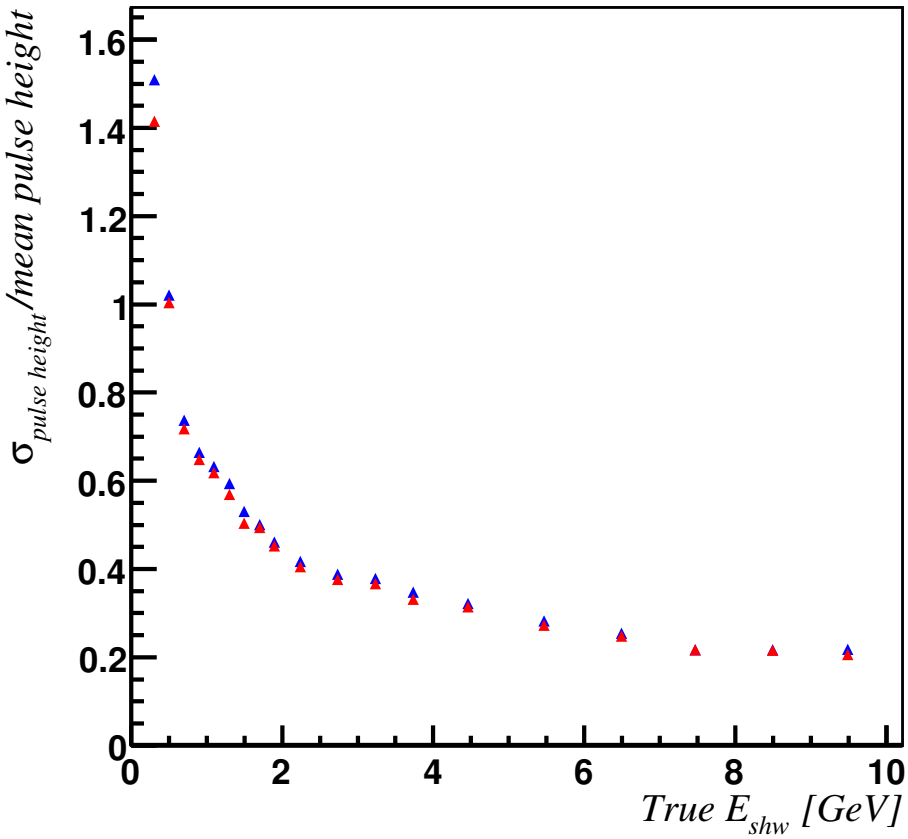

Figure 4.4: Relative uncertainties in corrected CC shower response using $\mathrm{d}E/\mathrm{d}x$ method (red line) and without (blue line) plotted against true E_{shw} for FD MC.

is most likely due to the low granularity of the MINOS detector, so at lower energies it requires a larger step in E_{shw} to deposit charge in additional strips and planes. The deviation from zero seen in the fractional offset plot is due to the tails that distort the Gaussian fits at low energies. Figure 4.6 shows the reconstructed CC E_{shw} distribution along with the true CC E_{shw} distribution for events within the calibration set.

4.9.2 Neutral Current (NC) and Electromagnetic (EM) Shower Calibration

It is necessary for the NC calibration set to pass the following cuts:

- Events are true NC ν_μ interactions
- There must be only one reconstructed shower in the event. The presence of more than one shower in the event would indicate a failure to completely reconstruct the shower.

No condition on the presence of a reconstructed track is required as depending on the topology of the NC shower, it may or may not have a track reconstructed with it. As there is no muon track that may deposit additional charge in the shower, no corrections to the reconstructed shower pulse height are necessary. The calibration process is then performed as for the CC showers. Very similar results to the CC shower calibration are achieved. The NC fractional E_{shw} resolution is found to be slightly better than CC equivalent, particularly at low E_{shw}. This is due to the fact that there is no added uncertainty from the muon charge removal or the chance that the muon path through the shower was mistracked. The calibration functions are slightly different than those used for the CC showers. This is because the CC and NC shower responses for a given true E_{shw} can be quite different at low energies due to acceptance affects. This arises from the fact that a snarl must have at least one reconstructed object to become an event, so while a very low true E_{shw} CC event may have a shower composed of several track strips along with some genuine shower strips, an NC shower of the same energy might fail the shower finding stage.

The EM shower calibration set was defined identically to the NC sample, except requiring that the events were true CC ν_e interactions. The EM showers are calibrated in the same way as the NC sample. As before slightly different constants from the NC calibration are

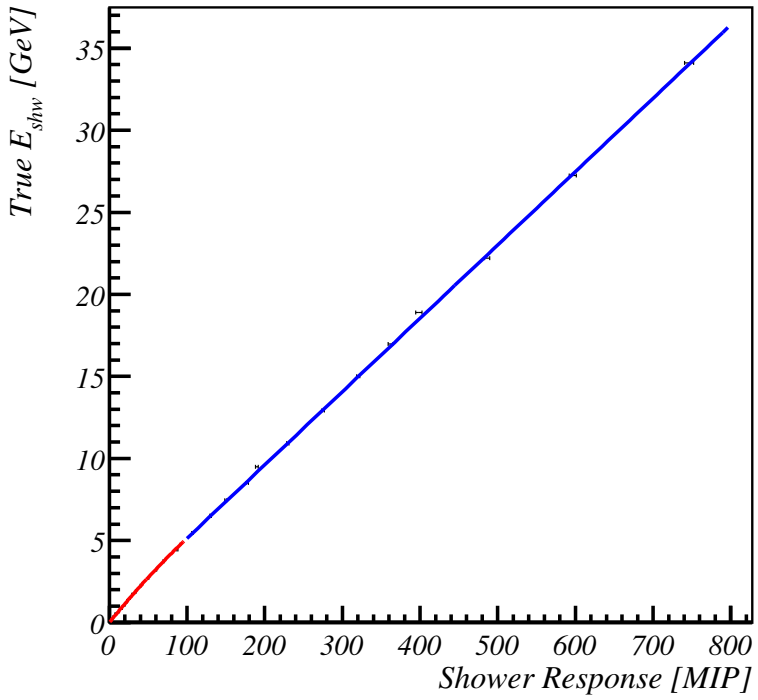

(a)

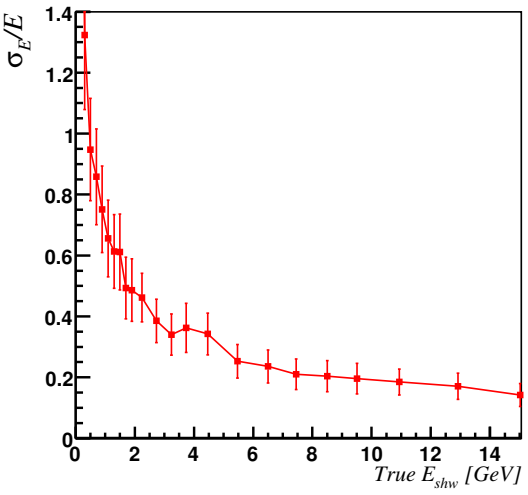

(b)

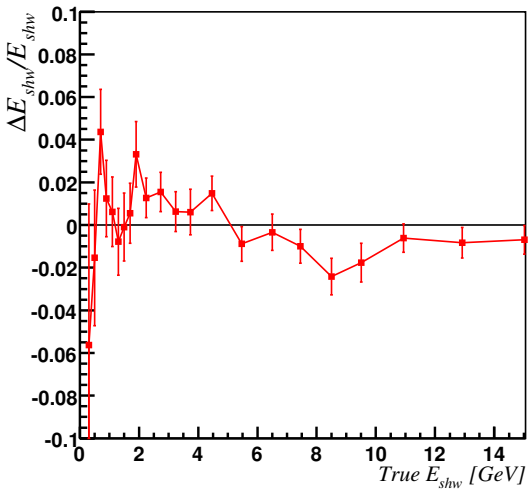

(c)

Figure 4.5: (a) Mean shower response binned in true E_{shw} and fitted with polynomials, (b) Fractional reconstructed E_{shw} resolution plotted against true E_{shw} , (c) Fractional offset from true E_{shw} plotted against true E_{shw} for CC showers in FD MC.

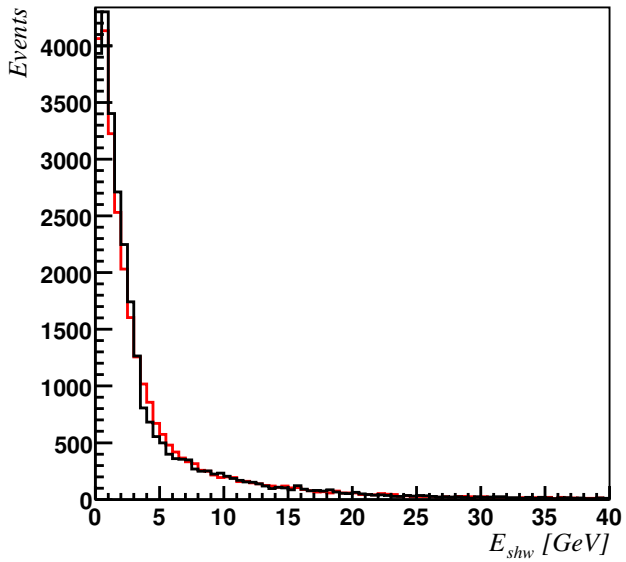

Figure 4.6: Distributions of reconstructed (black line) and true (red line) CC E_{shw} for FD MC.

required and the EM showers are found to have improved energy resolution over the NC shower sample. This is because showers from CC ν_e interactions have an electromagnetic component to their showers from the produced e^-.

4.9.3 Deweighted Shower Energy

The presence of large tails in the distribution of shower pulse heights at low energies degrades the ability of the MINOS experiment to accurately determine the energy of the interacting neutrino at energies where the oscillation minima is expected to occur (~ 1.5 GeV). These tails are caused by soft protons depositing large amount of charge in a small number of strips. In an attempt to improve the low energy E_{shw} resolution, instead of calibrating using the total shower pulse height for a given bin of true E_{shw}, the individual shower strip charges were deweighted by various powers before being summed and this value, $PH_{shw}^{Deweight}$, was then used in calibration:

$$PH_{shw}^{Deweight} = \sum_{i=1}^{n} Q_i^x$$

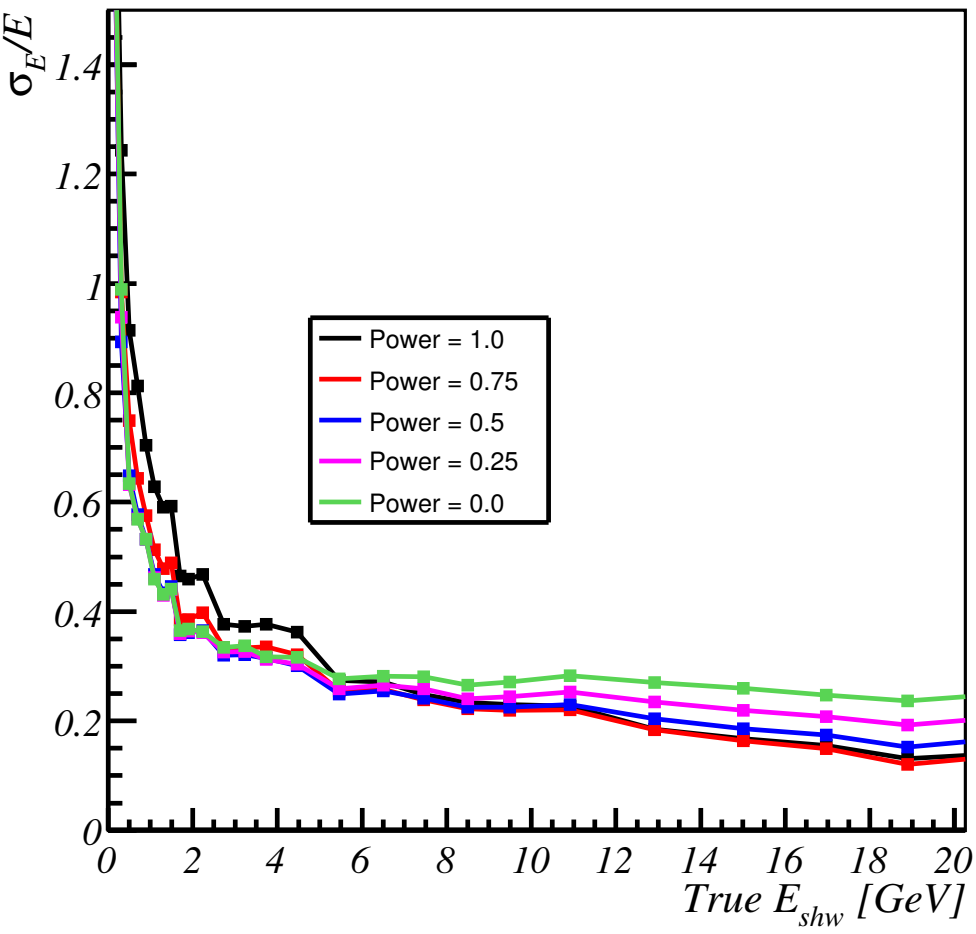

Figure 4.7: Shower energy resolution for different strip deweighting powers plotted against true E_{shw} for FD MC.

where Q_i is the charge of the i^{th} shower strip, n is the total number of strips in the shower and x is the deweighting power applied to each strip and is < 1. This deweighting has the effect of increasing the relative importance of the number of strips in the shower over the total shower charge. In the case of a low energy proton depositing a large charge in a small number of strips, the deweighted shower charge would be lower than that using the non-deweighted method. Using the deweighted shower charge suppresses the large fluctuations in deposited pulse height, thereby improving energy resolution for low energy showers.

Figure 4.7 shows the fractional CC E_{shw} resolutions plotted against true E_{shw} for a range of strip charge deweighting powers. The powers run from 1, which corresponds

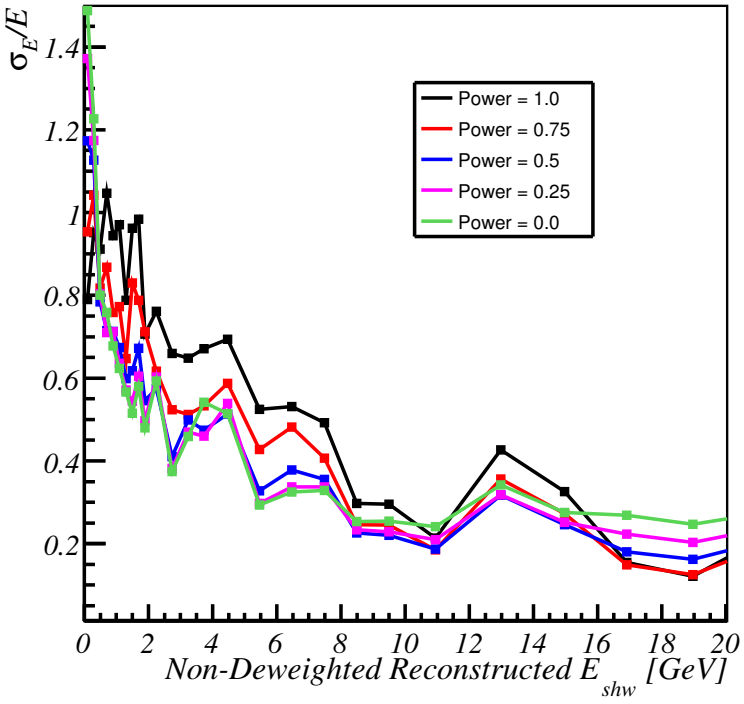

Figure 4.8: Shower energy resolution for different strip deweighting powers plotted against non-deweighted reconstructed E_{shw} for FD MC.

to summing the strip charges, to zero, which is equivalent to counting the number of strips in the shower. It can be seen that the lower the deweighting power, the greater the improvement in resolution at low E_{shw}. However, there is also a corresponding loss of resolution at high E_{shw} with decreasing deweighting power. This is to be expected as at higher energies the shower size begins to saturate, so the total strip charge becomes important in differentiating between showers with similar energies. The solution to this issue is only to deweight the shower strip charges of low energy showers and not high energy showers. It is therefore necessary to have an indicator of a shower's likely energy to determine the best level of deweighting to apply. The non-deweighted shower energy is a suitable variable to do this. Figure 4.8 shows the same information as Figure 4.7 but plotted against reconstructed E_{shw}. From this plot it is possible to see the optimal deweighting power for each region of reconstructed E_{shw}.

A curve of optimal deweighting power plotted against reconstructed E_{shw} can be then obtained, as shown in Figure 4.9. The deweighting power was constrained to be above 0.25 so as to make the method less sensitive to systematic differences between data and

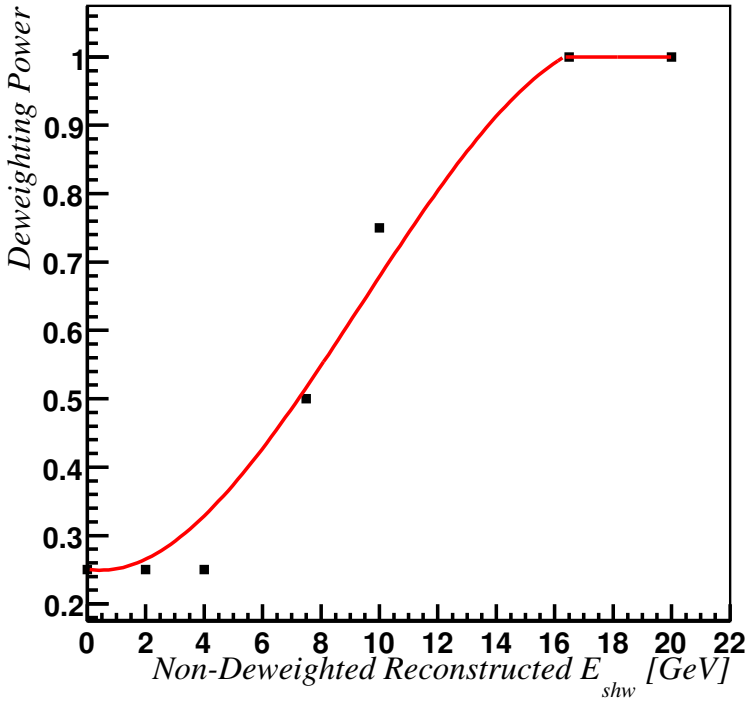

Figure 4.9: Plot of optimal deweighting power for each range of reconstructed energy fitted with a suitable polynomial to give the optimal deweighting function for FD MC.

MC such as noise levels and PMT thresholds. A third order polynomial is used to fit these points. Above $\sim$ 16 GeV, no deweighting is applied. This variable deweighting can now be applied to the strips of CC and NC showers. It is not used for EM showers as they will not experience the kind of fluctuations described above.

As individual shower strips are being considered, it is necessary to slightly alter the method of removing muon charge from CC showers. The most likely amount of charge deposited by the muon in a shower strip is calculated (based on its momentum and direction). If a strip which is shared between the track and the shower has a charge greater than this, then the muon charge is subtracted and the resulting difference is deweighted by the appropriate power and added to the total for the shower. If the strip charge is less than that from the muon then the strip does not contribute towards the total shower charge. This deweighted shower pulse height is then calibrated as before.

Figure 4.10 shows the results of the fit and the fractional energy resolution and offset from truth plotted against true E_{shw}. It can be seen that the deweighting introduces

some non-linearity into the shower response so higher order polynomials are used to fit most of the energy range. It is ensured that the higher energies use approximately the same first order polynomial as for the non-deweighted calibration to ensure that the two methods returned the same reconstructed energy for high energy showers. An improvement in low E_{shw} resolution is observed, giving $\sigma_E/E = 0.50 \pm 0.09$ for 1 GeV showers, compared to a resolution of 0.69 ± 0.13 using the non-deweighted method. There is no loss of resolution at high energies.

Figure 4.11 shows the true and reconstructed E_{shw} spectra using both the Deweighted and Non-Deweighted reconstructions. It also shows the distribution of deweighted plotted against Non-deweighted reconstructed E_{shw}. It shows agreement at high energies and some deviation at low energies which is to be expected due to the different weightings applied to low energy showers.

This process is repeated for NC showers, assuming the same optimal deweighting curve, but without the need for removing muon charge from the shower. As with the CC case, an improvement in low E_{shw} resolution is observed, giving $\sigma_E/E = 0.42 \pm 0.1$ for 1 GeV showers, compared to a resolution of 0.70 ± 0.17 using the non-deweighted method. There is no loss of resolution at high energies.

So far all the calibrations have been done in the Far Detector as the low event rate makes it easier to get high quality events for calibration. These calibrations will not be completely valid in the near detector due to the slicing process. This can have the effect of splitting up large showers or merging smaller showers into larger ones. To take this into account ND MC is used with the FD shower calibrations and a plot of $\Delta E_{shw}/E_{shw}$ plotted against true E_{shw} is used to determine a suitable correction that can be applied to the reconstructed ND E_{shw}. Generally a correction of the form:

$$\text{ND } E_{shw}^{corr} = E_{shw} \times (a \pm \exp \frac{-(E_{shw}+b)}{c})$$

is found to give the best results where a, b and c are constants. Figure 4.12 shows the fractional E_{shw} offset plotted against true E_{shw} before and after the correction for both CC and NC showers using the non-deweighted E_{shw} reconstructions. It can be seen that the offset are greatly reduced over most of the true E_{shw} range. Similar results are obtained using the deweighted energy reconstruction.

Figure 4.13 shows the Near Detector fractional E_{shw} resolution plotted against true E_{shw} for CC and NC showers using the non-deweighted reconstructions. It also shows the

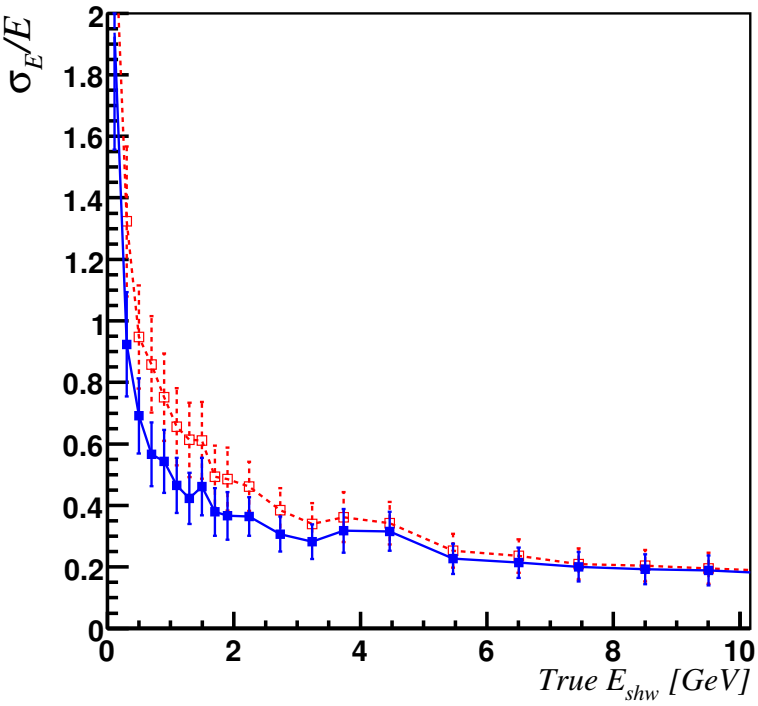

(a)

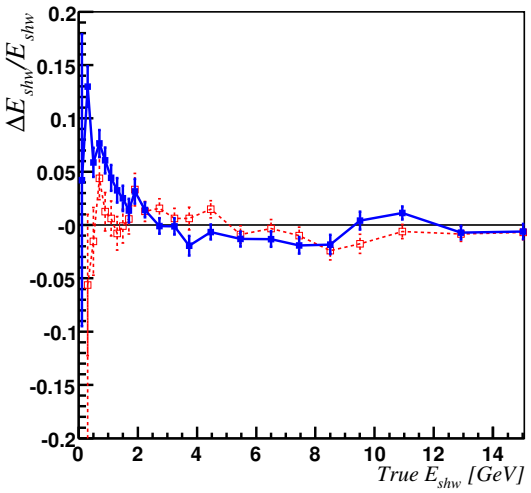

(b)

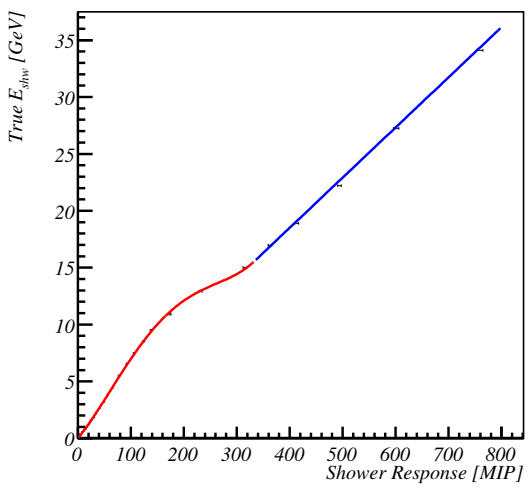

(c)

Figure 4.10: (a) Fractional reconstructed E_{shw} resolution, σ_E/E, plotted against true E_{shw}, (b) Fractional offset from true E_{shw} , $\Delta E/E$, plotted against true E_{shw} for CC deweighted showers in FD MC, (c) Mean shower response binned in true E_{shw} and fitted with polynomials. In plots (a) and (b) the non-deweighted E_{shw} reconstruction is represented by the dashed red line and the deweighted E_{shw} reconstruction is represented by the solid blue line.

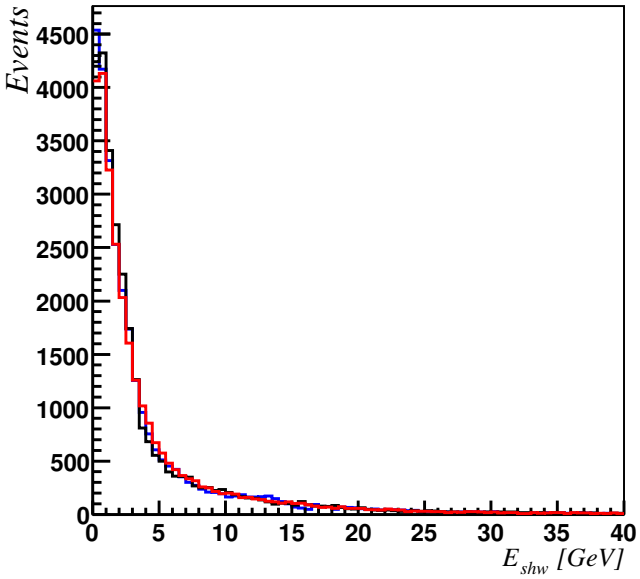

(a)

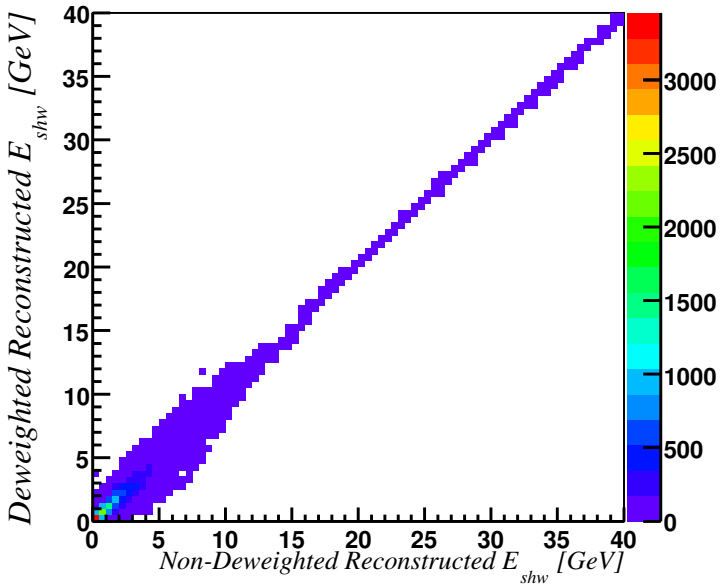

(b)

Figure 4.11: (a) True E_{shw} (black line), non-deweighted reconstructed E_{shw} (red line) and deweighted reconstructed E_{shw} (blue line), (b) Reconstructed Non-Deweighted E_{shw} plotted against Reconstructed Deweighted E_{shw} for CC showers in FD MC.

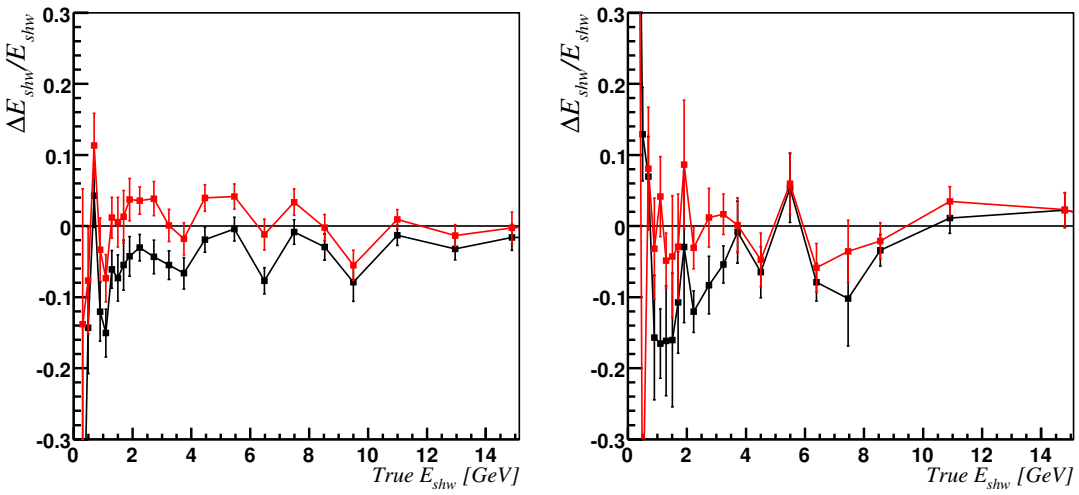

(a) (b)

Figure 4.12: Fractional E_{shw} offset plotted against true E_{shw} before (black line) and after (red line) correction for ND effects for (a) CC Non-Deweighted E_{shw}, (b) NC non-deweighted E_{shw}.

equivalent plots for the Far Detector and it can be seen that for the CC showers the E_{shw} resolutions of the two detectors are quite similar with the Far Detector having slightly improved resolution. This discrepancy is much larger for NC Showers. This additional uncertainty is due to the effect of slicing. Also events that do not have a reconstructed track will have a large uncertainty on their longitudinal strip position which will affect the attenuation correction. This effect will be larger in the Near Detector due to the fact that only one end of each strip is read out. Similar results are obtained using the deweighted energy reconstruction.

While the Deweighting E_{shw} reconstruction method is seen to improve energy resolution, it may also introduce additional systematic effects when applied to data. Possible sources of systematic effects are from the threshold levels of the PMTs which could alter the number of strips in the shower as well as optical cross-talk. This would have a large effect at low energies where the level of deweighting is highest. Also the effect of any incomplete modelling of the distribution of charge with the shower would be increased using the deweighting method. Near Detector Data and MC were used to determine the level of these effects. For selected events (see Section 5.1.2 for details of selection cuts) with a reconstructed shower, plots of deweighted E_{shw} plotted against non-deweighted

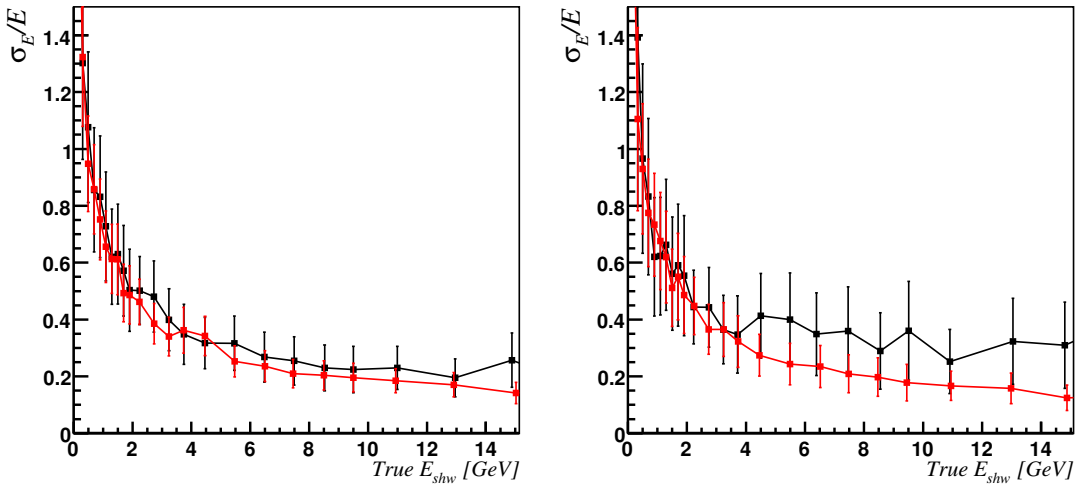

(a) (b)

Figure 4.13: Fractional E_{shw} resolution σ_E/E plotted against true E_{shw} for ND MC (black line) and FD MC (red line) for (a) CC non-deweighted E_{shw} ,(b) NC non-deweighted E_{shw}.

E_{shw} were made for Data and MC. For a given bin of non-deweighted E_{shw} , the fractional difference between Data and MC $((E_{shw}^{Data} - E_{shw}^{MC})/E_{shw}^{MC})$ using deweighted E_{shw} is calculated. Figure 4.14 shows the results of this comparison. It can be seen that there is very little Data/MC difference in deweighted E_{shw} at high energies. Below the level at which deweighting is introduced ($\sim 16\,\text{GeV}$) a Data/MC difference is observed that increases at lower energies before plateauing out. A zeroth order polynomial fit to this plateau region returns an offset of 2.3%. This is small in comparison to other expected shower systematics (see Section 7.2 for details) so the deweighted E_{shw} will be used as the default shower energy from now on.

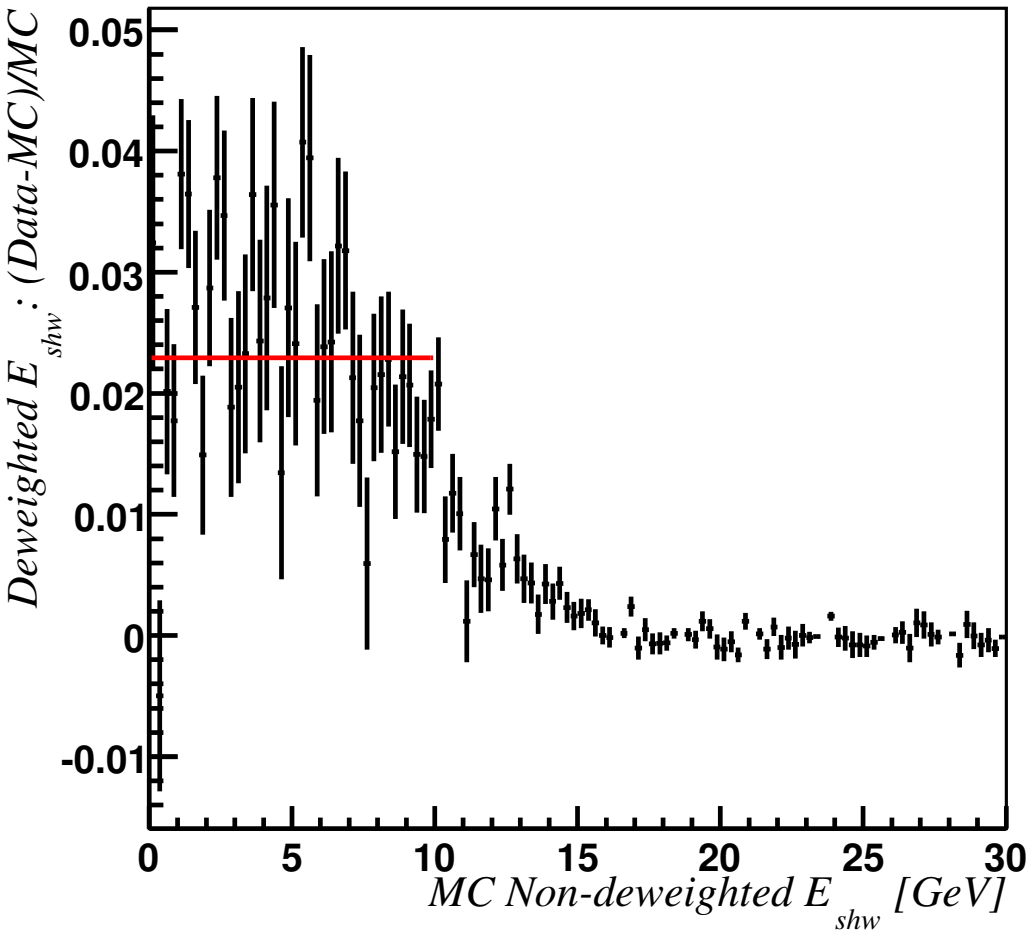

Figure 4.14: ND factional Data/MC difference in deweighted E_{shw} plotted against non-deweighted E_{shw}. A zeroth order polynomial fit to the plateau region is represent by a red line.

Chapter 5

Near Detector Results

"However beautiful the strategy, you should occasionally look at the results."
— Winston Churchill

5.1 Beam Data and Monitoring

The first run of the MINOS experiment took beam data between May 2005 and February 2006. During this period the NuMI beam achieved a total of 1.27×10^{20} protons delivered to the NuMI target (PoT). Figure 5.1 shows the rate at which the protons were delivered along with the cumulative total during the data taking period. The purpose of the Near Detector was to provide information on the spectrum, rate and composition of the NuMI beam. The Near Detector is triggered from the Main Injector signal to read out the detector for the duration of the SGATE window as described in Section 4.1.

It is necessary to show a comparison of MC and Data for the Near Detector to show that effects such as detector hardware, beam modelling, calibration and reconstruction have all been sufficiently understood. During the spill process many beam quantities were monitored, enabling only those events associated with good quality spills to be used in the analysis. The following quality requirements were placed on the beam spills:

- $0.5 \times 10^{12} <$ PoT in spill $< 50 \times 10^{12}$
- $|t_{snarl} - t_{spill}| < 1.0\,\mathrm{s}$ (where t_{snarl} is the time of the earliest edge of the SGATE

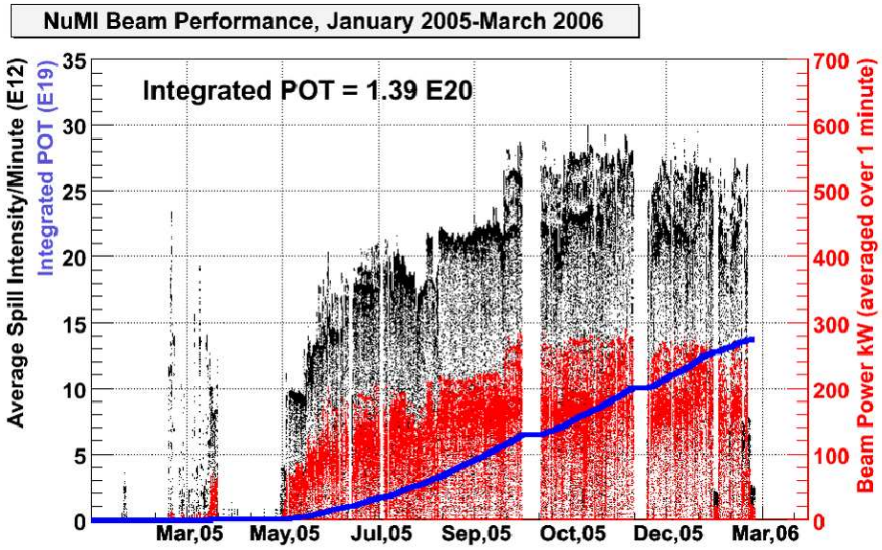

Figure 5.1: Average spill intensity (black points), beam power (red points) and integrated protons delivered to the target plotted against time for the NuMI beam during its first experimental run, taken from [55].

window and t_{spill} is the predicted time of the spill from the Main Injector as explained in Section 4.1)

- $-200 <$ Horn Current $< -155\,\text{kA}$
- Target is in the 'LE-10' configuration (where the z-position of the target is 10 cm less than the LE position)
- $-2.0 < \overline{x}$, the mean x-position of the beam spot $< -0.01\,\text{mm}$
- $0.01 < \overline{y}$, the mean y-position of the beam spot $< 2.0\,\text{mm}$
- $0.1 < \sigma_x$, the RMS of the x profile of the beam spot $< 1.5\,\text{mm}$
- $0.1 < \sigma_y$, the RMS of the y profile of the beam spot $< 2.0\,\text{mm}$

Due to the large excess of data relative to the available MC statistics, only a representative subset of the data was studied. At least two runs (each lasting $\sim 24\,\text{hrs}$) of data were taken from each month of operation (other than February where various systematic beam tests mean many spills failed the above cuts), giving a total of 1.0×10^{19} PoT of spills passing the above cuts. These data were compared to a sample of MC events equivalent to 3.0×10^{18} PoT. Both Data and MC have been processed with version 1.18.2 of the MINOS reconstruction software.

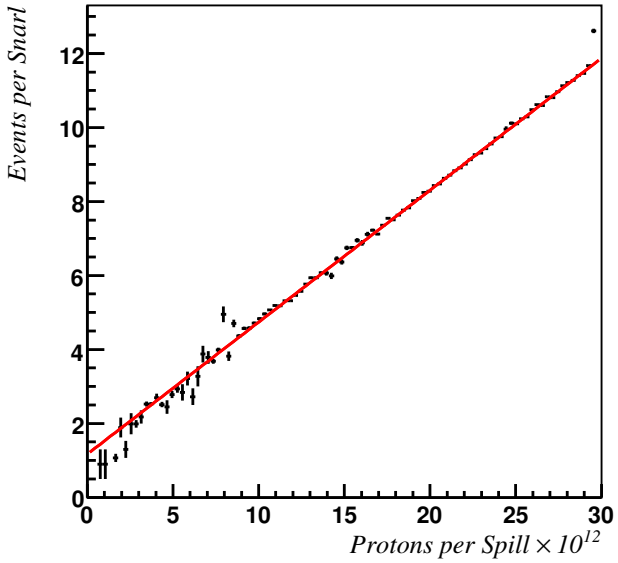

Figure 5.2: Number of reconstructed events against spill intensity along with a linear fit.

Figure 5.2 shows the number of reconstructed events per snarl against the intensity of its associated spill. It can be seen that there are no strong non-linearities, showing that the reconstruction software is unaffected by the additional events in each snarl for the range of beam intensities in the data sample. Figure 5.3 shows the ratio of reconstructed events to PoT plotted against time, and it can be seen that this has remained approximately constant throughout the data taking period.

The protons from the Main Injector are not delivered equally over the course of each spill but in 5 or 6 batches, with the each batch lasting for approximately 1.6 μs. Figure 5.4 shows the reconstructed neutrino energy spectrum associated with each batch. There is no significant variation in the beam energy spectrum between events from the different batches.

Figure 5.5 shows the reconstructed neutrino energy, E_ν, spectra for each month as well as the average (all normalised to the same PoT). No non-statistical deviations from the average are observed further demonstrating the stability of the data.

The fiducial volume is approximately centred on the beamspot. It allows hadronic showers to completely develop before the start of the muon spectrometer region and removes rock muons and cosmics. Due to the large amount of Near Detector data available, this volume can be relatively small; the fiducial mass is only 4.5% of the

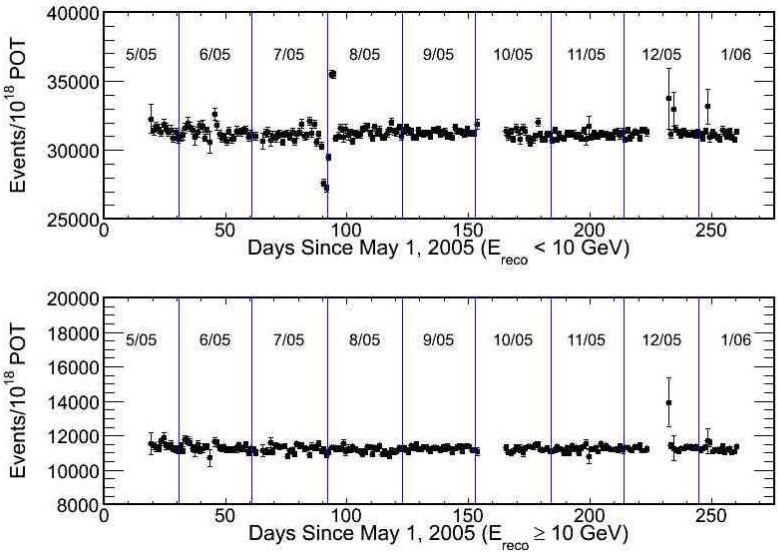

Figure 5.3: Number of reconstructed events/PoT in a day against time, taken from [55].

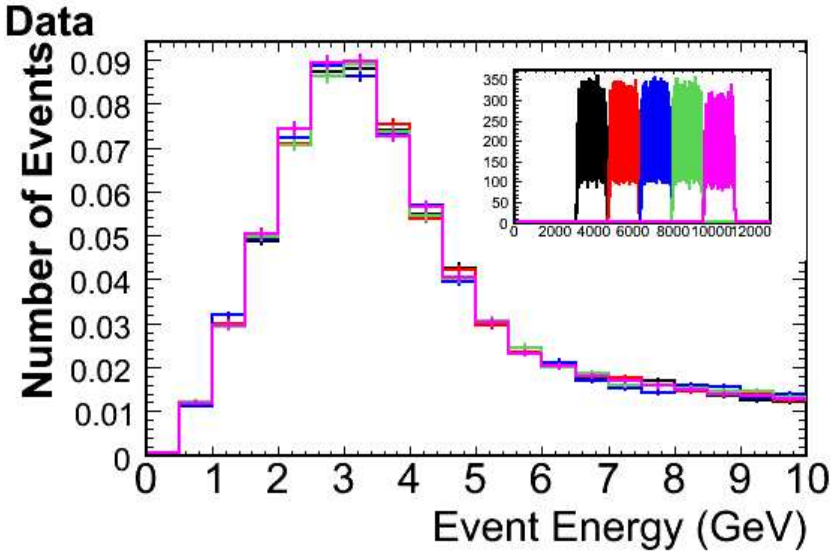

Figure 5.4: Reconstructed neutrino energy via batch with inlaid plot of the time structure of a spill with each colour representing a different batch, taken from [55].

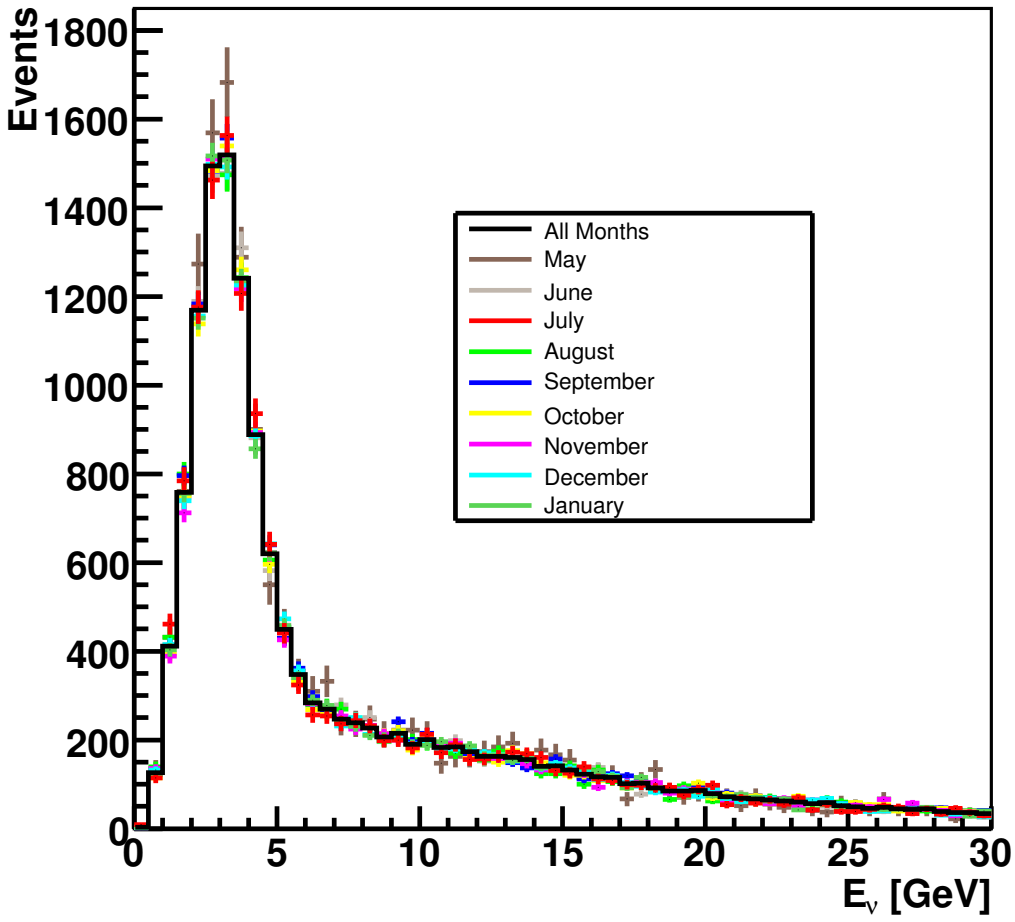

Figure 5.5: Reconstructed E_ν spectra for each month along with the average over all months.

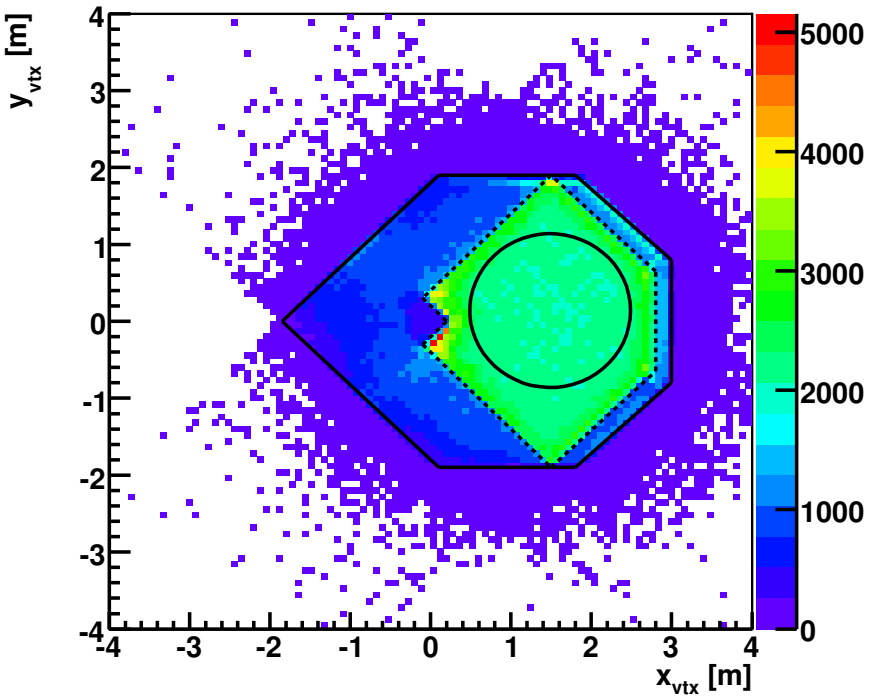

Figure 5.6: Data event vertices across Near Detector face. The position and shape of the fiducial volume is represented by the black circle. The outlines of the partially (dashed line) and fully (solid line) instrumented planes are also shown.

detector. The Near Detector fiducial volume is defined as:

- $1.0 < z_{vtx} < 5.0\,\text{m}$ (where z_{vtx} is the z position of the reconstructed event vertex)
- $r_{vtx} < 1.0\,\text{m}$ (where r_{vtx} is the radial position of the reconstructed event vertex from the centre of the fiducial volume, at $x = 1.4885$ m, $y = 0.1397$ m)

The distribution of data event vertices across the face of the detector is shown in Figure 5.6. It is possible to see the outline of the fully and partially instrumented planes as well as the coil hole. The vertices located outside the area of the fully instrumented planes are due to incorrect reconstruction of the longitudinal strip position of the vertex. This can be caused by the absence of a large number of track strips in one view, leading to an extrapolation of the longitudinal position in the other view to a point outside the detector.

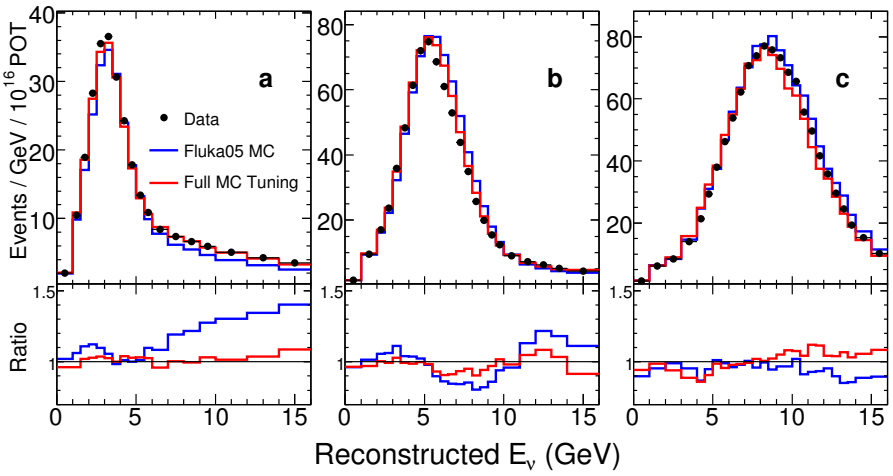

Figure 5.7: Reconstructed E_ν in the MINOS ND for three of the six beam configurations before and after the 15 parameter beam tuning procedure. The target location was modified to produce the different spectra: (a) Nominal, (b) target at 90 cm from nominal, (c) target at 240 cm from nominal. The lower inset shows the ratio of data to MC before and after tuning. Figure taken from [68].

5.1.1 Beam Reweighting

The main sources of systematic uncertainty in the MINOS Monte Carlo concern the production of the mesons in the target via $p + C \rightarrow \pi^{\pm} + X$ and $K^{\pm} + X$ that go on to produce the ν_μ beam and the interaction of these mesons as they propagate throughout the various components of the NuMI beamline. The beamline effects include horn current, horn alignment, proton spot size at the target, scraping of protons on target baffle and distribution of skin current depths in the horn. Systematic effects such as these introduce uncertainty into the Near Detector E_ν spectrum which leads to uncertainty in the predicted Far Detector spectrum. It is possible to improve the agreement between data and Monte Carlo by parameterising the hadron production and beam effects and then fitting the Monte Carlo to the data in the Near Detector.

The ability of the NuMI beamline to vary the horn current and target positions to produce different spectra allows fits to data from several beam configurations. This means that large ranges of hadron production and beamline effect spectra are probed. The seven parameter SKZP model is used to describe hadron production in the MINOS target and a full description of this process can be found in [69]. Figure 5.7 shows the effect of the reweighting on the Near Detector spectrum for several beam configurations. It can

be seen that it improves agreement with data over large ranges of reconstructed E_ν for each of the beam configurations. All Monte Carlo plots shown have been reweighted according to these fits.

5.1.2 Comparison of Data and MC

Figure 5.8 shows the distributions of reconstructed vertex positions and events per snarl for Near Detector MC and data. These plots along with all subsequent plots are for events with vertices within the Near Detector fiducial volume and the MC has been normalised to the same PoT as the data. It can be seen that shapes of the vertex position plots are consistent between MC and Data but an overall excess of data events is observed. The distribution of events per snarl does not show particularly good agreement between MC and data, with data snarls having a broader distribution of events than MC. This is not a serious issue though and is due to the fact that the Near Detector MC files have been created assuming a constant number of protons are delivered every spill.

Figure 5.9 shows the distributions of number of showers, number of tracks and number of showers plotted against number of tracks per event for Near Detector data and MC. The data show an excess of single shower events and a deficit of two shower events relative to the MC, that is independent of the number of reconstructed tracks. This is most likely to be due to poor modelling of hadronic showers in the MINOS detector.

A series of analysis cuts are then implemented to obtain a well reconstructed, high purity CC ν_μ sample. NC events must be removed as they are not sensitive to oscillations. Events are required to have at least one reconstructed track. CC ν_μ events will have a distinct track due to the muon (other than events with high y), whereas tracks in NC events will not emerge far from the shower. This means that NC event tracks are much more likely to be removed during the event building stage (see Section 4.8). It is also required that the Kalman Filter converged for the reconstructed track as this removes poorly reconstructed, non-physical tracks. The number of events with reconstructed tracks passing this cut is shown in Figure 5.10. It can be seen that after this cut that the difference between the data and MC is greatly reduced in terms of number of events.

The TrackFitter also provides information about the charge of the particle that made the track. A cut is applied on the reconstructed q/p of the track requiring it to be negative (i.e. consistent with being a μ^- rather than a μ^+). This is to select CC ν_μ

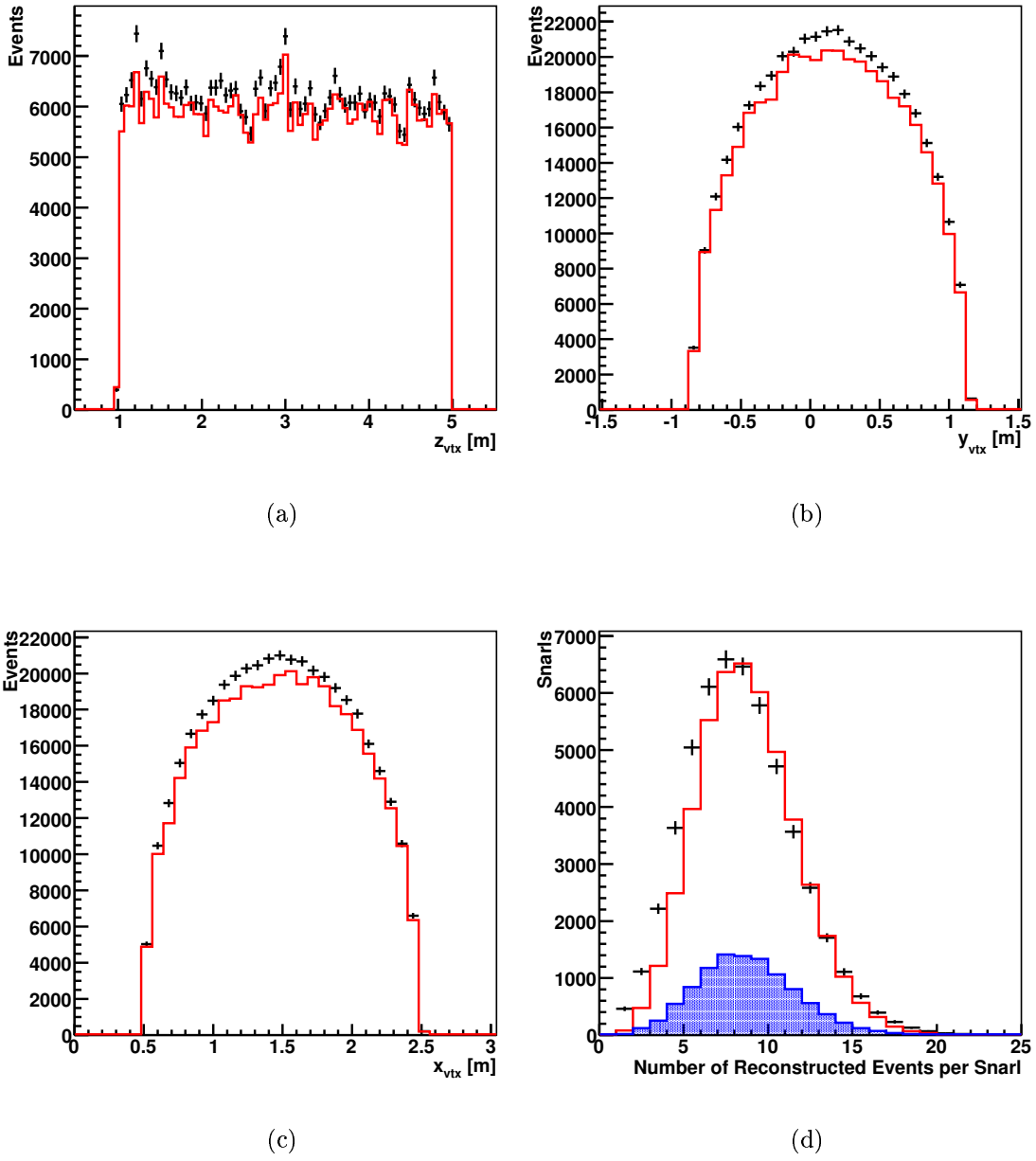

(a) (b)

(c) (d)

Figure 5.8: (a) z_{vtx} (b) y_{vtx} (c) x_{vtx} (d) Events per snarl for Near Detector data (black line) and MC (red line). The MC expectation of NC events is shown by the blue shaded area.

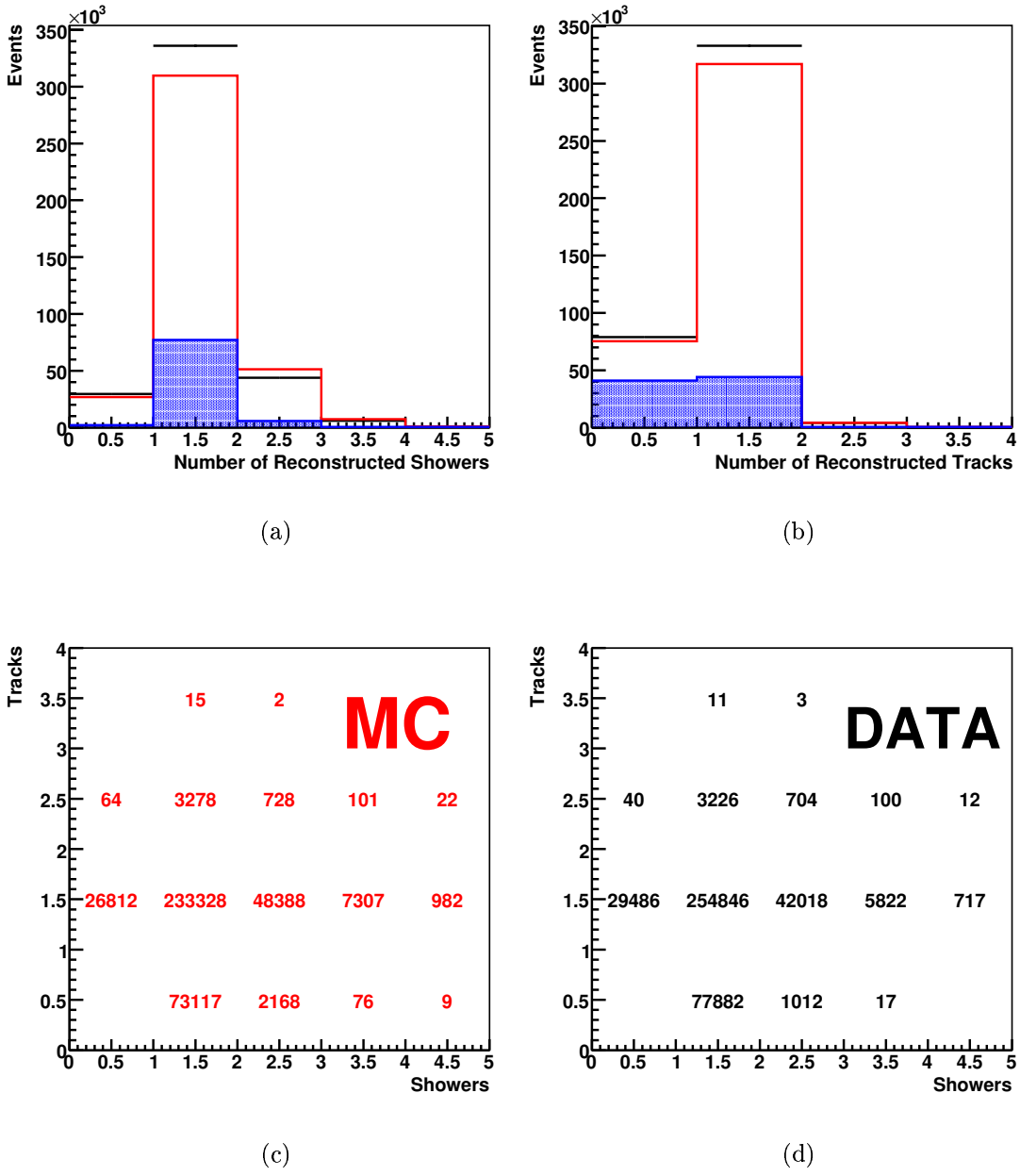

(a) (b)

(c) (d)

Figure 5.9: Numbers of (a) Reconstructed Showers (b) Reconstructed Tracks for Near Detector data (black line) and MC (red line). The MC expectation for the contribution from NC events is shown by the blue shaded area. (c) Number of tracks plotted against showers (MC) (d) Number of tracks plotted against showers (Data).

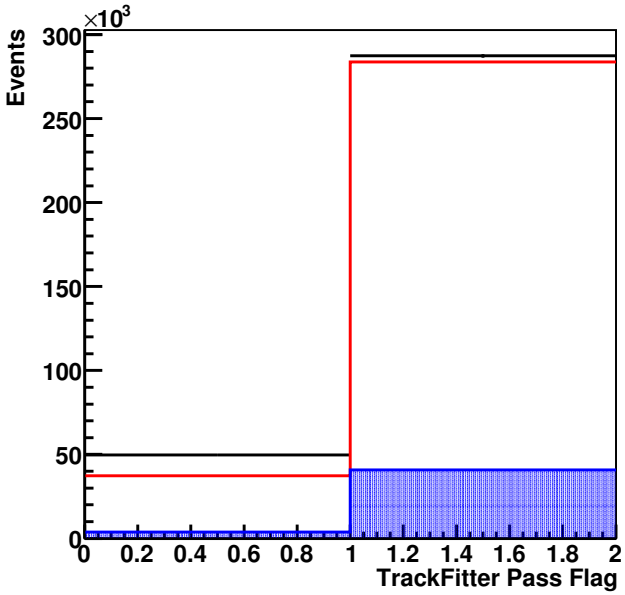

(a)

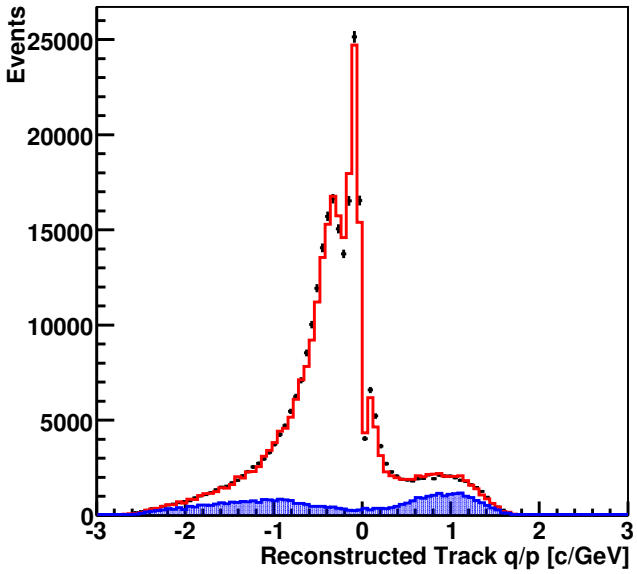

(b)

Figure 5.10: (a) Number of events with tracks that converged in the Kalman-Filter (b) Fitted track q/p for Near Detector data (black line) and MC (red line). The MC expectation for the contribution from NC events is shown by the blue shaded area.

events as opposed to CC $\overline{\nu}_\mu$ events. This cut also reduces the NC background as if an NC event has a reconstructed track, it is usually composed of random shower strips. The NC track is equally likely to curve in either direction and thus be reconstructed with positive or negative charge. There is good agreement between data and MC over the distribution of track q/p, also shown in Figure 5.10.

NC Background Removal

It is necessary to remove as much of the NC background as possible as this will obscure the shape of the CC ν_μ spectra. This is important at low energies (as NC events can deposit any energy less than E_ν in the detector) and so create additional uncertainty in the extrapolation of the Near Detector spectrum to the Far Detector. CC/NC separation is achieved using a likelihood method. Several discriminating variables are used and a PDF (Probability Density Function) of each is made for CC and NC events in MC. For each trial event the PDFs are used to obtain the probability associated with each variable for both the CC and NC hypotheses. CC and NC probabilities are defined as:

$$P_{CC} = \prod_{i=1}^{n} P_{CC}^{i}$$

$$P_{NC} = \prod_{i=1}^{n} P_{NC}^{i}$$

where i is the index of each of the discriminating variables and n is the total number of variables. The CC/NC PID parameter is then defined as:

$$\mathrm{PID} = \sqrt{\ln P_{CC}} - \sqrt{\ln P_{NC}}$$

For this analysis the following variables are used:

Event Length: The presence of the muon track in CC events means that they are typically longer than NC events. A 1 GeV muon will traverse approximately 20 planes compared to the highest energy NC showers which are rarely longer than 50 planes. Figure 5.11 shows the distributions of event length for data and MC. The rise in the distribution that occurs at higher event lengths is due to the contribution of uncontained

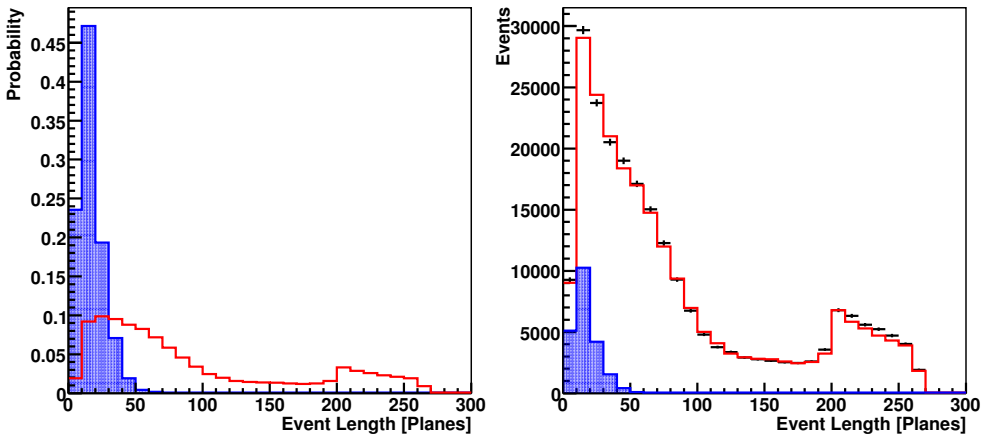

(a) (b)

Figure 5.11: (a) PDF of event lengths in planes for Near Detector CC (red line) and NC (blue shaded area) MC (b) Distribution Event Length in planes for Near Detector data (black line) and MC (red line). The MC expectation for the contribution from NC events is shown by the blue shaded area.

events that start towards the end of the calorimeter and propagate through the end of the muon spectrometer. The data are well described by the MC.

Fraction of Event Pulse Height in Track: In CC events a large fraction of the charge in an event is contained in the track, due to the presence of the muon. This fraction is much smaller for NC events as the reconstructed track does not typically extend far from the shower. Figure 5.12 shows distributions of this variable for data and MC. It can be seen that there is an excess of data events with very high pulse height fractions and a deficit of data events with pulse height fractions in the range 0.5 - 0.9 relative to MC predictions. This is likely to be due to incomplete modelling of hadronic showers in the MINOS detector.

Track Pulse Height Per Plane: The vast majority of tracks in CC events are due to muons. This means that they will deposit a reasonably constant amount of charge per plane crossed (except when they have very low momentum as $\mathrm{d}E/\mathrm{d}x$ rises sharply). Tracks in NC events typically consist of random shower strips, meaning that the amount of charge deposited per plane is much more variable as a variety of particles are tracked. Figure 5.13 shows the distributions of track pulse height per plane. This variable is measured in SigCorr per plane, where SigCorr is the raw PMT signal that has been

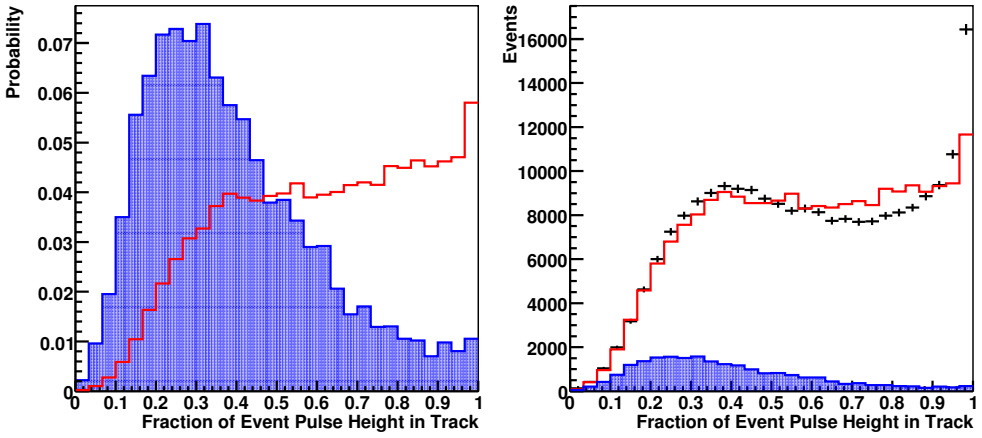

(a) (b)

Figure 5.12: (a) PDF of the fraction of event charge in the track for Near Detector CC (red line) and NC (blue area) MC (b) Distribution of the proportion of the fraction of event charge contained in the track for Near Detector data (black line) and MC (red line). The MC expectation for the contribution from NC events is shown by the blue shaded area.

corrected for PMT non-linearity and strip-to-strip variations. Reasonable agreement is observed between data and MC, with the data having a slightly lower and broader peak than the MC.

The resulting PID distribution is shown in Figure 5.14. There is good separation between CC and NC events. For this analysis, a PID cut at -0.1 will be applied and events with PID greater than this are included in the CC selected sample. This gives a selection efficiency (relative to events which have passed all previous cuts) of 85.8% and purity of 98.2%. In the high PID region, good agreement is observed between data and MC. However, the MC overestimates the data for PID values in the range $-0.4 - 0$ and underestimates it for PID values less than -0.6. This is due to the differences observed in the distributions that make up the PID and these are attributed to incomplete modelling of hadronic showers.

The high PID region is largely made up of low y CC events, so the PID value is mainly determined by the properties of the track of the event. This region shows good agreement between data and MC and differences grow a lot larger in the low PID region containing high y CC and NC events. The PID values for these events are mainly

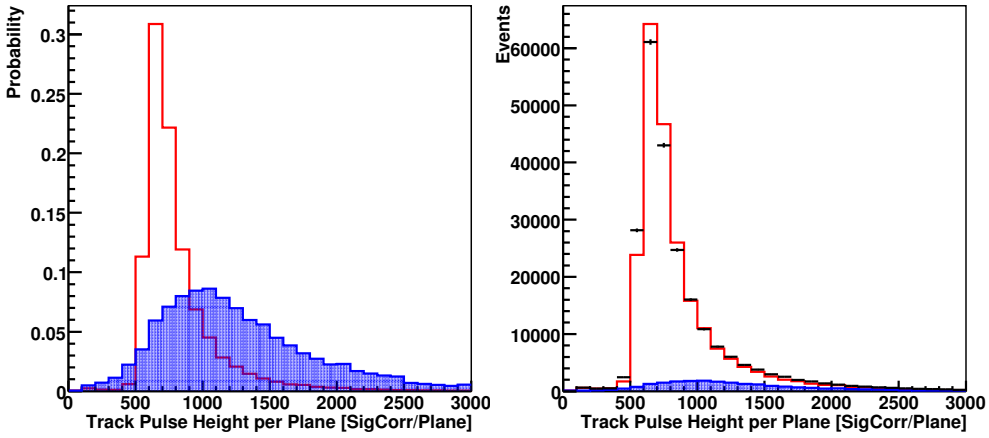

(a) (b)

Figure 5.13: (a) PDF of track pulse height per track plane for Near Detector CC (red line) and NC (blue area) MC (b) Distribution of track pulse height per track plane for Near Detector data (black line) and MC (red line). The MC expectation for the contribution from NC events is shown by the blue shaded area.

determined by the properties of the shower in the event. This makes it likely that the NC data PID distribution is in fact quite different from the MC prediction which could affect the level of NC events in the CC selected sample. This systematic effect is addressed in Section 5.2.

Figure 5.15 shows the distributions of shower strips, pulse height per shower strip and reconstructed E_{shw} for the selected CC sample. It can be seen there is good agreement between data and MC in the number of shower strips apart from at very low strip numbers. As well as the aforementioned incomplete shower modelling, this difference could also be due to systematic differences in the PMT gains between data and MC. This would have the effect of changing the charge threshold for shower strip formation. In the distribution of pulse height per shower strip it can be seen that the peak is higher and wider in data compared to MC. The distribution of reconstructed shower energies is seen to show an excess of lower energy showers in data.

Figure 5.16 shows the distributions of reconstructed track direction cosines with respect to the x, y, z and the beam axes. Generally good agreement between Data and MC is seen. The NuMI beam must be aimed below the horizon for it to intersect with the

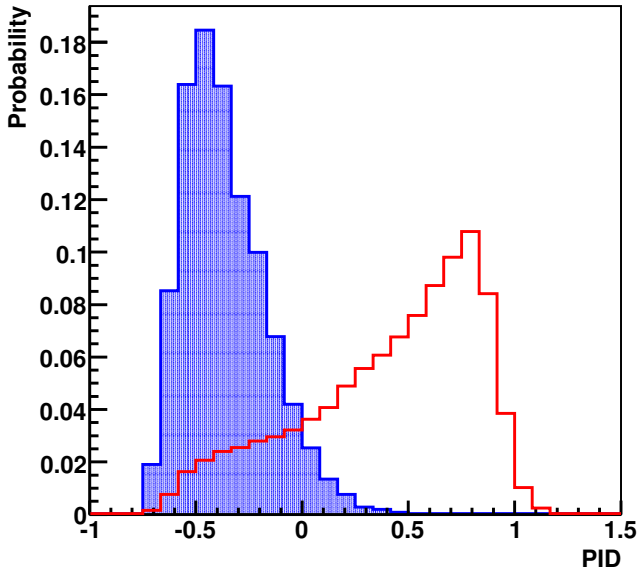

(a)

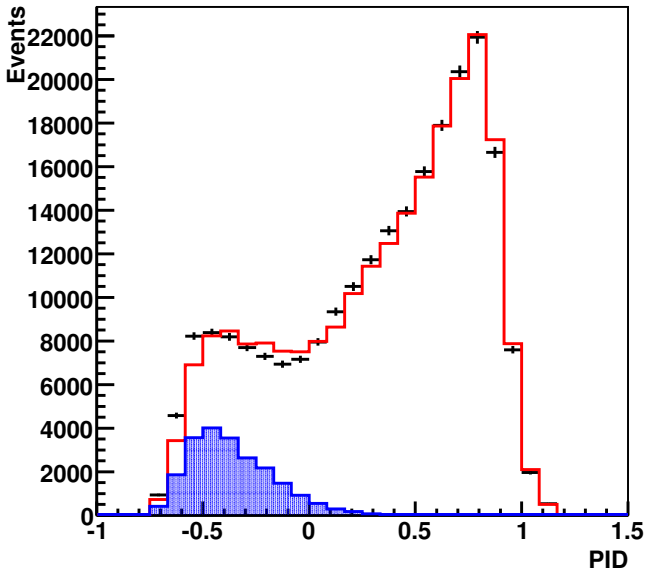

(b)

Figure 5.14: (a) PDF of PID distributions for CC/NC separation for Near Detector CC (red line) and NC (blue area) MC. (b) PID distribution for CC/NC separation for Near Detector data (black line) and MC (red line). The MC expectation for the contribution from NC events is shown by the blue shaded area.

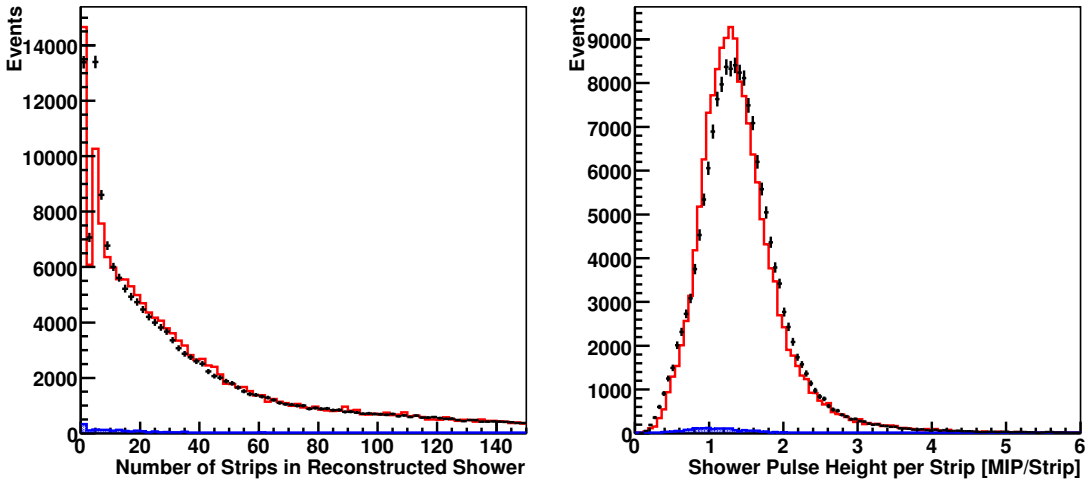

(a) (b)

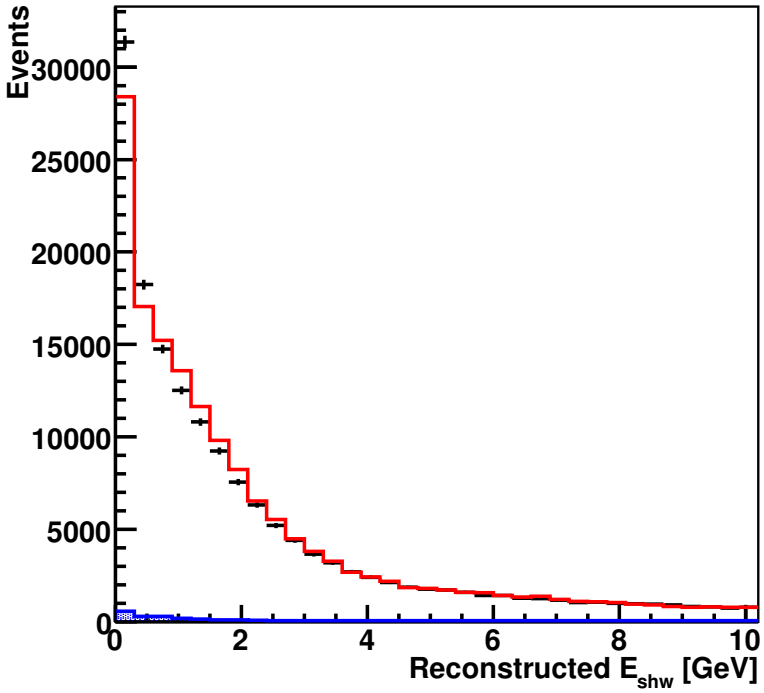

(c)

Figure 5.15: (a) Shower strips in a reconstructed shower (b) Shower pulse height per strip (c) Reconstructed E_{shw} for Near Detector data (black line) and MC (red line). The MC expectation for the contribution from NC events is shown by the blue shaded area.

Far Detector, and this slight negative offset can be seen in the distribution of $\cos\theta_y$. Figure 5.17 shows the distributions of reconstructed muon energy, y (the fraction of the neutrino's energy transferred to the nucleus: E_{shw}/E_ν) and E_ν. The reconstructed muon energy, E_μ, is calculated from range for fully contained tracks and curvature for partially contained tracks. The E_μ distribution shows good agreement between data and MC in the high energy tail but some differences are observed in the low energy peak. The peak at zero in reconstructed y corresponds to events with no reconstructed showers, and this bin shows good agreement between data and MC. However, in the region of low but non-zero y events there are obvious differences between the data and MC, corresponding to the excess of low energy reconstructed showers seen in data. The reconstructed E_ν spectra shows an excess of data events in the peak (with the peak centred slightly lower than MC) and a slight deficit in the tail.

5.2 NC Background Systematic

As discussed in the previous section, it is seen that poor hadronic modelling leads to Data/MC differences in the shape of the PID distribution and that this will affect the level of expected NC contamination in the selected CC sample. To determine the level of this effect, it is necessary to study hadronic showers in data. This is achieved by taking CC events and then removing the muon track, thereby leaving the hadronic shower. These 'CC showers', can then be put through the reconstruction and their PID distributions obtained after applying all other analysis cuts. If this is done for both Data and MC then the PID distributions for CC showers can be compared. This Data/MC ratio can be used as a correction that needs to be applied to the NC MC to make it agree with data. This method assumes that a CC shower will be same as an NC shower in the MINOS detector. One difference between CC and NC showers is the different charge of the hadronic system. The low granularity of the MINOS detector and the fact that the track finding software is tuned towards finding longer muon tracks, means individual particles within a shower are rarely resolved, so the MINOS detector is not very sensitive to the overall charge of the hadronic shower. The hadronic system charge difference might also create a slight bias in the species of the particles involved in the shower. This could result in differing pulse heights for CC and NC showers due to the varying $\mathrm{d}E/\mathrm{d}x$ of the particles within the shower. However, comparing the pulse heights of high y CC showers (thereby removing the muon charge) and NC showers at a given energy reveals no significant differences, so this effect is negligible.

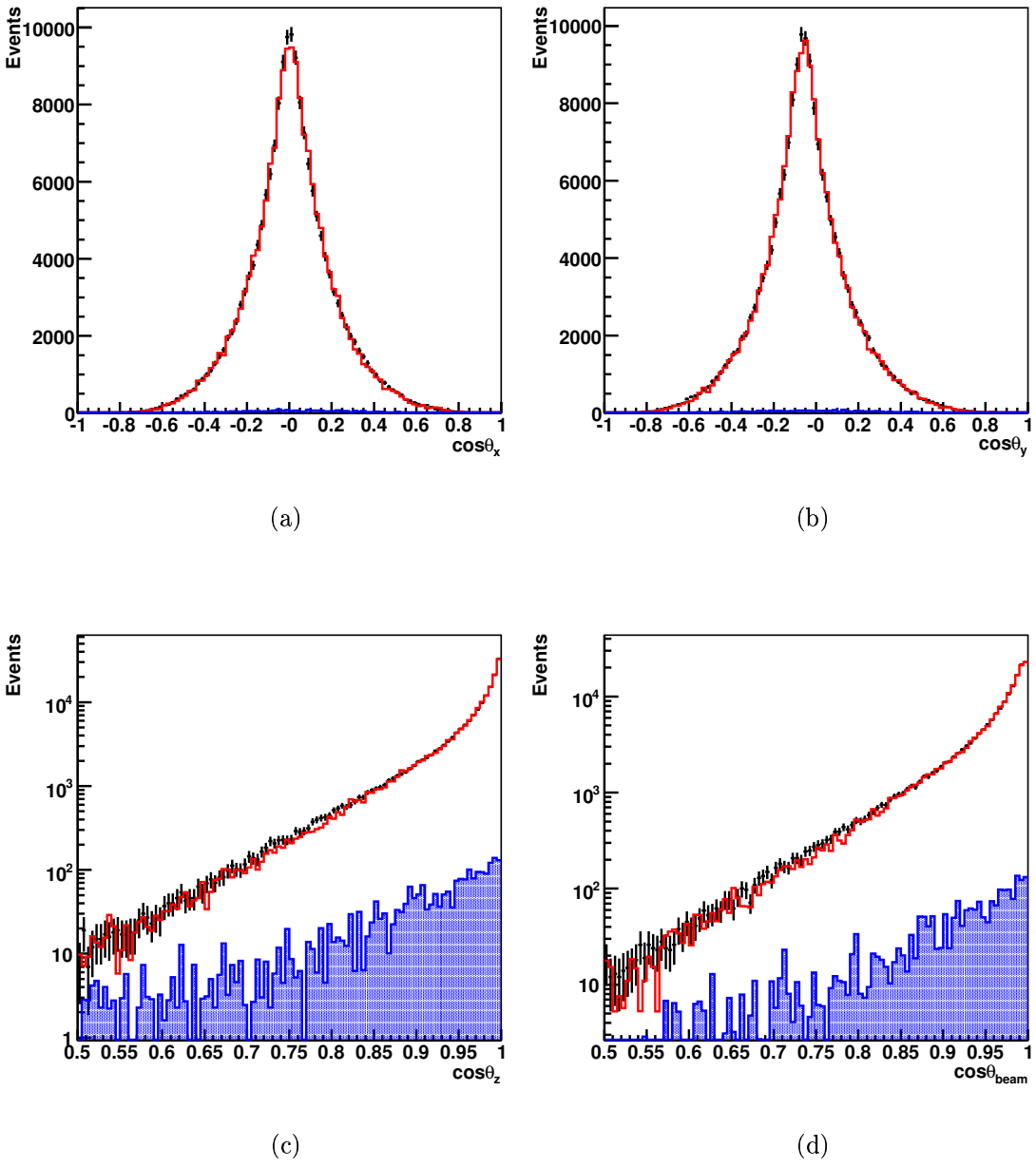

(a) (b)

(c) (d)

Figure 5.16: Reconstructed track direction cosines w.r.t (a) x axis (b) y axis (c) z axis (d) beam axis for Near Detector data (black line) and MC (red line). The MC expectation for the contribution from NC events is shown by the blue shaded area.

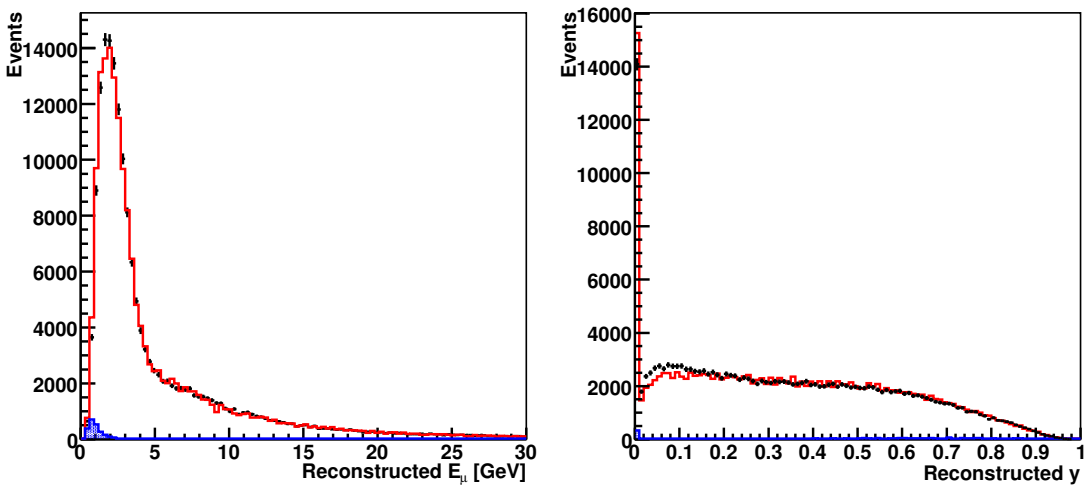

(a) (b)

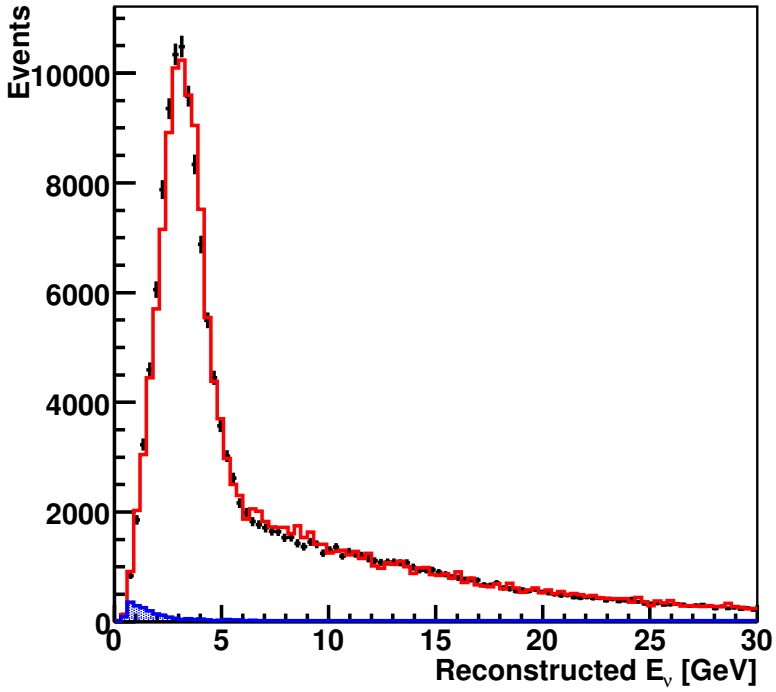

(c)

Figure 5.17: Reconstructed (a) E_μ (b) y (c) E_ν for Near Detector data (black line) and MC (red line). The MC expectation for the contribution from NC events is shown by the blue shaded area.

The challenge of this method is to effectively remove the muon from the hadronic shower, as even if a small remnant of the muon is left then it is likely that the TrackFinder will identify it as a track. It will be assumed that the track finding within the shower is perfect, so only the strips shared between the track and the shower will be considered as possibly containing muon charge, and all other shower strips will be formed into a new striplist. Due to the sparse nature of the showers in the detector, it is assumed that most of the shared strips will be solely due to the muon, apart from the very high pulse height strips that are more likely to be due to hadrons due to them having higher $\mathrm{d}E/\mathrm{d}x$. Figure 5.18 shows the PDF of track strip charges that occur within 2.7 m of the vertex for CC ν_μ events with no reconstructed shower. This distance from the vertex corresponds to the maximum range of hadronic showers from the NuMI beam in the MINOS detector. Therefore the PDF shows the distribution of muon charges in the region where showers can occur. If a cut is placed at 2.5 MIPs then this excludes $\sim 97\%$ of muon strips. The shared strips that pass this cut are then corrected for the likely muon charge that they contain. This is done by reducing their charges by $1.45\,\mathrm{MIPs}/\cos\theta_z$ to take the path length of the track through the strip into account and the origin of the 1.45 MIPs factor is discussed in Section 4.9. These strips are then added to the new strip list along with the original non-track strips. This new strip list is now composed only of strips due to the hadronic shower and so should resemble a typical NC event. The events are then run through the MINOS software reconstuction chain for a second time (starting with the Slicer) to identify any tracks or showers within them. Finally all the aforementioned analysis cuts are applied (excluding the PID cut).

Figure 5.19 and Figure 5.20 show the effect of this process on a Near Detector MC event. It can be seen that nearly all the strips in the initial track have been removed apart from one very close to the vertex (as this had high charge and was shared between the track and shower). With the obvious muon track removed the track finder has tracked a proton within the hadronic shower.

The spectra of reprocessed CC showers and NC showers are expected to display some difference for several reasons as well as the initial differences in y distributions for CC and NC events. Only events that are selected as being CC enter into the track removal process, which creates a bias against low energy, high y events that have low PID values. Also the track removal process is not completely successful and slightly alters the total charge and topology of the new events. An idea of how effective this process has been can obtained by comparing the PDFs of event variables of MC CC showers and NC events. For this study, ND MC files equivalent to 1.01E18 PoT and ND data from runs

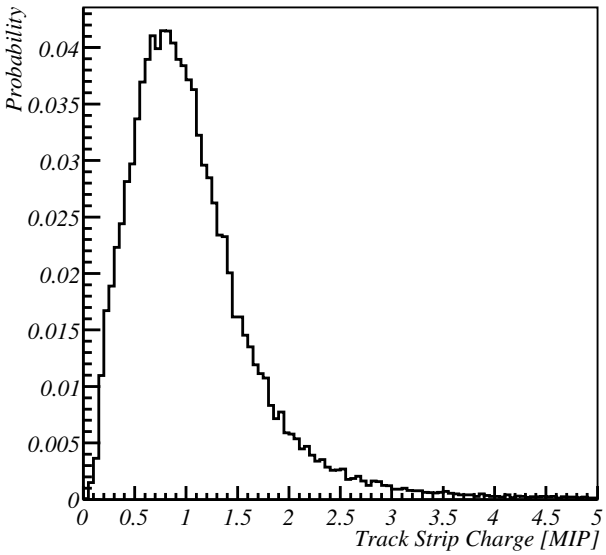

Figure 5.18: PDF of track strip charges for muon tracks within shower range for fiducial CC ν_μ events with no showers. A cut at 2.5 MIPs will remove the vast majority of these strips.

in December 2005 corresponding to 3.97E18 PoT were both processed with the method for isolating the shower strips as outlined above. As with other relevant samples in this chapter, all MC results have been reweighted according to the results of the beam and hadron production fits.

Figure 5.21 shows the probability of reconstructing at least one track in an event for MC CC showers and NC events versus true E_{shw}. It also shows the PDF of true E_{shw} for MC CC showers and NC events passing all analysis cuts prior to the PID cut. The reasonable agreement in track reconstruction probability over a large energy range suggests that the CC showers are topologically similar to NC showers, indicating that the muon track removal has introduced little bias. The PDF of the true shower energy spectra show some large differences at low energy, most likely due to the initial differing y distributions and the fact that only selected CC events enter the track removal process.

Figure 5.22 shows the comparison between the PDFs of the PID variables and overall PID distribution for CC showers and NC MC. The PDFs of event length show good agreement between the CC showers and NC MC. The fraction of event charge in the track is on average lower for CC showers relative to NC MC. CC showers also show a lower average track pulse height per plane compared to NC MC. The overall PID

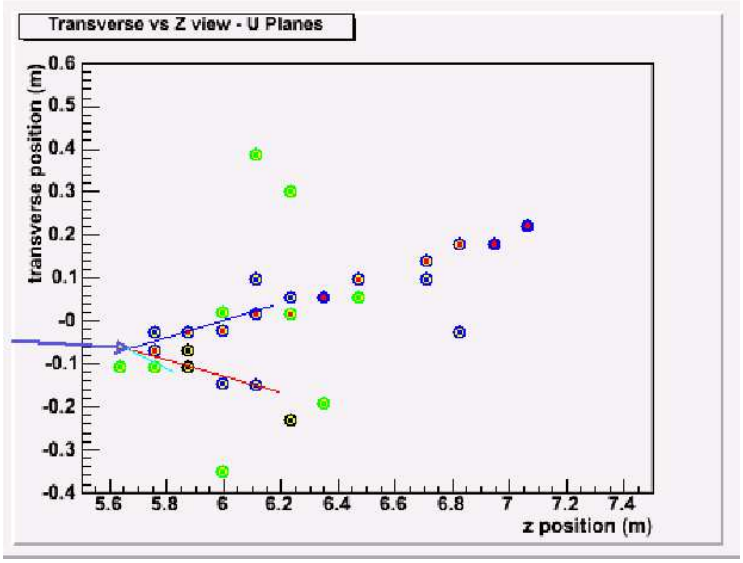

(a)

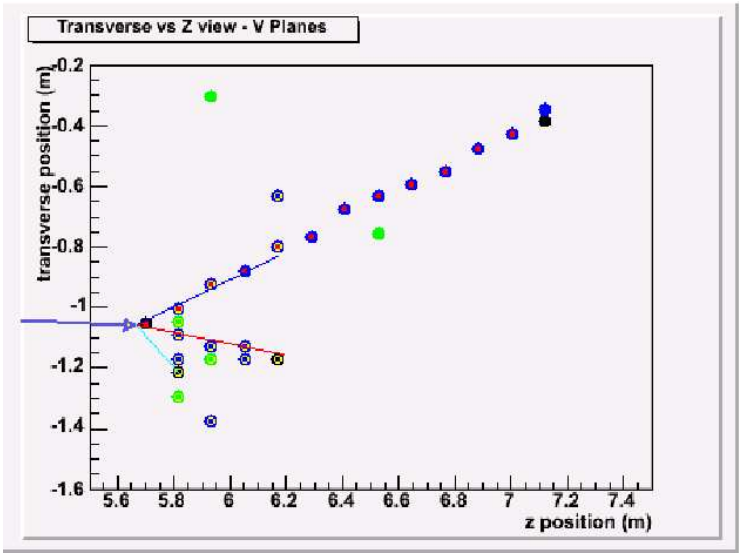

(b)

Figure 5.19: MINOS event displays showing the (a) U and (b) V plane views of a Near Detector event. The coloured lines show the truth information for the event: blue arrow (inbound neutrino), dark blue line (muon), red line (proton) and light blue line (neutral pion). The coloured circles represent the reconstructed strips with the colour representing the charge in PEs: green (< 2) blue (2 - 20) black (> 20). The red dots within the circles represent strips that have been included in the reconstructed track. The yellow rings within the circles represent strips that have been included in a reconstructed shower.

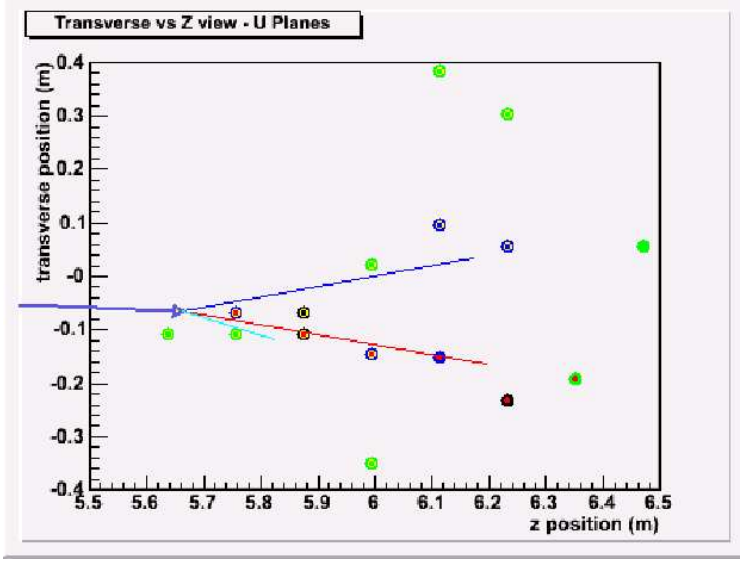

(a)

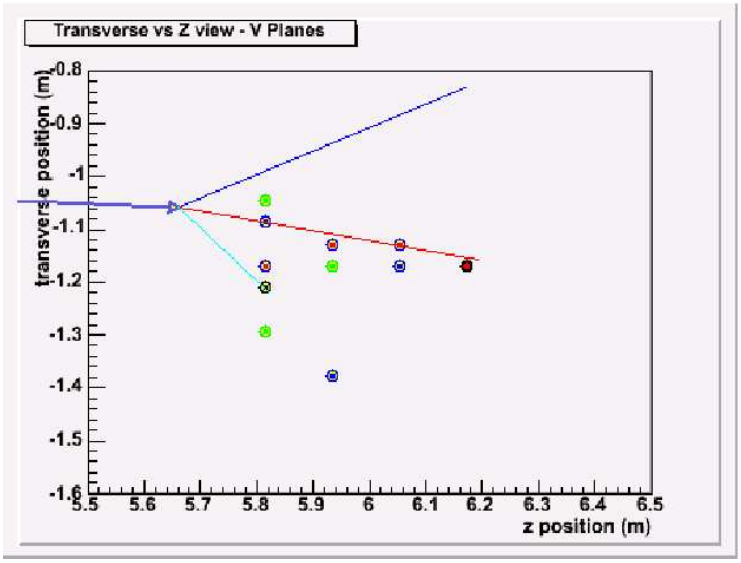

(b)

Figure 5.20: MINOS event displays showing the (a) U and (b) V plane views of the same event in the previous figure after the track removal process and subsequent reprocessing. The coloured lines show the truth information for the event: blue arrow (inbound neutrino), dark blue line (muon), red line (proton) and light blue line (neutral pion). The coloured circles represent the reconstructed strips with the colour representing the charge in PEs: green (< 2) blue (2 - 20) black (> 20). The red dots within the circles represent strips that have been included in the reconstructed track. The yellow rings within the circles represent strips that have been included in a reconstructed shower.

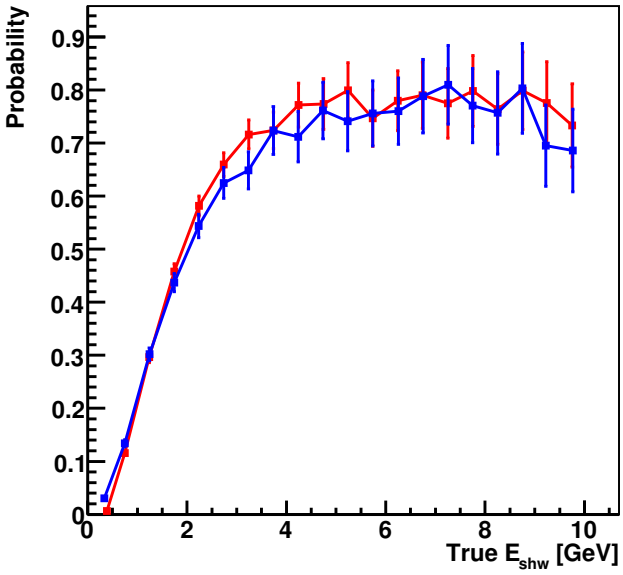

(a)

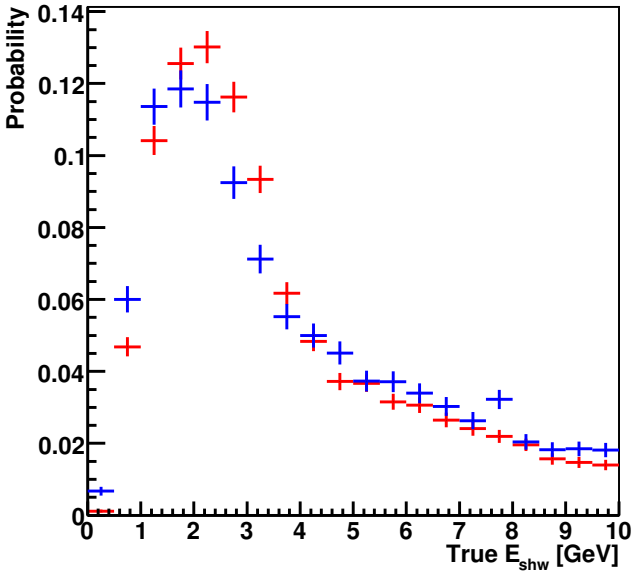

(b)

Figure 5.21: (a) Probability of reconstructing a track from the event for CC showers (blue) and NC (red) MC plotted against true E_{shw} (b) True E_{shw} distributions (normalised to unit area) for events passing all analysis cuts prior to the PID cut with the same colour scheme applying.

distribution shows reasonable agreement between CC showers and NC MC, with the CC showers peaking at a slightly higher PID value. Figure 5.23 shows the same distributions but now comparing CC shower MC with data and large differences are observed. CC showers in data are shorter and have much higher track pulse height per plane relative to MC. This leads to very different PID distributions, with CC shower data having much lower average PID values than for MC. This would indicate that the MC estimation of the PID shape of the NC background (and hence the proportion of it surviving the CC selection cuts) is not correct.

The data/MC ratio of PID distributions obtained from the track-removed event samples is used to provide a scaling of the MC prediction for the NC background as a function of PID parameter. To reduce the effect of the differences seen in the energy spectra of CC shower and NC MC, this process is carried out in bins of energy. The Data/MC ratios for the PID distributions are parameterised using a zero-order polynomial fit in the mid PID region ($-0.2 < \text{PID} < 0.3$) to determine the level of any systematic offset for NC background for that bin of reconstructed energy. This range is chosen so as to bound the PID cut at -0.1 and to include all of the NC tail in the CC selected region. The Data/MC ratio in the lower PID region is best described with a first or second order polynomial fit depending on the energy bin (this also has the effect of smoothing the ratio for low statistics or outlying bins). It should be noted that this method provides a prediction of the shape of the NC PID distribution and the normalisation. The effectiveness of the method can be tested by applying the scaling to the MC predictions of the NC background in the ND and observing whether the overall agreement between data and MC improves. The effects of this reweighting are shown in the PID distributions in Figure 5.24 to Figure 5.26. The reweighting is seen to improve the agreement between data and MC PID distributions, most notably at lower energies.

Table 5.1 summarises all the information from this study, showing the predicted NC level in the Near Detector selected CC sample compared to nominal MC using the track removal process and the effect of applying this weighting to the NC MC on the Data/MC χ^2/ndf, where:

$$\chi^2 = \frac{(N_i^D - N_i^{MC})^2}{N_i^D + 4N_i^{MC}}$$

N_i^D and N_i^{MC} are the numbers of events in the i^{th} bin of the Data and MC PID distributions and the factor of 4 represents the fact that the MC has been scaled up to

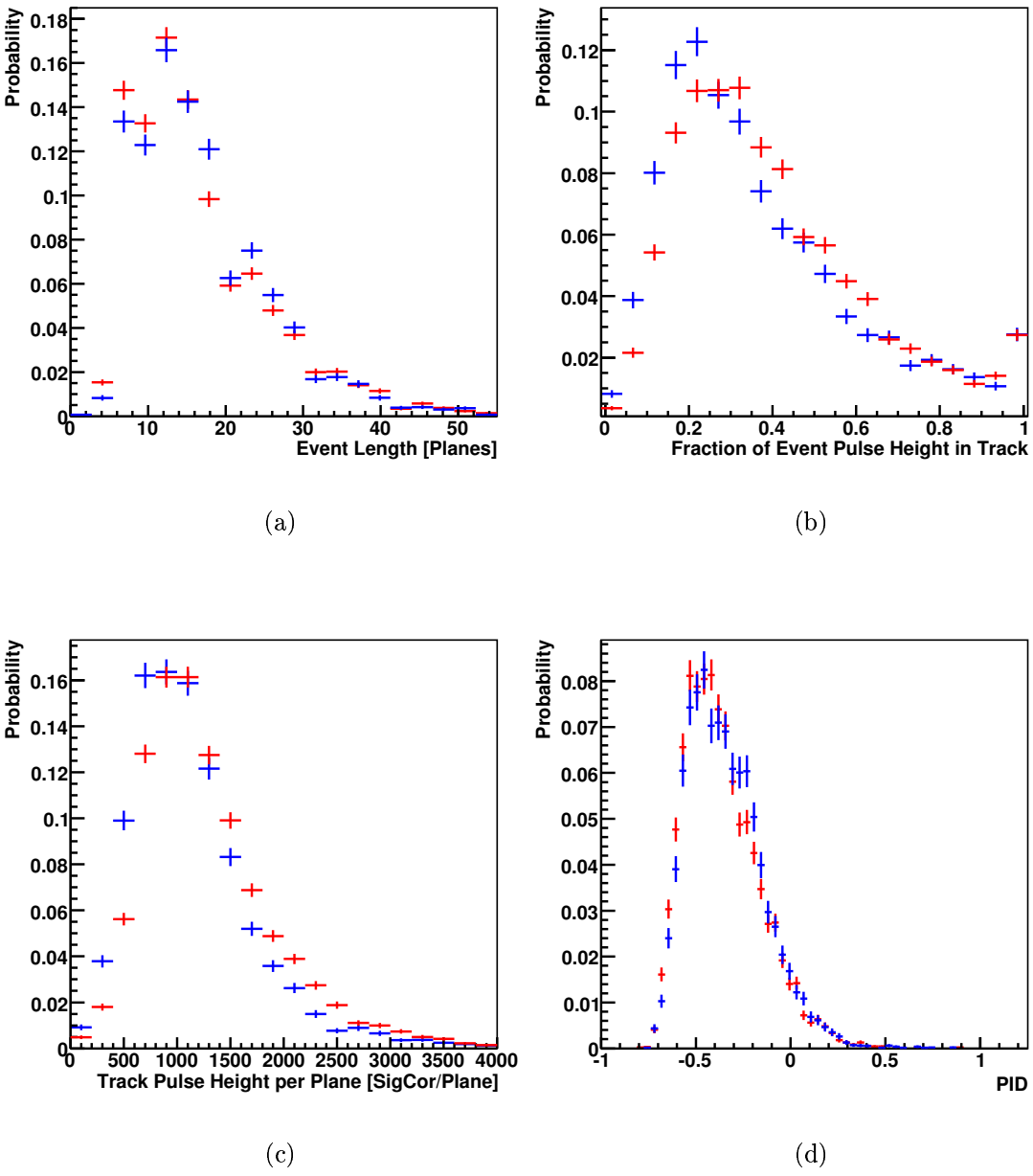

Figure 5.22: PID variable and overall PID distributions for MC CC showers (blue) and NC MC (red): (a) Event length (b) Fraction of event pulse height in track (c) Track pulse height per plane (d) PID. All plots are normalised to unit area.

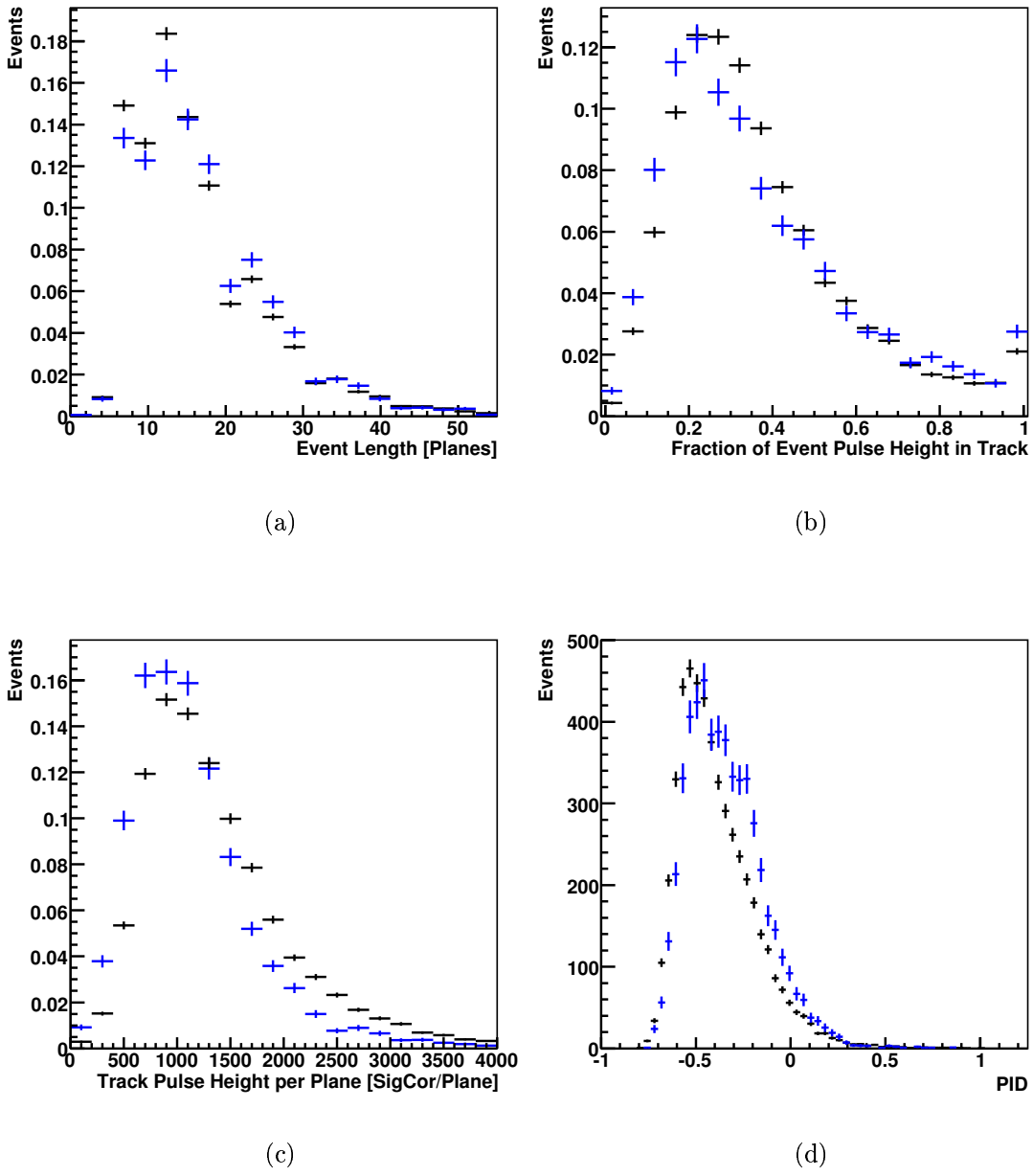

(a) (b)

(c) (d)

Figure 5.23: PID variable and overall PID distributions for MC CC showers (blue) and Data CC showers (black): (a) Event length (b) Fraction of event pulse height in track (c) Track pulse height per plane (d) PID. The first three plots are normalised to unit area and the last is normalised to PoT.

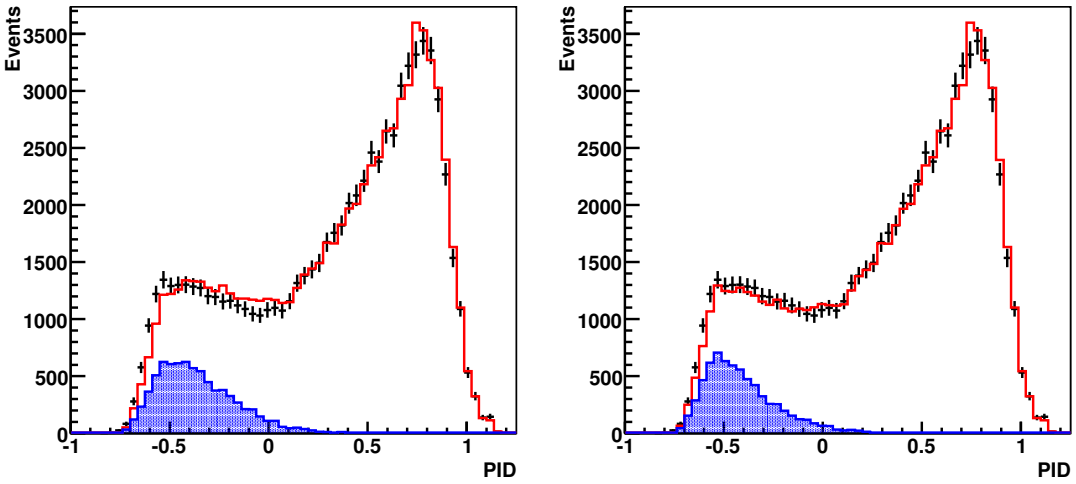

Figure 5.24: ND PID distributions for events with reconstructed $E_\nu < 30$ GeV for Data (black points), MC (red line) and NC component of MC (blue shaded area). The plot on the left is using nominal MC (with beam and hadron production reweighting applied) and the plot on the right has the NC weighting from the track removal study applied.

Reconstructed Energy	NC MC Correction	Nominal MC χ^2/ndf $(-0.2 < \text{PID} < 0.3)$	NC Weighted MC χ^2/ndf $(-0.2 < \text{PID} < 0.3)$
$0-1$ GeV	$-32.9\% \pm 5.6\%$	5.7/13	4.0/13
$1-2$ GeV	$-43.4\% \pm 3.8\%$	8.7/13	2.2/13
$2-4$ GeV	$-31.2\% \pm 4.9\%$	6.4/13	4.2/13
$4-6$ GeV	$-51.8\% \pm 5.2\%$	4.3/13	5.5/13
$6-12$ GeV	$-57.7\% \pm 4.2\%$	7.0/13	4.2/13
$12-30$ GeV	$-55.3\% \pm 5.9\%$	9.9/13	12.5/13
$0-30$ GeV	–	11.8/13	4.2/13

Table 5.1: Table showing corrections to the NC MC level in the selected CC sample and its effect on the Data/MC χ^2 per degree of freedom in the mid-range PID region $(-0.2 < \text{PID} < 0.3)$ for bins of reconstructed energy.

the same PoT as the data. It can be seen that there is a drift to higher negative offsets at higher energies. The NC reweighting, while giving good improvement at lower energies and overall, does not improve the Data/MC agreement at higher energies (this is not

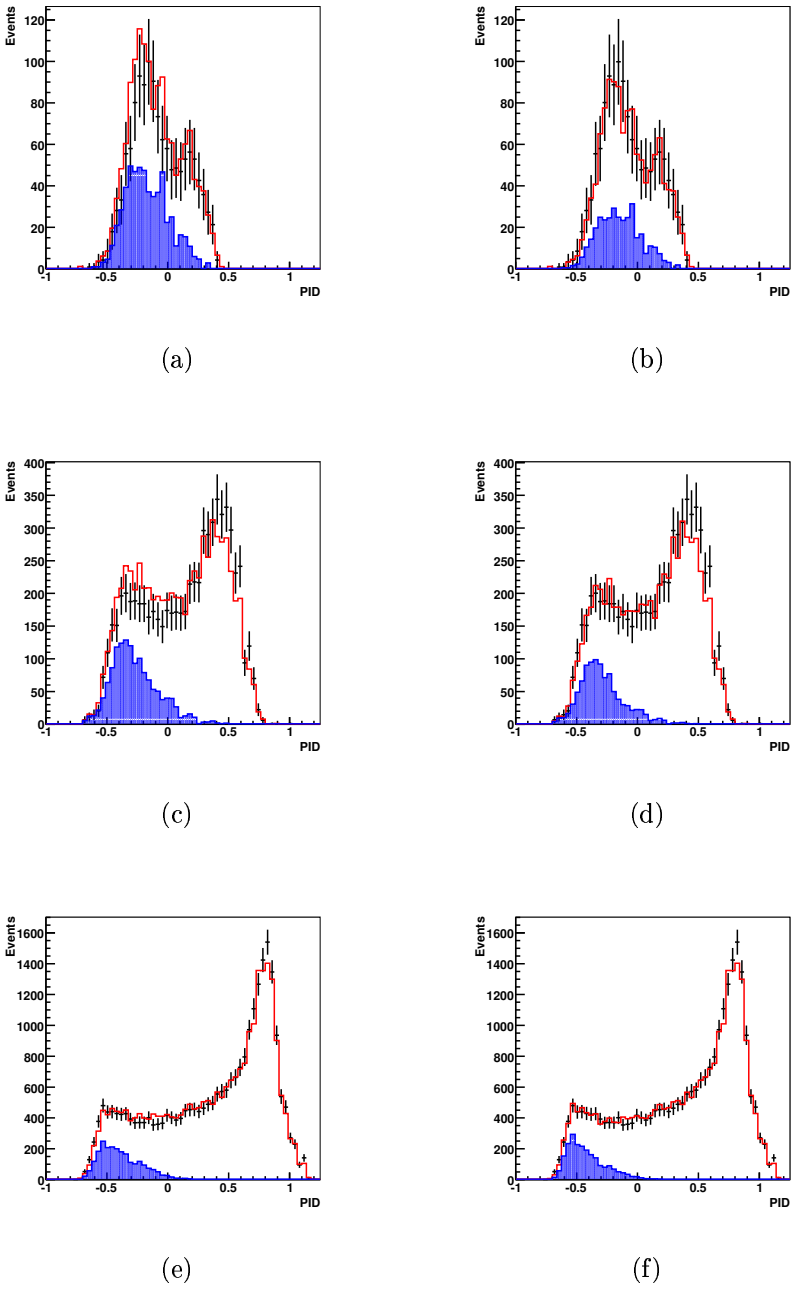

Figure 5.25: ND PID distributions for events with (a) & (b) Reconstructed $E_\nu < 1$ GeV, (c) & (d) $1 <$ Reconstructed $E_\nu < 2$ GeV, (e) & (f) $2 <$ Reconstructed $E_\nu < 4$ GeV. The plots on the left (a, c, e) show MC before NC reweighting and the plots on the right (b, d, f) show after NC reweighting with Data (black points), MC (red line).The MC expectation for the contribution from NC events is shown by the blue shaded area.

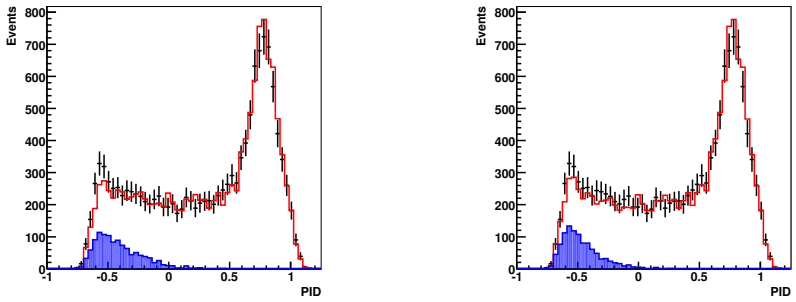

(a) (b)

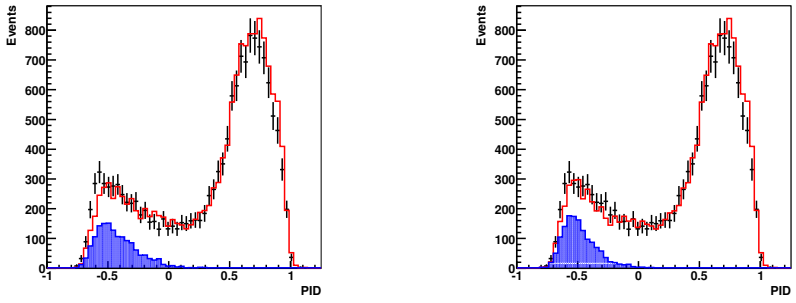

(c) (d)

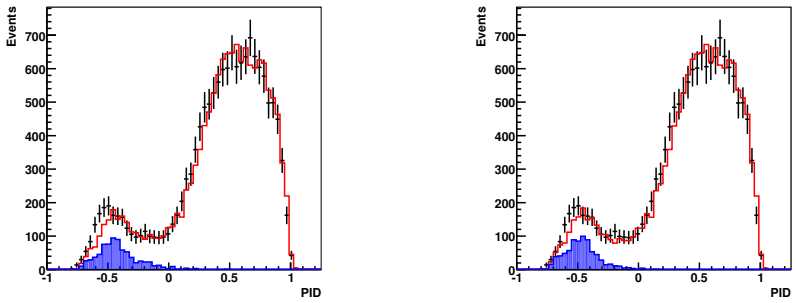

(e) (f)

Figure 5.26: ND PID distributions for events with (a) & (b) $4 <$ Reconstructed $E_\nu < 6$ GeV, (c) & (d) $6 <$ Reconstructed $E_\nu < 12$ GeV, (e) & (f) $12 <$ Reconstructed $E_\nu < 30$ GeV. The plots on the left (a, c, e) show MC before NC reweighting and the plots on the right (b, d, f) show after NC reweighting with Data (black points), MC (red line).The MC expectation for the contribution from NC events is shown by the blue shaded area.

very important as 76% of NC background has reconstructed $E_\nu < 4$ GeV). The errors quoted in the table are purely statistical and so are an underestimate as they do not take into account such factors as the slight disagreement between the CC showers and NC MC due to incomplete muon track removal. To reflect this, the NC population-weighted average correction over all energy bins is calculated and when the corrections are applied to the NC MC, the size of the correction is assigned as the uncertainty on the NC level.

Chapter 6

Far Detector Results

"Uncertainty and expectation are the joys of life."
— William Congreve

6.1 Far Detector Data and Quality Cuts

The Far Detector data used for this study was collected between May 2005 and February 2006. The detector was triggered from the SpillServer signal to collect the readout from the detector within the expected time window for beam events (as described in Section 4.1). As with near detector data, beam quality cuts are applied (described in Section 5.1). Due to the low expected event rate and requirement for well reconstructed events, additional quality cuts are placed on the Far Detector data. This involves only selecting events where all of the detector was active (i.e. no crates were dead), there was current in the coil producing the magnetic field, there were no HV trips and the GPS system for delivering the spill signal to the Far Detector was active. As the LI system is running throughout data taking, it is possible for a LI pulse to take place during the time window for beam and so be reconstructed as an event. The times of LI events are tagged and only snarls where no LI occurred during the spill window are used. Topological cuts are used to remove LI events that may have missed being tagged. LI events are characterised by extremely high pulse height showers in particular parts of the detector (they start and end on crate boundaries).

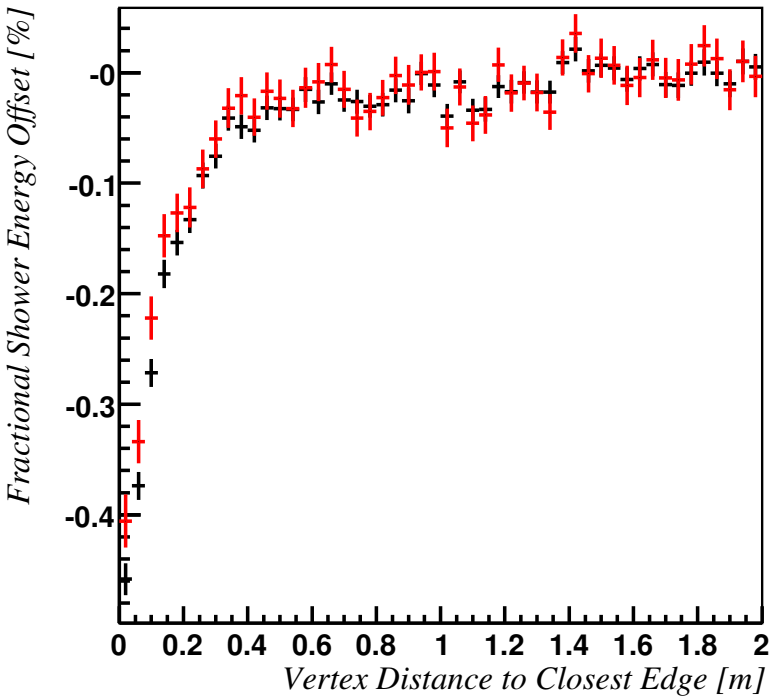

Figure 6.1: Fractional E_{shw} offset plotted against distance of the event vertex from closest detector edge for selected events with showers (black points) and events with true shower energy less than 2 GeV (red points) for FD MC.

6.2 Fiducial Volume and Cosmic Background

In trying to decide on an appropriate fiducial volume for the Far Detector the desire to maximise the number of data events must be balanced against the quality of the events and the level of cosmic ray muons potentially entering the data sample. In the xy plane, an octagonal cut is used to follow the outline of the detector. This means that the cut is defined in terms of distance between the event vertex and the closest edge of the detector. Proximity to the detector edge can result in E_{shw} being underestimated as some of the shower particles can leave the detector. Proximity to the detector edge has much less effect on E_{μ} reconstruction as not only does the magnetic field focus muons towards the coil hole but even if they are only partially contained an estimate of their energy can be obtained using the TrackFitter.

Figure 6.1 shows the average fraction of true E_{shw} that is is lost as a function of the distance of the event vertex from the edge of the detector for selected MC events. These

events were required to have $z_{vtx} > 50$ cm from the ends of the supermodules so as to make sure that only the radial effect of the detector edge was studied. It can be seen that there is a shift in reconstructed energy at low distances (less so for lower energy showers as they are smaller), so a cut is placed at 20 cm from the edge of the detector. This would lead to some low energy events suffering a $\sim 10\%$ offset in shower energy. This is acceptable as long as there is reasonable agreement between data and MC in the distribution of size of showers (the distribution of strips in reconstructed ND showers shown in Section 5.1.2 would indicate that this is the case). This distance to closest edge cut can be applied around the coilhole, which is only covered by scintillator from a radius of ~ 20 cm, resulting in a 40 cm minimum radial cut for event vertices. This will also reject cosmic ray and rock muons that enter the detector through the coil hole.

Cuts also need to be applied to z_{vtx} to reject cosmic ray and rock muons entering the front and back faces of the supermodules. The front faces of SM1 and SM2 along with the back face of SM1 are treated in a similar way. A 4-plane cut is applied to each of these regions as it is very unlikely that a muon could pass through 4 planes of scintillator without a strip being reconstructed. The back end of SM2 requires more consideration as a high energy shower starting in this region would be cut off by the end of the detector and E_{shw} would be underestimated. In addition there would be insufficient distance for the track and shower to separate leading to poor track fitting and finding. A cut will therefore be placed at the point that maximises sensitivity to oscillations. For a variety of back plane cut positions, MC events that passed all other cuts were oscillated with parameters similar to the best fit values from SK ($\Delta m^2_{23} = 2.5 \times 10^{-3}\,\mathrm{eV}^2, \sin^2 2\theta_{23} = 1.0$) to make a fake data set. The same MC sample was then oscillated with a range of Δm^2_{23} or $\sin^2 2\theta_{23}$ values (as just one oscillation parameter was to be varied while the other was held constant) and a negative log likelihood of the form:

$$-\ln \mathcal{L} = \sum_k N_k^{MC} - N_k^{DATA} \ln N_k^{MC}$$

was then calculated (where k is the k^{th} bin of the energy spectrum) for each value of the oscillation parameter. The 1σ resolution in each parameter is then estimated by taking their respective probability distributions and determining the distance in parameter space between the best fit point and the point where $\Delta \ln \mathcal{L} = 0.5$. The back plane cut is then optimised by finding the value for which the oscillation parameter resolutions are minimised.

Figure 6.2 displays the results of this oscillation sensitivity analysis, showing that for

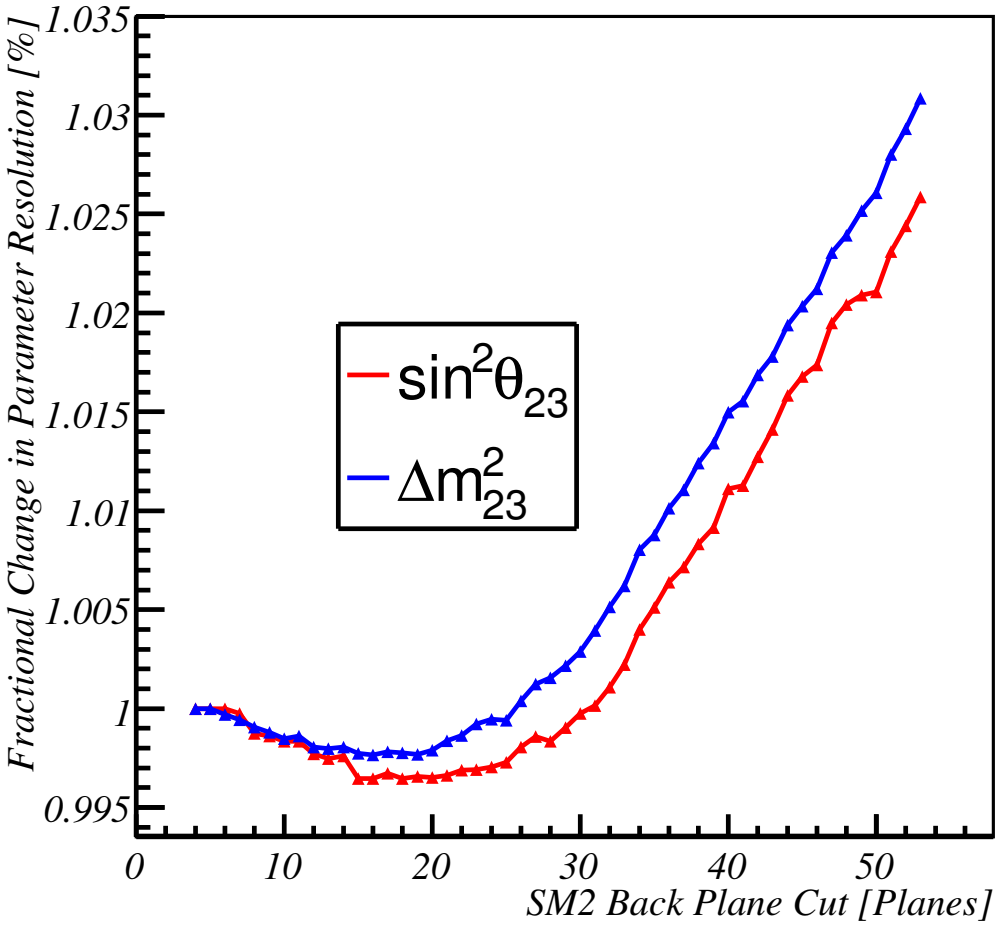

Figure 6.2: Fractional change in oscillation parameter resolution plotted against the SM2 back plane cut for Δm^2_{23} (blue line) and $\sin^2 2\theta_{23}$ (red line).

both Δm^2_{23} and $\sin^2 2\theta_{23}$ there is a small but clear minimum at higher plane cuts. This is due to the fact that events this close to the detector end would be poorly reconstructed and that the loss of these poorly reconstructed events improves the sensitivity despite the associated loss of statistics. Events will therefore be required to start at least 18 planes from the end of SM2.

To estimate the expected level of cosmic ray muons getting in the data sample, a quantity of full-spectrum cosmic muon MC corresponding to $\sim$ 36hrs exposure is processed with the beam configuration of the reconstruction software. Figure 6.3 shows the distributions of $\cos\theta_{beam}$ plotted against $\cos\theta_y$ for selected cosmic and beam MC. It can be seen that the beam and cosmic samples occupy very different parts of the parameter space and that the best way to remove the cosmics without loss of signal is with a cut on $\cos\theta_{beam}$ at 0.6. Using knowledge of the total PoT in the data sample, PoT_{total}, (1.27×10^{20} PoT), the average PoT per spill, $PoT_{avg.\,spill}$, (21.22×10^{12} PoT) and the width of the time window cut, $t_{spill\,window}$, ($50\,\mu$s), it is possible to estimate the total time in data that the detector could have accepted cosmics. Given that 153 Cosmic MC events passed all the analysis cuts (including the track direction cut) and that the MC sample was equivalent to 36 hrs, the rate of the MC cosmic background, Γ^{MC}_{cosmic}, can be calculated. It is then possible to estimate the level of cosmic background in the data sample as:

$$\begin{aligned} N_{bkg} &= \Gamma^{MC}_{cosmic} \times \frac{PoT_{total}}{PoT_{avg.\,spill}} \times t_{spill\,window} \\ &= \frac{153}{36\times3600} \times \frac{2.91\times10^{22}}{21.22\times10^{12}} \times 5 \times 10^{-5} = 0.353 \end{aligned}$$

which is negligible.

6.3 Comparison of Data and MC

The following comparisons between FD MC and Data use 2.91×10^{22} PoT worth of FD MC and Data corresponding to 1.27×10^{20} PoT. The MC is normalised to the data PoT. Both Data and MC have been processed with release version 1.18.2 of the MINOS reconstruction software. As with the Near Detector all MC plots have been reweighted according to the hadron production and beam effect fits. All events are required to pass the aforementioned beam and detector quality cuts, LI removal cuts and fiducial volume cuts. Given that the expected event rate in the Far Detector is vastly lower

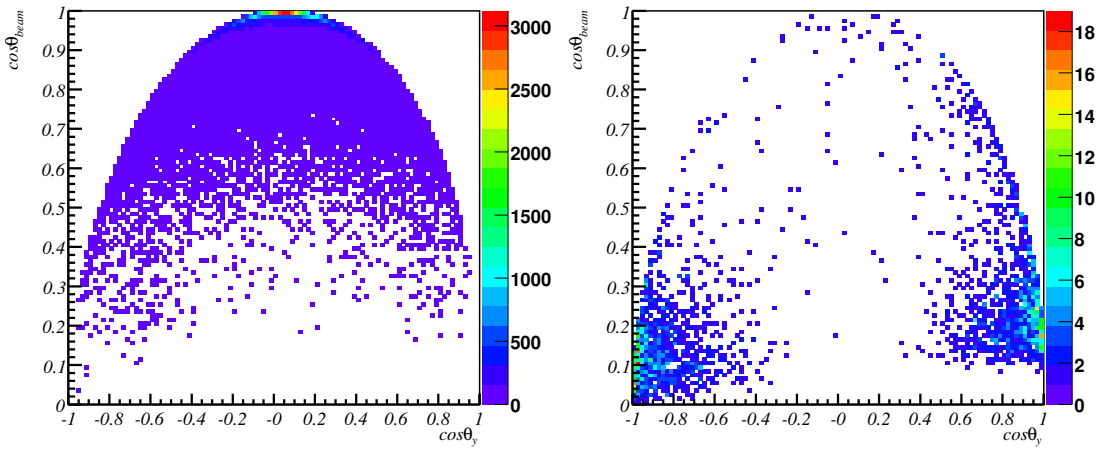

(a) (b)

Figure 6.3: $\cos\theta_{beam}$ plotted against $\cos\theta_y$ of reconstructed tracks in the FD for (a) beam MC and (b) cosmic MC processed with beam software configuration.

than the Near detector, it is not expected that there will ever genuinely be more than one real neutrino interaction in a snarl and that snarls with more than one event must have undergone some form of reconstruction failure (e.g. showers not being associated with tracks or split up). Rather than lose these events, for each snarl only the event with the highest total pulse height will be considered. Figure 6.4 shows the distribution of the difference between the Far Detector snarl time and the expected time from the Spill Server. It can be seen there is a large peak close to zero but also considerable non-Gaussian tails. The asymmetry in the tails is due to the fact that a $30\,\mu$s pre-trigger window before the start of the spill-server window is also read out every time there is a spill. Studying the events in these tails shows the vast majority to be noise events characterised by one small shower, giving zero track events with very low reconstructed energy ($\sim$ 0.1 GeV). The main source of these noise events is emission due to long-term relaxation of mechanical stress in the WLS fibres, natural radioactive decays in the detector and surrounding rock and dark noise in the PMTs. There will also be a very small contribution from cosmic ray muons with very steep tracks. To remove these events, a cut is placed on the time of the event such that the difference between it and the Spill Server Prediction is greater than $-20\,\mu$s and less than $30\,\mu$s.

Figure 6.5 shows the distribution of the number of tracks and showers per event for both MC and Data. To give an idea of the effect of neutrino oscillations, the dashed

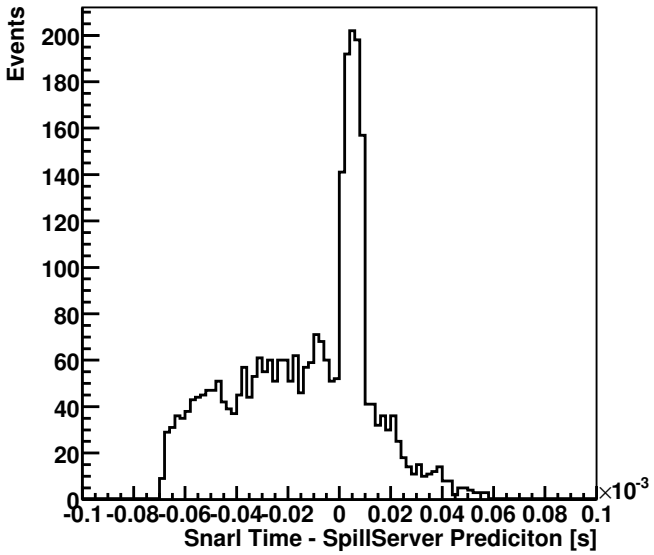

Figure 6.4: Plot of the difference between the snarl time and the expected time from the Spill Server for FD data.

red line represents FD MC that has been oscillated with SK-like parameters ($\Delta m^2_{23} = 2.5 \times 10^{-3} \text{eV}^2, \sin^2 2\theta_{23} = 1.0$). It can be seen that there is still a large excess of zero track and one shower events due to noise that has survived the timing cut. This is supported by Figure 6.6 that shows the distributions of the number of showers plotted against the number of tracks. They show a very large excess of one shower, zero track events in data. It can also be seen that for events with at least one track, there is a deficit in data compared to MC expectation and that the oscillated MC gives an improved agreement. Events are required to have at least one reconstructed track.

While the requirement of a reconstructed track will remove events caused by noise, there is also the issue of cosmic muons. These might co-incide with the Spill Server window and have a reconstructed vertex within the fiducial volume. In the beam configuration all tracks are reconstructed as forward going, so a backwards going cosmic muon that stops in the detector would be reconstructed as a forward going partially contained event. Cosmic muons typically have quite steep tracks whereas most beam muons approximately point back to Fermilab. Figure 6.7 shows the reconstructed track $\cos\theta_{beam}$ as well as the proportion of tracks passing the track fitter and their reconstructed q/p. It shows an excess of data events at low $\cos\theta_{beam}$ values that shows reasonable agreement with the predicted background from cosmic ray muons. As mentioned previously, a cut is applied requiring events to have $\cos\theta_{beam}$ greater than 0.6.

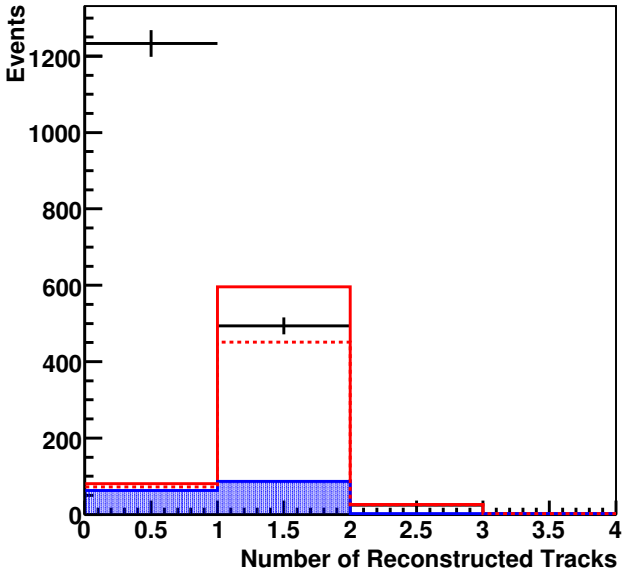

(a)

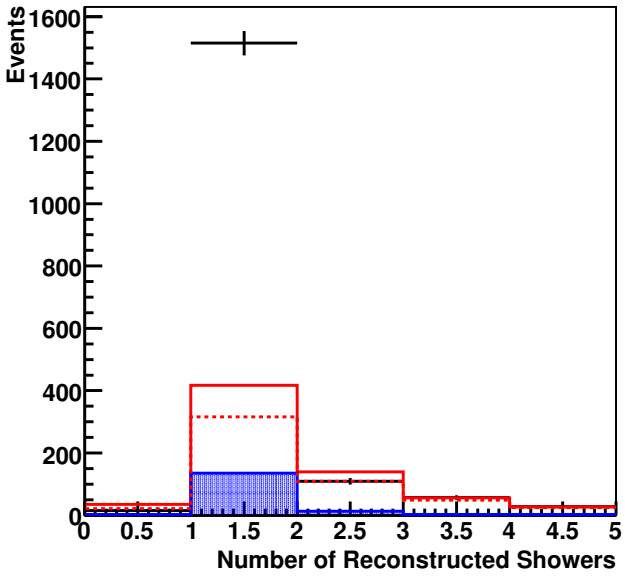

(b)

Figure 6.5: Number of reconstructed (a) Tracks (b) Showers per event for FD Data (black points), MC with no oscillations (red line), MC with SK oscillation parameters (red dashed line). The MC expectation of NC events is shown by the blue shaded area.

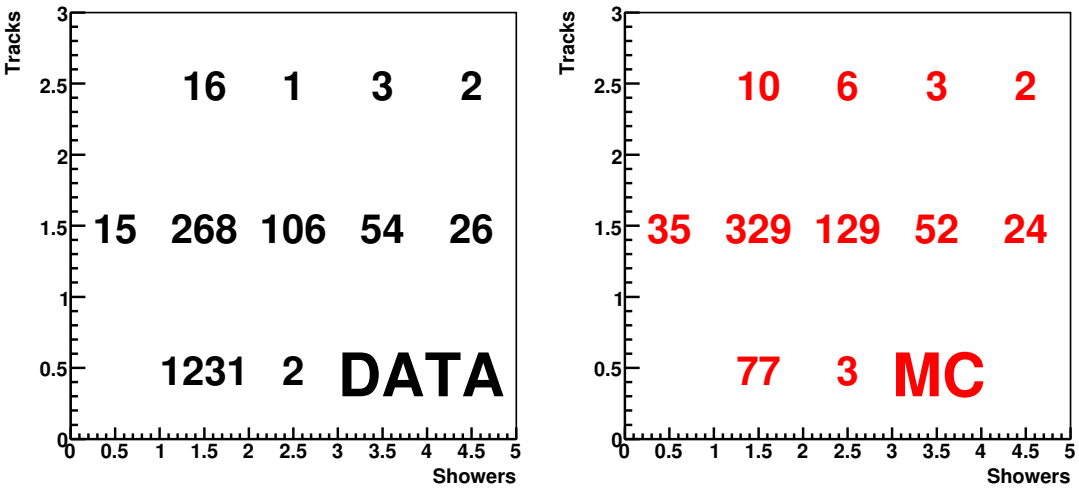

(a) (b)

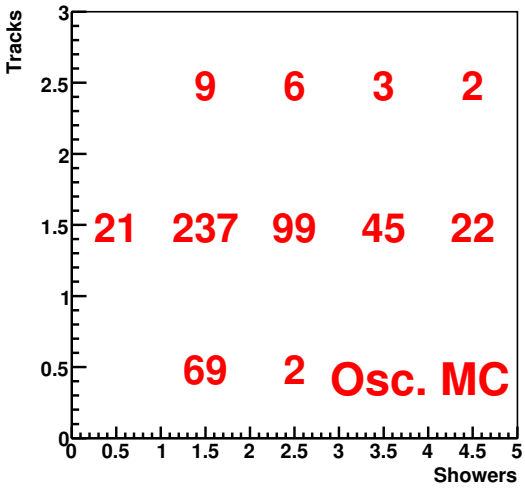

(c)

Figure 6.6: Number of tracks plotted against shower in an FD event: (a) Data (b) MC with no oscillations (c) MC oscillated with SK parameters.

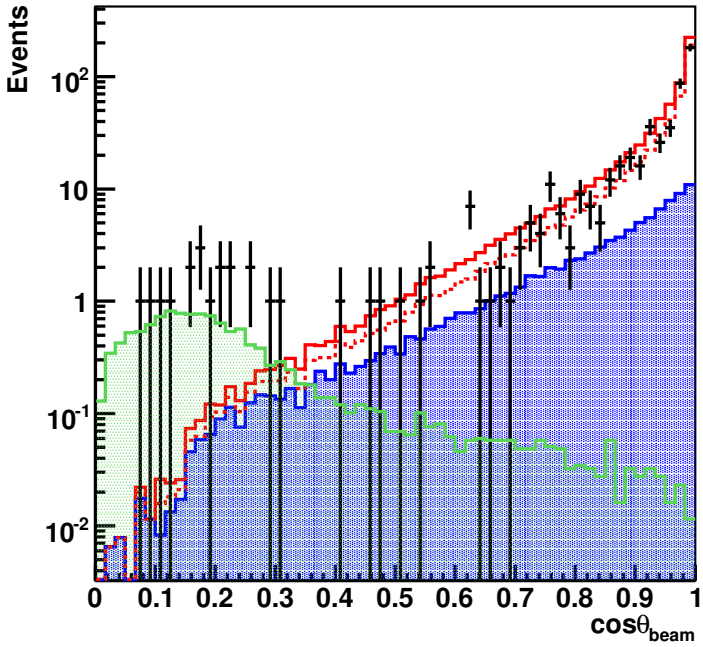

(a)

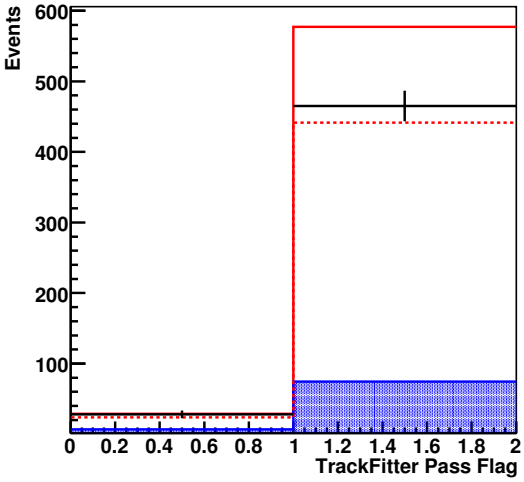

(b)

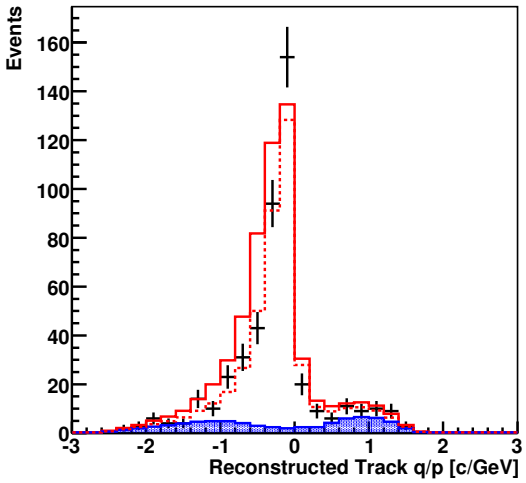

(c)

Figure 6.7: (a) $\cos\theta_{beam}$ (b) Number of tracks passing the track fitter (c) reconstructed track q/p for FD Data (black points), MC with no oscillations (red line), MC with SK oscillation parameters (red dashed line). The MC expectation for the contribution from NC events is shown by the blue shaded area. In plot (a) the expected contribution from cosmic ray muons is shown as the green shaded area.

The distribution of events with tracks passing the track fitter (i.e. the Kalman filter converged) and the resultant q/p distribution both show a deficit of data compared to MC and that the oscillated spectrum gives much better agreement. As in the Near Detector, selected events are required to have a reconstructed track that passes the fitter and have a negative value of q/p to select ν_μ rather than $\overline{\nu}_\mu$ interactions.

Removal of the NC background is achieved in the same way as in the Near Detector. PDFs of event length, fraction of event pulse height in the track and the track pulse height per plane are made for CC and NC MC. These are used to form a PID variable on which a cut can be made. Figures 6.8 - 6.11 show the PDFs for CC and NC MC as well as a Data/MC comparison. It can be seen that as this is Far Detector data and MC, the event length distribution now goes to much higher values than for the Near Detector. The PID distribution shows a deficit of Data events in the high PID (i.e. very CC-like) region with much less of a deficit in the low PID (i.e. NC-like) region, suggesting that it is only a deficit of CC events that is being observed. CC events are selected by requiring a PID value greater than -0.2. This corresponds to an efficiency and purity of 88.7% and 98.3% respectively (for events passing all previous cuts). This cut is slightly more relaxed than that which was used for the Near Detector (-0.1), so as to boost efficiency while give an equivalent purity of approximately 98%.

The vertex positions of selected events in z and in the xy plane are shown in Figure 6.12. The xy plot shows no obvious up/down or left/right asymmetries and there is no clustering at the edge of the detector or the coil-hole, indicating that the cosmic muons incident on the detector are successfully being removed with a combination of the timing, track direction and radial cuts. The z_{vtx} distribution shows no peaks at the start of the detector or around the gap between the supermodules. It can be seen that there is a fall off in the number of events at the end of the detector. This is most likely due to higher energy events that start near the end of the second supermodule not having time to develop fully and allow the shower and track to be easily separated, meaning they may fail the trackfitting or PID cuts. There is a deficit of data relative to the MC expectation with the oscillated MC providing improved agreement.

The reconstructed track direction cosines, $\cos\theta_x, \cos\theta_y, \cos\theta_z$ are shown in Figure 6.13 as well as the distribution of reconstructed E_μ. All three $\cos\theta$ distributions show the oscillated MC gives a better fit to the data. It is also possible to see in the $\cos\theta_y$ plot, the MC and Data peak at values higher than zero, reflecting the fact that the neutrinos enter the detector at a small angle due to the curvature of the Earth (the corresponding plot in the Near Detector was peaked at less than zero). The distribution of reconstructed

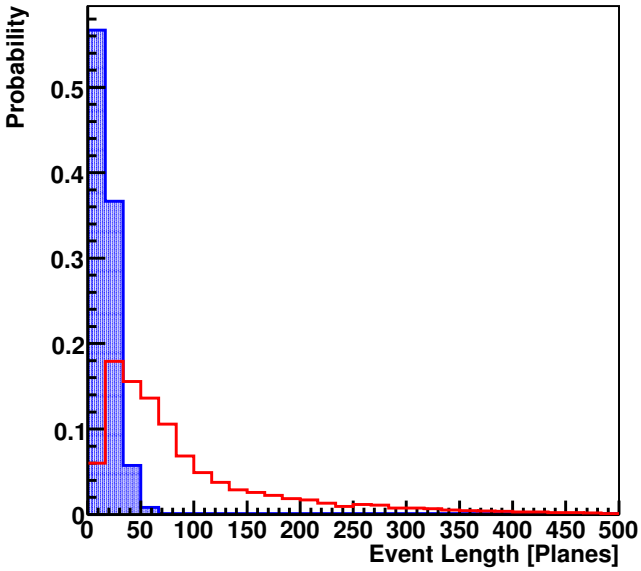

(a)

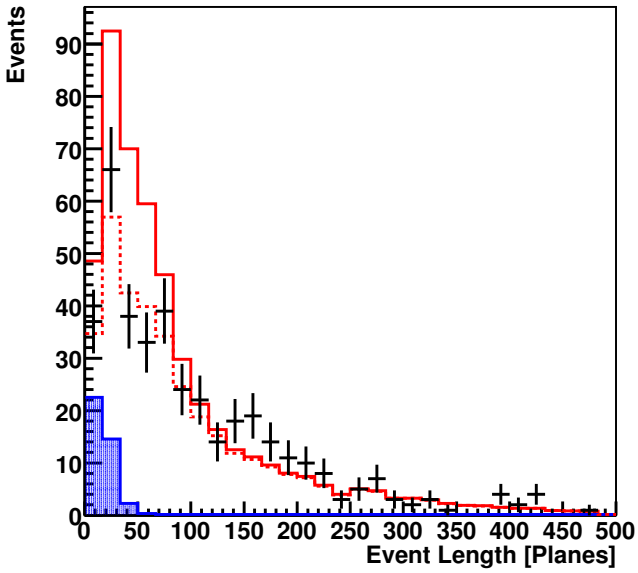

(b)

Figure 6.8: (a) PDF of event lengths for CC (red line) and NC (blue area) MC (b) Event Length in planes for data (black line), MC with no oscillations (red line), MC with SK oscillation parameters (red dashed line). The MC expectation for the contribution from NC events is shown by the blue shaded area.

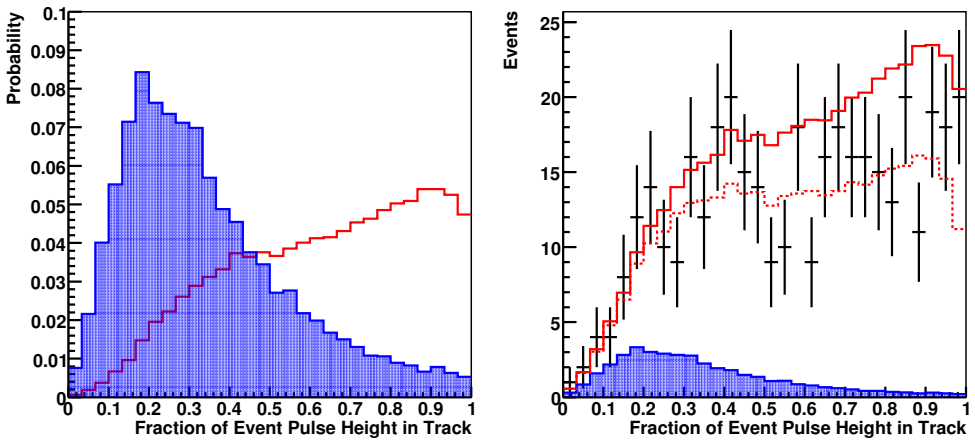

(a) (b)

Figure 6.9: (a) PDF of the fraction of the event's charge in the track for CC (red line) and NC (blue area) MC (b) Fraction of the event's charge contained in the track for data (black line), MC with no oscillations (red line), MC with SK oscillation parameters (red dashed line). The MC expectation for the contribution from NC events is shown by the blue shaded area.

E_μ shows a deficit in data at low energies in very good agreement with the oscillated MC. There is however, a large excess of data events in the 6-7 GeV bin. This is of potential concern as many cosmic muons that cross the detector have a reconstructed energy in this range due to the limiting dimensions of the detector. All the events in this bin were checked by eye and there were no suspect events that could have been a badly reconstructed cosmic muon, leading to the conclusion that the excess in this bin is due to statistical fluctuation.

The distributions of the number of strips in a reconstructed shower, the amount of shower charge per shower strip, reconstructed E_{shw} and reconstructed y are shown in Figure 6.14. The distribution of shower strips shows reasonable agreement between the data and oscillated MC. The distribution of shower pulse height per shower strip shows an excess of data at high MIP/strip values relative to both oscillated an unoscillated MC predictions. As in the Near Detector it is expected there will be differences between data and MC due to incomplete hadronic modelling. The reconstructed E_{shw} distribution shows a deficit of data events at low energy, with the oscillated MC giving better agreement with data. The reconstructed y distribution shows a consistent deficit

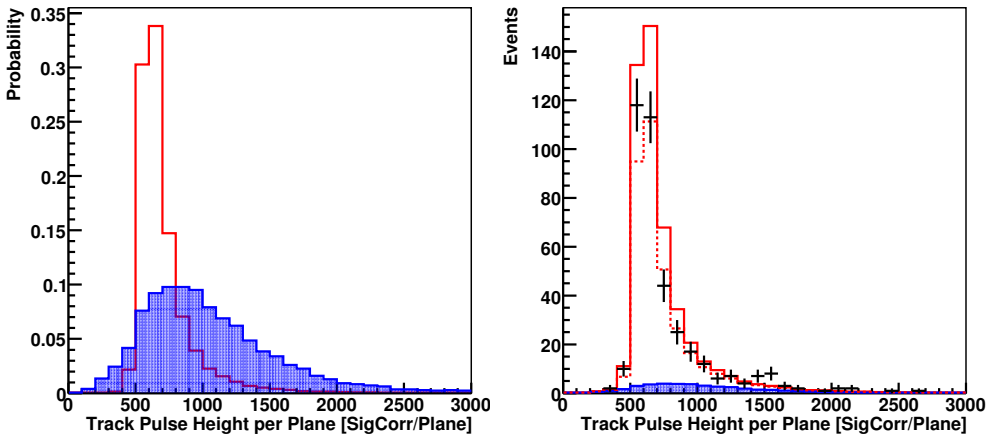

(a) (b)

Figure 6.10: (a) PDF of track pulse height per track plane for CC (red line) and NC (blue area) MC (b) Track pulse height per track plane for data (black line), MC with no oscillations (red line), MC with SK oscillation parameters (red dashed line). The MC expectation for the contribution from NC events is shown by the blue shaded area.

of data events relative to the unoscillated MC for $y < 0.75$.

The reconstructed E_ν spectrum for data showing in Figure 6.15, displays a deficit of low energy events which is in reasonable agreement with the oscillated MC. There is an excess of data for the 6-7 GeV bin, caused by a similar excess in the muon energy spectrum. Again the relevant events have been closely scrutinised and it has been concluded that this is due to statistical fluctuation. The ratio of Data and unoscillated MC (along with the ratio of oscillated and unoscillated MC) plotted against reconstructed E_ν shows a clear deviation from unity at lower energies in good agreement with the oscillated MC, though low statistics in the first bin prevent the identification of a clear minimum.

The general trend of the Far Detector data distributions is to show a deficit of events compared to non-oscillated MC, and various event variable distributions are distorted in such a way as to show much better agreement with oscillated MC (using SK best fit parameters). In the selected CC sample there are 307 events, compared with a non-oscillation hypothesis of 393 ± 21. The estimate of the error on the non-oscillated prediction is achieved by considering the effect of several systematic effects that would affect the total number of events (see Section 7.2 for a thorough treatment of systematic

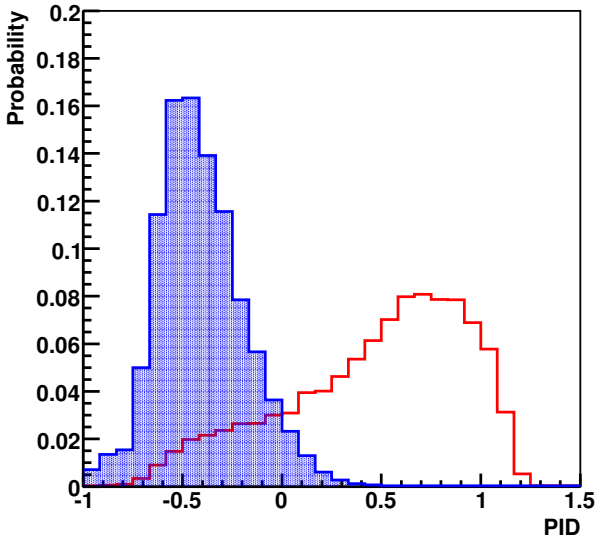

(a)

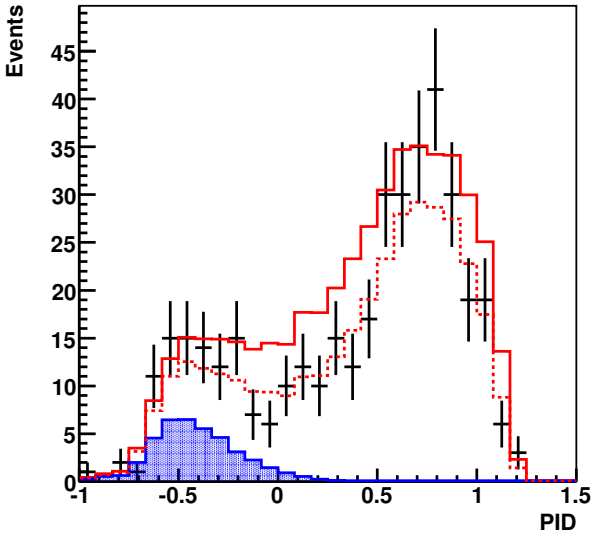

(b)

Figure 6.11: (a) PDF of PID distributions for CC/NC Separation for CC (red line) and NC (blue area) MC (b) PID distribution for CC/NC Separation for data (black line), MC (red line), MC with SK oscillation parameters (red dashed line). The MC expectation for the contribution from NC events is shown by the blue shaded area. In plot (b) the reweighting for the NC component of the MC, as discussed in Section 5.2 has not been applied.

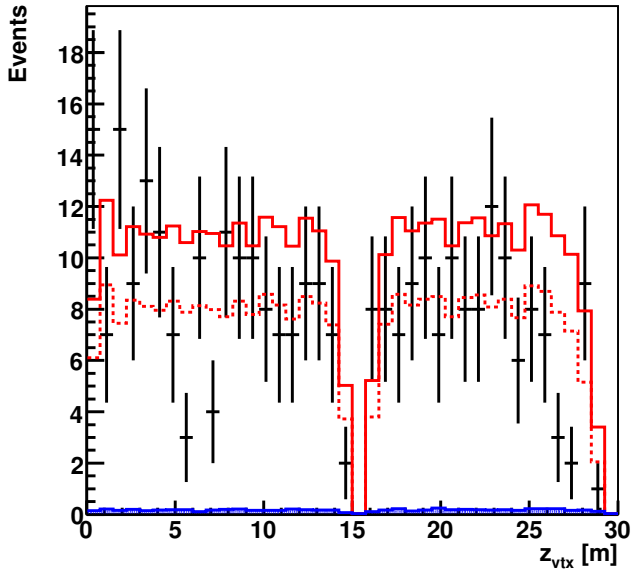

(a)

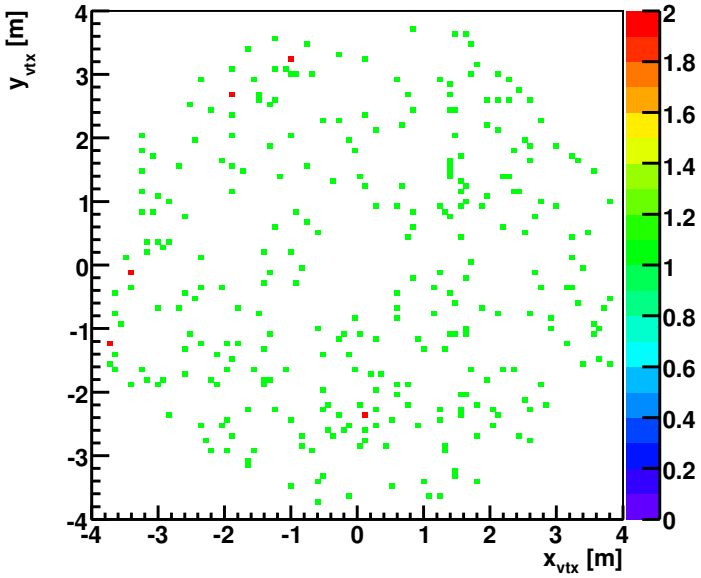

(b)

Figure 6.12: (a) z_{vtx} for selected FD Data (black points), MC with no oscillations (red line), MC with SK oscillation parameters (red dashed line). The MC expectation for the contribution from NC events is shown by the blue shaded area. (b) y_{vtx} plotted against x_{vtx} for FD Data.

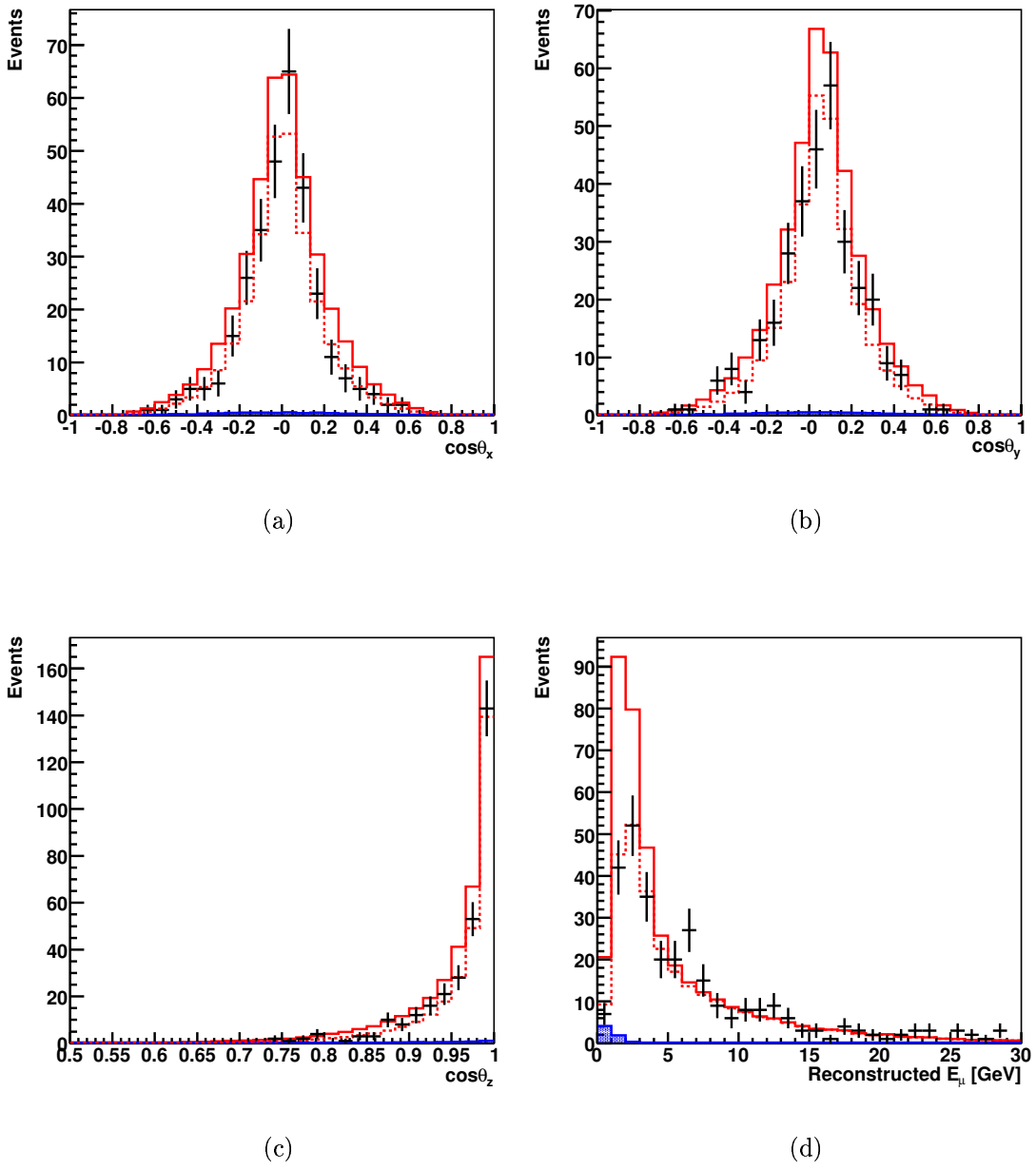

Figure 6.13: (a) $\cos\theta_x$ (b) $\cos\theta_y$ (c) $\cos\theta_z$ (d) E_μ for selected FD Data (black points), MC with no oscillations (red line), MC with SK oscillation parameters (red dashed line). The MC expectation for the contribution from NC events is shown by the blue shaded area.

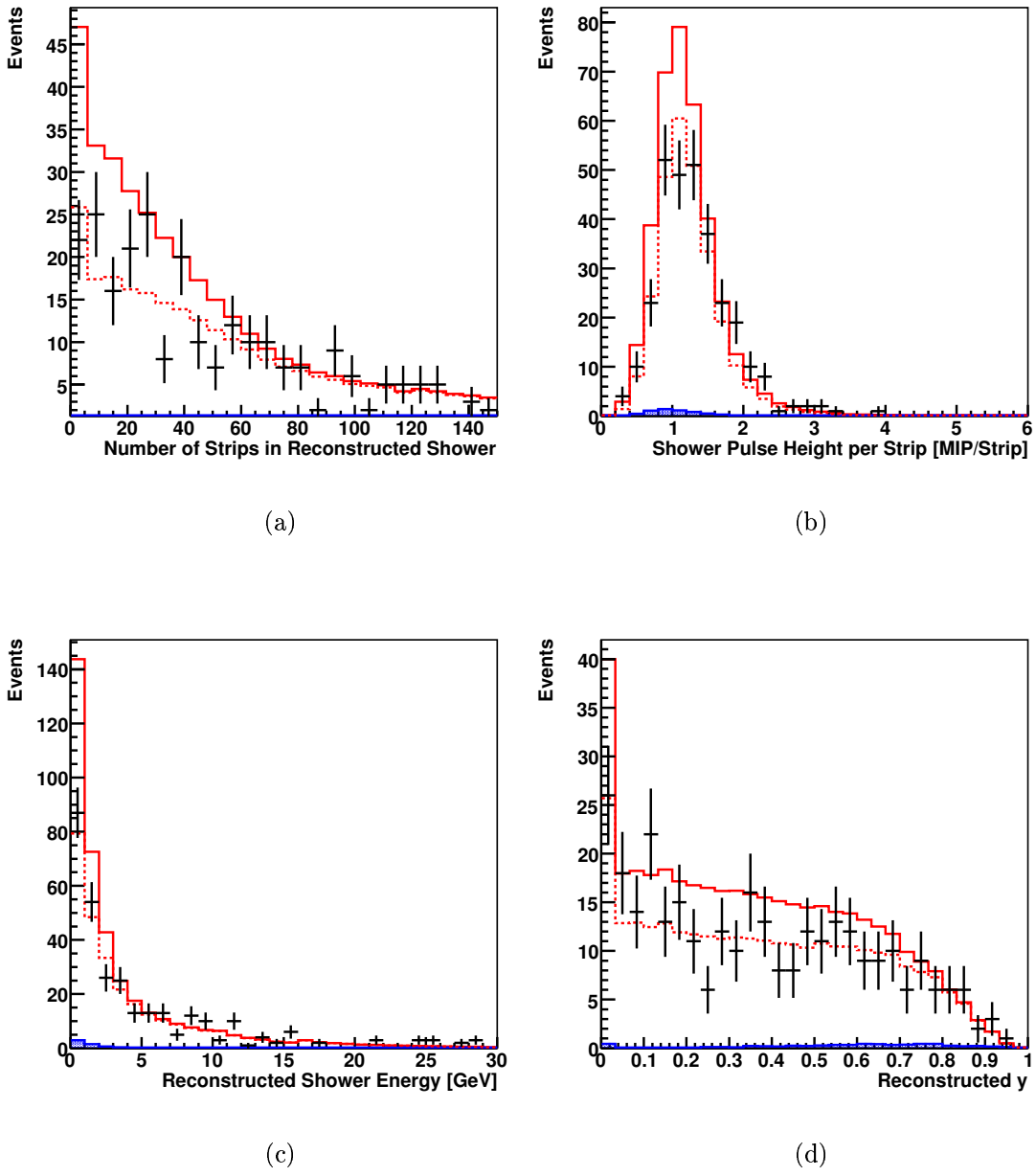

Figure 6.14: (a) Shower strips in a reconstructed shower (b) Shower pulse height per strip (c) Reconstructed E_{shw} (d) Reconstructed y for selected FD Data (black points), MC with no oscillations (red line), MC with SK oscillation parameters (red dashed line). The MC expectation for the contribution from NC events is shown by the blue shaded area.

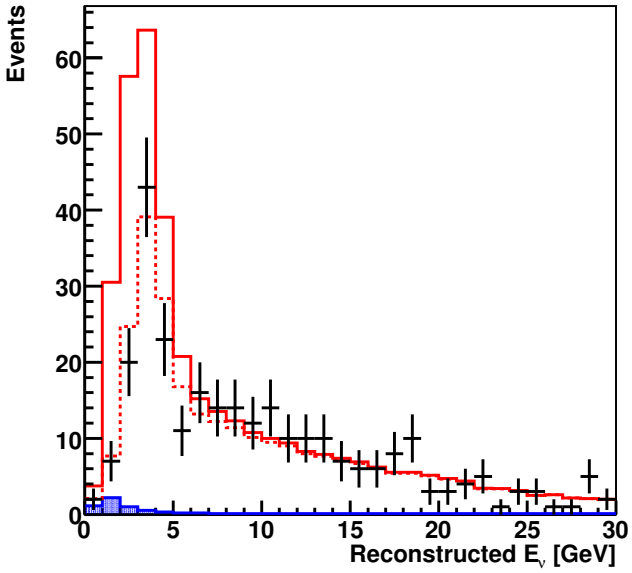

(a)

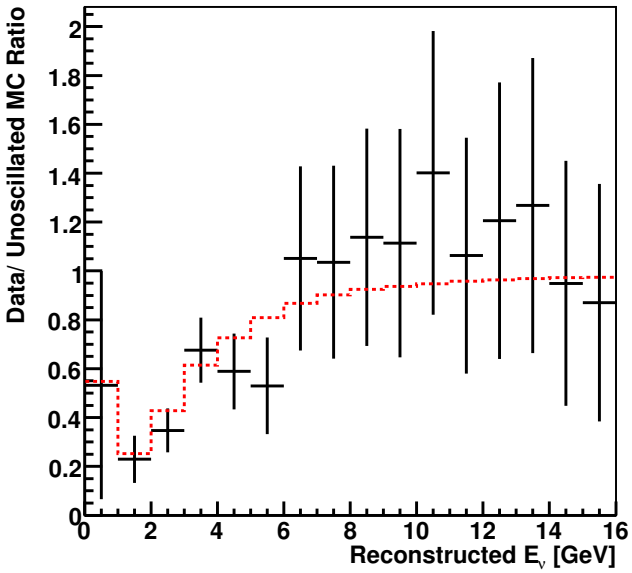

(b)

Figure 6.15: (a) Reconstructed E_ν (b) Ratio of Data and unoscillated MC for selected FD Data (black points), MC with no oscillations (red line), MC with SK oscillation parameters (red dashed line). The MC expectation for the contribution from NC events is shown by the blue shaded area.

errors). For events with reconstructed $E_\nu \leq 10\,\text{GeV}$ the number of events are 162 and 276 ± 14 respectively, showing the deficit is strongly energy dependent. The PID distribution shows a much greater deficit in the CC-like region than the NC-like region, indicating that there is only a deficit of CC events. These results strongly suggest that neutrino oscillation have taken place along the NuMI beamline, so an oscillation analysis will be carried out in the next chapter.

6.4 Extrapolating the Beam Spectra to the Far Detector

It has been seen in Section 5.1.2 that even after MC reweighting to account for hadron production and beamline effects, there are still some significant differences between the reconstructed neutrino energy spectra of data and MC. This has implications for the FD MC as the Far Detector will only see a small section of the NuMI beam, meaning that the data/MC differences observed in the Near Detector could potentially be amplified in the Far Detector. Figure 6.16 shows the PDFs of Near and Far true E_ν spectra for CC ν_μ events with true vertices in the fiducial volume of their respective detector. It also shows the Near/Far ratio for these PDFs. It can be seen that there are significant differences at low energy caused by the range of pion momenta and directions after focusing and the finite size of the Near Detector.

To get around this problem a method (known as the 'Beam Matrix' Method [70]) has been developed that takes the Near Detector reconstructed data energy spectrum and using knowledge of the efficiency, purity and energy resolution from Near and Far MC, and extrapolates it to the Far Detector to produce an expected Far Detector spectrum.

The first stage of this process is to obtain the Near Detector true CC ν_μ spectrum from the selected reconstructed E_ν spectra. This is done by first correcting the reconstructed spectra for purity (i.e. removing the MC expectation for the NC component from the selected sample) using the ratio of the reconstructed E_ν spectra of selected CC ν_μ events and all selected events in the sample. The NC component of the Near Detector MC used to construct this ratio has been adjusted via the reweighting scheme as discussed in Section 5.2, so as to propagate the correction to the Far Detector predicted spectrum. The true selected CC ν_μ spectra is then obtained from the reconstructed selected CC ν_μ spectra using a matrix of true E_ν plotted against reconstructed E_ν with the bins of

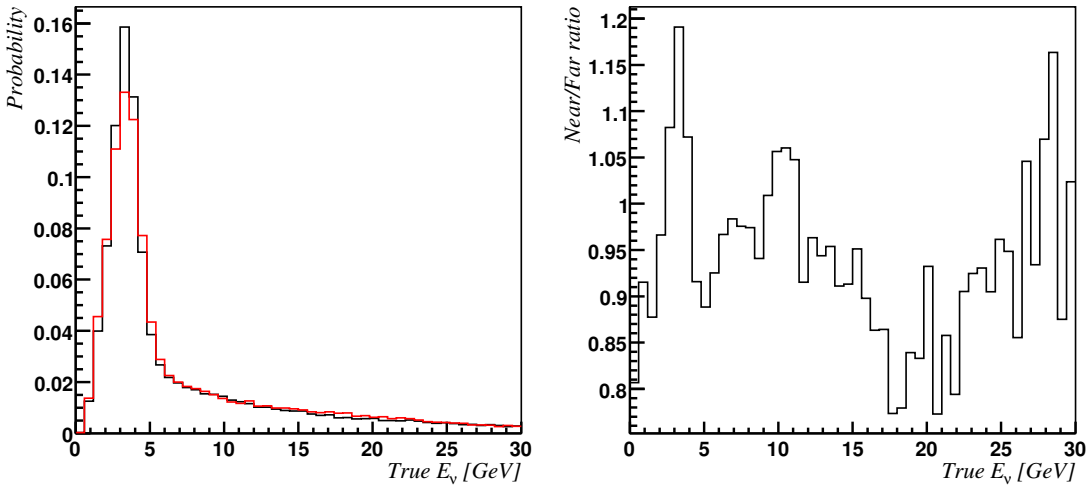

(a) (b)

Figure 6.16: (a) Near (black line) and Far (red line) true E_ν spectra for CC ν_μ events with true fiducial vertices, both normalised to unity (b) The ratio of the Near and Far PDFs.

true E_ν normalised to unity for a given reconstructed E_ν (i.e. it gives the PDF of true energies for a given reconstructed energy). The true CC ν_μ spectra then needs to be corrected for efficiency using the ratio of the selected CC ν_μ and CC ν_μ true spectra. These ratios and the matrix are shown in Figure 6.17. It can be seen that both purity and efficiency are approximately constant at high E_ν before reducing sharply at low E_ν. This purity distribution is expected as NC events can deposit any energy less than true E_ν in the detector so they will pile up at low energies. High energy NC events are easily removed whereas low energy NC events are more topologically similar to CC events. The drop in efficiency at low energies is due to CC events with short tracks being less likely to pass the TrackFitter, q/p or PID cut.

Now that the true CC ν_μ spectra at the ND has been obtained it can be extrapolated to the Far Detector. This involves using the MC flux files to obtain all the information about the parent particle that produced the neutrino. The neutrino flux at a given energy at both detectors depends on the probability that a decaying parent particle with a given momentum, radial and longitudinal position (determined by the hadron production, the beam focusing system and the parent decay probability) will produce a neutrino of a given energy that will intersect with the volume of the detector (determined by two-body

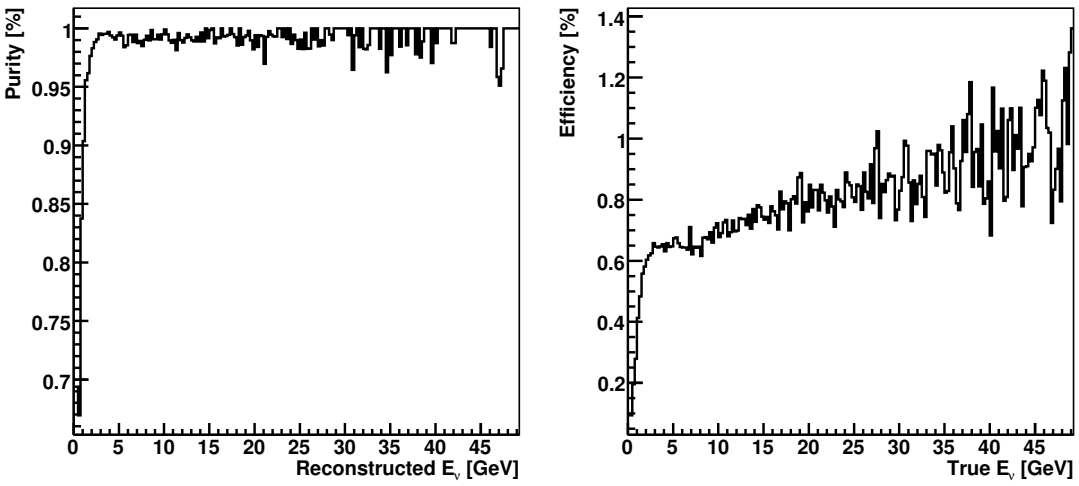

(a) (b)

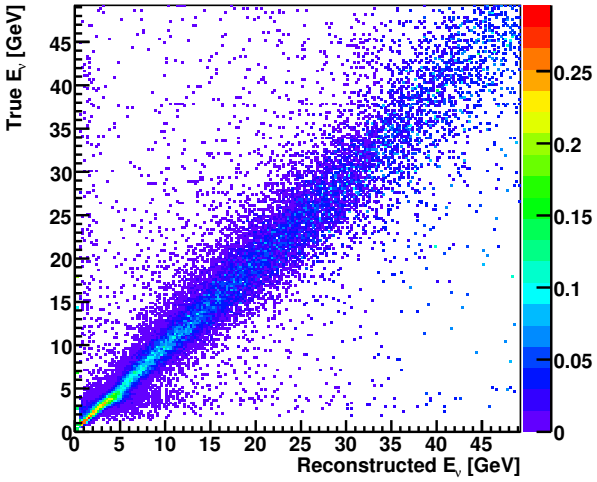

(c)

Figure 6.17: (a) Selected sample purity plotted against reconstructed E_ν (b) CC sample efficiency plotted against true E_ν (c) True vs reconstructed E_ν for CC ν_μ events for ND MC. Plot (c) is normalised to give the PDF of true E_ν for a given reconstructed energy. The 50 - 200 GeV overflow bin is not shown.

kinematics only). These flux distributions are then weighted by the cross-section of the interaction of a neutrino with the detector and also the weightings from the MC beam reweighting (as outlined in Section 5.1.1). For each parent particle the flux contributions to the Near and Far detectors can be plotted against each other such that each bin of Near detector energy provides the distribution of Far Detector energies. However, it is possible that neutrino events in the flux files fail the reconstruction (i.e. there were no reconstructed objects in the snarl) despite there being a neutrino interaction in MC. Also due to the slicing process in the Near Detector it is possible for large events to be divided up into several reconstructed events while still coming from the same true interaction or for small events to be merged with larger ones. The ratios of the true CC ν_μ spectra before and after reconstruction are used to correct this in both the Near and Far Detector. These ratios along with the Near-Far matrix are shown in Figure 6.18. It can be seen that the magnitude of the correction is much smaller in the Far Detector as there are no slicing effects. The direction of the Near Detector correction changes with energy due to the slicer merging low energy events and splitting up high energy ones.

The reconstructed Far Detector E_ν spectrum is then recovered using a matrix of reconstructed E_ν plotted against true E_ν for CC ν_μ events, where the each row of the matrix is normalised to unity, so as to give the PDF of reconstructed energies for a given true energy. The reconstructed CC ν_μ spectrum is then corrected for efficiency, multiplying by the ratio of the selected CC ν_μ and CC ν_μ reconstructed energy spectra. Finally the spectrum is corrected for purity by dividing by the ratio of the CC ν_μ selected and selected reconstructed spectra. The efficiency and purity corrections along with the true-reco matrix are shown in Figure 6.19. As in the case of the Near Detector, it can be seen that the purity and efficiency corrections are approximately constant at high E_ν before reducing sharply at low E_ν.

The Far Detector spectrum obtained when the selected Near Detector data spectrum is put through this chain is shown in Figure 6.20 along with the original FD MC spectra and their ratio. It can be seen that there are considerable deviations from the original FD MC spectra, with the matrix method predicting more events than the original MC on the lower edge of the peak and in the high energy tail and a deficit at intermediate energies. This predicted spectra will be used for the oscillation analysis.

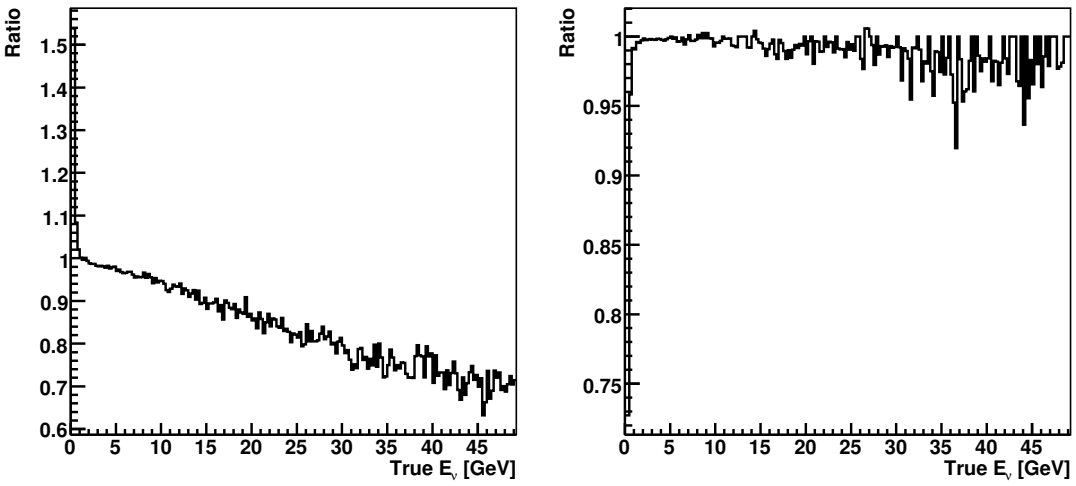

(a) (b)

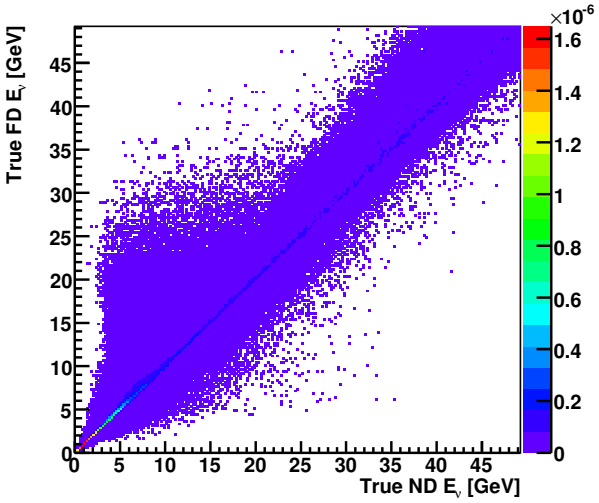

(c)

Figure 6.18: (a) Ratio of true and reconstructed CC ν_μ ND events plotted against true E_ν (b) Ratio of reconstructed and true CC ν_μ FD events plotted against true E_ν (c) Far plotted against Near true CC ν_μ E_ν spectra. The 50 - 200 GeV overflow bin is not shown.

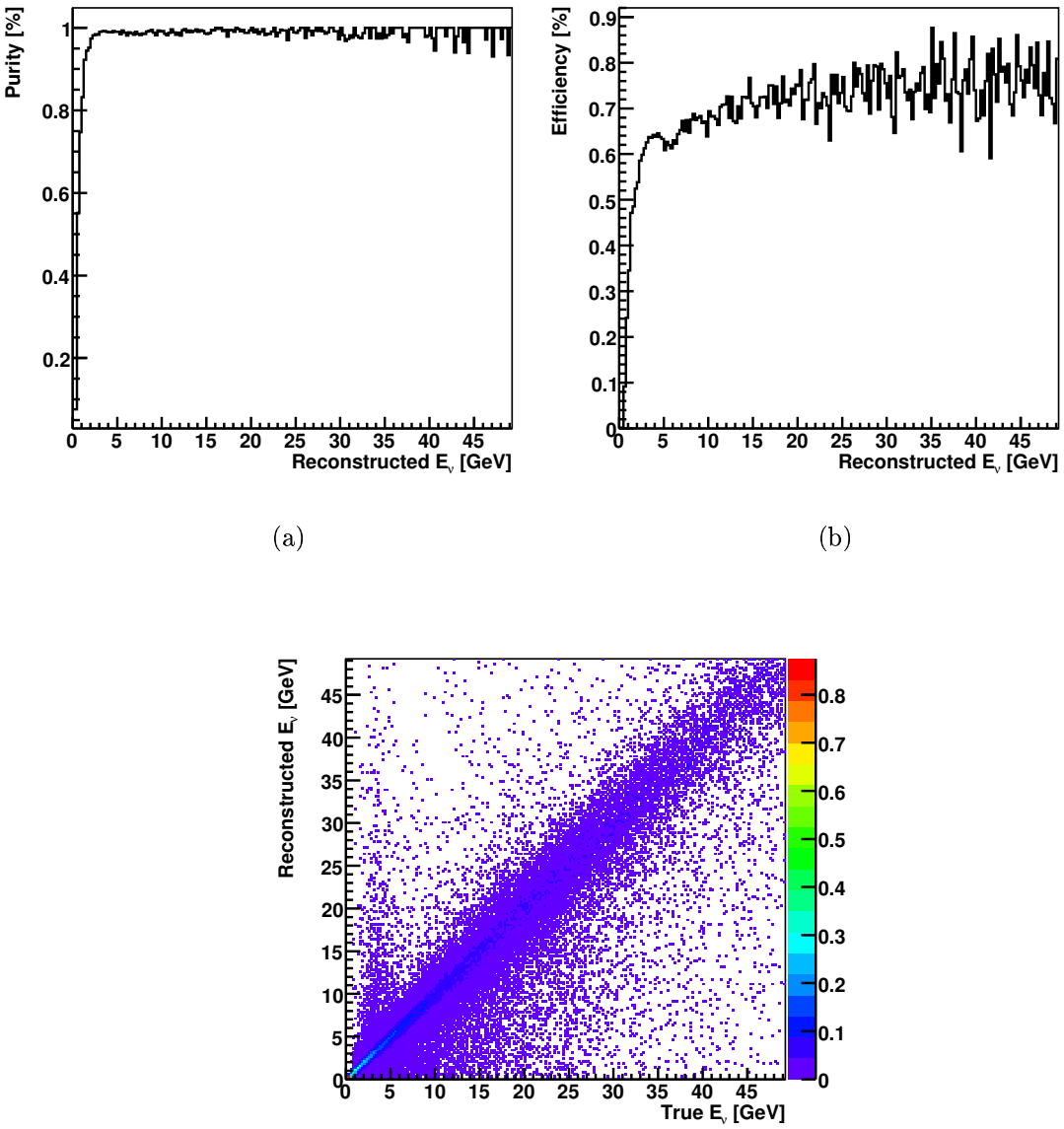

(a) (b)

(c)

Figure 6.19: (a) Selected sample purity plotted against reconstructed E_ν (b) CC sample efficiency plotted against reconstructed E_ν (c) Reconstructed plotted against true E_ν for CC ν_μ events for FD MC. Plot (c) is normalised to give the PDF of reconstructed E_ν for a given true energy. The 50 - 200 GeV overflow bin is not shown.

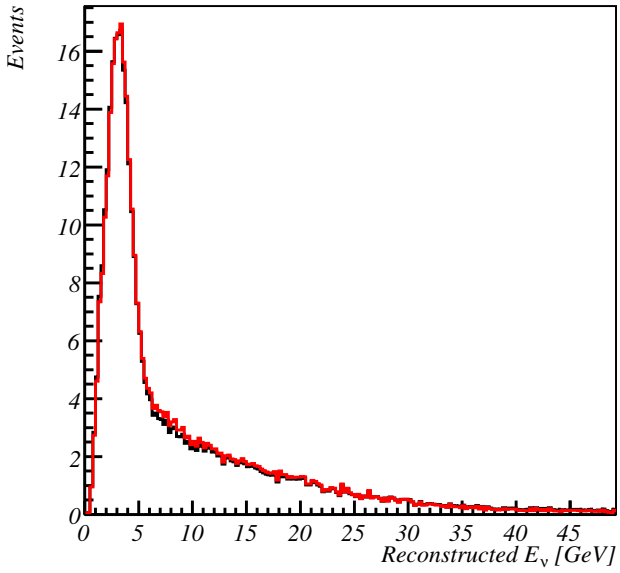

(a)

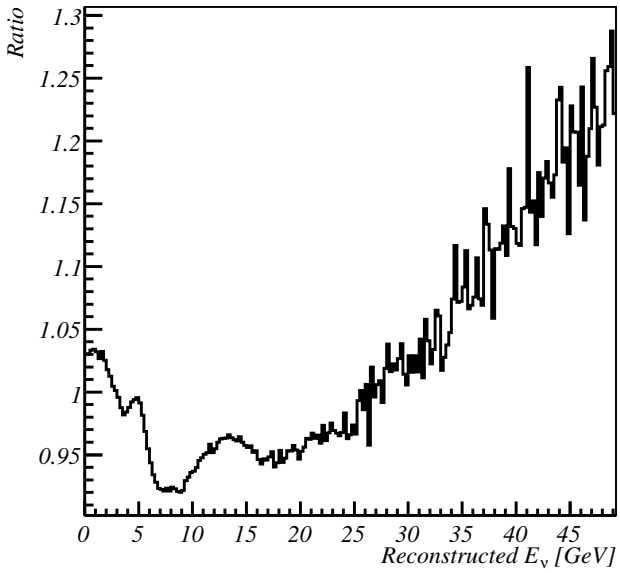

(b)

Figure 6.20: (a) FD MC selected spectra (red line) and FD predicted spectra from using the ND data with the Beam Matrix method (black line) (b) Ratio of original FD MC and Beam Matrix predicted spectra. The 50 - 200 GeV overflow bin is not shown.

Chapter 7

Oscillation Analysis

"In physics, your solution should convince a reasonable person. In math, you have to convince a person who's trying to make trouble. Ultimately, in physics, you're hoping to convince Nature. And I've found Nature to be pretty reasonable."

—

Frank Wilczek

7.1 Event Energy Resolution

Given the relatively small data sample available at this stage of the MINOS experiment, it is highly desirable to make as much use of each event as possible, extracting the maximum amount of information from it. In addition to an event's reconstructed energy, it is also possible to estimate how reliable that reconstructed energy is (e.g. an event consisting of a long, fully-contained track will have significantly better resolution that an event with a small partially contained track and a large hadronic shower). If it were possible to assign an energy resolution to each event then this could be used to improve the oscillation analysis.

A Bayesian approach has been taken to this issue as described in [71], that has been successfully applied to the MINOS atmospheric analysis [47]. We want to obtain the PDF of true E_ν for a given set of measured quantities of an event. The measured quantities that are considered are the reconstructed muon energy, the reconstructed hadronic

shower energy and the cosine of the reconstructed neutrino-muon angle (assuming the neutrino is coming from Fermilab). Applying Bayes' theorem gives:

$$\mathrm{P(E_\nu|\ Reco\ quantities)\ P(Reco\ quantities) = P(Reco\ quantities\ |\ E_\nu)\ P(E_\nu)}$$

where P(Reco quantities) is a constant as the event has already been measured. It also needs to be considered that the measured event variables do not depend simply upon $\mathrm{E_\nu}$ but also on the kinematic variables y and $\mathrm{W^2}$ that determine the true muon angle and shower and muon energies before the detector response function determines the distribution of the measured variables. This means that for a given $\mathrm{E_\nu}$ it is necessary to integrate over all possible values of y and $\mathrm{W^2}$ as these will change the distributions of the event variables, so the expression becomes:

$$\mathrm{P(E_\nu|\ Reco\ quantities) = \int\int P(Reco\ quantities\ |\ E_\nu,}y,\mathrm{W^2)\ P(}y,\mathrm{W^2\ |\ E_\nu)\ dW^2d}y$$

Another consideration is the different neutrino-nucleus interactions: Quasi-Elastic (QE), Resonance (RES) and Deep Inelastic Scattering (DIS), all of which will have different kinematic distributions and detector response functions, so the $\mathrm{E_\nu}$ PDF is calculated separately for each of these. For each of the interaction types the term P(Reco quantities | $\mathrm{E_\nu}$,y,$\mathrm{W^2}$) is determined by using large MC samples of selected CC ν_μ events. Limited statistics over all energy ranges and interaction types mean the width of these distributions has to be restricted. The following distributions are made for:

- Reconstructed E_{shw} - true $\mathrm{E_\nu}y$ (in the range +5 GeV to -5 GeV) for different true $\mathrm{E_\nu}y$
- Reconstructed $\mathrm{E_\mu}$ (from range) - true $\mathrm{E_\mu}$(in the range -2.5 GeV to +2.5 GeV) for different true $\mathrm{E_\mu}$, if track was fully contained
- $\frac{q/p_{reco}-q/p_{true}}{\sigma_{q/p}}$ (in the range -10 to +10) for different true $\mathrm{E_\mu}$ (this is necessary as the fitter calculates q/p for the track) if the track was partially contained
- Scalar product of true and reconstructed muon direction (in the range 0.5 to 1.0) for different true $\mathrm{E_\mu}$

The term P(y,$\mathrm{W^2}$ | $\mathrm{E_\nu}$) is obtained using 2 billion NEUGEN events producing y distributions of QE events and y plotted against $\mathrm{W^2}$ distributions of RES and DIS events

for separate bins of E_ν of width 0.1 GeV from 0.2 - 10 GeV and in bins of width 0.5 GeV from 10 - 100 GeV. The PDF of the cross-section for each interaction type is also obtained. An example of these distributions is shown in Figure 7.1. It can be seen that there is a cut off in W^2 at slightly less than 3 GeV^2 in the distribution for RES events and there is a step in the distribution at the same level in W^2 for DIS events. This discontinuity arises in the NEUGEN model from attempts to combine two different models describing RES and DIS events respectively [72].

For each event, the quantity P(E_ν| Reco quantities) is calculated for E_ν values between 0.2 GeV and 100 GeV in steps of 0.1 GeV. This is done separately for each of the three interaction hypotheses, $P_{\text{Interaction}}(E_\nu|$ Reco quantities):

$$
\begin{aligned}
P_{\text{Interaction}}(\mathrm{E}_\nu|\text{ Reco quantities}) = \mathrm{P}(\text{Interaction}|\mathrm{E}_\nu)\ \times \\
\Bigg[\sum_j \sum_i P(\mathrm{E}_\mu{}^{measured}|\text{Interaction}, \mathrm{E}_\mu{}^j) \\
\times P(E_{shw}^{measured}|\text{Interaction}, \mathrm{E}_\nu, \mathrm{E}_\mu{}^j) \\
\times P(\cos\theta_{\nu\mu}^{measured}|\text{Interaction}, \cos\theta_{\nu\mu}^i, \mathrm{E}_\nu, \mathrm{E}_\mu{}^j) \\
\times P(y, \mathrm{W}^2|\text{Interaction}, \mathrm{E}_\nu, \mathrm{E}_\mu{}^j, \cos\theta_{\nu\mu}^i)\Bigg]
\end{aligned}
$$

where $\mathrm{E}_\mu{}^j$ are E_μ values within ± 2.5 GeV of the reconstructed E_μ in 200 bins and $\cos\theta_{\nu\mu}^i$ is the cosine of the muon-neutrino angle, with values between 0.5 and 1 in 200 bins. P(Interaction|E_ν) is the probability of the event being a QE, RES or DIS interaction for a given E_ν. It is obtained from the relevant NEUGEN distribution and a combination of distributions is used if it is close to the edge of one of the energy bins. Within the loop over $\mathrm{E}_\mu{}^j$, the probability of obtaining the measured E_μ, $P(\mathrm{E}_\mu{}^{measured}|\text{Interaction}, \mathrm{E}_\mu{}^j)$, is determined by looking up the appropriate energy resolution distribution. The value of $\mathrm{E}_\mu{}^j$ is also used in conjunction with the considered E_ν to calculate the true value for the hadronic shower energy, y and the true muon-neutrino angle, $\theta_{\nu\mu}$, for the QE hypothesis. The true hadronic shower energy is then used to determine the probability of obtaining the measured shower energy, $P(E_{shw}^{measured}|\text{Interaction}, \mathrm{E}_\nu, \mathrm{E}_\mu{}^j)$. In the case of the QE interaction hypothesis, the probability of obtaining the considered y value, given E_ν, P(y|QE,E_ν,$\mathrm{E}_\mu{}^j$), is also determined at this point.

Within the E_μ loop, a second loop is performed over the muon-neutrino angle cosine, $\cos\theta_{\nu_\mu}^i$. This is used along with the considered E_ν and $\mathrm{E}_\mu{}^j$ values to determine the probability of obtaining the measured $\cos\theta_{\nu_\mu}$, $P(\cos\theta_{\nu\mu}^{measured}|\text{Interaction}, \cos\theta_{\nu\mu}^i, \mathrm{E}_\nu, \mathrm{E}_\mu{}^j)$.

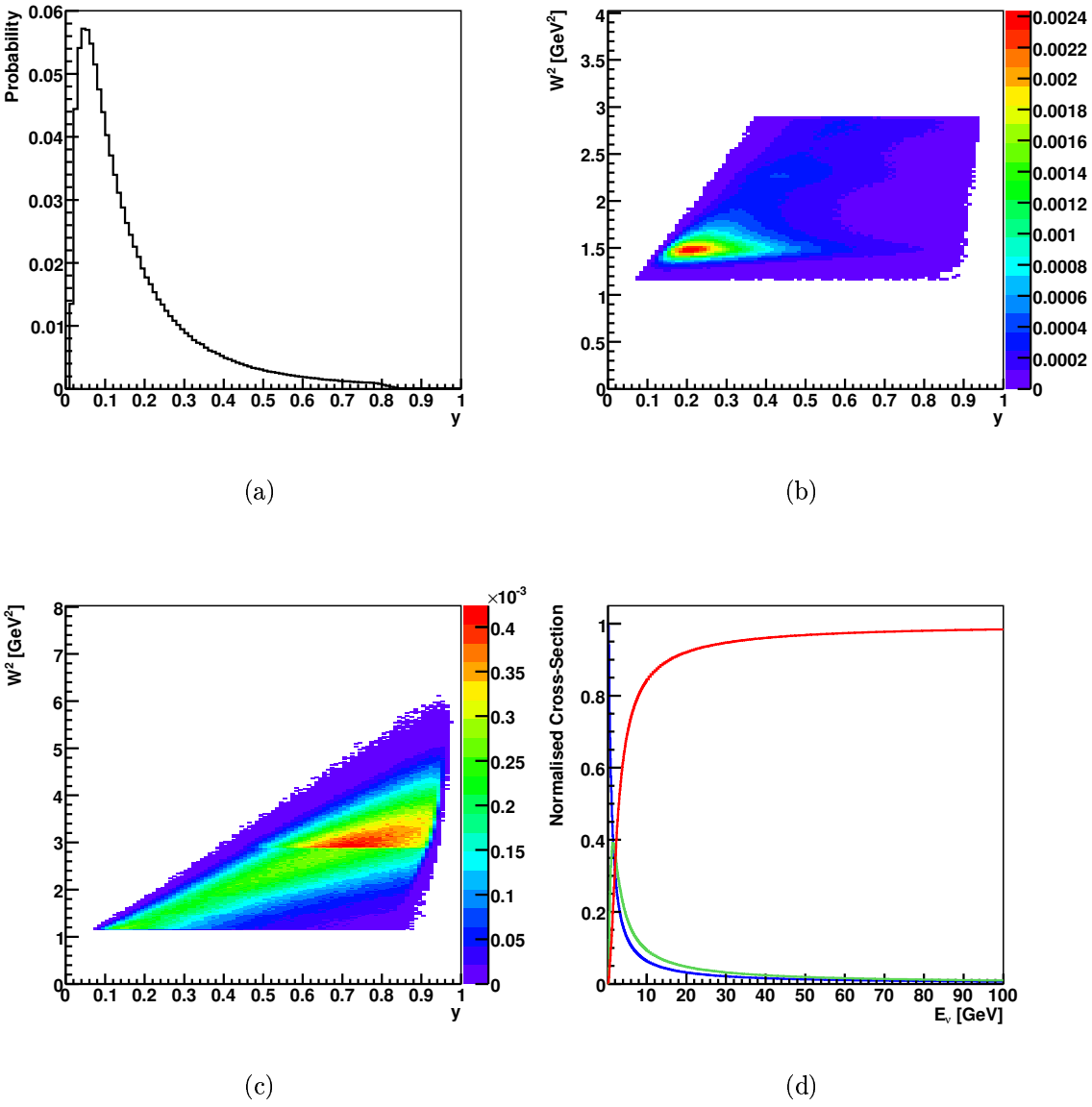

Figure 7.1: Kinematic distributions for CC ν_μ events with E_ν in the range 2.1 - 2.2 GeV for (a) QE, (b) RES and (c) DIS events. (d) Normalised Cross-Sections for the different interaction hypotheses, QE (blue line), RES (green line) and DIS (red line) plotted against E_ν for CC ν_μ NEUGEN events, taken from [73].

For the QE interaction hypothesis this is done using the only value of $\cos\theta^i_{\nu\mu}$ that satisfies the kinematic constraints from the values of E_ν and ${\mathrm{E}_\mu}^j$. This combination of variables is also used to calculate W^2, so that the probability of the y, W^2 combination, $P(y, \mathrm{W}^2|\mathrm{Interaction}, \mathrm{E}_\nu, {\mathrm{E}_\mu}^j, \cos\theta^i_{\nu\mu})$, can be found from the relevant NEUGEN distribution.

This results in $P_{\mathrm{Interaction}}(\mathrm{E}_\nu|$ Reco quantities) distributions for each of the three interaction hypotheses, which are summed to give a distribution of $\mathrm{P}(\mathrm{E}_\nu|$ Reco quantities) for the event. Figure 7.2 shows these event energy PDFs (along with the individual interaction PDFs) for a true QE event, a true RES event and a true DIS event. It can be seen that the correct interaction hypothesis will peak close to the true energy and typically has the highest peak and greatest integrated probability. As expected from their cross-sections, the interactions will typically peak in the order QE, RES and DIS in terms of E_ν.

The greatest oscillation sensitivity results from this fit were obtained when the peak of the interaction PDF with the highest maxima was fitted with a quadratic and this peak, E_{fit}, was taken as the best estimate for the energy of the event. This means that the other interaction hypotheses can not skew the peak which is important for low energy QE events as these are most sensitive to oscillations with the expected parameters. The information from the other interaction PDFs will not be discarded as they contribute to the width of the total PDF which is used to assign the expected energy resolution of an event.

Figure 7.3 shows the fractional E_{fit} resolution compared to that from summing E_μ and E_{shw}. It can be seen that E_{fit} provides slightly improved energy resolution, although it suffers from a small negative offset. The reason for this can be seen in the fractional energy resolution plots for the different interaction types. It can be seen that E_{fit} for QE events is reasonably well centred and gives a significant resolution improvement on the standard reconstruction. The resolutions for RES and DIS events show a skewing to lower energies. This is caused by events having been mistakenly identified as QE interactions, so the peak of the QE distribution, typically at a lower energy than the RES or DIS peaks, is taken as E_{fit}. This is acceptable as QE events dominate the region where the oscillation probability is expected to maximal, so an improved QE energy resolution will produce improved oscillation sensitivity, despite the loss of resolution for RES and DIS events.

Another application of the results of this method is obtained by integrating the probabil-

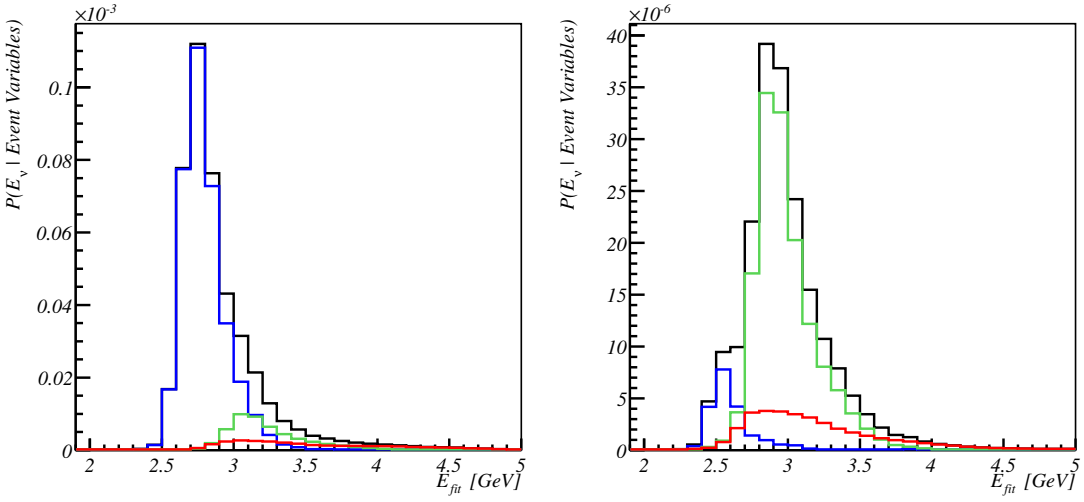

(a) (b)

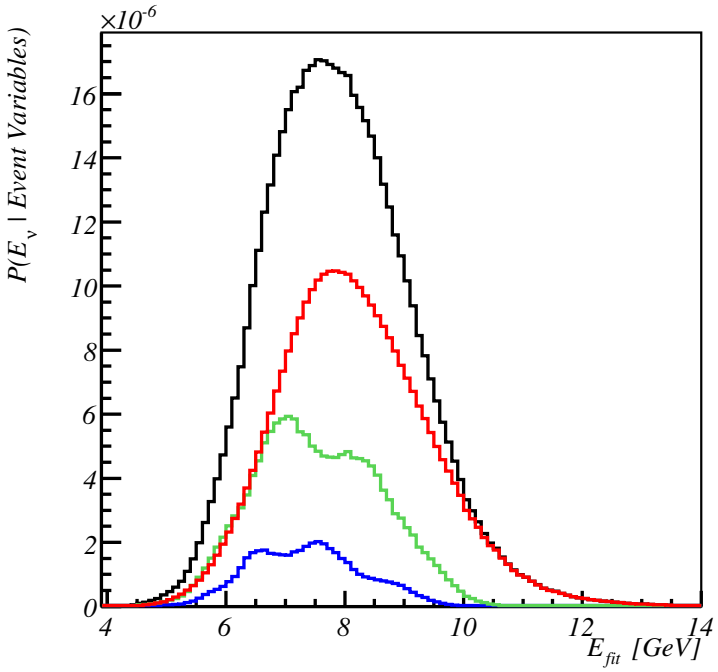

(c)

Figure 7.2: Probability plotted against E_ν from Bayesian fitting method for (a) A true QE event with $E_\nu = 2.79$ GeV (b) A true RES event with $E_\nu = 2.89$ GeV (c) A true DIS event with $E_\nu = 7.62$ GeV. It shows the overall probability (black line) as well as the probabilities of the individual interaction hypotheses: QE (blue line), RES (green line) and DIS (red line).

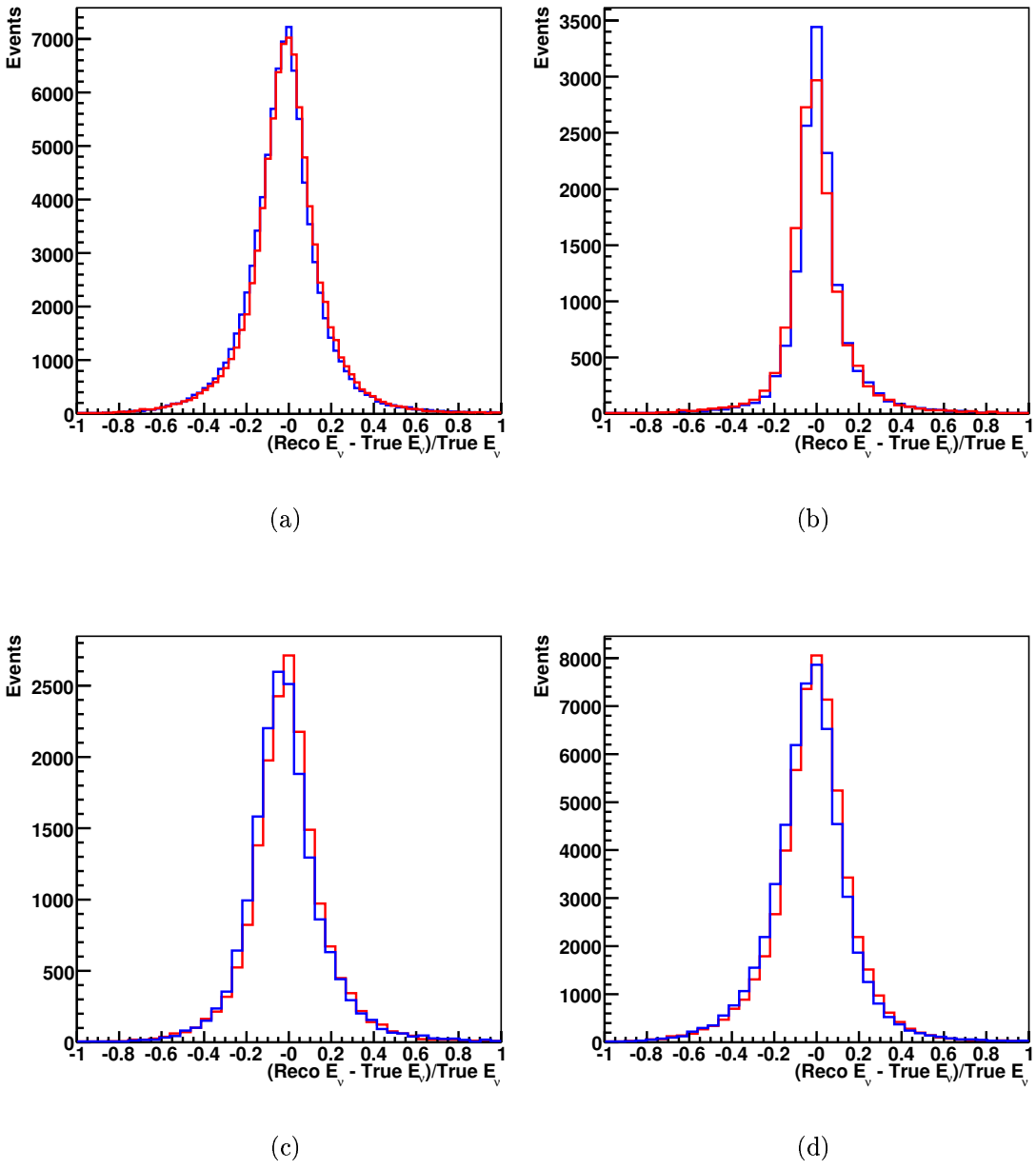

Figure 7.3: Fractional E_ν resolution of selected CC $\nu_\mu$events using the Bayesian fit results (blue line) and standard energy reconstruction (red line) for Far Detector MC for: (a) All interaction types (b) QE events (c) RES events (d) DIS events.

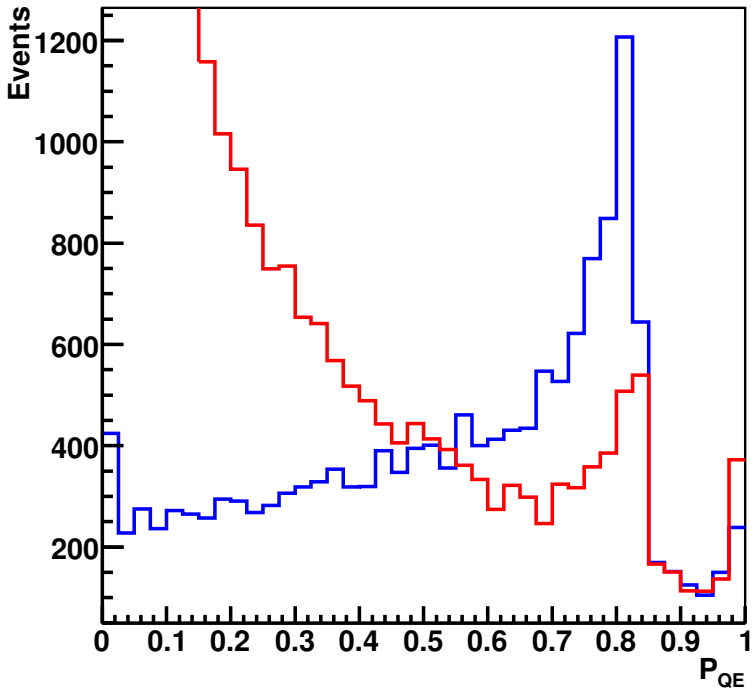

Figure 7.4: P_{QE} distributions from Bayesian fit for QE (blue line) and non-QE (red line) selected CC Far MC events.

ity distributions of the individual interaction hypotheses to define a fractional interaction probability relative to the integrated total probability:

$$P_{Interaction} = \frac{\sum_{i=1}^{n} P_{Interaction}(\mathrm{E}_\nu{}^i)}{\sum_{i=1}^{n} P_{QE}(\mathrm{E}_\nu{}^i) + P_{RES}(\mathrm{E}_\nu{}^i) + P_{DIS}(\mathrm{E}_\nu{}^i)}$$

This is particularly useful for QE event identification. Figure 7.4 shows the distribution of P_{QE} for both QE and non-QE events. It can be seen that there is reasonable separation between the samples, although there are a significant number of non-QE events in the high P_{QE} region, most likely due to failure to reconstruct a shower. A cut at $P_{QE} > 0.5$ gives a sample with an QE efficiency and purity of 59% and 60.8% respectively.

The most useful information obtained from the Bayesian fit method is the width (σ_E) of the total probability distribution. This can be used to divide the sample into subsamples

of different energy resolutions. This would allow an oscillation fit to consist of separate shape fits to the E_{fit} spectra of the subsamples as well as an overall normalisation fit. Figure 7.5 shows the distributions of σ_E/E_{fit} and $\sigma_E/\sqrt{E_{fit}}$. It can be seen that there is good agreement between data and the oscillated MC. It can also be seen that the $\sigma_E/\sqrt{E_{fit}}$ distribution has a much lower NC background, relative to the σ_E/E_{fit} distribution, in the areas where oscillations have the greatest effect. Therefore the sample will be divided up via the quartiles of the $\sigma_E/\sqrt{E_{fit}}$ distribution for CC ν_μ events with $E_{fit} < 5$ GeV, so as to accurately represent the events that are most sensitive to oscillations:

- 1st Resolution quartile: $0 < \sigma_E\,(\text{GeV})/\sqrt{E_{fit}\,(\text{GeV})} < 0.285$
- 2nd Resolution quartile: $0.285 < \sigma_E\,(\text{GeV})/\sqrt{E_{fit}\,(\text{GeV})} < 0.39$
- 3rd Resolution quartile: $0.39 < \sigma_E\,(\text{GeV})/\sqrt{E_{fit}\,(\text{GeV})} < 0.485$
- 4th Resolution quartile: $0.485 < \sigma_E\,(\text{GeV})/\sqrt{E_{fit}\,(\text{GeV})}$

It should be noted that these distributions in Figure 7.5 were made with events that have passed all analysis cuts other than the PID cut. This is because the Bayesian fit method is able to distinguish between low energy CC and NC events, due to their differing kinematics. The assumption of CC kinematics in the fit means that NC events return very broad PDFs with a low total probability. This means that they are placed in the low resolution subsample and so have less effect on the oscillation fit. With the PID cut, many of the NC events are removed but so are a large number of low energy CC events that would be very sensitive to oscillations. For this reason an analysis done using the Bayesian fit will not use the PID cut.

The distributions of E_{fit} for the various quartiles for FD data and unoscillated and oscillated MC are shown in Figures 7.6 - 7.9 along with the ratio to unoscillated MC. It can be seen that there is good agreement between the data and the oscillated MC and that the ratio plot shows greatly reduced sensitivity to oscillations in the last quartile as this contains the most of the NC background and CC events with poor energy resolution.

For this method to be used in an oscillation analysis, it has to be compatible with the Beam Matrix method. This means that true plotted against E_{fit} matrices as well as efficiency and purity corrections have to be made for the events in each of the resolution quartiles. However the true E_ν distributions for each of the Bayesian quartiles has to

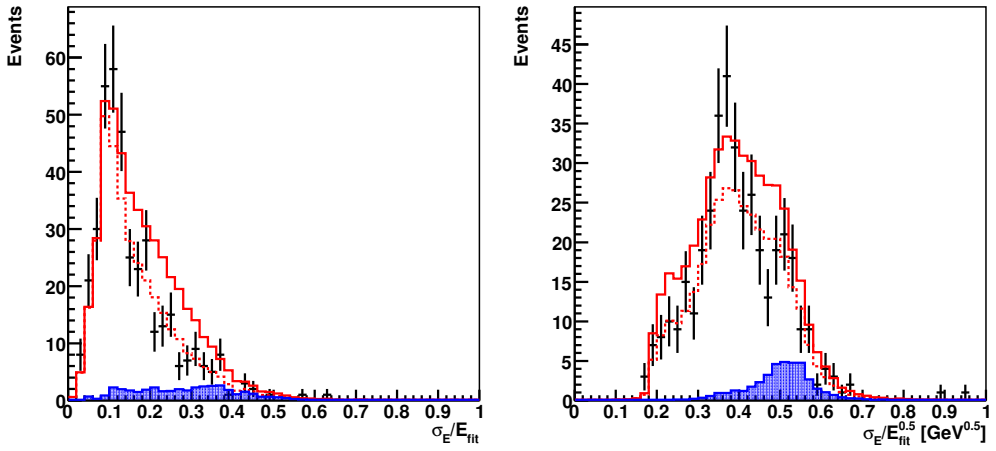

(a) (b)

Figure 7.5: (a) σ_E/E_{fit} and (b) $\sigma_E/\sqrt{E_{fit}}$ from the Bayesian fit for FD data (black line), MC (red line), MC oscillated with SK parameters (red dashed line). The MC expectation for the contribution from NC events is shown by the blue shaded area.

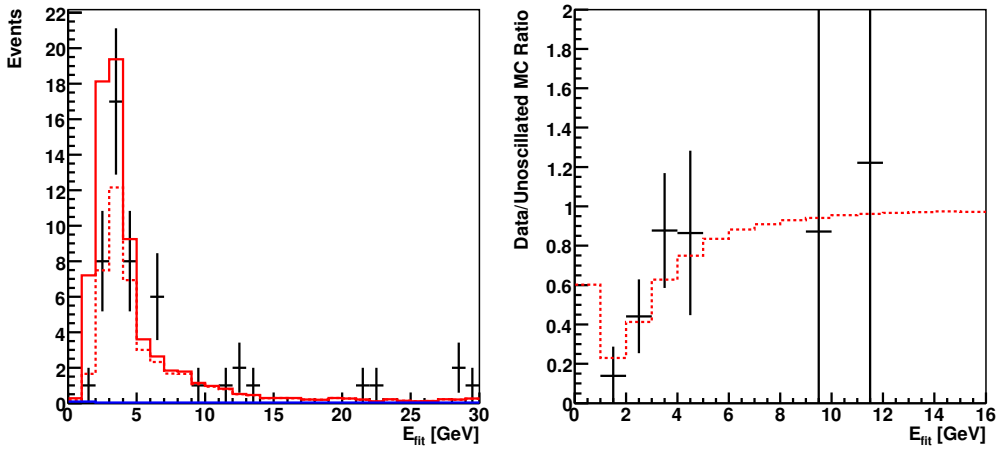

(a) (b)

Figure 7.6: (a) E_{fit} and (b) Data/unoscillated MC ratio for events in the 1st resolution quartile where FD data (black line), MC (red line), MC oscillated with SK parameters (red dashed line). The MC expectation for the contribution from NC events is shown by the blue shaded area.

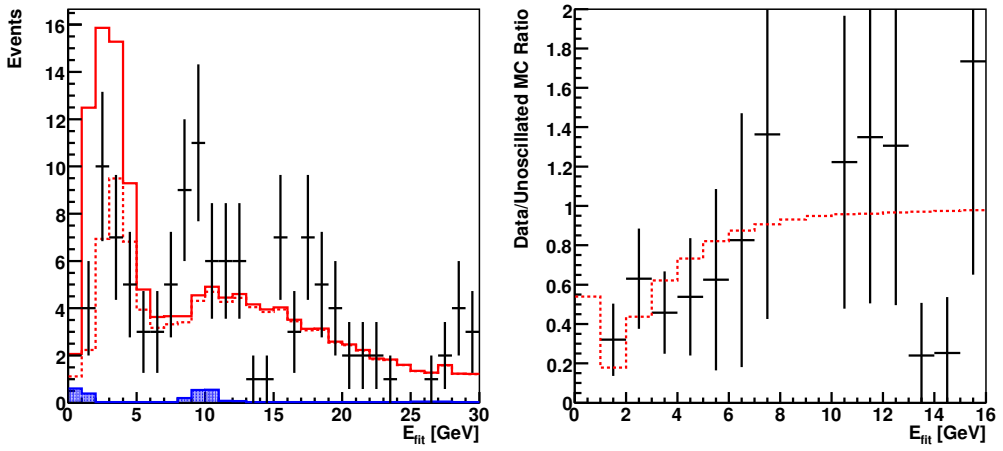

(a) (b)

Figure 7.7: (a) E_{fit} and (b) Data/unoscillated MC ratio for events in the 2nd resolution quartile where FD data (black line), MC (red line), MC oscillated with SK parameters (red dashed line). The MC expectation for the contribution from NC events is shown by the blue shaded area.

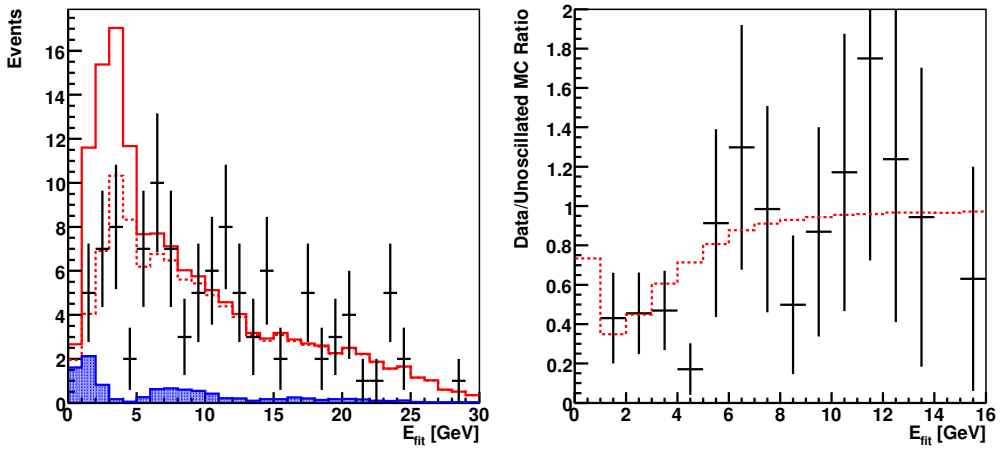

(a) (b)

Figure 7.8: (a) E_{fit} and (b) Data/unoscillated MC ratio for events in the 3rd resolution quartile where FD data (black line), MC (red line), MC oscillated with SK parameters (red dashed line). The MC expectation for the contribution from NC events is shown by the blue shaded area.

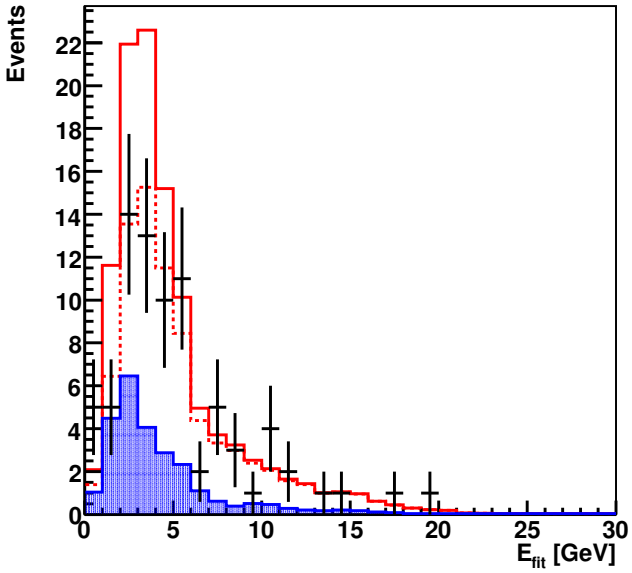

(a)

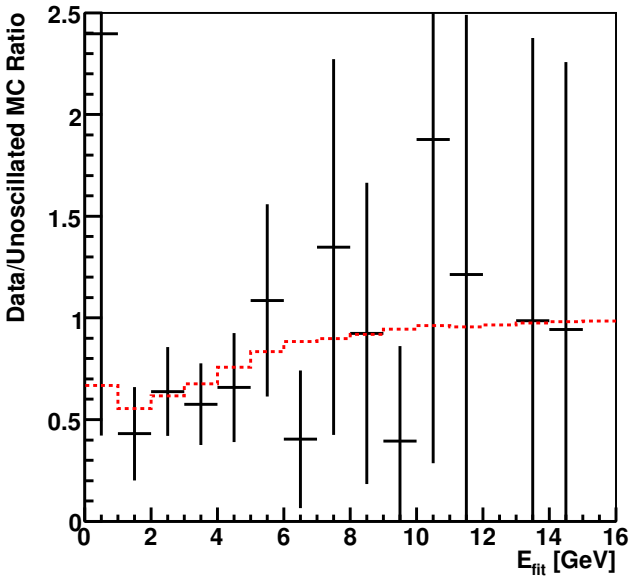

(b)

Figure 7.9: (a) E_{fit} and (b) Data/unoscillated MC ratio for events in the 4th resolution quartile where FD data (black line), MC (red line), MC oscillated with SK parameters (red dashed line). The MC expectation for the contribution from NC events is shown by the blue shaded area.

be corrected via the ratio in Figure 6.20 to make them the same as the predicted true Far Detector spectrum from the Beam Matrix method.

7.2 Comparison of Methods

Over the course of this thesis, several techniques have been developed with the aim of improving the limits of any measured oscillation parameters. To assess the impact on the combined statistical and systematic sensitivity afforded by each of these methods, oscillation analyses were carried out using the following configurations:

- 1. Using standard shower energy reconstruction and fiducial volume comprising 72.9% of the Far Detector mass, as used in first MINOS beam paper [68].
- 2. Using standard shower energy reconstruction and fiducial volume comprising 84.3% of the Far Detector mass, as described in section 6.2.
- 3. Using deweighting shower energy reconstruction and fiducial volume comprising 84.3% of the Far Detector mass, as described in section 6.2.
- 4. Using Bayesian fitted energy and fiducial volume comprising 84.3% of the Far Detector mass, as described in section 6.2.

For each of these configurations, the MC Far true CC energy spectra (or 4 Bayesian quartile spectra in the case of the fourth configuration) is then oscillated, by weighting the spectrum with the ν_μ survival probability, with parameters of $\Delta m^2_{23} = 2.74 \times 10^{-3}$ eV^2 and $\sin^2 2\theta_{23} = 1.0$, taken from the most recent MINOS oscillation analysis of the 1.27×10^{20} PoT data sample [68]. The reconstructed, selected Far Detector predicted oscillated spectra is then obtained as outlined in Section 6.4, using a matrix of true and reconstructed energy as well as purity and efficiency corrections (that have been adjusted to include oscillations) and forms the fake data for the statistical sensitivity test. The spectra is the binned in the following way, which will be used for all further oscillation analyses:

- 1 GeV bins, 1-10 GeV
- 2 GeV bins, 10-20 GeV

- 10 GeV bin, 20-30 GeV
- 20 GeV bin, 30-50 GeV

This process is then repeated for a variety of values of Δm^2_{23} ($1.0 - 4.0 \times 10^{-3}$ eV^2 in steps of 5.0×10^{-5}) and $\sin^2 2\theta_{23}$ (0.6-1.0 in steps of 0.01), each spectra is compared to the fake data spectrum and a negative log-likelihood is calculated of the form:

$$-\ln \mathcal{L} = \sum_k N_k^{MC} - N_k^{DATA} \ln N_k^{MC}$$

where k refers to the k^{th} bin of the spectra. However, when using the Bayesian quartiles it is necessary to perform a separate shape and normalisation fit of the form:

$$-\ln \mathcal{L} = N^{MC} - N^{DATA} \ln N^{MC} + \sum_i^{n_{bins}} \sum_k^{n_{quartiles}} \mu_k^i - N_k^i \ln \mu_k^i$$

where N^{MC} and N^{DATA} are the total number of events in the MC and Data samples respectively, i = 1,2,3,4 and represents the four resolution quartiles, μ_k^i is value of the k^{th} bin of the PDF of the MC spectrum and N_k^i is the number of events in the k^{th} bin of the data spectrum. The minimum point is found and contours corresponding to 68% and 90% confidence intervals are obtained. The 1 σ limits on the joint measurement of the oscillation parameters are obtained by taking the outermost vertical and horizontal limits of the contour with a $\Delta \log \mathcal{L} = 0.5$, allowing a comparison of the different analysis methods. The expected contours are shown in Figure 7.10.

Configuration	Δm^2_{23} 1σ Limits 10^{-3}eV^2	Δm^2_{23} $\pm 1\sigma$ Range 10^{-3}eV^2	$\sin^2 2\theta_{23}$ 1σ Limits
1	2.516 - 3.151	0.635	≥ 0.8520
2	2.527 - 3.131	0.604	≥ 0.8587
3	2.531 - 3.109	0.578	≥ 0.8652
4	2.519 - 3.076	0.557	≥ 0.8767

Table 7.1: 1σ Statistical sensitivity limits on oscillation parameters using different analysis configurations.

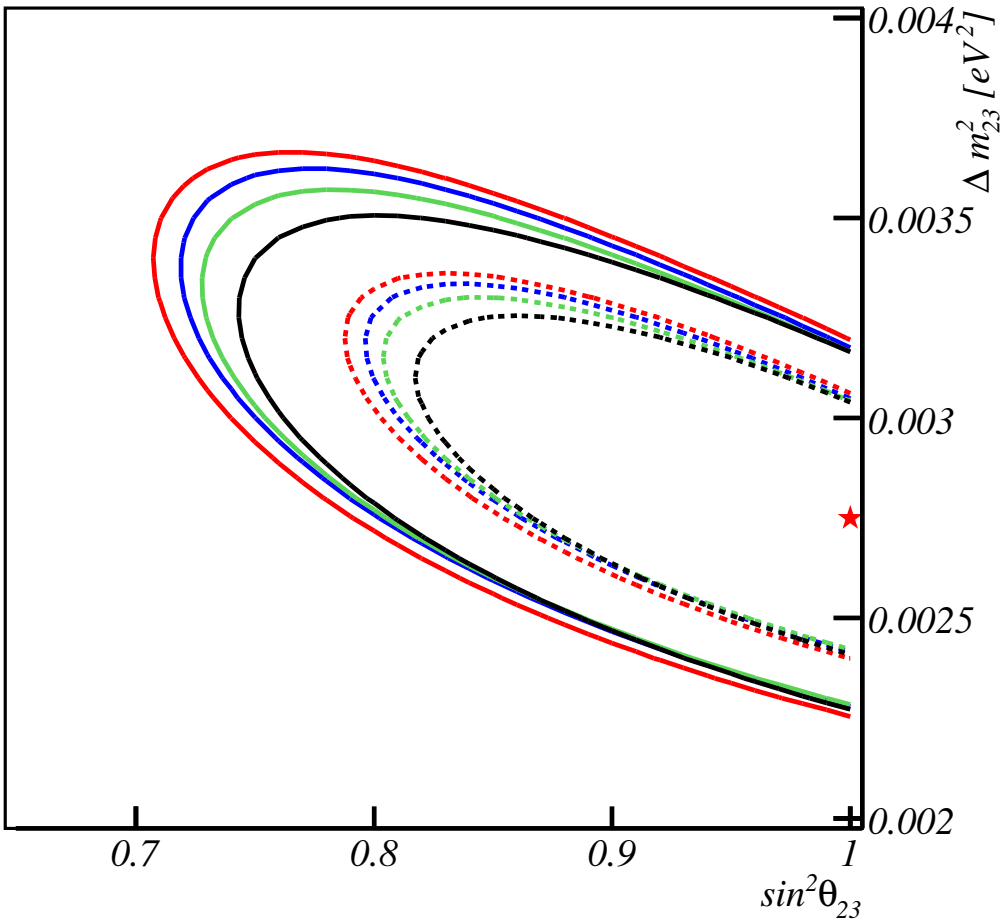

Figure 7.10: 90% (solid line) and 68% (dashed line) expected confidence limits on oscillation parameters using MINOS MC and analysis configuration 1 (red lines), 2(blue lines), 3(green lines) and 4 (black lines). The red star represents the best fit point.

It can be seen from Figure 7.10 and table 7.1 that configuration 4 gives the best resolution for $\sin^2 2\theta_{23}$, a 16% increase in resolution compared to configuration 1 is observed (i.e. equivalent to $\sim$ 30% more data). It can also be seen that configuration 4 gives the best resolution in Δm^2_{23}, a 12% increase in resolution compared to configuration 1. It can be seen that each of the subsequent configurations improves the resolution by a similar amount. This method of evaluating the uncertainites may give a very slight overestimate in the lower limit of Δm^2_{23} when compared to a χ^2 fit, due to the fact that the log likelihood method is by definition contrained to be in the physical region.

It is desirable to determine which systematic effects will have the greatest influence on the fitted parameters and determine how much these systematic shifts vary between the four analysis configurations investigated here. For each of the four analysis configurations the reconstructed Far Detector MC spectra is oscillated according to the aforementioned parameters and forms the fake data sample. The Near Detector MC reconstructed spectrum is extrapolated to the Far Detector via the beam matrix method and as before this MC expectation is oscillated and a maximum likelihood is carried out to find the best fit point in Δm^2_{23} and $\sin^2 2\theta_{23}$. It should be noted that the values returned by this fit are very slightly different than for the previous fit. This is due to differences between the Far Detector MC spectra and predicted Far Detector spectra from the matrix method caused by the fact they come from statistically independent MC samples. The fitted values of the oscillation parameters for all four configurations are noted. A systematic effect was then introduced to the Near and Far Detector reconstructed spectra. As before the Far Detector MC sample was oscillated and formed the fake data set. The Near Detector spectra was extrapolated to the Far Detector using the efficiency and purity ratios and reconstructed-true E_ν matrices derived from the nominal MC (i.e. with no systematic effect), thereby introducing the systematic effect into the Far Detector MC prediction. The maximum likelihood fit was repeated and the shift in fitted oscillation parameters was noted. As the fake data was oscillated with $\sin^2 2\theta_{23} = 1$ and the maximum likelihood is only defined for $\sin^2 2\theta_{23} \leq 1$, for this purpose it was assumed that the systematic shift in fitted $\sin^2 2\theta_{23}$ would be symmetrical around 1. The systematic effects considered, their magnitudes and effects on the fitted values of Δm^2_{23} and $\sin^2 2\theta_{23}$ are shown in tables 7.2 and 7.2. Assuming that the systematic effects are independent, the errors are added in quadrature to give an idea of the total systematic error for each configuration for each oscillation parameter.

The systematic effects covered here were found to be the most influential in an earlier more exhaustive study described in [74]. The Normalisation effect was implemented

by simply scaling the Far Detector spectrum relative to the prediction from the Near Detector and the magnitude comes from considering the uncertainty in the fiducial mass of the detectors and in the measuring the total PoT. The NC level effect was implemented by scaling the NC component of the Near and Far Detector MC and the magnitude was derived from the studies of CC hadronic showers in the Near Detector, as discussed in 5.2. The E_{shw} scaling and offset systematics reflect the uncertainty in the level of intra-nuclear re-scattering [75]. The E_{shw} offset was only implemented for events with a reconstructed shower and in the case of the negative offset, E_{shw} was not allowed to be less than zero. In the configuration 4, where there was no separate estimation of E_{shw} as E_{fit} was being used, the reconstructed value of y was used to determine how E_{fit} should be divided. The E_{μ} scaling was determined by considering systematic uncertainties in the determination of muon momenta from range and curvature. As before with configuration 4, reconstructed y was used to determine how E_{fit} should be divided between the track and the shower so the scaling could take place. CCMA refers to the axial mass involved in the CC RES and QE interactions, which affects their cross-sections and hence the E_{ν} spectrum. This effect is implemented at the MC reweighting stage. The effect of the uncertainties in the fits for hadron production and beamline effects (BEAM + SZKP) that are used for MC reweighting are also considered. $\sigma_{BEAM+SZKP}$ represents the 1σ values for the 7 parameters of the SZKP model and 5 beamline effect parameters and this is implemented at the MC reweighting stage. To take into account the additional systematic effect introduced by using the deweighting algorithm for calculating E_{shw}, configurations 3 and 4 had an additional separate E_{shw} scale systematic of 2.5% applied. It was assumed that the E_{shw} scale and oscillation parameter shift varied linearly, so the parameter shift from the previously calculated E_{shw} scale systematic (10%) was quartered. It can be seen that this was negligible when added in quadrature with the other systematic effects.

Systematic Effect	Magnitude	Δm^2_{23} shift cfg 1 $10^{-5}eV^2$	Δm^2_{23} shift cfg 2 $10^{-5}eV^2$	Δm^2_{23} shift cfg 3 $10^{-5}eV^2$	Δm^2_{23} shift cfg 4 $10^{-5}eV^2$
Normalisation	+4%	-9.0	-7.0	-7.0	-8.0
Normalisation	-4%	+6.0	+6.0	+6.0	+7.0
NC Level	+40%	+5.0	+7.0	+7.0	-2.0
NC Level	-40%	-3.0	-2.0	-2.0	+8.0
E_{shw} Scale	+10%	+6.0	+5.0	+6.0	+7.0
E_{shw} Scale	-10%	-6.0	-4.0	-7.0	-8.0
E_μ Scale	+2%	+3.0	+3.0	+4.0	+4.0
E_μ Scale	-2%	-4.0	-4.0	-4.0	-5.0
E_{shw} Offset	+150 MeV	+6.0	+7.0	+9.0	+10.0
E_{shw} Offset	-150 MeV	-5.0	-3.0	-6.0	-8.0
CCMA (QE+RES)	+10%	–	–	–	+2.0
CCMA (QE+RES)	-10%	-2.0	-1.0	-1.0	-1.0
Beam + SZKP	$+\sigma_{BEAM+SZKP}$	-2.0	–	–	–
Beam + SZKP	$-\sigma_{BEAM+SZKP}$	–	–	–	–
E_{shw} Deweighting	+2.5%	0	0	+1.5	+1.75
E_{shw} Deweighting	-2.5%	0	0	-1.75	+2.0
Total		±12.0	±11.0	±13.0	±16.0

Table 7.2: Systematic effects, their magnitudes and their effect on Δm^2_{23} for the different analysis configurations. The symbol '–' is used when there was no observed change in the fitted parameter (i.e. Δm^2_{23} shift $< \pm 10^{-5}eV^2$).

It can be seen that the largest effects are produced by the hadronic energy systematics and well as NC level and overall normalisation. It can also seen from the results of the study that all configurations give approximately the same error in $\sin^2 2\theta_{23}$ but there is some variation in the errors for Δm^2_{23}. Configurations 3 and 4 are more sensitive to variations in E_{shw} scale and offset due to the fact that they use the deweighted E_{shw}.

Systematic Effect	Magnitude	$\Delta(\sin^2 2\theta_{23})$ cfg 1	$\Delta(\sin^2 2\theta_{23})$ cfg 2	$\Delta(\sin^2 2\theta_{23})$ cfg 3	$\Delta(\sin^2 2\theta_{23})$ cfg 4
Normalisation	+4%	–	-0.01	-0.01	–
Normalisation	-4%	+0.01	+0.01	+0.01	+0.01
NC Level	+40%	-0.03	-0.04	-0.04	-0.04
NC Level	-40%	+0.03	+0.04	+0.04	+0.04
E_{shw} Scale	+10%	+0.01	+0.02	+0.01	–
E_{shw} Scale	-10%	-0.01	-0.02	-0.01	–
E_μ Scale	+2%	+0.01	–	–	–
E_μ Scale	-2%	–	–	–	–
E_{shw} Offset	+150 MeV	+0.02	+0.03	+0.02	+0.02
E_{shw} Offset	-150 MeV	-0.02	-0.03	-0.02	–
CCMA (QE+RES)	+10%	–	–	–	–
CCMA (QE+RES)	-10%	–	–	–	–
Beam + SZKP	$+\sigma_{BEAM+SZKP}$	–	–	–	–
Beam + SZKP	$-\sigma_{BEAM+SZKP}$	–	–	–	–
E_{shw} Deweighting	+2.5%	0	0	–	–
E_{shw} Deweighting	-2.5%	0	0	–	–
Total		$\pm$0.04	$\pm$0.05	$\pm$0.05	$\pm$0.04

Table 7.3: Systematic effects, their magnitudes and their effect on $\sin^2 2\theta_{23}$, $\Delta(\sin^2 2\theta_{23})$, for the different analysis configurations. The symbol '–' is used when there was no observed change in the fitted parameter (i.e. $\sin^2 2\theta_{23}$ shift $< \pm 0.01$).

7.3 Oscillation Analysis of Beam Data

An oscillation analysis is carried out on the selected beam data events using the fitted Bayesian energy and dividing up the sample into quartiles of resolution. As well as fitting combinations of oscillation parameters, the following nuisance parameters are considered as they were identified as having the largest systematic effect in the previous section: hadronic energy scale, normalisation and NC level. The log likelihood expression used is also altered to find the best fit of the nuisance parameters at each point in oscillation parameter space:

$$-\ln\mathcal{L} = N^{MC} - N^{DATA}\ln N^{MC} + \sum_{i}^{n_{bins}}\sum_{k}^{n_{quartiles}} \mu_k^i - N_k^i \ln \mu_k^i + \sum_{l}^{n_{sys}} \frac{(a^l-1)^2}{2\sigma_l^2}$$

Where n_{sys} = Hadronic Scale, Normalisation, NC Level, a is the magnitude of the systematic effect and σ is the uncertainty of each nuisance parameter. The following nuisance parameters were used. For each, the range over which it was varied and the assumed uncertainty is as follows:

- Hadronic Scale: range $\pm 30\%$, $\sigma = 10\%$
- Overall Normalisation: range $\pm 12\%$, $\sigma = 4\%$
- NC level: range 0 - 250%, $\sigma = 40\%$

It is also necessary to consider any contribution from CC interactions of ν_τ that have oscillated from beam ν_μ. A sample of ν_τ MC with an identical spectrum to the NuMI beam and normalised to have an equivalent PoT to the beam data is passed through the Bayesian fit and divided into the same resolution quartiles as for the beam events. Selected events are then weighted via the $\nu_\mu \rightarrow \nu_\tau$ oscillation probability to give the expected Far Detector ν_τ spectrum, which is added to the MC prediction before the likelihood is calculated. This is expected to be very low because the $\nu_\mu \rightarrow \nu_\tau$ oscillation probability is only large for low energies and the neutrino energy threshold to produce a tau lepton is 3.5 GeV. Also a large proportion of the tau decays will not produce a muon. This means their events will not topologically resemble a CC ν_μ interaction so are likely to fail the selection cuts, further reducing the ν_τ contribution.

Figure 7.11 shows the results of the fit along with the results of several other neutrino oscillation experiments. The best fit point is found to be $\Delta m^2_{23} = 2.55 \times 10^{-3}\,\mathrm{eV}^2$ and $\sin^2 2\theta_{23} = 1.0$. As before, the 1σ limits on the joint measurement of the oscillation parameters are obtained by taking the outermost vertical and horizontal limits of the contour with $\Delta \log\mathcal{L} = 0.5$. The 1σ limits on the parameters are $2.31 \leq \Delta m^2_{23} \leq 2.94 \times 10^{-3}\,\mathrm{eV}^2$ and $\sin^2 2\theta_{23} \geq 0.869$.

The best fit values for the nuisance parameters at the best fit point are:

- Hadronic Scale: -6%
- Overall Normalisation: +4%

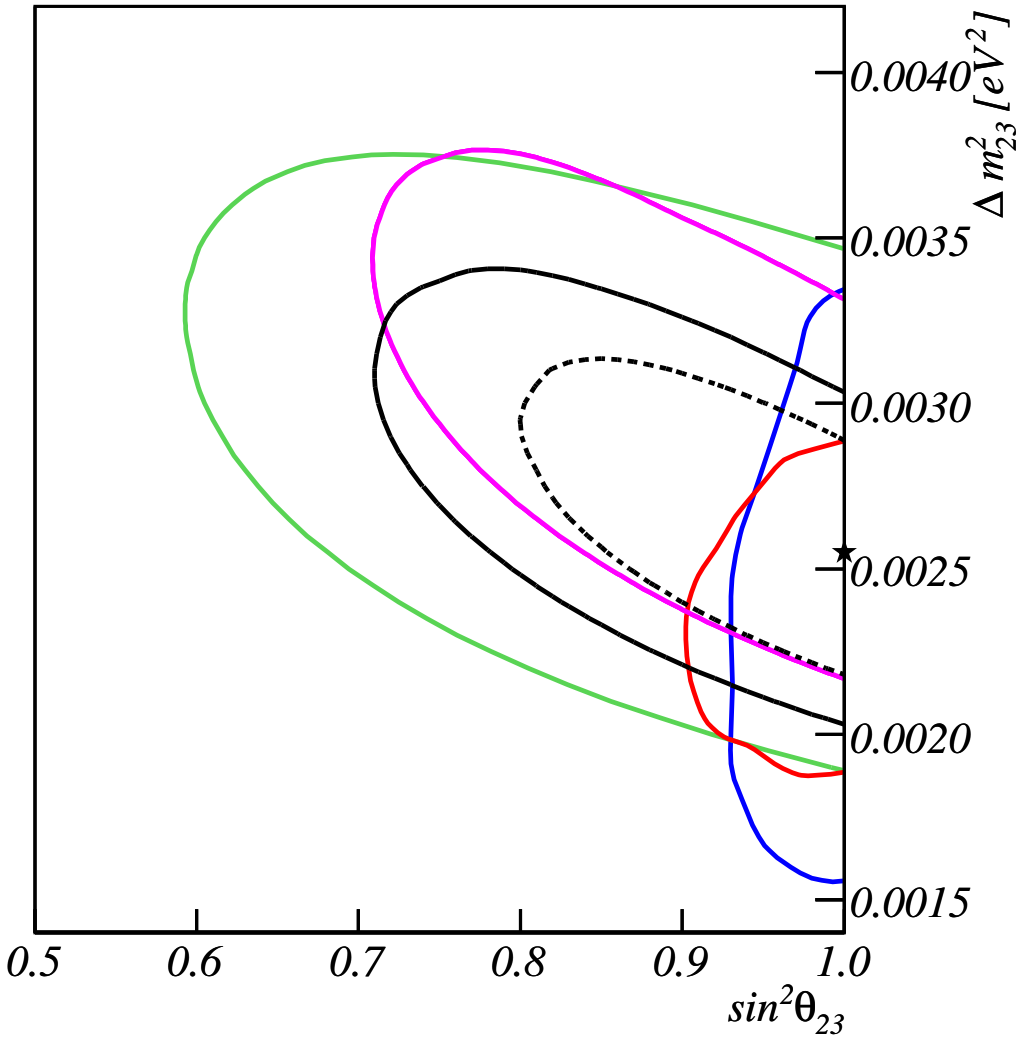

Figure 7.11: 90% (solid line) and 68% (dashed line) confidence limits on oscillation parameters. The different colors represent different experiments and anlyses: K2K (green) [76], SK - zenith angle (blue) [19], SK - L/E (red) [46], MINOS PRL [68] (pink), MINOS - this analysis (black). The star represents the best fit point of this analysis.

- NC level: +25%

It can be seen that the fitted value for the oscillation parameters agrees well with the other experiments and that there is a slight improvement in the limits over the existing MINOS analysis due to the improvements outlined in this thesis. This level of improvement would have been greater if these two results had the same fitted Δm^2_{23} as oscillation parameter sensitivity scales with Δm^2_{23} due to the shape of the NuMI beam spectrum. Figure 7.12 shows the E_{fit} distributions for data, MC (both unoscillated and oscillated with best fit parameters) and the best fit NC and tau backgrounds. It can be seen that there is good agreement between the best fit and the data. It can also be seen that the ν_τ contribution is small; giving a total of 1.97 events. The best fit nuisance parameters include an increase in NC and overall normalisations levels, this is why in some bins in the plots, the best fit MC is greater than the unoscillated prediction. The total number of data events in the selected sample was 378, compared with a best fit prediction of 360 ± 24 and a non-oscillation prediction of 459 ± 31. For events with $E_{fit} \leq 10$ GeV these numbers are 221, 228 ± 15 and 326 ± 22 respectively. These numbers were obtained by combining the four resolution quartiles.

To determine the level at which the null hypothesis of no oscillations is disproved, the following χ^2 was calculated:

$$\chi^2 = \sum_i^{n_{bins}} (2(e_i - o_i) + 2o_i \ln \frac{o_i}{e_i}) + \sum_j^{n_{sys}} \frac{\Delta s_j^2}{\sigma_{s_j}^2}$$

where e_i and o_i are the number of events in each bin of the Far Detector unoscillated MC expectation and data respectively. Δs is the change in the level of nuisance parameter and σ_s is its associated error. The same nuisance parameters are used as for the oscillation analysis. The χ^2 was minimised with respect to the nuisance parameters and the minimum value was 61.4/17. This disproves the null hypothesis at a confidence level greater than 99.99%, providing very strong evidence for oscillations. The above expression is also used to quantify the quality of the fit. The best fit spectra of the four resolution quartiles are added together, shown in Figure 7.13, to increase the statisitcs to make the use of Gaussian statistics reasonable. The combined best fit spectra returned a χ^2/ndf value of 15.0/15, showing good agreement between the best fit and the data. Figure 7.14 shows the ratio of data (and best fit oscillated MC) and non-oscillated MC for a combined sample of the 1st and 2nd resolution quartiles. This sample has the best

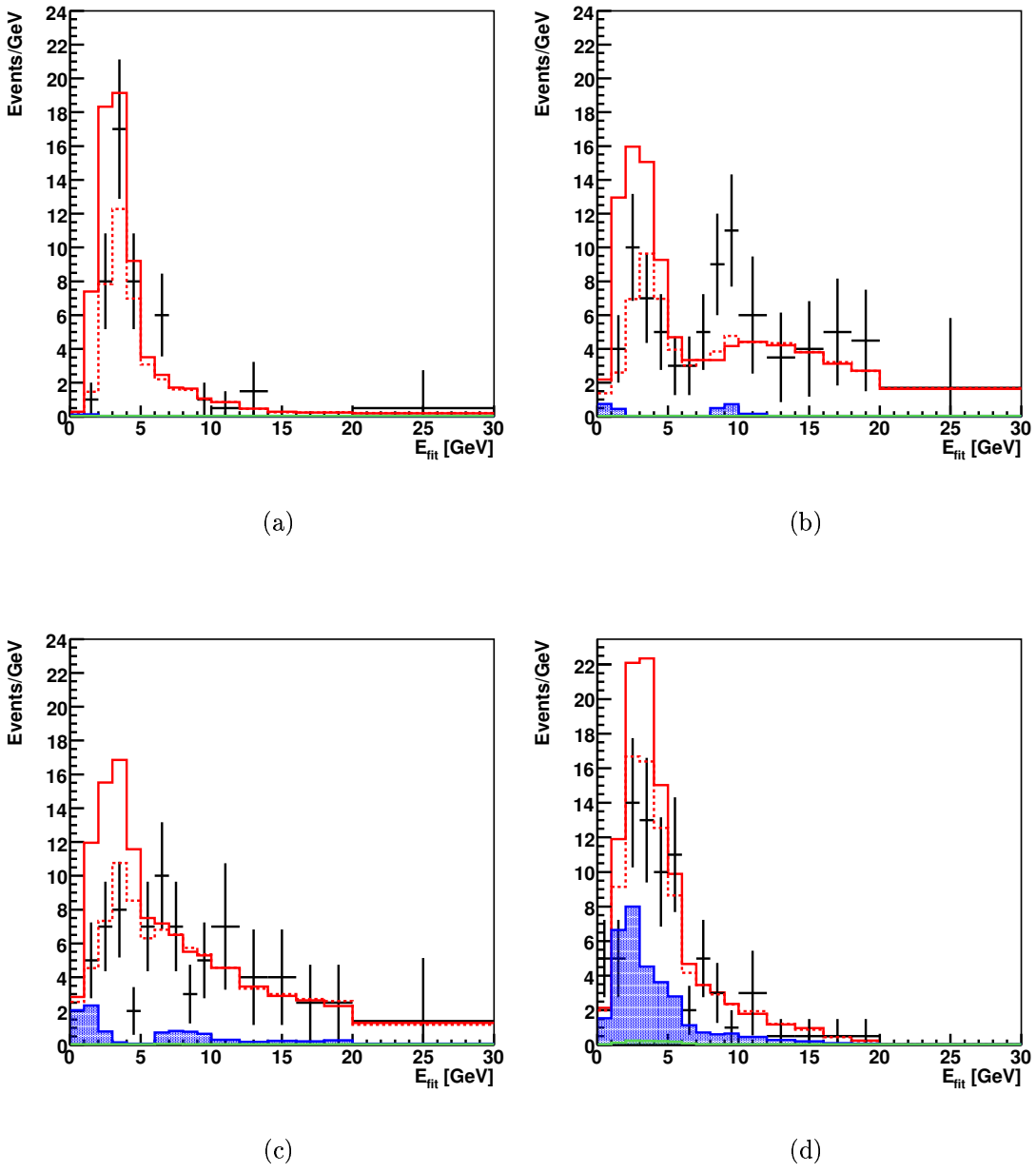

Figure 7.12: Far Detector E_{fit} for the four quartiles of energy resolution (a) 1st quartile (b) 2nd quartile (c) 3rd quartile (d) 4th quartile. The plots show data (black points), MC expectation with no oscillations (solid red line), MC expectation at the best fit point (red dashed line), MC expectation for the contribution from NC events at the best fit point (blue shaded area) and tau component of the MC at the best fit point (green shaded area).

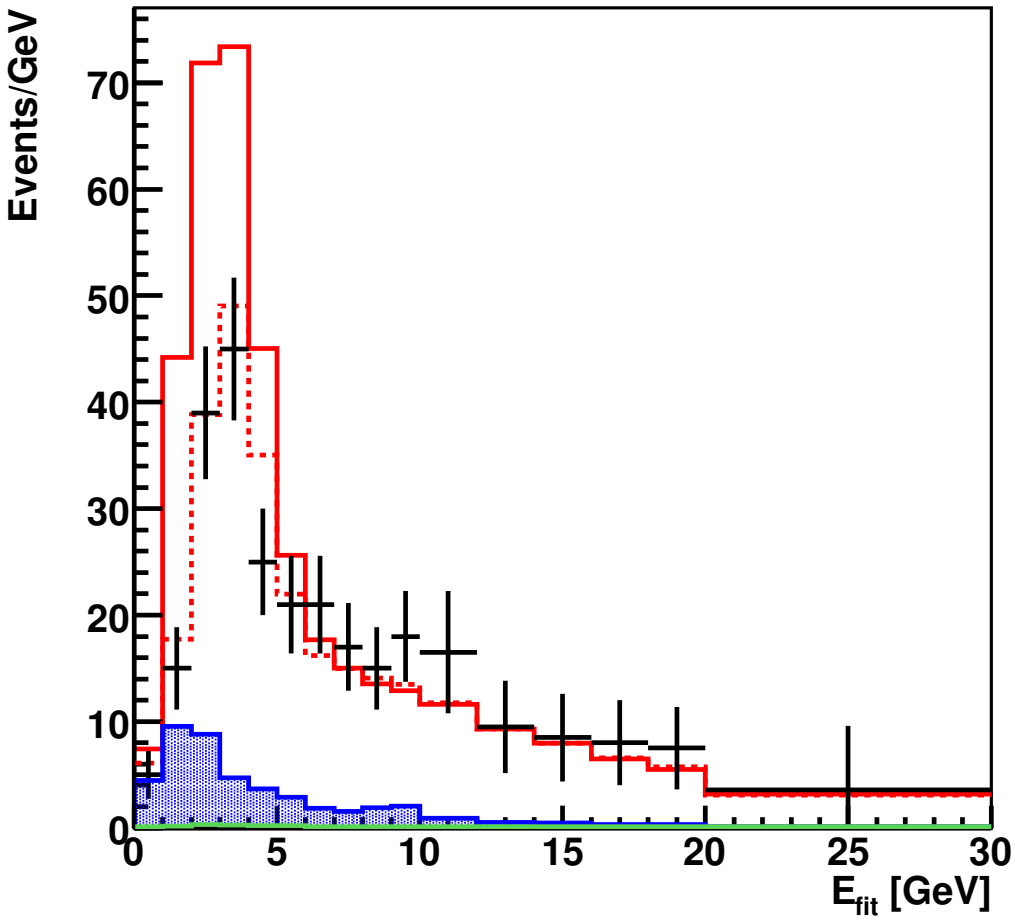

Figure 7.13: Far Detector E_{fit} summed over the four resolution quartiles. The plots show data (black points), MC expectation with no oscillations (solid red line), MC expectation at the best fit point (red dashed line), MC expectation for the contribution from NC events at the best fit point (blue shaded area) and tau component of the MC at the best fit point (green shaded area).

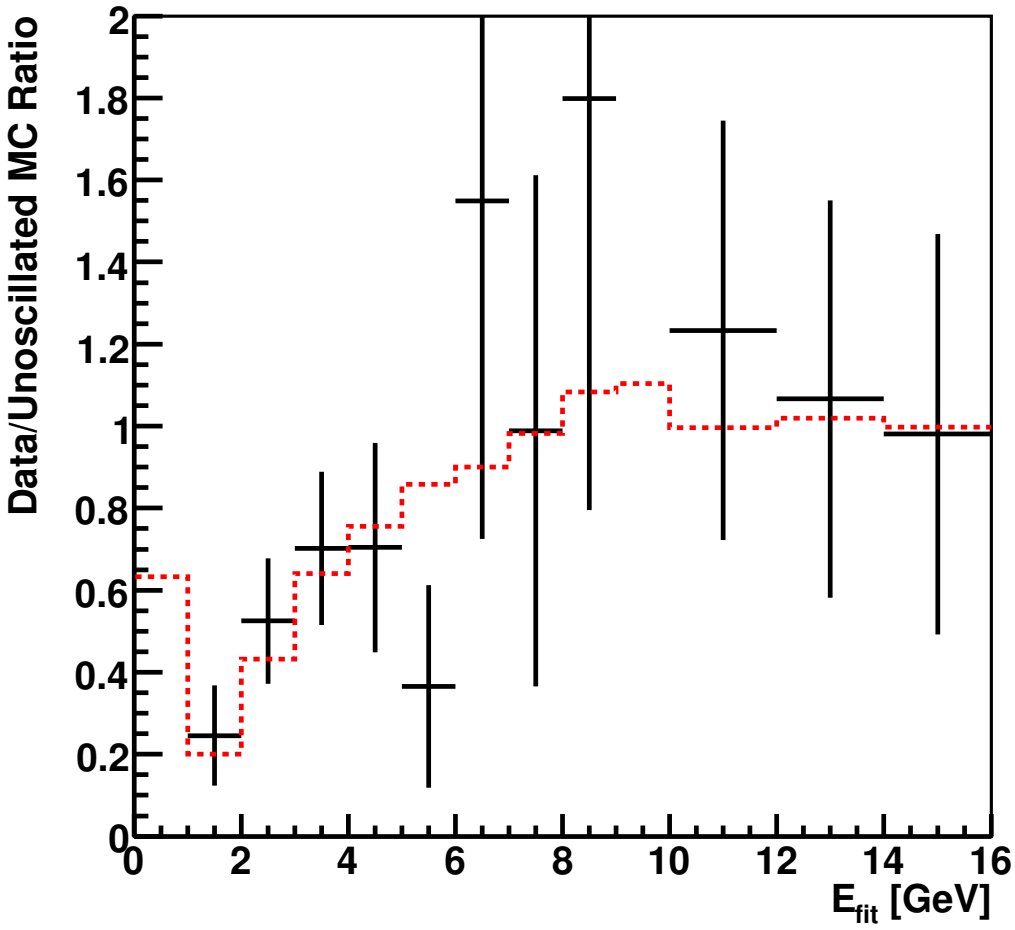

Figure 7.14: Far Detector E_{fit} ratio of Data/Unoscillated MC for combined 1st and 2nd resolution quartiles. The best fit oscillated MC is shown as the dashed red line.

energy resolution while containing very little NC background. It can be seen that the minimum point in the ratio is at 0.25. In the decoherence hypothesis [30], this ratio can never go below 0.5. This shows that the MINOS data significantly favour the oscillation hypothesis over decoherence.

Chapter 8

Conclusions and Outlook

"If you want a happy ending, that depends, of course, on where you stop your story."
— Orson Welles

The Fermilab Main Injector has currently delivered 1.27×10^{20} PoT to the NuMI target. The interactions of the resulting ν_μ beam have been observed in the Near and Far MINOS detectors between May 2005 and February 2006. A GPS signal is used to define a time window for the expected time of arrival at both detectors. During the experimental run, the conditions of the beam and detector systems have been continuously monitored to ensure the quality of the data. The response of both detectors has been calibrated using cosmic muons.

The MINOS reconstruction software is optimised to search for and determine the energy of ν_μ CC events consisting of a muon track and a hadronic shower. The same algorithms are used in both detectors apart from certain special cases such as removing the 8-fold strip ambiguity in the Far Detector and slicing overlapping events in the Near Detector. A method based on deweighting the charges associated with individual shower strips is used to suppress fluctuations in deposited charge from soft protons and so improve low energy shower resolution. A fractional E_{shw} resolution for 1 GeV CC showers of 0.50 ± 0.09 is obtained, compared to 0.69 ± 0.13 without the deweighting.

To address uncertainties in the production of hadrons that make the neutrinos in the NuMI beam and their propagation through the various components of the beamline, the beam was run in several different configurations and a model was developed to

parameterise hadronic production in the NuMI target. This model was then used to fit the MINOS Monte Carlo to the data over all configurations. Further Data/MC comparison shows generally good agreement in most event variables but some differences are observed related to incomplete modelling of the hadronic showers in the detector. The removal of NC background is achieved using the PDFs of several non-correlated discriminating quantities to define a PID variable. An estimate for the systematic error in the level of NC background in the sample surviving this PID cut, caused by the incomplete shower modelling, is achieved by studying Data/MC differences of CC events that have had the muon track removed. Applying the corrections obtained from this study to the NC component of the Near Detector MC is seen to improve agreement with the data PID distribution.

The Near Detector Data spectrum is extrapolated to the Far Detector using information about the neutrinos parent particles from the MC flux files. The Far Detector fiducial volume is optimised so as maximise the number of data events in the sample, while ensuring the quality of these events and that the background due to cosmic muons remains negligible. The optimised fiducial volume is 16% larger than that used for the original MINOS analysis [68]. A Bayesian approach is used to assign each selected event an energy based on its reconstructed quantities. Each event is also assigned an uncertainty, allowing the sample to be divided into subsamples of varying energy resolution. Using this fitted energy and subsamples in an oscillation analysis improves the resolutions of Δm^2_{23} and $\sin^2 2\theta_{23}$ by 4% and 9% respectively compared with a single sample using the standard reconstructed energy. A total of 378 events are selected in the Far Detector data, showing a clear deficit from the MC prediction of 459 ± 31 events, and significant low energy spectral distortion is also observed.

Comparisons of the statistical and systematic sensitivity achieved with different reconstruction and fitting methods for an oscillation analysis are carried out. A maximum likelihood analysis, assuming two flavour oscillations, returned a best fit values for Δm^2_{23} and $\sin^2 2\theta_{23}$ of $2.55^{+0.39}_{-0.24} \times 10^{-3}\,\mathrm{eV}^2$ and > 0.87 (68% C.L.) respectively. This represents a 10% improvement in Δm^2_{23} resolution relative to the original MINOS analysis. This fit also included the systematic parameters of overall normalisation, NC background level and hadronic energy scale. The null oscillation hypothesis is disproved at a probability greater than 99.99% and the best fit MC/Data χ^2/ndf is calculated as 15.0/15.

The goal of the MINOS experiment is to set new sensitivity limits for Δm^2_{23} and $\sin^2 2\theta_{23}$. Should the experiment reach its intended 5 year goal of 7.4×10^{20} POT, then the expected limits on Δm^2_{23} and $\sin^2 2\theta_{23}$(assuming the same best fit values) will be $2.55 \pm$

$0.21 \times 10^{-3}\,\mathrm{eV}^2$ and > 0.93 (68% C.L.) respectively. The beam analysis could gain additional sensitivity by including information from rock muons in the fit. These are muons created by NuMI beam neutrinos that interact in the rock around the detector whose tracks end within the detector and could be selected by tight timing cuts around the spillserver predicted time and requiring that the muon tracks pointed back towards Fermilab. MINOS will also continue to collect atmospheric neutrino data and will be able to search for CPT violation by comparing the oscillation analyses of neutrino and anti-neutrino data as identified by the magnetic field.

By reversing the direction of the current in the magnetic focusing horns, it is possible to focus π^- and K^- that are produced in the target volume and defocus positive particles leading to a $\overline{\nu}_\mu$ beam. It may be necessary to remake the PID variable PDFs and recalibrate the shower energy due to there being a different charge on the hadronic system, which could affect shower properties and $\overline{\nu}_\mu$ events would be selected by requiring tracks with $q/p > 0$. An analysis could then be carried out to attempt to measure any difference between between $\Delta \mathrm{m}^2_{23}$ and $\sin^2 2\theta_{23}$ and the oscillation parameters of anti-neutrinos, $\Delta\overline{\mathrm{m}}^2_{23}$ and $\sin^2 2\overline{\theta}_{23}$.

One of the important systematic errors in MINOS is the uncertainty associated with hadronic production in the NuMI target, that determine the E_ν spectrum in the Near Detector. These will hopefully be reduced with the results from the MIPP experiment [77], which will study particle production from π, K and p beams on a variety of target materials. The experiment uses a large range of detection methods including a time projection chamber, ring-imaging Cherenkov detector, Electromagnetic and Hadronic calorimeters and drift and proportional chambers to identify nearly all produced charged particles. MINOS will especially benefit, as MIPP will be conducting a special run where protons from the Main Injector will be diverted to MIPP in which a copy of the NuMI target will be installed, resulting in detailed knowledge of hadronic production in the NuMI target.

The Bayesian method described in this analysis would benefit massively from a large increase in Far Detector MC statistics, as this would allow for much greater widths of the detector response functions and as well as a much finer binning for the fitted energy. Also if the method was adapted for the near detector (as the detector response functions would change due to slicing) then the ability to define samples of different interaction type could be useful for determining neutrino interaction cross-sections.

The observation of ν_e interactions, associated with the NuMI beam in the MINOS Far

Detector would be very significant as the appearance of ν_e in a ν_μ beam via $\nu_\mu \rightarrow \nu_e$ oscillations requires a non-zero value of θ_{13} that would allow future studies of CP violation in the leptonic sector as well as the chance to determine the neutrino mass hierarchy. However, unambiguous identification of ν_e is challenging in the MINOS, due to the coarseness of the detectors, contamination from ν_e produced in the NuMI beamline and a large background of NC events. Identification of ν_e events is achieved via 3-Dimensional topological analysis of EM showers in MC. It is expected that after two years running, MINOS should be able to improve the CHOOZ limit on θ_{13} by a factor of two [78].

Bibliography

[1] D. H. Perkins, *Introduction to High Energy Physics*, CUP, 2000.

[2] E. Fermi, An attempt of a theory of beta radiation, *Zeit. Phys.* **88**, 161 (1934).

[3] F. Reines and C. Cowan, Detection of the free neutrino, *Phys. Rev.* **92**, 830 (1953).

[4] G. Danby *et al.*, Observation of high-energy neutrino interactions and the existence of two kinds of neutrinos, *Phys. Rev. Lett.* **9**, 36 (1962).

[5] The DONUT Collaboration, Observation of tau neutrino interactions, *Phys. Lett.* **B504**, 218 (2001).

[6] L. Goldhaber, M. Grodzins and A. Sunyar, Helicity of neutrinos, *Phys. Rev.* **109**, 1015 (1958).

[7] C. Kraus *et al.*, Final results from the phase II of the Mainz neutrino mass search in Tritium β decay, *Eur. Phys. J.* **C40**, 447 (2005).

[8] K. Assamagan *et al.*, Upper limit of the muon neutrino mass and charged pion mass from momentum analysis of a surface muon beam, *Phys. Rev.* **D53**, 6065 (1996).

[9] Roney J., Review of the tau neutrino mass, *Nucl. Phys. Proc. Suppl.* **91**, 287 (2001).

[10] D. Barger, V. Marfatia and A. Tregre, Neutrino mass limits from SDSS, 2dFGRS and WMAP, *Phys. Lett.* **B595**, 55 (2004).

[11] K. S. Krane, *Introductory Nuclear Physics*, Wiley, 1988.

[12] J. Bahcall and M. Pinsonneault, What we do (not) know theoretically about solar neutrino fluxes?, *Phys. Rev. Lett.* **92**, 121301 (2004).

[13] B. Pontecorvo, Inverse beta processes and non conservation of lepton charge, *Sov. Phys. JETP* **7**, 172 (1958).

[14] The Super-Kamiokande Collaboration, Solar neutrino precision measurments using all 1496 days of Super-Kamiokande I data, *Nucl. Phys. Proc Suppl.* **118**, 25 (2003).

[15] The SNO Collaboration, Electron energy spectra, fluxes and day-night asymmetries of ^{8}B neutrinos from measurements with NaCl dissolved in the heavy-water detector at the Sudbury Neutrino Observatory, *Phys. Rev.* **C72**, 055502 (2005).

[16] The KAMLAND Colaboration, Measurement of Neutrino Oscillation with Kamland: evidence of spectral distortion, *Phys. Rev. Lett.* **94**, 081801 (2005).

[17] K. Zuber, , *Acta Phys. Polon.* **B37**, 1905 (2006).

[18] M. Kobayashi and T. Maskawa, CP violation in the renormalisable theory of weak interaction, *Prog. Theor. Phys.* **49**, 652 (1973).

[19] The Super-Kamiokande Collaboration, A measurement of atmospheric neutrino oscillation parameters by Super-Kamiokande I, *Phys. Rev.* **D71**, 112005 (2005).

[20] L. Wolfenstein, Neutrino oscillations in matter, *Phys. Rev.* **D17**, 2369 (1978).

[21] S. Mikheev and A. Smirnov, Resonant amplification of neutrino oscillations in matter and solar neutrino spectroscopy, *Nuovo. Cim.* **9**, 17 (1986).

[22] M. Bahcall, J. Pinsonneault and S. Basu, Solar models: current epoch and time dependencies, neutrinos and helioseismological properties, *Astrophys. J.* **555**, 990 (2001).

[23] J. Bahcall and P. Carlos, Solar Models and Solar Neutrino Oscillations, *New J. Phys.* **6**, 63 (2004).

[24] S. Degl'Innocenti *et al.*, Helioseismology and standard solar models, *Astrop. Phys.* **7**, 77 (1997).

[25] B. Cleveland *et al.*, Measurement of the solar electron neutrino flux with the Homestake chlorine detector, *Astrophys. J.* **496**, 505 (1998).

[26] The SAGE Collaboration, Solar neutrino flux measurements by the Soviet-American Gallium Experiment (SAGE) for half the 22 year solar cycle, *J. Exp. Theor. Phys.* **95**, 181 (2002).

[27] The GALLEX Collaboration, GALLEX solar neutrino observations: results for GALLEX IV, *Phy. Lett.* **B447**, 127 (1999).

[28] The GNO Collaboration, Complete results for five years of GNO solar neutrino observations, *Phys. Lett.* **B616**, 174 (2005).

[29] The Super-Kamiokande Collaboration, Determination of solar neutrino oscillation parameters using 1496 days of Super-Kamiokande I data, *Phys. Lett.* **B539**, 179 (2002).

[30] G. Barenboim *et al.*, Quantum decoherence and neutrino data, *Nucl. Phys.* **B758**, 90 (2006).

[31] Barger V., Neutrino decay as an explanation of atmospheric neutrino observations, *Phys. Rev. Lett.* **82**, 2640 (1999).

[32] M. Apollonio *et al.*, Search for neutrino oscillations on a long baseline at the CHOOZ nuclear power station, *Eur. Phys. J.* **C27**, 331 (2003).

[33] The Double CHOOZ Collaboration, Double CHOOZ: Optimising CHOOZ for a possible θ_{13} measurement, *Nucl. Phys. Proc. Suppl.* **155**, 227 (2006).

[34] J. Cao, Daya bay neutrino experiment, *Nucl. Phys. Proc. Suppl.* **155**, 229 (2006).

[35] The MINOS and NOvA Collaborations, The MINOS and NOvA experiments, *Nucl. Phys. Proc. Suppl.* **149**, 150 (2005).

[36] The T2K Collaboration, T2K experiment, *Nucl. Phys. Proc. Suppl.* **145**, 178 (2005).

[37] R. Becker-Szendy *et al.*, Neutrino measurments with the IMB detector, *Nucl. Phys. Proc. Suppl.* **38**, 331 (1995).

[38] The Kamiokande Collaboration, Atmospheric ν_μ/ν_e ratio in the Multi-GeV energy range, *Phys. Lett.* **B335**, 237 (1994).

[39] The Frejus Collaboration, Study of atmosheric neutrino interactions with the Frejus detector, *Phys. Lett.* **B227**, 489 (1989).

[40] The NUSEX Collaboration, Experimental study of atmospheric neutrino flux in the NUSEX experiment, *Europhys. Lett.* **8**, 611 (1989).

[41] T. Gaisser and M. Honda, Flux of atmospheric neutrinos, *Ann. Rev. Nucl. Part. Sci.* **52**, 153 (2002).

[42] M. Mann, Atmospheric neutrinos and the oscillation bonanza, *Int. J. Mod. Phys.* **A15S1**, 229 (2000).

[43] C. Smith, *Calibration of MINOS detectors and extraction of neutrino oscillation parameters*, PhD thesis, University College London, 2002.

[44] The Soudan 2 Collaboration, Measurement of the L/E distributions of atmospheric neutrinos in Soudan 2 and their interpretation as neutrino oscillations, *Phys. Rev.* **D68**, 113004 (2003).

[45] The MACRO Collaboration, MACRO results on atmospheric neutrinos, *Nucl. Phys. Proc. Suppl.* **145**, 116 (2005).

[46] The Super-Kamiokande Collaboration, Evidence for an oscillatory signature in atmospheric neutrino oscillation, *Phys. Rev. Lett.* **93**, 101801 (2004).

[47] The MINOS Collaboration, First observations of separated atmospheric ν_μ and $\overline{\nu}_\mu$ events in the MINOS detector, *Phys. Rev.* **D73**, 072002 (2006).

[48] The K2K Collaboration, Evidence for muon neutrino oscillation in an accelerator based experiment, *Phys. Rev. Lett.* **94**, 081802 (2005).

[49] The LSND Collaboration, Evidence for neutrino oscillation from the observation of $\overline{\nu}_e$ appearence in a $\overline{\nu}_\mu$ beam, *Phys. Rev.* **D64**, 112007 (2001).

[50] The MiniBooNE Collaboration, Current status of the MiniBooNE experiment, *Int. J. Mod. Phys.* **A20**, 3062 (2005).

[51] The KARMEN Collaboration, Upper limits for $\overline{\nu}_\mu \to \overline{\nu}_e$ from muon decay at rest, *Phys. Rev.* **D65**, 112001 (2002).

[52] Y. Declais *et al.*, Search for neutrino oscillations at 15 metres, 40 metres and 95 metres from a nuclear power reactor at Bugey, *Nucl. Phys.* **B434**, 503 (1995).

[53] Yao W. and others, Review of particle physics, *J. Phys.* **G33**, 1 (2006).

[54] J. Hylen *et al.*, NuMI technical design handbook, *Internal NuMI report* (2003).

[55] D. Petyt, First results from the NUMI beam, *Numi-1680* (2006).

[56] N. Felt *et al.*, MINOS far detector electronics users' manuel, *Numi-901* (2003).

[57] J. Drake, G. Dawson and C. Nelson, Overview of the front end electronics for the MINOS near detector, *Numi-L-628* (1999).

[58] M. Kokdosky, *Hadronic Interactions in the MINOS detectors*, PhD thesis, University of Texas at Austin, 2004.

[59] P. Vahle, *Electromagnetic Interactions in the MINOS detectors*, PhD thesis, University of Texas at Austin, 2004.

[60] J. Hartnell, *Measurement of the calorimetric energy scale in the MINOS*, PhD thesis, St. John's College, Oxford University, 2005.

[61] A. Fasso *et al.*, Fluka: a multi-particle transport code, *CERN-2005-10* (2005).

[62] H. Gallagher, The NEUGEN neutrino event generator, *Nucl. Phys. Proc. Suppl.* **112**, 188 (2002).

[63] T. Gaisser, *Cosmic rays and particle physics*, CUP, 1990.

[64] N. Tagg, Global event timing in MINOS, *Numi-ANA-1090* (2005).

[65] N. Tagg, Blindness Implementation, *Numi-1070* (2006).

[66] M. Thomson, Alternative DeMuxer: AltDeMux, *Numi-2535* (2006).

[67] P. Ballester, Hough transform for robust regression and automated detection, *Astron. Astrophys.* **286**, 1011 (1994).

[68] The MINOS Collaboration, Observation of muon neutrino disappearance with the MINOS detectors and the NuMI neutrino beam, *Phys. Rev. Lett.* **97**, 191801 (2006).

[69] Z. Kopp, S. Pavlovic and T. Vahle, Fitting the beam MC to the ND data, *Numi-1548* (2006).

[70] M. Szleper and A. Para, Neutrino Spectrum at the Far Detector Systematic Errors, *Numi-781* (2001).

[71] M. Thomson, Possible Applications of Bayesian Fitting to the Beam Analysis, *Numi-1433* (2006).

[72] H. Gallagher, Event tuning in the resonance region for the MINOS experiment, *Nucl. Phys. Proc. Suppl.* **159**, 229 (2006).

[73] J. Chapman, Private Communication.

[74] J. Evans *et al.*, Oxford systematics study for the 1.3E20 PoT CC analysis, *Numi-2094* (2006).

[75] R. Merenyi *et al.*, Determination of pion intranuclear rescattering rates in $\nu_\mu -$ Ne versus $\nu_\mu -$ D interactions for the ν atmospheric flux, *Phys. Rev.* **D45**, 743 (1992).

[76] The K2K Collaboration, Measurment of neutrino oscillation by the K2K experiment, *Phys. Rev.* **D74**, 072003 (2006).

[77] The MIPP Collaboration, Physics of the MIPP Experiment, *Nucl. Phys. Proc. Suppl.* **142**, 453 (2005).

[78] A. Sousa, *Studies of $\nu_\mu \rightarrow \nu_e$ Oscillation Appearence in the MINOS Experiment*, PhD thesis, Tufts University, 2006.

List of Figures

List of Tables